University of the Free State

Masters Thesis

The search for pulsed radio and gamma-ray emission from the cataclysmic variable system AE Aquarii using MeerKAT and Fermi-LAT data.

Author: Spencer Tendai Madzime

Supervisor: Professor. P.J. Meintjes

Co-Supervisor: Dr. H. J. van Heerden

This thesis is submitted in fulfilment of the requirements
for the degree, Master of Science

in the

Faculty of Natural and Agricultural Sciences
Department of Physics

December 16, 2021

Declaration of Authorship

I, Spencer Tendai MADZIME, declare that this thesis titled, "The search for pulsed radio and gamma-ray emission from the cataclysmic variable system AE Aquarii using MeerKAT and Fermi-LAT data." and the work presented in it are my own. I confirm that:

- This work was done wholly while I was a student for a research degree at this University.
- It is clearly indicated where any section of this thesis has been previously submitted for a degree or any other qualification at any other institution or this University.
- Where I have made use of others' published work, this is always clearly attributed.
- a source is always given where I have quoted from others' work.
- I have acknowledged all main sources of help.

Signed:

Date:

Abstract

The search for pulsed radio and gamma-ray emission from the cataclysmic variable system AE Aquarii using MeerKAT and Fermi-LAT data.

by Spencer Tendai MADZIME

The nova-like AE Aquarii was extensively studied using $\sim$ 11 years of data and contemporaneous optical data with the aim to establish pulsed gamma-ray emission at the rotational period (33.08 s) of the white dwarf and the first harmonic (16.54 s). In addition the study was also aimed at identifying pulsed radio emissions at or near the fundamental frequency. Therefore the search of pulsed radio and gamma-ray emission using MeerKAT (radio) data and upgraded Fermi-LAT pass 8 (gamma-ray) datasets is presented.

The L-band 45 mins observation of AE Aquarii resulted in the first detection of this source by the MeerKAT telescope. Also, the pulsed radio emission search resulted in the first detection of pulsed emission modulated at the white dwarf's rotational period (33.08 s). Further investigation resulted in no indication of any pulsations at the first harmonic (16.54 s). The pulsed signal's overall strength is confined to lower L-band frequencies at the onset of the flare event. No pulsations were significant at the peak of the flare-like event. The spectral variation investigations revealed an optically thin spectrum. This optically thin spectrum observed in the MeerKAT data appears to be uncorrelated to the overall radio spectrum up to $\sim$ 1000 GHz. Hence, a correlation between the MeerKAT data and observations at higher frequencies could be an exciting topic for in-depth follow-up studies.

Investigation for gamma-ray emission from AE Aquarii was conducted using an $\sim$ 11-year baseline of the archived upgraded Fermi-LAT pass 8 dataset. The standard binned and unbinned analyses techniques resulted in no detection of any significant gamma-ray excess in the region of AE Aquarii. However, the search for transient burst-like gamma-ray emission through a light curve revealed sections of the data with an excess significance of 2 σ. A search for pulsed gamma-ray emission from these sections resulted in substantial evidence of pulsed signal from some of these sections with excess significance. An additional search for pulsed gamma-ray emission using shorter time bins resulted in detecting more significant pulsations at both the fundamental (33.08 s) and the first harmonic (16.54 s) frequencies. The stacked periodogram displayed clear evidence of particle acceleration from two polar zones of the white dwarf in AE Aquarii, which resulted in a double pulse. Periods contemporaneous to observed optical flares displayed weak pulsations in the noise level. After stacking the periodograms, a significance of over 4 σ is seen at the fundamental frequency (33.08 s). A further search for evidence of sporadic burst-like gamma-ray emission from AE Aquarii using refined or more selective filtered data resulted in the detection of AE Aquarii with a significance of $\sim$ 14 σ from both the binned and unbinned analyses techniques. The gamma-rays detected from a more constrained refined filtered dataset show clear gamma-ray spectral hardening above the galactic gamma-ray emission. These results have significant implications for follow-up studies of AE Aquarii using ground-based Cherenkov telescopes.

Acknowledgements

I would like to express my sincere gratitude towards the following:

- Professor P. J. Meintjes for his willingness to have me as his student and his unmatched effort towards this work's quality, which includes a multitude of advice and suggestions. His parental guidance, continuous motivation, moral support, and financial assistance have been of immense importance.
- Dr. H. J. van Heerden for his unparalleled input towards the success of this project, not also forgetting to mention the input of Dr. R Britto and Dr. K. K. Shingh.
- My family members, relatives, and friends for their encouragement and moral support.
- The members of the UFS Department of Physics and the members of the UFS High-performance computing. Many thanks to the HoD, Professor J. J. Terblans, for allowing me to participate in the departmental activities, e.g., tutoring undergraduate students.
- The Inter-University Institute for Data Intensive Astronomy (IDIA) data intensive research cloud for data processing team. IDIA is a South African university partnership involving the University of Cape Town, the University of Pretoria and the University of the Western Cape.
- The National Research Foundation (NRF) for financial assistance.
- My God, who saw me through moments of despair and success.

Contents

List of Figures

List of Tables

Dedicated to my late parents
Robert Madzime (Father) and Maria Madzime (Mother)

Chapter 1

Introduction

The astrophysical source AE Aquarii (AE Aqr) has been studied extensively since the early 20th century. AE Aqr is a cataclysmic variable (CV) binary star which consists of a rapidly rotating magnetised white dwarf orbiting a late-type main sequence companion star. Zinner [24] discovered the nova-like variable characteristics of AE Aqr due to its rapid variability with a visible magnitude ranging between $m_v \sim 12$ (quiescence) and $m_v \sim 10$ (flares) at optical wavelengths. Further spectroscopic studies showed that the system is a close binary system with an orbital period of 9.88 hours (h) [25, 26, 27]. AE Aqr is a magnetic CV which was initially erroneously classified as a DQ Her system, based on some similarities with DQ Herculis. But later studies revealed that the system is significantly different, since the white dwarf currently accretes very little material as a result of magnetospheric propellering from the rapidly rotating magnetosphere of the white dwarf driving the mass transfer flow from the secondary star out of the binary system [7, 28].

The system exhibits a high amount of transient emission, with regular flaring, lasting from minutes to hours. For example AE Aqr shows regular but aperiodic outbursts ($\Delta m_v \sim 2$) in optical emission [24, 27] as well as numerous smaller flares ($\Delta m_v \sim 1$) also occurring on a regular basis (e.g., [5, 27, 29]). In addition Bookbinder & Lamb [8] discovered non-thermal radio emission from AE Aqr. The emission was tentatively associated with synchrotron emission from moderate relativistic electrons, powered by magnetohydrodynamic torque coupling of the magnetic white dwarf to either an accretion disk or the secondary star with a strong magnetic field. Follow-up work (e.g., Bastian, Dulk & Chanmugam [30]) utilising several different frequency bands revealed the highly transient nature of the emission. Even though the spectrum manifests a variety of short term characteristics, at times decreasing with frequency, at other times increasing with frequency or sometimes flat, the long-term averaged spectrum resulted in an increasing function of frequency. Also, the study resulted in no detection of circular polarisation. These authors successfully explained the flaring as a superposition of expanding synchrotron emitting clouds (the so-called van der Laan process). The van der Laan [31] is a very successful model to explain non-thermal emission in radio galaxies. The search for quasi periodic outbursts (QPOs) and coherent pulsations in radio emission using Very Large Array (VLA) observations resulted in an upper limit, with no evidence of QPOs or coherent pulsations at the 33 seconds (s) spin period of the white dwarf [32]. The study also found no evidence of any association between the observed flaring and the orbital phase. The fact that the radio emission is non-thermal motivates a search for non-thermal emission at higher energies as well.

Terada et al., [10] discovered a non-thermal hard X-ray signature using Suzaku data. The analysis of Suzaku hard X-ray data in the energy range 12-25 keV exhibited significant excess above the extrapolated model. The search for pulsed hard X-ray emission seems to detect pulsations with 33.08 s in the spin-folded hard X-ray light curve which displayed two sharp spikes separated by $\sim$0.2 cycles in phase, even though it was different from nearly sinusoidal profiles seen at energies below $\sim$ 4 keV. Since the measurements of a time-averaged spectrum resemble a non-thermal spectrum, the excess was explained in terms of two possibilities, either a non-thermal power law distribution or a third thermal component. The pulsed hard X-ray emission was associated with synchrotron emission from relativistic electrons generated by some kind of particle acceleration process that is active within the system.

Initially, it was thought that the radio and optical outbursts could be associated with enhancements in the accretion rate onto the white dwarf. Nevertheless, Patterson [5] showed that there was no significant increase in the pulsed fraction of the periodic optical emission during flares, which casts doubt whether enhanced mass accretion is, in fact, the driving mechanism behind the transient multi-wavelength emission from AE Aqr. The magnetospheric propeller process associated with AE Aqr put the flaring, as well as the anti-correlation of the pulsed fraction and flaring, in context. It was shown [33] that a fragmented blobby mass transfer stream from the secondary star ejected by the rapid rotating white dwarf (i.e. a magnetospheric propeller) could in fact drive the optical flaring, which explains why the pulsed fraction of the 33.08 s rotation period does not increase significantly during flaring. The magnetospheric propellering was modelled effectively through magnetic friction when the magnetosphere sweeps across diamagnetic blobs [7, 28], or through the development of Kelvin-Helmholtz instabilities between the magnetosphere and mass-flow stream [34]. This provides an attractive vehicle to explain the non-thermal radio flares observed from AE Aqr due to the development of magnetic bubbles produced by this instability which may contain a large population of relativistic electrons produced in rapid magnetic reconnection in the turbulent magnetised plasma. These accelerated electrons, continuously pumped by the sweeping white dwarf magnetosphere, will produce non-thermal radio to infrared (IR) flaring emission with the observed van der Laan-type Spectral Energy Distribution (SED) (e.g.,[34]). This unequivocally linked the magnetic propeller in AE Aqr to episodes of particle acceleration and transient non-thermal emission (e.g., [35]), which makes this source a unique laboratory for transient multi-wavelength studies.

The transient non-thermal radio flares observed from AE Aqr, and its similarities with Cyg X-3 (albeit at a lower level), provided the first motivation to embark on a search for TeV emission from this source (e.g., [36, 12]). Two of the observations made during the 1988 observing season showed indications for abnormal increases above the expected cosmic-ray background [12] at a period very close to 33.08 s, which is the rotation period of the white dwarf. Subsequent studies ([37, 6, 13]) showed consistent pulsed emission, associated with optical flaring (simultaneous optical- TeV observations were performed), as well as short burst-like TeV gamma-ray (duration $\sim$1-2 minutes) events at significance levels of approximately 5-6 σ ([6, 13]). It has never been confirmed with the High Energy Stereoscopic System (H.E.S.S.) and MAGIC facilities, perhaps due to a lack of sufficient observation time. The detection of non-thermal hard X-ray emission from Suzaku data renewed the interest to search for emission from AE Aqr at higher energies [10]. A Fermi Large Area Telescope (Fermi-LAT) search, using the pass 7 pipeline [16] revealed a weak but consistent pulsation at 16.54 s, which is just the first harmonic of the spin period of the white dwarf, which can be explained in terms of pulsar-like emission from both poles or polar zones from the fast rotating white dwarf. Therefore, a proper re-evaluation with pass 8 pipeline, with a longer baseline, and upgraded data processing may result in a clearer picture related to the potential pulsed gamma-ray emission from this enigmatic source.

The goal of this study is to search for non-thermal emission from AE Aqr in two wavebands; radio and gamma-ray. A follow-up search for steady and pulsed radio emission will be performed utilising the MeerKAT radio telescope. The previous studies with VLA revealed flare-like events in the radio emission, but no pulsations at 33.08 s, the rotational period of the white dwarf, or QPOs were detected. Therefore a deep search for pulsed radio emission will be conducted, taking advantage of the superior sensitivity and resolution of the MeerKAT telescope. Perhaps the nature and origin of the flare-like events in radio emission can be established, confirming the presence of a particle acceleration in AE Aqr. A follow-up search for steady and pulsed gamma-rays will be conducted using the Fermi-LAT pass 8 pipeline with upgraded data and extended baseline ∼10 years. In support of the search for pulsed gamma-ray emission, this study will utilize data from the MeerKAT L-band (0.9-1.67 GHz) and the Fermi-LAT data in the energy ranges 0.1-500 GeV, where steady, episodic, or pulsed emission will be searched. The search for steady emission will be conducted in the Fermi-LAT data using Fermi standard techniques, i.e., unbinned and binned likelihood analyses. On the other hand, the search for periodic emission on these data will be conducted using pulsar timing analysis, which forms part of the Fermi science tools. The reduction and analysis of AE Aqr's radio emission will be performed using the Common Astronomy Software Applications package (CASA), and the search for pulsed radio emission will be done using the Lomb-Scargle techniques.

This thesis will take the following format. Chapter 2 presents a general discussion of cataclysmic variables, especially where AE Aqr fits into the structure, with the rest of the chapter focusing on a detailed discussion of the properties of AE Aqr that are associated with multi-wavelength emission from radio to TeV gamma-ray energies. Chapter 3 focuses on particle acceleration processes that may be relevant in AE Aqr. A thorough discussion of radio observations, analysis, and results will be presented in Chapter 4 . Chapter 5 consists of a thorough discussion of the methodology used, the analyses, and the results from the search for very high energy giga electron volts (VHE-GeV) non-thermal emission from the Fermi-LAT pass 8 data pipeline. Chapter 6 presents a final discussion of the findings and conclusions. Additionally, Appendix A explores non-thermal radiation processes relevant to non-thermal emission from AE Aqr, with Appendix B presenting a general discussion on Fermi-LAT log-likelihood analysis processes, and all Fermi-LAT data analysis diagrams not utilized in Chapter 5.

Chapter 2

Cataclysmic Variables

Introduction

This study focuses on AE Aqr, a nova-like cataclysmic variable, which is perhaps the most peculiar among all known cataclysmic variable systems. One of the unique features is the transient multi-frequency emission from radio to possibly very high gamma-rays (TeV γ-ray [38]), and the propeller mechanism which may be closely linked to this multi-wavelength emission. To put AE Aqr into perspective, the main features of cataclysmic variable systems will be highlighted, with emphasis on magnetic systems.

Cataclysmic variables (CVs) are defined as interacting binary stars in which a low-mass main-sequence star transfers mass onto a white dwarf (see the following references [39, 40, 41] for reviews). Hence they are known as interacting binaries. There are many categories of CVs, e.g., dwarf novae, classical novae, nova-likes, recurrent novae, and magnetic CVs. Initially, the classification of CVs was based on their optical variability, but now the classification involves the intrinsic properties of the CV system. These properties include the spin period of the primary star, strength of the magnetic field of the primary star, mass transfer rate, and lifespan of each outburst, which in most cases is comparable to the orbital period. The typical size of a CV system is comparable to the size of the Earth-Moon system. Their formation and long term evolution are driven by mass transfer and angular momentum losses through magnetic braking and gravitational radiation. The orbital period of these systems ranges from 1-10 h, which is partially dependent on their stage of evolution (e.g., [42], [40, page 28-29]), although studies have shown that most CVs have short orbital periods below 2 h.

Most CVs are characterized by multi-frequency emission, which means they emit in most wavebands across the electromagnetic spectrum. The emission nature of most CVs is linked to mass transfer, accretion processes, and an accretion disk. Due to these characteristics, the binary system parameters such as distance, magnetic field, the mass of the secondary star, and the orbital period can be obtained (e.g., [27, 43]). The mass streaming from the secondary star, either accretes onto the white dwarf via an accretion disk or directly along the magnetic field lines if the white dwarf has a very strong magnetic field. In some systems, the mass flow will be expelled from the system by the co-rotating magnetic field of the primary star, i.e., the so-called propeller mechanism (e.g., [7, 28]). The primary star in most CVs undergoes occasional outbursts each time the primary accretes enough mass for nuclear processes. These outbursts last as long as adequate fuel is available, but the system's emission will thereafter return to its normal brightness. The unpredictability and consistent variability of CVs makes them the ideal targets for professional and amateur astronomers due to their variability and brightness. Most discoveries of known CVs were through the nature of their variability and/or their significant optical and X-ray emission. The hotspot of most CVs is responsible for the increased optical emission observed as orbital humps in the light curves (e.g., [3, pages 7-13], [44, page 103]).

2.1 Magnetic Cataclysmic Variables

The magnetic CVs are systems with a magnetic field playing a dominant role in the mass transfer, mass accretion process, and the resulting multi-frequency emission. These systems have subclasses according to the strength of the magnetic field, i.e., polars and intermediate polars. Polars are highly magnetised CVs with the magnetic field of the primary star having field strengths above 10 Mega Gauss (MG), where intermediate polars (IPs) have magnetic field strengths between 1-10 MG (e.g., [1, 2]). There is no clear dividing line between these categories at the intersection values. The classification of magnetic CVs is determined by the interaction between the mass transfer and subsequent accretion with the magnetosphere of the primary star.

The fundamental properties of magnetic CVs are intimately related to the magnetic properties of the primary star. A clear distinction between the non-magnetic and magnetic CVs is seen in their emission, e.g., the hard X-rays observed in most polars produced by bremsstrahlung are one of the signatures of magnetised binary systems. The polars also emit soft X-rays, which originate from thermalized sub-photospheric deposition and reprocessed bremsstrahlung (e.g., [45, 46]). A more formal discussion of the properties of the subclass of magnetic CVs will now be presented.

2.1.1 Polars

Polars are also known as the AM Her (AM Herculis) systems. These systems do not have an accretion disk because the strength of the magnetic field of the primary star disrupts the formation of an accretion disk. They are also characterized by synchronized spin and orbital period (e.g., [40, page 361, 470-471], [47]).

The strength of the magnetic field will result in the magnetosphere of the primary star (R_{Alfven}) extending beyond the circularization radius (R_{circ} corresponds to the radius of the circular orbit around the primary star for which the angular momentum corresponds to the momentum of material passing into the Roche Lobe at L_1) and connecting with the magnetic field of the secondary star i.e., $R_{Alfven} > R_{circ}$. Any material escaping into the Roche lobe of the primary star will be channelled towards the poles of the primary star along the field lines. Mass flow from the secondary star behaves in two different ways depending on the strength of the magnetic field.

If the magnetospheric radius extends beyond the inner Lagrange point (L_1), magnetic fields will dominate the mass flow from the L_1 point. The mass flow will encounter the magnetic field impediment from the onset and flow along the magnetic field lines throughout the entire trajectory (e.g., [48, 1]). For the accretion stream to follow the magnetic field lines, it must divert from the orbital plane and split into two upon encountering the magnetic field. One part will flow along the south pole field lines towards the south magnetic pole, with the remaining part following the north pole field lines towards the north magnetic pole (see Figure 2.1). Since field

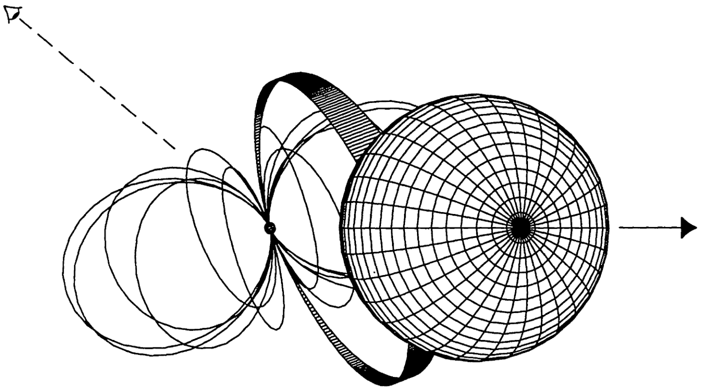

Figure 2.1: The trajectory of the mass streaming from the secondary star to the highly magnetised primary star, e.g., AR UMa[1].

lines converge as they approach the primary star, the mass flow is channelled onto a single small spot near the poles. The mass assumes a radial flow towards the primary star, virtually in free-fall. This is then defined as case I, applicable when the magnetosphere extends beyond the L_1 point.

In case II, the magnetosphere radius extends beyond the circularization radius, but its influence is weak towards the L_1 point. In this configuration, the mass flow from the secondary star will follow the ballistic trajectory as in the non-magnetic CVs until the mass reaches the point where the magnetosphere pressure balances the mass flow ram pressure (see Figure 2.2). At this point the magnetosphere acts as a barrier and guides the accretion flow along the field lines, and fragmentation can take place due to Rayleigh-Taylor instabilities (e.g., [49, 2]).

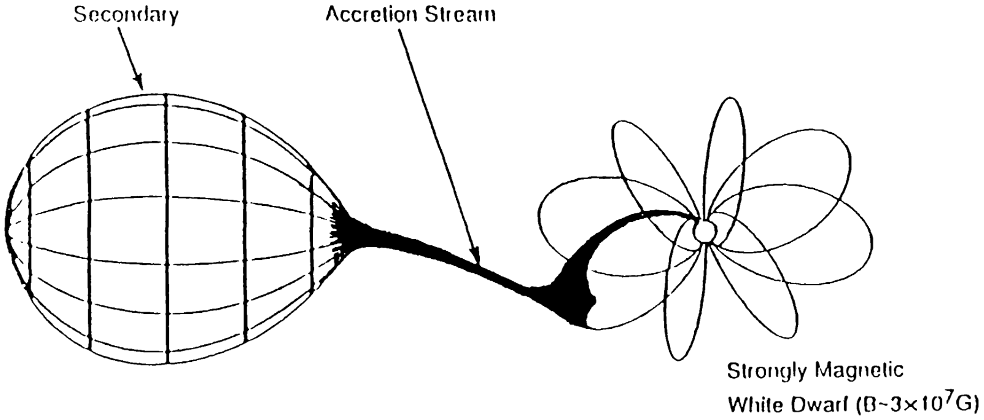

Figure 2.2: The trajectory of the mass streaming from the secondary star to the moderately magnetised primary star, e.g., AM Her[2].

The mass stream following the magnetic field will reach supersonic velocities under free-fall. This mass stream will lose velocity and gain temperature upon traversing a standing shock above the surface of the primary star [3, page 174-178]. The process will result in the release of gravitational potential energy and hard X-rays (e.g., [46]) from the hot dense plasma of the accreted material. Accreted material and hard X-rays upon passing through the shock front will heat the surface of the primary star to produce low energy radiation, i.e., soft X-rays (see Figure 2.3). These systems are characterized by cyclotron radiation and strong circular polarization, polarized optical and infra-red emission, soft X-rays, and sometimes hard X-rays.

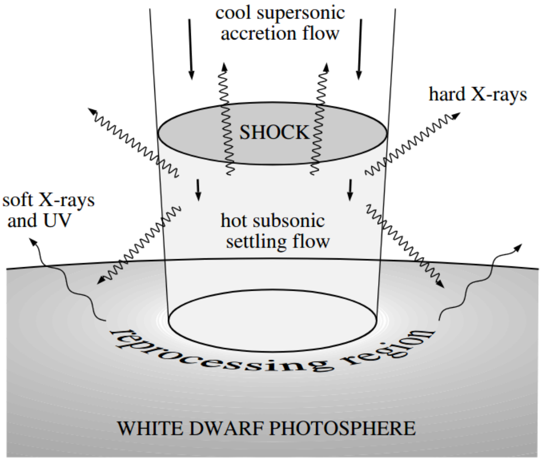

Figure 2.3: The standard accretion column geometry showing sites for hard and soft X-rays [3, page 178].

2.1.2 Intermediate Polars

The intermediate polars (IPs) are systems with integrated traits of non-magnetic systems and magnetic systems. The accretion in IPs is facilitated by a magnetically truncated accretion disk contrary to Polars, which do not have an accretion disk. The accretion disk of IPs differs from the disk of non-magnetic interacting binaries, which extends to the surface of the primary star. The accretion disk of IPs is truncated at small radii by the magnetic field of the primary star, which is sufficiently strong to influence the mass flow (see Figure 2.4). In IPs, the orbital period is not synchronized with the spin period of the primary star, i.e., most of the primary stars rotate with periods expressed as a fraction of the orbital period $P_{\text{spin}}/P_{\text{orb}} \leq 0.1$ (e.g., [50]). However, there are exceptional IPs with high ratios $0.1 \leq P_{\text{spin}}/P_{\text{orb}} \leq 0.6$ [51], $0.4 \leq P_{\text{spin}}/P_{\text{orb}} \leq 0.7$, e.g., DW Cancri [52], V1025 Cen and EX Hya [53, 54], and $SDSSJ233325.92 + 152222.1$ [55]. An unsynchronised spin period is perhaps due to the weaker magnetic field, higher accretion rate, and large orbital separation between the primary and the secondary star [4].

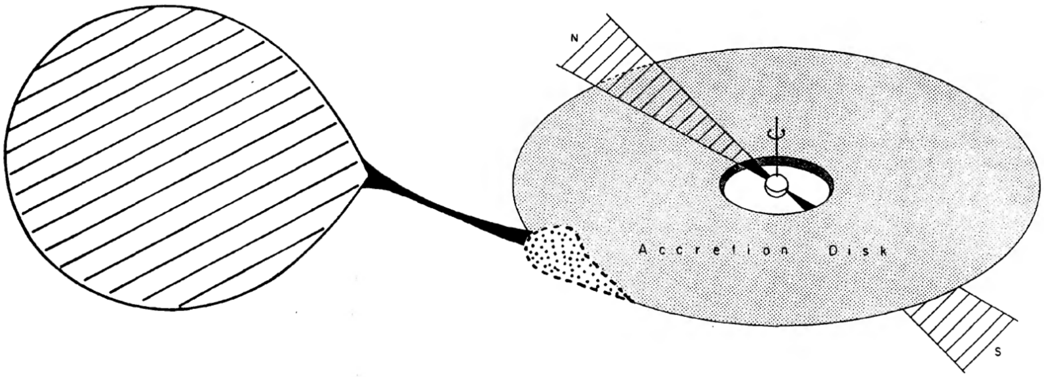

Figure 2.4: The magnetic field of the primary star carves out the magnetic cavity inside the accretion disk [4]

The accretion disk develops from the ring structure formed at the circularization radius. The formation of this ring structure is not possible when $R_{circ} < R_{mag}$, where

R_{mag} [1] is the magnetospheric radius. In a scenario where the magnetosphere radius is less than the circularization radius, i.e., $R_{circ} > R_{mag}$, the stream from the secondary can follow the normal process of accretion disk formation. But the inward spreading of the disk will stop at the magnetospheric radius. The accretion disk can only develop if the magnetic moment of the primary star does not exceed [56],

$$\mu_{34} \leq 0.4\dot{M}_{18}^{1/2} \left(\frac{P_{orb}}{4hr}\right)^{7/6} \left(\frac{M_1}{M_\odot}\right)^{5/6}, \tag{2.1}$$

where μ_{34} represents the magnetic moment of the white dwarf (in units of 10^{34} G cm^3), M_1 the white dwarf mass (in units of solar mass), and $\dot{M}_{18}$ the mass transfer rate (in units of 10^{18} g s^{-1}). A well-developed accretion disk is expected to facilitate mass accretion onto the primary star.

2.1.3 DQ Her systems

CVs with similarities to DQ Herculis are known as DQ Her systems. These systems fall under IPs, but they have a very short primary spin period below 100 seconds, and their magnetic fields range between 10^4 and 10^7 Gauss (e.g., [57]). Although some systems in this category lack hard X-ray emission, most of these sources are known as hard X-ray emitters. DQ Her systems are mainly identified by circular polarization and strong periodic X-ray emission. Other characteristics are high excitation spectra, and very stable X-ray and optical pulsations on light curves [4]. The lightcurves of IPs consist of beats produced by emission modulated at the spin period and the orbital period. The emission is due to the accretion processes close to the magnetic poles. Analogous to IPs, DQ Her systems also have an unsynchronised spin period, which suggests that these systems may perhaps accrete from an accretion disk.

Bath, Evans, and Pringle [58] developed the oblique disk rotator model to explain the properties of DQ Her. Pulsed emission from disk-accreting DQ Her systems and IPs is the direct result of the accretion of gas onto the exposed magnetic poles of the primary star, which is tilted with respect to the spinning axis. The mass flow from the secondary star will fall on the accretion disk before being channelled to the primary star, but if the kinetic energy density ρv^2 of the gas is locally less than the magnetic energy density $B^2/8\pi$, the mass falling on this location will be led by field lines of the magnetic fields to accrete onto the primary star radially [4]. The lighthouse effect results from a continual appearing and disappearing of the pole heated by the accretion. The result is pulsed emission modulated at the rotational period of the primary star.

It should be remembered that magnetic CVs, i.e., polars and intermediate polars and their subclasses, are also known as magnetic nova-like systems. The discussion was based on the various magnetic CVs, along with their fundamental properties. The aim is to present the characteristics of the nova-like system, AE Aqr, which is the subject of this thesis. The enigmatic system will now be discussed in detail in the next section.

---

[1] The magnetospheric radius is the radial distance from the accreting object where there is equilibrium between the gas and the magnetic pressure.

2.2 Properties of the Nova-Like Variable AE Aqr

The non-eclipsing interacting binary system AE Aqr consists of a late-type secondary star and a fast rotating magnetised white dwarf (e.g., [59, 60]). The white dwarf is spinning with a rotational period of 33 s [5], orbiting the companion with a period of 9.88 h [61]. AE Aqr is one of the most highly asynchronous cataclysmic variable binary systems [62]. The companion star is a red dwarf K3-5 spectral type (e.g., [60]), filling its Roche lobe, thus transferring mass to the white dwarf. In contrast to most CVs, the system does not have a M-type star as a companion, implying that the K-type secondary star present in this system suggests a different evolutionary path [63]. The approximate masses of the system components are: white dwarf $M_1 = 0.79 \pm 0.16 M_\odot$, and secondary star $M_2 = 0.5 \pm 0.1 M_\odot$ inclined at an angle of $i = 58 \pm 6^\circ$ (e.g., [60]). The system has a binary separation of $a \sim 1.8 \times 10^{11}$ cm.

AE Aqr was discovered on photographic plates and initially classified as a U Gem variable system [24]. Later the system was reclassified as a nova-like variable (e.g., [25, 26, 64, 65]), which is the current classification of the source, but for a time, it was identified as a DQ Her system, based on the short rotation period and the frequent flaring similar to DQ Herculis (e.g., [5, 4, 35]). In this classification, the secondary star in AE Aqr is assumed to be transferring matter onto the surface of the white dwarf via an accretion disk. The emission from DQ Her systems is linked to the mass that accretes at the polar cap regions and subsequently releasing gravitational potential energy in the process. Patterson [4] reviewed the properties of DQ Her systems and associated these systems with strong X-ray emission, high-excitation spectra, and very stable X-ray and optical pulsations in the light curves. The absence of observational evidence of an accretion disk indicates that AE Aqr requires reclassification as a new subclass of magnetic CVs rather than a DQ Her system. AE Aqr does not fit in any of the above discussed classes. The white dwarf in this system accretes only a minute fraction of the mass transfer from the secondary since the larger fraction is being thrown out of the system due to the magnetospheric propeller effect of the rapidly rotating magnetosphere of the white dwarf (e.g., [7, 28]). Multi-frequency studies conducted on this source since its discovery will be discussed in the rest of this chapter.

2.2.1 Optical-UV studies

AE Aqr is highly variable and has a visual magnitude ranging between 10 and 12 (see Figure 2.5). In quiescence, the optical emission is dominated by the contribution from the secondary ($\sim$ 95 %), with the remaining percentage coming from the primary component. The optical brightness of the system varies roughly three magnitudes in the U band on time scales from minutes to hours. There is a consistent oscillation in the optical emission modulated at the spin period of the primary star.

Patterson [5] was the first to perform a systematic study of the nature of the optical emission and revealed the steady pulsations at the fundamental period of 33.076737 s with the first harmonic at 16.54 s also having a comparable power. The optical emission was pulsed with an average amplitude of 0.2-0.3 %, which increases to 1 % when the source is flaring (see Figure 2.6). This pulsed fraction is anomalously low for disk-accreting white dwarfs and provided the first clue as to its possible misclassification as a disk-accreting DQ Her system. It was also shown through timing analysis around the binary that the pulsation has its origin at the white dwarf,

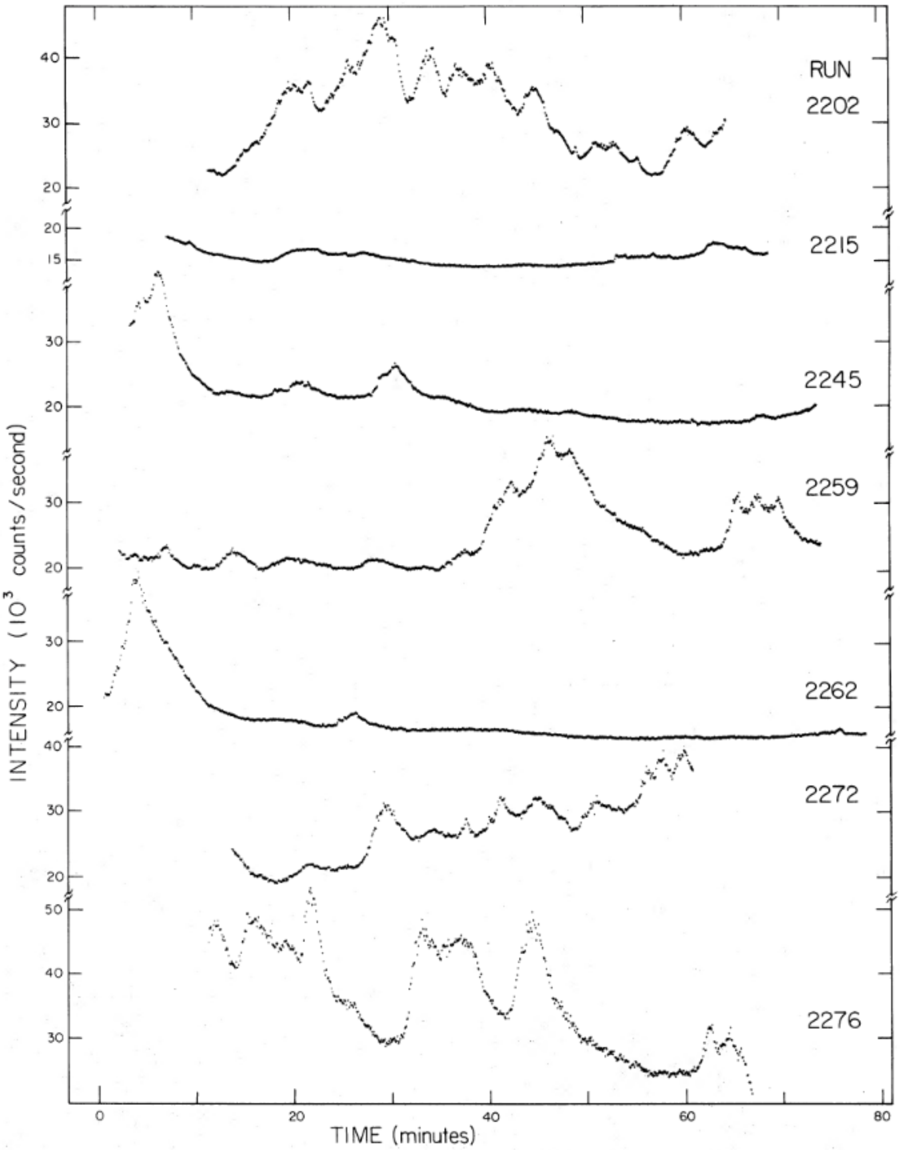

Figure 2.5: The optical light curve of AE Aqr showing the flaring activities [5]

which also led to the precise measurements of the projected orbital velocity. The periodograms [5] revealed strong quasi-periodic activity during flares with periods slightly longer than the 33 s white dwarf spin period and its associated 16.5 s first harmonic. The white dwarf in AE Aqr was believed to be accreting mass on its polar caps from the accretion disk analogous to other DQ Her systems. Therefore the observed QPOs of AE Aqr, like in other cataclysmic variables, were confined to eruptive events. It was suggested that the QPOs of AE Aqr originate from the inner accretion disk edge because of their periodic characteristics.

Patterson proposed the oblique rotator model to explain the pulsed emission from AE Aqr since the source has some similarities to other DQ Her systems. In the framework of the oblique rotator model the short 33 s rotation period and its 16.5 s first harmonic are the results of one heated polar cap sweeping through the line of sight of the observer, with the first harmonic possibly the result of reprocessed emission from the inner edge of the accretion disk being irradiated by the other pole. The QPOs were interpreted in terms of self-luminous blobs following Keplerian orbits

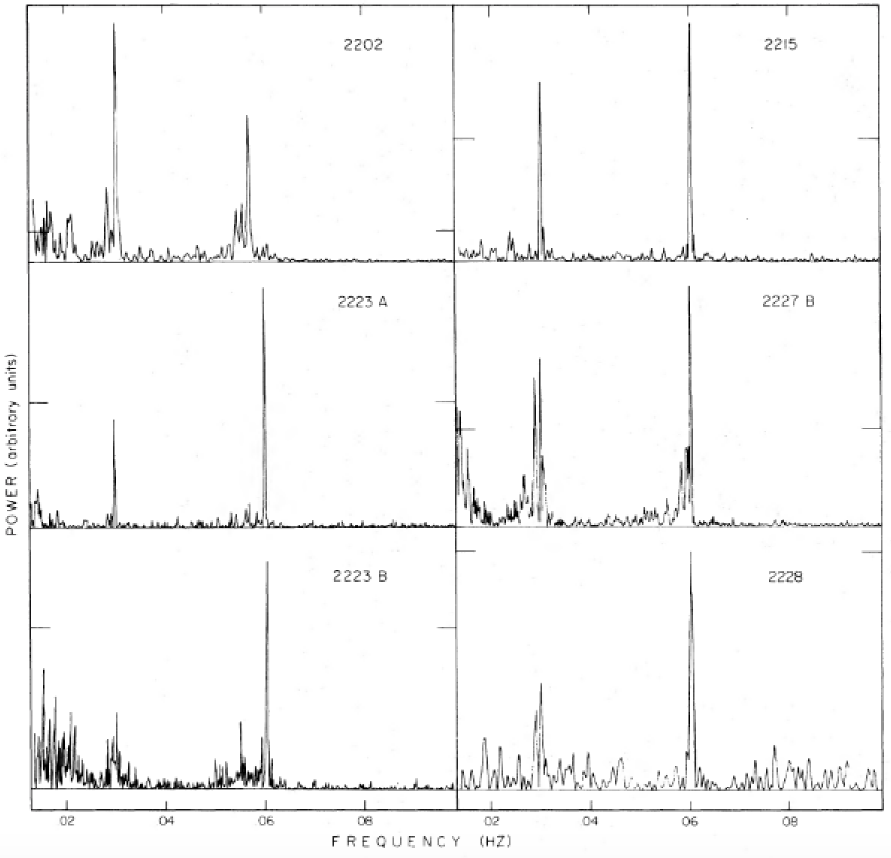

Figure 2.6: The power spectra for pulsed optical emission with peaks at the fundamental frequency and the first harmonic. The horizontal marks represent the 0.2 % amplitude [5]

in the disk at radii outside the co-rotation radius. Subsequent studies have also revealed that the 33 s pulse amplitude increases to approximately 1 % during the flaring state, but often the coherent pulse dies out during the most energetic flares [6]. The disappearance of the 33 s pulse during outbursts suggests that optical flares are not strongly tied to enhanced accretion on to the polar caps.

Subsequent spectroscopic studies [27] resulted in a measurement of the orbital period of 0.4116537 days with $\mathrm{K}_1 = 135$ km s^{-1} for emission and K_2 =159 km s^{-1} for absorption-line component, where $q = M_2/M_1$ =0.85 and $asin(i)$=1.66 $\times 10^{11}$ cm with i= 64°. This mass ratio (q) is consistent with the mass ratio of CVs. They found a K5V spectral type for the absorption-line component, with the mass of the white dwarf M_1= 0.82 $\mathrm{M}_\odot$ and the companion star M_2= 0.69 $\mathrm{M}_\odot$.

The photometric and spectroscopic studies by Robinson et al., [66] also resulted in the orbital period of 0.4116580(±2) days and radial velocity variation amplitude of K_1 = 122±8 km s^{-1}. Their spectroscopic studies determined the masses of the white dwarf and secondary star as $M_1 sin^3(i) = 0.62 \pm 0.05\ M_\odot$ and $M_2 sin^3(i) = 0.54 \pm 0.05 M_\odot$ respectively, with a mass ratio of q = 0.88±0.06. These authors, from the oscillation time-delay curve with respect to the emission-line radial velocity curve, found a phase shift of $\sim$ 60°. This value however was later discovered to be an artefact from erroneous analysis. They also derived the orbital inclination to lie between 63° and 70°.

High-speed spectroscopy performed at Mount Wilson revealed 75° phase shifted emission-line velocities [61]. Thus the result could not be used as the orbital motion tracer for the white dwarf. Nevertheless, the oscillation orbit was shifted by only $5°\pm3°$, strengthening the theory that the oscillations originate at the region concentric with the compact object (white dwarf). Accordingly, the oscillations' arrival time gives a measure of the apparent orbital velocity of the white dwarf, independent of the measurements of emission-line radial velocity. These authors recalculated the orbital inclination as $56° \lesssim i < 70°$ and mass range values of the system as $0.64 < \mathrm{M}_1/\mathrm{M}_\odot \lesssim 0.91$ and $0.49 < \mathrm{M}_2/\mathrm{M}_\odot \lesssim 0.70$ using $\mathrm{M}_1\ sin^3(i) = 0.528\pm0.017\ \mathrm{M}_\odot$.

De Jager and Meintjes performed the first investigation of anomalous short optical outbursts ($\sim$ 1 min) [67]. These authors gave the first report of a few seconds rise and decay time of the short optical bursts with a duration of $\lesssim$ 1 minute. These rapid light curve variations with large amplitude and short time scales are presumably associated with the white dwarf magnetosphere's dynamic activity. Large electric fields are expected to be produced through the Faraday induction process in the magnetosphere of the fast spinning white dwarf. Thus a corresponding large potential drop can be induced. Large potential drops in a low conductivity plasma are associated with particle acceleration; hence short optical bursts could indicate the presence of high energy emission. Short time scale burst-like emission in TeV gamma-rays was once reported at the 6 sigma significance level contemporaneously by two independent groups (e.g., [13, 67]).

While the nature and origin of the oscillations in optical, UV and X-ray emission were still in question, the rapid spin-down of the 33 s spin period of the white dwarf in AE Aqr was discovered with a rate of $\sim 5.64 \times 10^{-14}$ s s^{-1} [68]. The long-term stability of the 33 s spin period performed over a baseline of approximately 14.5 years revealed a rapid spin-down of the white dwarf. In the same study, the orbital period derived by Welsh et al., [61] was confirmed, and it was shown that the companion star's absorption-line radial velocities give the accurate phasing for the 33 s oscillations if they arise at the white dwarf. Utilising the pulse phase delays' amplitude $\alpha_{wd} sin(i) = 2.04$s, they calculated the mass of the white dwarf and showed that it lies between $0.9M_\odot$ and $1.0M_\odot$. One of the important results from their study was the resulting spin-down power $P \sim -I\dot{\Omega}\Omega = 6 \times 10^{33}$ erg s $^{-1}$, which exceeds the inferred accretion luminosity by a factor of $\sim$ 120. De Jager et al., [68] pointed out that a fraction of the spin-down power may be converted to particle acceleration like in a pulsar, which may explain the non-thermal emission observed from AE Aqr. Employing the mass-radius expression [69], these authors calculated the radius of the white dwarf as $R_* \sim 5 \times 10^8 (M_*/0.9M_\odot)$ cm [33], which, in return, was used to estimate the magnetic moments and it was also shown that the companion star lies above the main sequence. Friedjung showed that the radius of a main sequence star of the same spectral type has a smaller radius than the radius of the cool component in AE Aqr [70, 71]. This suggests that the secondary star is over-luminous for its mass, suggesting that it is somewhat evolved. The inferred magnetic moment $\mu_* = B_* R_*^3 \sim 10^{32}$ G cm^3 determined by adopting the surface magnetic fields of 1 MG is compatible with the expected white dwarf magnetic field in DQ Her systems (e.g., [4, 56]).

The high time resolution UV spectroscopic observations conducted from the Hubble Space Telescope (HST) using the Faint Object Spectrograph, and the contemporaneous UBVR photometry obtained at McDonald Observatory, exhibited a 40 % pulsed signal strength in the UV wavelength range [72]. The average pulse profiles have two unequal broad peaks separated by half an oscillation cycle. On the other hand, the pulse profiles in the UV corresponds to the pulse profiles of the optical waveband with no observable shifts. The UV pulse's orbital delay curve therefore implies that the origin of the pulsations could be fixed to the white dwarf surface. The white dwarf model atmosphere (with temperature $\sim$ 26 000 K) satisfactorily characterizes the pulsation spectrum for both the UV and optical. The study found no oscillations in the UV emission line fluxes and their velocities down to 800 km s^{-1} present the same result. These authors, inferring from the properties of the UV emission, propose that the 33 s oscillations arise at the X-ray heated magnetic polar caps of the white dwarf. Following this deduction, these authors generated maximum entropy maps of the distribution of brightness on the white dwarf surface to aid further investigations by regenerating the mean pulse profile. They interpret the fluctuations in the amplitude of the oscillation as tiny fluctuations in the accretion rate. They also found that the profiles and amplitude of the profiles were not strongly influenced by the extensive aperiodic flares shown by the system. In conclusion, these authors argued that flares are not associated with mass accretion on the white dwarf surface or within its magnetosphere.

The strong pulsed signal strength observed from the UV studies of the 33 s white dwarf rotation period was first interpreted as direct accretion on the white dwarf polar caps. Although the inferred accretion luminosity ($L_{acc,*} \sim 2 \times 10^{31}$ (D/100 pc)^2 erg s^{-1}) in the UV band is 500 times less than the inferred spin-down power. Patterson [4] was the first to suggest the propeller action in AE Aqr since the system consists of a fast rotating magnetised white dwarf that will propel the mass flow from the secondary away from the binary before it can accrete onto the white dwarf. Earlier observations performed in the UV band by van Paradijs et al., [29] revealed an optical luminosity of $L = 10^{32}$ erg s^{-1}. There is however an inconsistency between the ground-based and HST results in the UV band observation, where ground-based observations resulted in much weaker signal strength, i.e., 0.1-0.6 % (e.g., [5, 12, 6]). The weak signal strength during the flare implies that most of the luminosity contribution comes from the energy produced in the magnetosphere [4] not close to the white dwarf's surface. Eracleous and Horne [33] estimated a total possible accretion power of $L \sim 1.2 \times 10^{33}$ erg s^{-1}. Their estimation was based on the total available potential energy per nucleon produced in an accretion induced magnetospheric shock. It was suggested that nearly all of the accretion stream is expelled by the magnetic propeller mechanism, which results in a much lower power released through direct mass accretion on the white dwarf's polar caps (e.g., [17, 7]). The observed emission can be explained by the radiative cooling of the propelled matter, where the emission is explained by thermal processes [33]. However, the observed luminosity is still lower than the spin-down power, which means that there is an excess reservoir of power for the production of high-energy particles and non-thermal emission.

Further investigation of the system parameters was conducted utilising contemporaneous high-resolution H_α spectroscopy and high-speed photometry, with the main focus directed on the characterization of the properties of the donor star [73]. The analysis focus was on the absorption lines of the donor star. Weak absorption lines were observed in the spectrum of AE Aqr. Welsh et al., [73] modelled the line emission and estimated the spectral type of the mass-donor as $K3 - K5$, its rotational velocity at $V_{rot} sin(i) = 85 - 108$ km s^{-1}, its orbital velocity at $K_1 \sim 138\pm$ 6 km s^{-1} , $K_2 \sim 157.9 \pm 0.8$ km s^{-1}, and its contribution on the system's total flux at 69-94%. They derived the mass ratio from $V_{rot} sin(i)$ and K_2 and found the range 0.58 < [$q = (M_2/M_1$] < 0.89) to depend on the limb darkening and spectral type. The mass

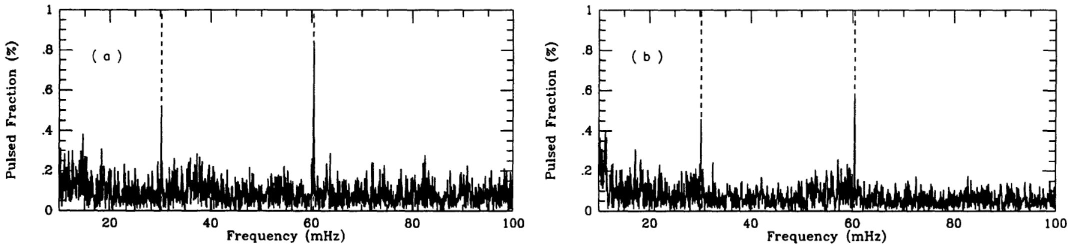

Figure 2.7: Optical FFT of AE Aqr during quiescence (left) and flares (right) showing the fundamental $\sim$ 30 mHz (P_* $\sim$ 33 s) spin period of the white dwarf and the first harmonic at $\sim$60 (P_1) $\sim$ 16.5 s)[second pole]. The pulsed fraction is unusual low for an accreting system[6].

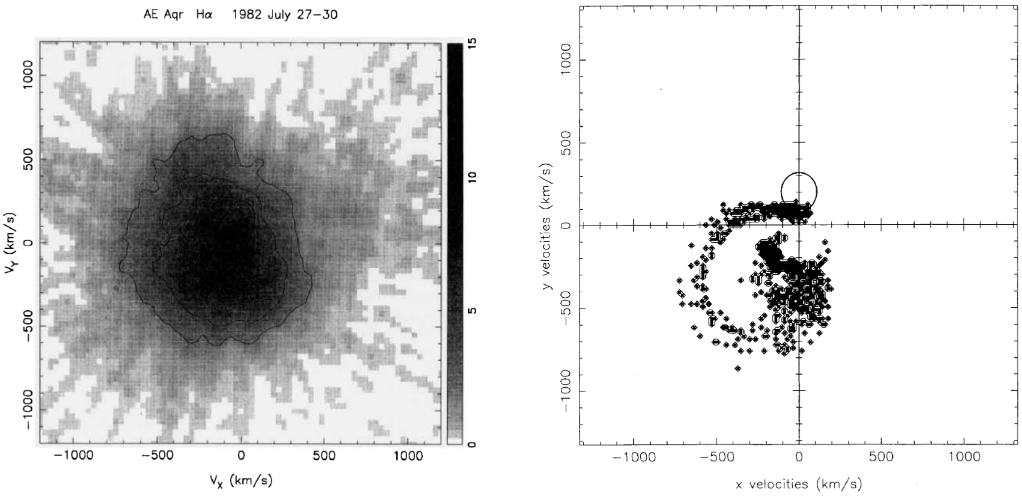

Figure 2.8: Observed H_α of AE Aqr (left) v_x and v_y are inertial velocities plotted with respect to a corotating coordinate system the x-axis is along the line of centres of the binary, and the y-axis is in the direction of the instantaneous motion. Simulated Doppler tomogram of the gas flow of the AE Aqr (right) The tomogram was produced assuming a system inclination of 55^o [7]

ratio of the system was also estimated at $q = 0.646 \pm 0.013$. These authors also observed the lack of flux variations in the absorption lines, and through the assumption that the variations are ellipsoidal, they derived the inclination angle $i = 49° \pm 15°$ from the ellipsoidal amplitude. Nevertheless, they found notable deviations from the anticipated ellipsoidal variations, which suggest a non-uniform distribution of absorption line strength across the donor star, indicating perhaps a star spot region. Utilising Monte Carlo simulations, the mass limit of the white dwarf was set at $< 1.4\ M_\odot$, the realistic distribution of the stellar masses and inclination angles were calculated. The simulation resulted in $M_1 = 0.89 \pm 0.23\ M_\odot$, $M_2 = 0.57 \pm 0.15 M_\odot$ and $i = 55° \pm 7°$.

The pulsed emission of optical emission from AE Aqr was detected at longer periods than the spin period of the white dwarf. It was argued that the emission is produced further from the white dwarf. Through ultraviolet studies, it was argued that the flaring region is outside the magnetosphere of the white dwarf[72]. The idea was supported through the photometric and time-resolved polarimetric studies, which resulted in the calculation of the degree of circular polarization [74]. The observation was performed at the Crimean Astrophysical Observatory, and for five nights, the average circular polarisation was 0.06 ± 0.01%. This circular polarization value corresponds well with the values obtained by Cropper [2]. An important result drawn from the constant circular polarization is its interpretation in the frame of the cyclotron mechanism, which eliminates the model that supports the accreting white dwarf. Beskrovnaya et al., [74] pointed out that the optical flaring radiation is best characterized by thermal models. The flare colour indices found in their study were close to that of a blackbody with temperature T $\sim$ 15000 - 20000 K and an area of emission of S $\sim 10^{20}$ cm^2. These authors therefore concluded that the location of the flaring energy release is outside the magnetosphere of the white dwarf.

Welsh et al., [75] presented the results of the analysis of H_α emission lines from high speed spectrophotometric observations of AE Aqr. They obtained over 10 000 spectra using a sampling rate of $\sim$ 6 s. The analysis revealed no detection of 16.5 and 33 s oscillations either in the continuum or line spectra, and neither was there any detection of quasi-periodic oscillations. The analysis revealed a complex behaviour of the H_α line with noticeable variations in flux, which increases or decreases by $\sim$ 3 orders of magnitude in a few hours. These authors reported that the emission lines are a component of a superposition of emission components that are velocity localized. It was also reported that the H_α emission arrival time is delayed and decays more gradually than the continuum during flares. Also, there was no linear correlation between the H_α variations and the continuum variations. A close inspection of the Doppler tomogram and the trailed spectrograms exhibited no indications of an accretion disk but rather strengthens the idea that a propeller mechanism is ejecting mass from the system. In addition, the HST observations do not support enhanced mass accretion as the driving force behind the flares since the data revealed that the 33 s pulsed fraction in the UV was not strongly affected by large flares [72].

Contrary to other DQ Her systems, which accrete matter from the accretion disc, the spectroscopic studies of AE Aqr show no evidence of an accretion disk. [76]. In addition to the absence of an accretion disc, a low pulsed fraction of the 33 s oscillation in optical was observed for an accreting system (see Figure 2.7). This, together with the structure of the H_α Doppler tomogram (e.g., [7]), posed questions as to whether the system is a DQ Her type cataclysmic variable, accreting mass from the secondary via a well developed accretion disk (see Figure 2.8).

2.2.2 Radio and infrared studies

The non-thermal radio emission from AE Aqr was first detected by Bookbinder & Lamb (1987) [8] utilising the Very Large Array (VLA). The observations centred on 1.4 GHz and 4.9 GHz wavebands, and yielded radio emission flux densities of 3-5 mJy and 8-16 mJy respectively (see Figure 2.9).

Bastian et al., [30] on a follow-up study with wavebands centred on 1.5, 4.9, 15.0 and 22.5 GHz, found a highly transient nature for the emission, showing flaring activity with flux levels varying nearly continuously between 1 and 12 mJy, mimicking CygX-3, just on a lower scale. The first microwave-wavelength observations and detection of AE Aqr were performed by Abada-Simon et al., [77] with the wavebands centred on wavelengths 3.4 and 1.25 mm using the interferometer at the Plateau of de Bure, France, and VLA, respectively. Abada-Simon et al. [43] carried out a follow-up study in the cm to mm wavelength intervals, and the results showed similarities to the high-mass X-ray binary system Cyg X-3. These results were compatible with

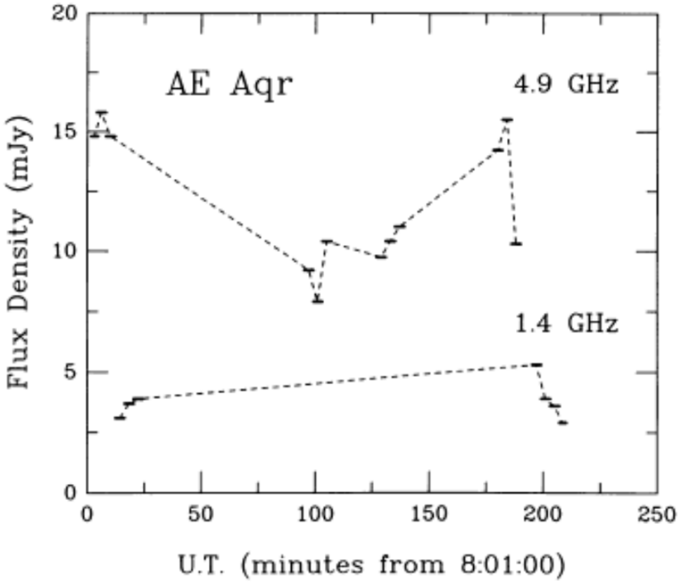

Figure 2.9: AE Aqr time variability emission on wavebands 1.4 and 4.9 GHz [8]

the model previously proposed to explain the emission [30]. In the same study IR emissions were also detected at 90 μm, but only an upper limit for the flux was obtained 160 μm. The IR observations were carried out in the range previously unexplored from 4.8 μm to 170 μm using the Infrared Space Observatory (ISO) during the multi-wavelength campaign from radio to optical wavelengths [78]. The study confirmed the previously detected emission at 90 μm, and the upper limits at 170 μm were again estimated. It also resulted in the detection of emission at 60 μm and estimation of upper limits at 12, 25, and 100 μm.

The spectrum of AE Aqr's radio emission is too complex to put the origin of the emission into context since, at times, it increases as frequency increases. In some instances, it decreases with frequency, and sometimes it is relatively flat with an increase in frequency [30]. The calculated long term average of the spectrum obtained at the frequency bands 1.5, 4.9, 15, and 22.5 GHz resulted in a relatively flat spectrum , $S_\nu \propto \nu^\alpha$ with $\alpha = 0.3 - 0.4$ [30]. The spectrum found by Abada-Simon et al., [77] was also consistent with the supposed spectrum for the superposition of flare-like events. They found a power law $f(S_0) \propto S_0^\epsilon$ with index $\epsilon = 1.8$ for the frequency distribution of the flux density. The radio and infrared observations conducted by Abada-Simon et al. ([78]) on frequencies that extend up to 3333 GHz still resulted in the self-absorbed spectrum, $S_\nu \propto (\nu\ /\mathrm{GHz})^{0.5}$. The flux densities obtained by Abada-Simon et al. (e.g., [62, 78]) are not consistent with the flux densities obtained by Tanzi et al., [79]. The spectrum associates the origin of the emission to the secondary star (e.g., [62, 78]). The derived spectrum from 4.8 μm and 7.3 μm showed that a significant fraction arises from the secondary star spectrum, including some thermal component from the accretion stream, and probably some additional cyclotron radiation generated from the post shock of accreting matter close to the magnetised white dwarf [62]. The spectrum obtained at 90 μm, unlike all other results, resembles the optically thin part of the synchrotron spectrum [43].

Multi-instrument observations (IRS, IRAC and MIPS) using the Spitzer Space Telescope were employed during follow-up observation of AE Aqr in the wavelength range 5-70 μm [9]. The spectral energy distribution showed an excess significance

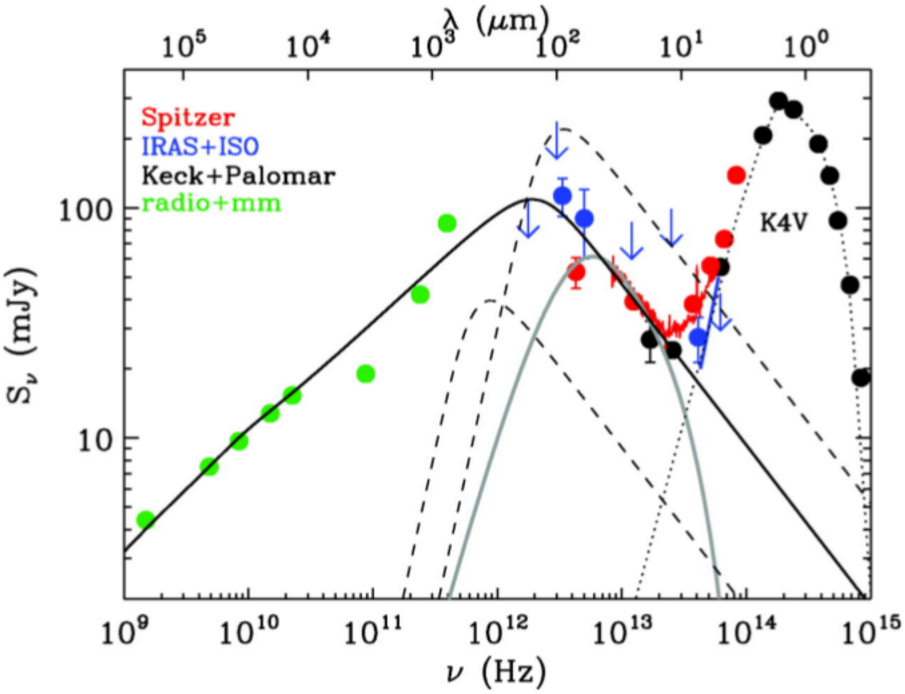

Figure 2.10: The spectral energy distribution of AE Aqr from radio to optical emission with proposed model behind the emission[9]

above the K4 V spectrum of the secondary star. It was revealed that the flux levels are directly proportional to the wavelength above 12.5 μm. The previously obtained results and arguments of the origin of the emission were confirmed in the same study. The spectral energy distribution of AE Aqr from radio to optical wavelength was also constructed (see Figure 2.10).

In contrast to the initial understanding that radio and optical flares could be linked with enhancements in the accretion rate onto the white dwarf, Patterson [5] showed that there was no significant increase in the pulsed fraction of the periodic optical emission during flares. A contemporaneous observation of radio and optical outbursts from AE Aqr revealed that the outbursts are not associated with any desired position on the orbital frame of the binary system [62] since the outbursts appear at any orbital phase. Part of the data revealed recurrent outburst characteristics, but results from complete dataset were less compelling [32]. The radio outbursts revealed no sign of the presence of coherent oscillations at the compact object spin period or quasi-period oscillations [32]. Pulsations at the white dwarf spin period are only observed from optical and X-ray emission, but no quasi-periodic or periodic oscillations were detected at 8.4 GHz from AE Aqr [80]. The search for pulsations in this radio waveband only resulted in the upper limit of 0.1 mJy.

Bookbonder & Lamb [8] pointed out that the observed radio flares can be powered by the magnetohydrodynamic (MHD) torque coupling the secondary star and the magnetised white dwarf if the secondary star has a substantial magnetic field. On the other hand, Bastian et al., [30] described the short time scale variability of the radio emission and the obtained spectrum as the superposition of synchrotron radiation-emitting plasma clouds, which, as they expand, change from optically thick to optically thin. In their model, they showed that a power law could model the data they observed for the time-averaged radio spectrum. Kuijpers et al., [81] provide an alternative model, the magnetic pumping model. In this model, the radio variability or outbursts are a result of the eruption of bubbles of fast particles from the white dwarf magnetosphere. The subsequent studies [19] described the observed radio spectrum that represents a self-absorbed power law as a superposition of several expanding, strongly magnetised blobs in different stages of their evolution. In this model the magnetised blobs possess highly tangled magnetic fields with strength ($B_0 \geq 1000$ Gauss) which forms part of the mass transfer stream from the companion star, and are continuously pumped by the rapidly spinning white dwarf magnetosphere in an induction Betatron acceleration process which accelerates electrons to relativistic energies of about 1 MeV. The relativistic electrons confined in magnetised blobs are flung out by the propeller mechanism, which in turn will produce non-thermal radio to infrared (IR) flaring emission with the observed Van Der Laan-type SED. The ejected magnetised blobs expand and become optically thin. The simulated spectral results correspond well with the values reported by Abada-Simon et al., [78].

2.2.3 X-ray studies

Patterson et al., [82] using the Einstein Observatory satellite, discovered 33 s pulsations in the soft X-ray light curve of AE Aqr in the energy range 0.1-4.0 keV. The pulsations are coherent and in harmony with the optical pulsations in both phase and period. They attribute the periodicity to the accretion induced hot spot on a fast rotating, magnetised compact object (white dwarf). The X-ray emission is analogous to a 1 keV thermal bremsstrahlung spectrum with a measured luminosity of $L_X \sim 5 \times 10^{30}(D/100pc)^2$ erg s^{-1} [82, 83]. The Einstein Observatory observations revealed a single 33 s pulse in X-ray power spectra, with no hint of a 16 s pulse. Investigations of the dependence of the 33 s pulsed fraction with count rate (CR) in Einstein Observatory X-ray data reveals an increase in the relation PF(%) = 45%/ s^{-1}CR(s^{-1}) in the observed count rate range of 0.15-0.5 s^{-1} [12]. The investigation of the hardness ratio as a function of the count rate showed no increase in the ratio [12]. During a more vigorous X-ray flare, an increase in spin-modulated X-ray flux was observed in ROSAT data during a 1993 Whole Earth Telescope (WET) campaign, where the flux increased threefold [84], but no such effect was observed during the subsequent *ROSAT* observations [85].

An analysis of X-ray observations made with Ginga in 1988 and ASCA in 1995 resulted in the detection of pulsations with sinusoidal pulse profiles at periods of 33.076 ± 0.001 s for Ginga, and ASCA observations at 33.077±0.003 s [59]. These authors reported a relatively small pulse amplitude with almost uniform modulated flux where the flux levels rise by a factor of three during the flaring state. Using the thermal model component, they produced a time-averaged spectrum in the energy range 0.4-10 keV utilising two different combinations of temperatures, kT$_1$=0.68$^{0.01}_{-0.02}$ keV and kT$_2$=2.9$^{0.3}_{-0.2}$ keV. It was also pointed out that there was no notable difference between the flare and quiescent energy spectra, even though there was a hint of spectral hardening during the flaring state. They also interpret their results with a model where the binary system is in the propeller regime. In the frame of the propeller, they suggest that the X-ray emission arises from magnetospheric radiation.

Itoh et al., [60] reported results from the analysis of the X-ray observations with XMM-Newton. Through high-resolution spectroscopy of He-like triplets of N and O with Reflection Grating Spectrometer the group determined the emitting plasma's electron density $n_e = 10^{11}$ cm^{-3}, and estimated the geometrical scale ($l_p \simeq$ (2-3)$\times 10^{10}$ cm) of the plasma emitting the He-like triplet of N and O lines. The geometrical scale and the density did not correlate with the magnetic cataclysmic's standard post-shock accretion column. Therefore, these authors argued that the plasma could not be the product of mass accretion on the compact object of AE Aqr. On the other hand, the observed velocities of H-like, Kα line of N and O (1250-1600 km s^{-1}) correspond to the magnitude of the dispersion of the thermal velocity of the hottest part of the plasma. The group suggested all broad emission lines from optical and X-ray wavebands are generated in the course of adiabatic cooling of the plasma once heated up to maximum temperature (T$_{max}$) in the deep gravitational potential of the white dwarf. They argued that the absence of a high-velocity component in the H$_\alpha$ emission line could be interpreted by a scenario where the plasma flung out due to the propeller action is still too hot to form an H$_\alpha$ line inside a region $r < l_p$. In this view, the propeller will drive the mass from a region $r < l_p$ from the compact object where the high-velocity component of the H$_\alpha$ line is likely to originate.

Mauche [86] using the X-ray data from XMM-Newton, ASCA, and Chandra, which span over ten years recalculated the rate at which the white dwarf is spinning down. Using a 27 year cumulative baseline, he found that the white dwarf is spinning down at a slightly faster rate than what was calculated by the de Jager et al., [68] spin ephemeris. He found that the observed evolution of the period is consistent with an additional component, either a quadratic term ($\dot{P}$ = 2.0 $\pm$1.0 $\times 10^{-15}$ d d^{-1}, which is compatible with a moderate gain in the accretion torques slowing down the spinning white dwarf), or a cubic term ($\ddot{P}$ = 3.46 $\pm$ 56 $\times 10^{-19}$ d^{-1}, which is not consistent in magnitude and sign with losses of magnetic dipole moments).

Observations with Suzaku resulted in the detection of both soft and hard X-rays [87]. The detection of hard X-rays was the first indication of possible non-thermal X-ray emission. Observations were performed using X-ray Imaging Spectrometer (XIS, [88]) at a soft X-ray energy range of 0.2-12 keV for 47.0 ks, and Hard X-ray Detector (HXD, [89]) at 10-70 keV for 52.7 ks for hard X-rays. The folded light curve produced for the lower end HXD (10-25 keV) at a period of 33.07975 $\pm$ 0.00002 s correlates with the folded light curves from XIS (0.5-4 keV and 4-10 keV). The spectra of the wide-band pulse component exhibit both thermal and non-thermal components fitted with a simple power law at the energy range 3-25 keV and 10-100 keV with a photon index of 2.29 $\pm$ 0.04 and a flux of 3.5 $\pm$ 0.2 $\times$ 10 $^{-12}$ erg cm^{-2} s^{-1}.

Further investigation of thermal and non-thermal X-ray emission using the same data observed in 2005 and new data observed in 2006 with Suzaku resulted in the detection of both soft and hard X-rays (see X-ray spectra Figure 2.11 [10]). The study confirmed a precise spin modulation in the 0.5-10 keV band of the soft X-ray data at a barycentric corrected period of 33.0769 $\pm$ 0.0001 s, with the 10-30 keV hard X-ray data also exhibiting statistically notable periodic signals at a consistent period. The spin-folded hard X-ray light curve displayed two sharp spikes separated by $\sim$ 0.2 cycles in phase, contrary to nearly sinusoidal profiles seen at energies below $\sim$ 4 keV. It is noteworthy that the folded 4-10 keV soft X-ray light curves are assumed to be a superposition of those pulse profiles. They modelled the 1.5-10 keV phase averaged data with a thermal model, the first component at a temperature of $0.53^{0.13}_{-0.14}$ keV, and the second component at $2.9^{0.20}_{-0.16}$ keV. They observed an excess of hard X-rays in HXD (12-25 keV) data above the extrapolated model, and they explained this excess in terms of two possibilities, either a power law with a photon index of $1.12^{0.63}_{-0.62}$ or a third thermal component with a temperature of $54^{0.26}_{-0.47}$ keV. The resulting luminosity

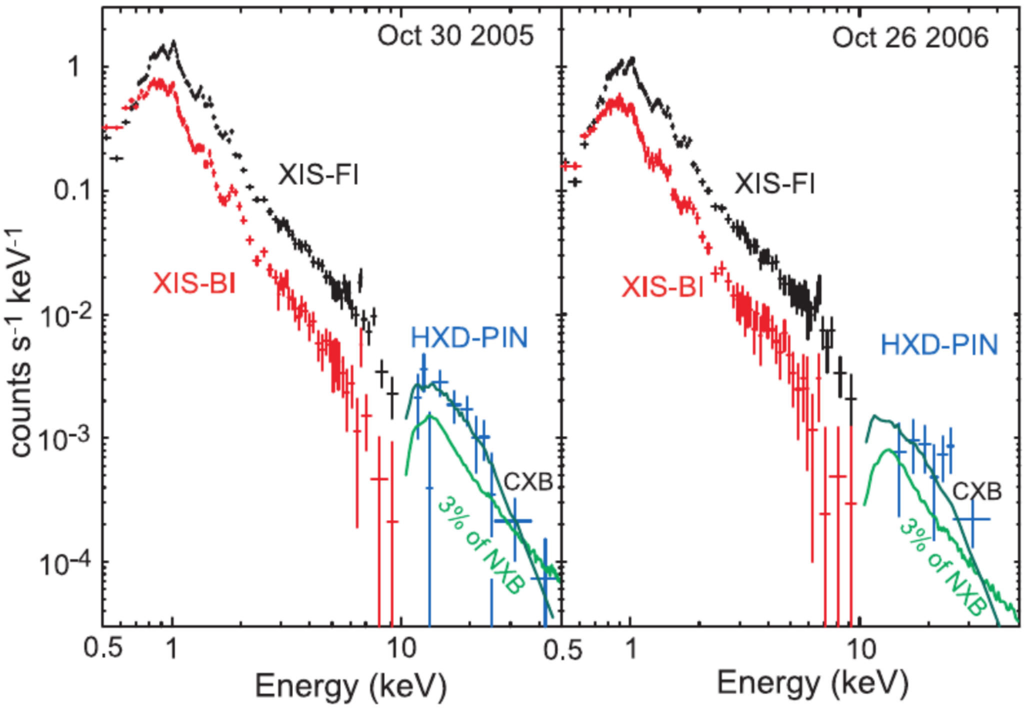

Figure 2.11: The X-ray spectra from the Suzaku data of AE Aqr [10]

for the thermal and additional component on the energy band 4 - 30 keV at a distance of 102 pc was determined as $1.7^{1.3}_{-0.6}$ - $5.3^{1.53}_{-0.3}$ $\times$ 10^{29} erg cm^{-2} s^{-1}. This luminosity compares to 0.09 % of the white dwarf spin-down power. These authors associated the pulsed hard X-ray emission with relativistic electrons generated by a particle acceleration mechanism within the strong fields of the rapidly rotating white dwarf.

Contemporaneous observations of soft and hard X-rays from Chandra and Swift were analyzed and modelled by Oruru and Meintjes [21]. The X-ray emission at energies below 10 keV exhibited thermal dominance. These authors revealed that the X-ray spectra could be reproduced by models of multi-component thermal emission with a time-averaged luminosity of $L_X = 10^{31}$ erg s^{-1}. Chandra and Swift also confirmed the pulsed 33 s soft X-ray emission below 10 keV. These authors associate the X-ray emission at energies below 10 keV with plasma heating at the radius of the magnetosphere, resulting from the gravitational potential energy dissipation. The calculated efficiency of conversion α $\sim$0.01 is sufficient to heat the plasma to temperatures of $kT \leq 10$ keV, which is high enough to drive the emission below 10 keV. These authors suggest that the Suzaku hard X-ray emission exhibits non-thermal properties that could be associated with synchrotron emission from relativistic electrons accelerated by the fast rotating white dwarf. They also pointed out that the contribution of the calculated luminosity on the spin-down power is sufficient to place AE Aqr in the category of the spin-powered pulsars that falls between 2 and 20 keV. They also showed that electrons could be accelerated to higher energies above 10 TeV outside the radius of the light cylinder.

Kitaguchi et al., [90] observed AE Aqr with NuSTAR imaging hard X-ray observatory to search for possible thermal emission above 10 keV and to investigate and characterize the narrow feature in its pulse profile. The phase averaged spectrum of the energy band 3-30 keV can be fitted by two possible optically thin thermal models,

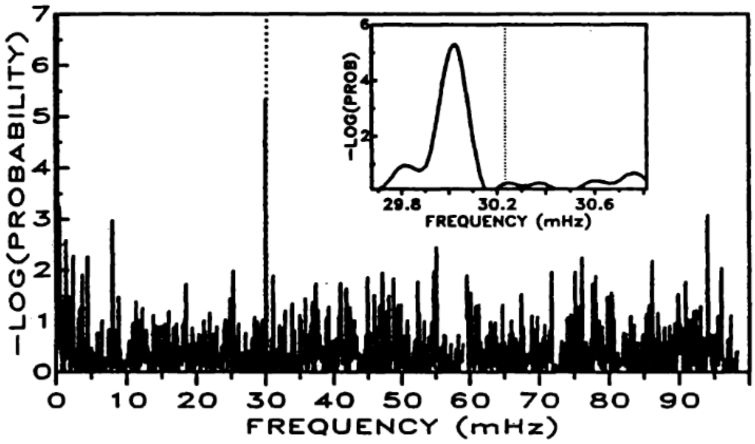

Figure 2.12: The periodogram of the very high energy Tera electron volts (VHE-TeV) pulsed emission of AE Aqr. The dotted line represent the very stable white dwarf spin frequency of 30.23 mHz, where the insert shows the shifted p VHE-TeV periodic signal [11].

where the first model has two components with the first component at a temperature of 2.3 keV and the second component at 8.7 keV. The second proposed model also has two components with the first component at a temperature of 3.9 keV, and the second one fitted with a power law with a photon index of 2.2. The first model was slightly preferred because it complements the statistics. The analysis confirmed the previously obtained sinusoidal pulse profiles in the hard energy band 3-30 keV with a pulse fraction of 16.4± 2.4%. Nevertheless, the sharp pulse feature reported on the energy band 3-30 keV was not found in this analysis.

Ryspaeva [91] re-analyzed the archival X-ray observations of AE Aqr, acquired using XMM-Newton and Chandra in 2001 and 2005, respectively. The analysis was performed using independent timing analysis along with two numerical methods. The presence of a 33 s spin period of the white dwarf in AE Aqr was confirmed. Nevertheless, X-ray pulsations at the period of the first harmonic were not detected. This author suggests that since the 16.5 oscillations were detected in optical and UV emission, the absence of these oscillations in X-ray may imply that a different process produces the X-ray emission, i.e., they originate from one of the poles close to or on the white dwarf surface.

2.2.4 Gamma-ray studies

The first report of positive gamma-ray identification from AE Aqr was given by Brink et al., [11]. The pulsed emission signal was observed at red-shifted periods with a Rayleigh statistic of 24.5, and the chance of occurrence probability less than 0.01, after statistical penalties have been introduced (see Figure 2.12). These shifted periods were explained in terms of the Cheng and Ruderman disk-fed model, which suggests that during the flares, the very high energy Tera electron volts (VHE-TeV) pulsed emission from AE Aqr will be observed at periods slightly shifted. The compatibility between the VHE-TeV results and the model implies that AE Aqr has an accretion disk component.

Meintjes et al., [12] using the Nooitgedacht Mk I Cherenkov telescope, observed AE Aqr between 1988 and 1991. Some of these observations were made near-simultaneously

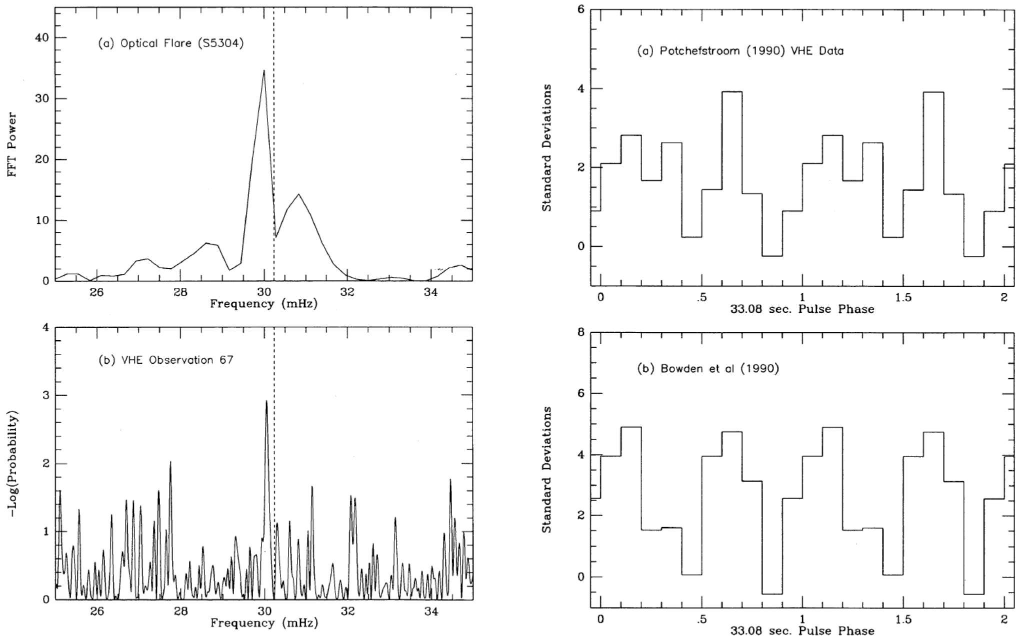

Figure 2.13: Pulse profile of optical and VHE gamma-ray (left panel), almost identical pulse phase of near simultaneous observations by two different groups (right panel) [12, 13]. The dotted line represent most regular QPO frequency of 30 mHz

with optical photometric observations, amounting to a total of 93 observations resulting in the detection of VHE gamma-ray emission. Evidence of consistent strong pulsed VHE-TeV emission with the significance of 4σ contemporaneous with optical flares at frequencies close to the rotational frequency of the white dwarf in AE Aqr, i.e., $\sim$29.9-30 mHz and the fundamental frequency F_0=30.23 mHz was reported. The detection of pulsed VHE-TeV emission at the same frequency with optical emission was a remarkable outcome, which confirmed the hypothesis that the pulsed VHE-TeV gamma-ray is correlated with optical emission during the optical flares (see Figure 2.13). The resulting time-averaged luminosity from this study at the threshold energy of $\sim$ 2.4 TeV has the value of $L_\gamma \sim (1.5 \pm 0.3) \times 10^{32}$ erg s^{-1}, which is equal to conversion efficiency of 15 % of the spin-down power to facilitate high energy gamma-ray emission. Another significant result was the similarity between the VHE gamma-ray pulse profile and the optical profile obtained during near-simultaneous observations by two groups, e.g., Durham and Potchefstroom (see Figure 2.13 [12, 22]).

Bowden et al., [13] also conducted VHE gamma-ray studies in 1990 and 1991 utilising the Durham University Mark III and IV VHE gamma-ray telescopes at Narrabri, NSW, Australia. Four distinct datasets were acquired, each spanning approximately 10 days. The datasets from October 1990 and August 1991 manifest periodicity at a chance probability of 10^{-1} and 0.016, respectively. The optical and VHE gamma-ray oscillation period were similar over at least 10 days, with most of the pulse power concentrated in the first harmonic. The most significant outburst was on the 13^{th} of October 1990, which lasted for about a minute, and two independent telescopes detected it. These short outbursts exhibit the 33 s periodic pulse structures with pulses that are in phase with pulses seen during the strongest sustained periodic signal in the observed data on an observation that lasted for 3 h.

The simultaneous VHE-TeV gamma-ray and optical observations between July 1992 and June 1993 confirmed the previously obtained periodicity results at the 0.001 level without any period search, and the duty cycle of these periodicities was also confirmed at 10 % [6]. The strongest signal of VHE-TeV outbursts seems to be confined to just before the start of a strong optical flare. These authors explained the red-shifted VHE-TeV gamma-ray periodicities in terms of the pulsar-like spin-down of the white dwarf that pushes the accretion disk further outside the co-rotation radius. After an optical flare, very short (about 1-3 min) rapid bursts were observed with three independent telescopes. The largest outburst had a significance of 4.6 σ per minute with a 5.3×10^{-4} probability of obtaining such outburst given all trials. It was pointed out that the observed spin-down power $-\Omega\dot{\Omega} = 6\times10^{33}$ ergs s^{-1} can explain the energy released by a VHE-TeV accelerator in AE Aqr.

Chadwick et al., [22] also conducted a follow-up study with data acquired in the period July 1992-October 1993 using the Durham University VHE gamma-ray telescopes at Narrabri, NSW, Australia. The total observations time was 78 h, and no continuous low-level pulsed emission distinguishable above an energy threshold of 350 GeV was detected. Nevertheless, a significant excess of pulsed VHE gamma-rays was detected on 11 October 1993. The outburst was approximately 4200 s long, and it took place at phase 0.62-0.74 in the orbital period (9.88 h) of the system. The significance of the count rate was measured at the 99.997 % confidence level, and most of the power was at the first harmonic of the 33 s rotational period of the white dwarf. The chance occurrence of such an event has a probability of 10^{-7}, after considering the degrees of freedom for burst-like pulsed emission. The outburst flux was $\sim$ 4 % of the total cosmic ray background at energies above 350 GeV with a peak pulsed luminosity of 10^{32} ergs s^{-1}

Another follow-up observations of AE Aqr was conducted over the epoch 1991-1992 using the Whipple Telescope [92]. The imaging technique was employed, and the VHE-TeV gamma-ray data were analyzed utilising supercuts. No evidence of either periodic or steady gamma-ray emission was found in a 36 hour long dataset. Using Whipple again the nova-like system was observed for 27.5 h in July-October 1995 [93]. The search for VHE-TeV gamma-rays at either the fundamental or first harmonic frequencies resulted in no detection of any pulsed emission and a search for very short burst events yielded no evidence of gamma-ray emission. Lang et al., [94] did a subsequent search for VHE-TeV emission using a total of 68.7 h data observed between 1991 and 1995 utilising the Whipple Observatory telescope. The analysis resulted in no detection of episodic or pulsed VHE-TeV gamma-ray emission. The study resulted in an upper limit flux value for a steady emission of 4.0 $\times10^{-12}$ photons $cm^{-2}s^{-1}$ at threshold energy of 900 GeV, where this upper limit value is 3 orders of magnitude less than the flux values reported during burst events.

Multi-frequency campaign observations, simultaneous in the optical, UV, radio, X-ray, and gamma-ray, were conducted on four consecutive nights in August 2005 using the MAGIC telescope [95]. The study resulted in no detection of any episodic or pulsed gamma-ray emission. The upper limit flux value for a steady emission was $\sim$ 8.0 $\times10^{-12}$ photons cm^{-2} s^{-1} at threshold energy of 350 GeV, and the pulsed emission upper limit flux obtained was $\sim$ 4.0 $\times10^{-12}$ photons cm^{-2} s^{-1} at the first harmonic of the rotational period of the white dwarf.

One of the recent gamma-ray campaigns was the multi-frequency observations (simultaneous optical, X-ray, and gamma-ray), conducted during the period 15 May and 19 June in 2012 [14]. The mission of the campaign was to get conclusive results about the VHE gamma-ray emission from AE Aqr. The X-ray and optical wavebands

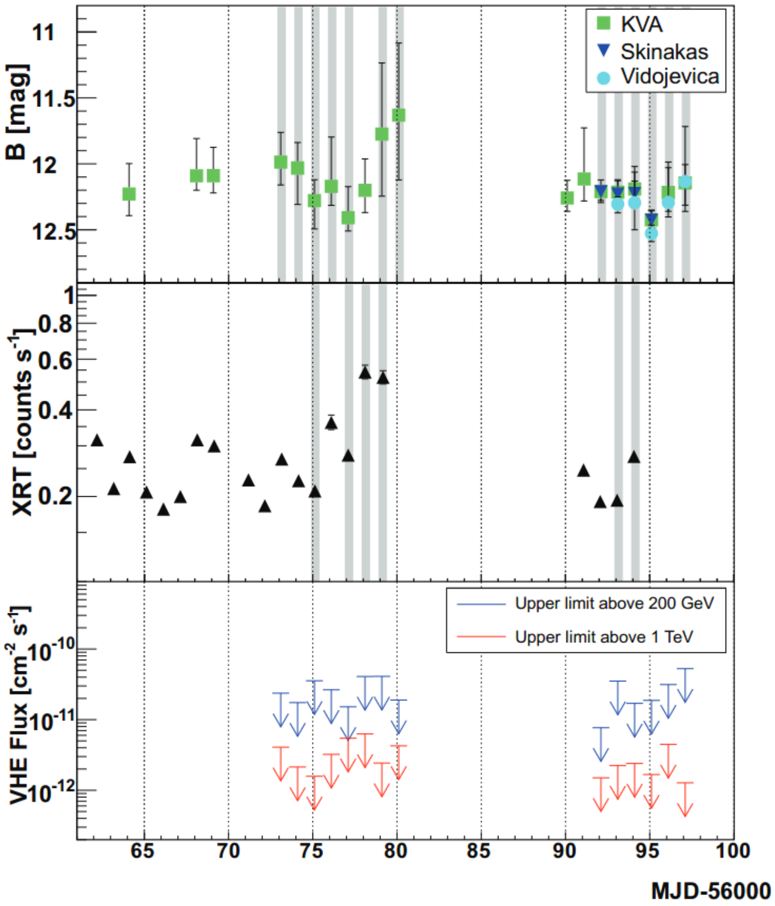

Figure 2.14: Light curves of optical, X-ray and gamma-ray emission from AE Aqr. [14]

displayed a level of brightness and variability consistent with previous observations (see Figure 2.14). The source exhibited a higher state in X-ray and a lower state in optical than the baseline in several days. The lowest state in optical (B band) was at magnitude of 12.5, which is 1.5 magnitudes fainter than the high state, and in the X-ray, the peak state was 3 times above the baseline. The correlation among these wavebands was established; the search was either between the optical and gamma-ray upper limit or X-ray and gamma-ray upper limit. It was found that the upper limit of the gamma-ray emission did not respond to changes in the state exhibited in X-ray and optical emission. For the entire observation, both pulsed and steady gamma-ray emission was searched for periods coincident with optical emission, and unfortunately, no significant gamma-ray emission was detected. The most restrictive upper limit was calculated at threshold energies of 200 GeV (6.4×10^{-12} photons cm^{-2} s^{-1}) and 1 TeV (7.4×10^{-12} photons cm^{-2} s^{-1}). The resulting upper limit values were 3 orders of magnitude lower than the flux values reported in the early 90's. These authors pointed out that the value of the upper limit is consistent with flux values predicted by the ejector white dwarf model.

Unfortunately, other Cherenkov telescopes could not detect any gamma-rays and only produced upper limits. A search for pulsed emission utilising the Fermi-LAT pass 7 exhibited no steady emission above the noise level, it however revealed some weak coherent pulsed signatures at the first harmonic $2F_0 = 60.46$ mHz (16.54 s) of the fundamental frequency $F_0 = 30.229$ mHz (33.08 s, see Figure 2.15, [15]). Investigation of this pulsation in separate energy bins revealed a coherent modulation at

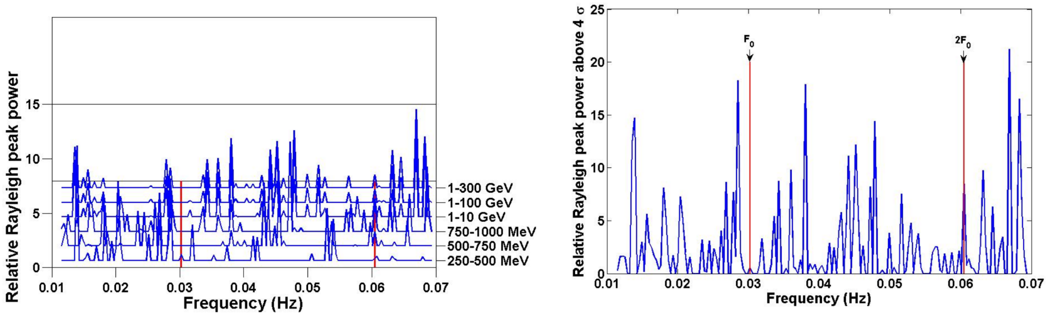

Figure 2.15: A search for pulsed emission from Fermi-LAT data in all energy bins resulted in a weak pulsed modulation in all energy bins (left), and a combined power spectrum also resulted in weak pulsations at the fundamental frequency (right) [15].

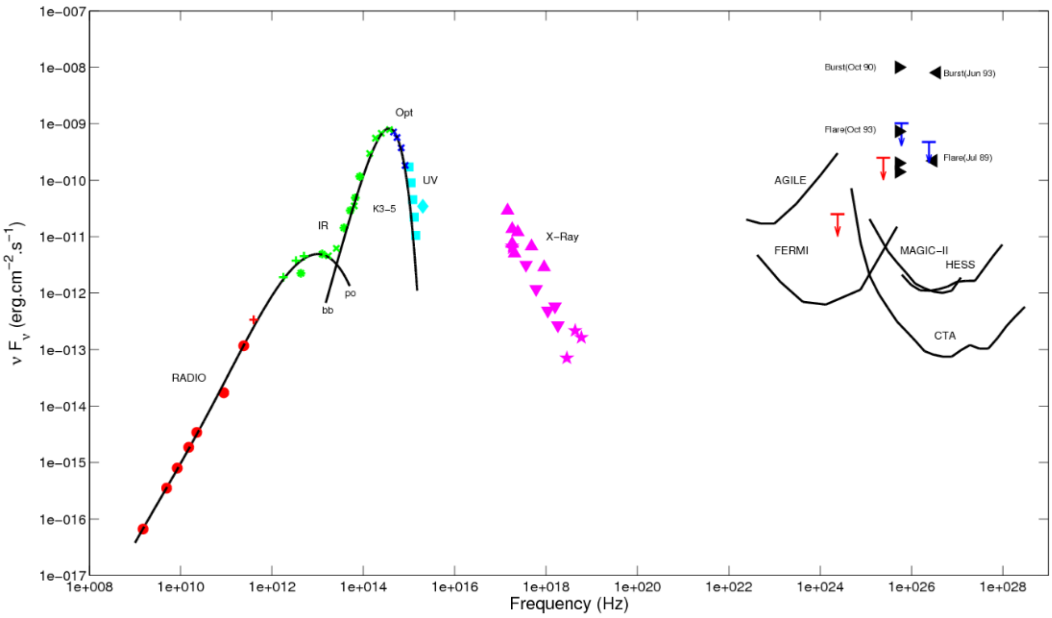

Figure 2.16: The spectral energy distribution of AE Aqr, with sensitivity curves of gamma-ray satellites and ground based telescopes. [16]

$2F_0 = 60.46$ mHz in all energy bins. At the same time, the power spectrum of combined energy bins reveals a coherent pulsation of $2F_0 = 60.46$ mHz in the noise level for the overall significance.

Li Jian et al. [96] conducted the first deep search for pulsed and steady gamma-ray emission using a 7-year pass 8 dataset from Fermi-LAT. These authors used the archival X-ray data from ASCA, XMM-Newton, Chandra, Swift, Suzaku, and NuSTAR spanning 20 years. The 20 year X-rays dataset substantially improve the spin ephemeris of AE Aqr. The search for pulsations at the spin period of the white dwarf was performed using the derived ephemeris. The analysis resulted in no detection of pulsed gamma-rays above 3 σ significance. Neither variable gamma-rays nor phased averaged emission from AE Aqr was detected. The most restrictive upper limit was calculated in the energy range of 0.1-300 GeV, and the result was estimated at 1.3×10^{-12} erg cm^{-2} s^{-1}

A discussion of emission properties of AE Aqr since the discovery of this binary system till to date has been given. A short summery of the periodic nature of emission from AE Aqr will now be given. A rapid periodic oscillation in the optical light curve

Waveband	Fundamental period P_0	First harmonic period $2P_0$
Optical	33.078 ± 0.002	16.54 s
UV	33.076737 s	
Soft X-ray	33.06 ± 0.10 s	
Hard X-ray	33.0764 ± 0.0005 s	
Gamma-ray	33.289 ± 0.055 s	16.54 s

Table 2.1: The summery of the periodic emission from AE Aqr, here is an overview of the various values of the spin period at different frequencies.

of AE Aqr were first detected by Patterson [5]. These oscillations were observed at both the fundamental period and the first harmonic with an amplitude range 0.2 - 0.3 % but can exceed 1% in flares. A year after the discovery of pulsations in the optical band soft X-ray periodic signals were also detected at the fundamental period but no pulsations were confirmed at the first harmonic [82]. In the same study the significance of F_1 and F_2 peaks near the fundamental frequency F_0 were also observed. Studies for coherent oscillations at the fundamental period in the UV were also conducted and large amplitude were detected in the UV band i.e., 40 % of the mean quiescent level [72]. The search for pulsed hard X-ray emission revealed oscillations at the fundamental period [10]. In the early 90's pulsed gamma-ray emission were detected by two independent groups [13, 6]. Gamma-ray pulsations were measured at both the fundamental period and the first harmonic, and they were measured from near simultaneous optical-TeV gamma-ray observations. Near the fundamental frequency F_1 and F_2 peaks were also observed in the gamma-ray band. The measured periods for all aforementioned bands are listed in Table 2.1. The search for pulsation from radio waveband revealed no pulsed signal at either the fundamental or the first harmonic [32].

The multi-frequency studies performed on AE Aqr are sufficient to classify this source as a transient source. The broad-band multi-frequency emission from radio to possibly TeV gamma-rays have distinguished this source from other CVs. Perhaps its unique characteristics, among other CVs, is the reason why it has become one of the best-studied sources in the sky, from radio to TeV gamma-rays (e.g., [30, 5, 12, 6, 22]). AE Aqr exhibits both non-thermal and thermal emissions up to very high energies as can be seen on the spectral energy distribution, Figure 2.16.

Chapter 3

Magnetic propeller and particle acceleration in AE Aqr

Introduction

The multi-frequency non-thermal emission from AE Aqr is associated with the propeller action, magnetohydrodynamic (MHD) processes, and possibly also the pulsar-like behaviour of the white dwarf (e.g., [17, 35, 28]). There is substantial evidence for non-thermal multi-frequency emission from radio to possibly VHE gamma-rays that have been observed and reported (e.g., [18, 38]). The Suzaku discovery of hard X-ray emission above 10 keV has strengthened the notion of a spin-powered pulsar-like behaviour, which affirms this source's non-thermal nature (e.g., [10, 21]). It is believed that the transient emission is intimately linked to the magnetic propeller process, which is the driving mechanism behind MHD processes that lead to particle acceleration. A brief discussion of these processes will now be presented.

3.1 Propellering action in AE Aqr

3.1.1 Diamagnetic Blob propeller

The diamagnetic blob propeller process in AE Aqr will be discussed following the discussions presented by Wynn et al., [7]. These authors were the first to apply the magnetospheric propeller mechanism to AE Aqr. Their model assumed a fragmented diamagnetic blob-like mass flow from the secondary to the white dwarf. This approach assumes that the magnetospheric field sweeps across the magnetised blobs and transfers the mechanical energy to the diamagnetic blobs of length l_b and density ρ_b on a time scale

$$t_{mag} \simeq \frac{c_A \rho_b l_b}{B^2} \frac{|v_\perp|}{|(v - v_f)_\perp|}, \tag{3.1}$$

where v_f and v are field and blob velocities, respectively, and $v_\perp$ is the velocity perpendicular to the field line, C_A is the Alfvén speed in the interblob plasma, and B is the local field. If $v > v_f$ the blobs decelerate, the process is analogous to what happens with satellites crossing the earth's magnetic field lines, resulting in the satellites losing orbital height. When the field sweeps faster over the diamagnetic blob than the blob's orbital speed, the effect is propulsive because the magnetic field transfers angular momentum. Given the condition $|v| \gg |\mathrm{v}_f|$ the velocity component disappears and the time-scale reduces to $t_{mag}(slow) \simeq c_A \rho_b l_b / B^2$, where the condition is only applicable to slow rotators. The blob will in this frame now follow a ballistic trajectory, which is reduced by the magnetic drag resulting in an effective gravity

$$g_{mag} = -k[v - v_f]_\perp \tag{3.2}$$

where the drag coefficient k is a function of $t_{mag}(slow)$ i.e., $k \sim l/t_{mag}(slow)$. The rotational period of the white dwarf P_{spin} is introduced into the magnetic acceleration term g_{mag} through the velocity difference. The white dwarf's rotational period P_{spin} directly influences the flow of plasma in the magnetosphere. In the case mentioned above, blobs may be either ejected or accreted, depending on k and the spin period P_{spin}. For a stable mass accretion to occur in intermediate polars (IPs) the relationship $P_{spin} \simeq 0.07\,\mathrm{P_{orb}}$ [17, 7] seems to apply. For the white dwarf in AE Aqr this implies a white dwarf rotational period of $P_{spin} \sim 2500$ s, which is certainly not the case. These authors showed that there are similarities between the model predicted Doppler tomogram and the observed emission line profiles.

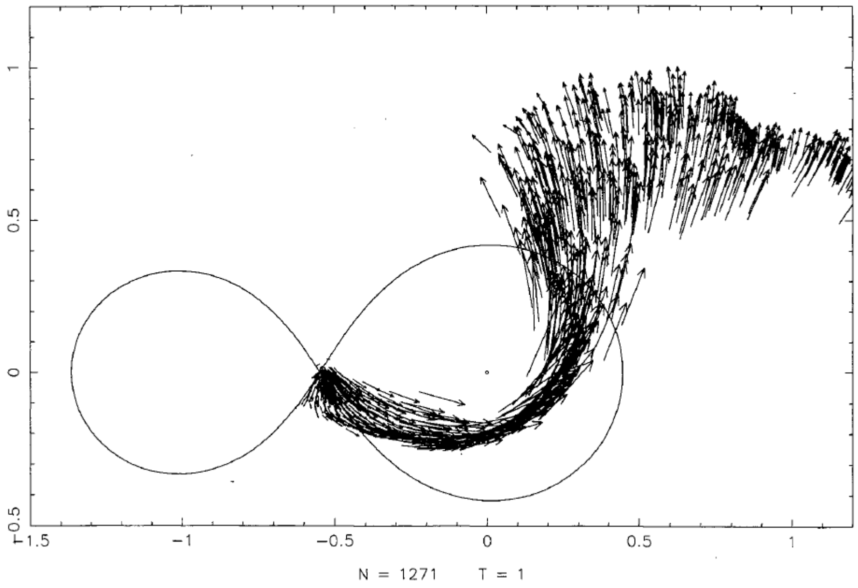

Figure 3.1: Mass flow streaming out of the system of AE Aqr ejected by the propeller mechanism [17].

Wynn et al., [7] concluded that there is no accretion disk in AE Aqr, and they assumed that most of the mass flow is ejected with little or no accretion onto the white dwarf surface (see Figure 3.1). This finding contradicts the scenario depicted by Patterson [5], who proposed the existence of an accretion disk in the system. The spin-down of the white dwarf is accounted for by the inhomogeneous diamagnetic accretion model. Wynn et al., [7] explained the inconsistency in the observed luminosity and the large spin-down power in terms of the kinetic energy carried away by the ejected matter. They also calculated a magnetic dissipation rate of $\sim 10^{33}$ erg s^{-1}. They assumed that a small fraction of the energy would be driven to the surface of the white dwarf as Alfvén waves produced by the blobs as they pass through the magnetosphere. This process results in the observed X-ray hot-spots and UV emission. The spectroscopy of flares in the UV band using the HST provide the observational evidence for mass ejection, where observed emission lines in the UV band are explained in terms of shock heating [33] as faster blobs collide with slower blobs in the outflow.

3.1.2 Kelvin-Helmholtz propeller

Mass transfer from the companion star into the Roche lobe of the white dwarf will follow a ballistic trajectory under the influence of the gravitational pull of the white dwarf. It will settle in a ring-like structure with the same angular momentum as the L_1 region, at the so-called circularization radius. A ring-like structure will develop due to energy dissipation through shocks and subsequently orbit the white dwarf at a radius of $R_{circ} \sim 2 \times 10^{10} \left(\frac{P_{orb}}{9.88\,\mathrm{h}}\right)^{2/3}$ cm (e.g., Frank, King , Raine [3, page 61-62]). Since the circularization radius is further out from the white dwarf than the co-rotation radius, i.e., where the speed of the gas equals the rotation speed of the white dwarf, the ring exerts a drag force on the white dwarf as it interacts with the fast rotating magnetosphere with a local azimuthal velocity of $\mathrm{V}_\phi \sim R\Omega_* \sim 40000(R/R_c)(P_*/\ 33\ \mathrm{s})\ \mathrm{km\ s^{-1}}$. This drag force causes the white dwarf to spin-down. The rapidly rotating white dwarf will try to force the clumpy gas ring at radius R_c to co-rotate with the magnetosphere. This process will give rise to the shearing of the magnetic field and generate a strong azimuthal magnetic fields B_ϕ. If an equilibrium pressure is assumed at R_c with the average pressure estimated by $P_{acc} = \rho V_{\mathrm{ff}}^2 = (\dot{M}V_{\mathrm{ff}}/\pi R_c^2)$, the azimuthal magnetospheric field is approximated by $B_\phi \sim (\dot{M}V_{\mathrm{ff}}/R^2)^{1/2}$, which can a have an estimated value of

$$B_\phi \leq 1000 \left[\frac{\dot{M}}{5 \times 10^{17}\,\mathrm{g\ s^{-1}}}\right]^{1/2} \left[\frac{M_*}{0.9\,\mathrm{M}_\odot}\right]^{1/4} \left[\frac{R}{R_c}\right]^{-5/4} \mathrm{G}. \tag{3.3}$$

The magnetic pitch is now given by $\gamma_\phi = (B_\phi/B_p) = 50(B_\phi/1000)/(B_p/20\,\mathrm{G})$, since the azimuthal magnetic field is B_ϕ and B_p is the poloidal dipolar magnetospheric field at R_c. An important phenomenon occurs when $\gamma_\phi > 10$, magnetic reconnection cannot be avoided as the magnetic field in the shear layer becomes highly unstable [97]. Through reconnection processes, the energy stored in the sheared fields will be released and power the non-thermal and thermal emission in AE Aqr. Since the MHD propeller process is intimately tied to distorted B-fields it opens up the possibility for particle acceleration due to magnetic reconnection and other inductive processes like double layers, which will now be briefly reviewed.

The model proposed by Meintjes and de Jager [35] consists of an intermediate clumpy ring that interacts with the magnetosphere at the circularization radius, where the mass flow stream intersects itself. The momentum transfer between the magnetic field and the ring-like structure occurs through the diffusion of the field into the gas via a Kelvin-Helmholtz instability, which transfers angular momentum to blobs propelling it out of the system. This interaction between the field and the ring will result in angular momentum transfer from the field to the matter in the ring. The effective transfer of angular momentum to the plasma results in mass outflow from the system if the escape velocity is reached. Further, it is believed that the mass outflow from the system may be the driving mechanism behind thermal and non-thermal outbursts.

Wang and Robertson ([98]), modelled the magnetosphere angular momentum transfer to accreting gas in disk accreting neutron stars, and showed that strong MHD instabilities could be produced in a shear layer, resulting in the gas mixing with the fast moving field lines. They also showed that in the boundary layer the gas would twist and distort the magnetic field lines to implement co-rotation and generate loops that will float outwards, transferring angular momentum to the medium [98]. Generated loops would increase in size and unravel, and the angular momentum flux will result in propelled gas streaming away from the propeller zone. Their study also mentioned that the reconnection of magnetic fields between the neighbouring loops should be expected, recombining them into more uniform structures. The current dissipation induced by the magnetic reconnection processes will convert the energy stored in the sheared magnetic field lines into kinetic energy, and the currents produced by sheared field lines will flow along flux tubes in a global circuit that interconnects the white dwarf with the propeller region [99]. Induced currents are very unstable in regions where the density is very low. Meintjies and de Jager [35] showed that in the propeller region the interblob plasma has a very low density, $\beta = (P_{gas}/P_{mag}) = 8\pi N_e k_B T_{\rm eff}/B_p^2 \ll 1$, where B_p is the poloidal dipole field in the magnetosphere, N_e the electron density and T the temperature. For appropriate parameters related to AE Aqr

$$\beta \leq 10^{-7} \left[\frac{B_\phi}{1000\,\mathrm{G}}\right]^{-2} \left[\frac{N_e}{10^{10}\,\mathrm{cm}^{-3}}\right] \left[\frac{T_{\rm eff}}{10^4\,\mathrm{K}}\right]. \tag{3.4}$$

The current in the circuit is sustained through the generation of a large field-aligned potential drop (double layers). The process is similar to mechanical stresses in a material that causes fractures, mostly in regions removed from where the stresses are applied, i.e., the fracture zone. These equivalent fracture zones, which contain low density plasma, are sites where particles are accelerated. This will be discussed in the next sections.

3.2 Particle acceleration

3.2.1 Particle acceleration through magnetic reconnection

In the propeller zone, the poloidal magnetic field will be immensely sheared and twisted, followed by amplification of the magnetic pitch, which will be amplified to values higher than 10. Accordingly, the magnetic intensity will increase in size rapidly, producing an instability in the propeller region, a favourable condition for reconnection of magnetic fields [100, 101, 97]). A detailed discussion of particle acceleration through magnetic reconnection and energy dissipation is found in the following references (e.g., [102, page 301], [103, page 771]). The reconnection process is possible when the magnetic field lines with opposite polarity combine at a neutral point ($B = 0$). Current dissipation in this mechanism may be converted to kinetic and thermal energy in the plasma under some special conditions (e.g., [104, 105]). The electric field induced by the current produced by the reconnection of magnetic field lines is estimated using the Faraday's induction law (e.g., [106, 104]) and the ratio between the merging speed (V_m) of the field lines and the Alfvén speed V_A is $V_m/V_A \sim 0.1$ (e.g., [103, 100]). A particle spiralling in the field, before the azimuthal field recombines, will find a magnetic flux $\Phi_B \sim B\pi R_L^2$ that passes through a hypothetical surface confined by its orbit decreasing with a rate of $\mathrm{d}\Phi_B/\mathrm{d}t \sim -(B\pi R_L^2/\tau_r)$, where $\tau_r = R_L/V_m$ and R_L are the reconnection time scale and the Larmor radius respectively. Faraday's induction law is used to determine the work done per unit charge (*emf*) per single orbit [106]

$$emf = 2\pi R_L E_{DR} = \left[\frac{\pi B_\phi R_L V_m}{c}\right]. \tag{3.5}$$

The magnitude of the induced electric field must be the same as the magnitude of the electric field (E_{DR}) that drives current through the dissipation region (DR) or the current sheet. The electric field induced in the reconnection zone (RZ) as a result of the motion of charge across the the magnetic field ($V \times B$) is given by $E_{RZ} = (\pi B_\phi V_m / c)$ and E_{DR}, according to Ampere's law, will be $E_{DR} = (1/\sigma) J$ (e.g., [107]), where σ represents the conductivity of the plasma and J the current density. High conductivity of a plasma prevents the process of reconnection, thus to generate very strong electric fields in the neutral sheet through current dissipation, the conductivity must be lower than the classical conductivity [103]. Meintjes and de Jager [35] pointed out that since the plasma density in the propeller region is very low, with the magnetic pitch $\gamma_\phi > 10$, the currents produced through the MHD activity may experience current carrier deficits in the regions where the density of the particles become anomalously low, resulting in low electrical conductivity in the local region. The particle accelerating in the resultant electric field gains energy, and its gyro radius (Larmor radius) also increases. Optimum energy is accomplished when the Larmor radius becomes comparable to the current sheet width determined by Ampere's law,

$$w = (cB_\phi / 4\pi j) \sim 5 \times 10^4 \left[\frac{B_\phi}{1000\,\mathrm{G}}\right] \left[\frac{N_e}{10^{10}\,\mathrm{cm}^{-3}}\right]^{-1} \left[\frac{T_{\mathrm{eff}}}{10^4\,\mathrm{K}}\right]^{-1/2} \mathrm{cm}, \tag{3.6}$$

where $j = eN_e V_d$ is the current density in the dissipation region (e.g. [107]). Haerendel [108] determined the electron drift velocity as $V_d \leq fC_s$ with C_s the speed of sound and $f = 10$. Micro-instabilities are triggered in the plasma above the optimum energy limit, increasing the resistivity. The maximum energy ($\varepsilon_{max} = e\Phi_{max}$) to which a particle like an electron can be accelerated is

$$\varepsilon_{max} = \left[\frac{e\pi B_\phi V_A w}{c}\right] \sim 300 \left[\frac{\epsilon}{0.1}\right] \left[\frac{B_\phi}{1000\,\mathrm{G}}\right]^2 \left[\frac{N_e}{10^{10}\,\mathrm{cm}^{-3}}\right]^{-3/2} \left[\frac{T_{\mathrm{eff}}}{10^4\,\mathrm{K}}\right]^{-1/2} \mathrm{MeV}. \tag{3.7}$$

The synchrotron loss rate influences the maximum energy that can be reached by particles (e.g., electrons) in the dissipation zone since the energy loss rate of an electron resulting from relativistic bremsstrahlung is significantly lower than the energy loss rate through synchrotron processes. Given a magnetic field of strength 1000 G and the ion density of $N_i \sim N_e = 10^{10}$ cm^{-3}, the ratio of the synchrotron loss rate to bremsstrahlung is

$$\alpha = \left[\frac{\dot{\varepsilon}_{syn}}{\dot{\varepsilon}_{brem}}\right] = 2 \times 10^5 \left[\frac{B_\phi}{1000\,\mathrm{G}}\right]^2 \left[\frac{N_i}{10^{10}\,\mathrm{cm}^{-3}}\right]^{-1} \left[\frac{\varepsilon_{max}}{300\,\mathrm{MeV}}\right]. \tag{3.8}$$

The minimum time scale of energy loss plays a significant role in the effectiveness of the process. The process is fast if the energy loss time scale exceeds the acceleration time scale given by, $\tau_a \sim w/V_m$. Meintjes and de Jager [35] showed that the synchrotron loss time scale exceeds the acceleration time scale, for the following representative parameters, i.e.,

$$K = \left[\frac{t_{acc}}{\tau_{syn}}\right] = 10^{-4}\left[\frac{\gamma}{600}\right]\left[\frac{B_{\phi}}{1000\,\mathrm{G}}\right]^{2}\left[\frac{N_e}{10^{10}\,\mathrm{cm}^{-3}}\right]^{3/2}\left[\frac{T_{\mathrm{eff}}}{10^{4}\,\mathrm{K}}\right]^{-1/2}. \tag{3.9}$$

For large-scale acceleration of electrons, the induced electric field in the dissipation region must exceed the Dreicer field [$E_D \sim 2\times10^{-10}(N_e/T_{\mathrm{eff}})$ statvolt cm^{-1}]. This is the critical electric field above which electrons accelerate freely in the plasma (e.g., [109, 107]). Meintjes and de Jager [35] showed that the electric field in the dissipation zone exceeds the Dreicer field by five orders of magnitudes,

$$\eta = \left[\frac{E_{DR}}{E_D}\right] \sim 10^{5}\left[\frac{B_{\phi}}{1000\,\mathrm{G}}\right]^{2}\left[\frac{N_e}{10^{10}\,\mathrm{cm}^{-3}}\right]^{-3/2}\left[\frac{T_{\mathrm{eff}}}{10^{4}\,\mathrm{K}}\right]. \tag{3.10}$$

Thus the electrons in the dissipation region (DR) plasma will accelerate freely, free from particle collisions that will thermalize the gas.

The inductive circuits have a unique property of generating huge currents, where in low conductivity regions, there is a possibility of production of relativistic electrons. Meintjes and de Jager [35] argued that for the case of AE Aqr this is enough to account for the observed highly variable non-thermal radio-IR outbursts detected ([30, 77, 110]). These authors also showed that the energy radiated by electrons in the dissipation zone is radiated at the rate of $P_s = 2.37\times10^{-3}B_{\phi}^{2}\varepsilon^{2}$ erg s^{-1}, with maximum radiation at $\nu = \gamma^2\nu_c = \gamma^2(eB_{\phi}/2\pi m_e c)$, here ν_c represents the cyclotron frequency. They also showed that an electron accelerated in the dissipation zone would radiate its optimum energy at

$$\nu_m \leq 10^{15}\left[\frac{\gamma}{600}\right]^{2}\left[\frac{B_{\phi}}{1000\,\mathrm{G}}\right]\ \mathrm{Hz}. \tag{3.11}$$

The resulting synchrotron luminosity is

$$L \sim \Omega S_{\nu} D^{2} = \Phi P_s N_{\gamma} 2\pi R_c \delta R_c l, \tag{3.12}$$

where $\Phi \sim (w/R_c)^2$ is the scale factor introduced by Meintjes and de Jager [35] to determine the relative fractional area of the propeller zone responsible for producing particle acceleration in the dissipation zone. l and P_s represent the length of the dissipation zone and the synchrotron power of a single electron, respectively. They determine the expected synchrotron luminosity from the propeller region by assuming that $\delta R_c = R_c = l$,

$$L_s \sim 10^{32}\left[\frac{\Phi}{10^{-10}}\right]\left[\frac{\gamma_e}{600}\right]^{3}\left[\frac{B_{\phi}}{1000\,\mathrm{G}}\right]^{2}\left[\frac{l}{R_c}\right]\left[\frac{R_c}{2\times10^{10}\,\mathrm{cm}}\right]^{2}\left[\frac{N_e}{10^{10}\,\mathrm{cm}^{-3}}\right]\ \mathrm{erg\,s^{-1}}, \tag{3.13}$$

and assuming that energy is mainly radiated at the frequency ν_m, they showed that the flux density $I_{\nu} = S_{\nu}/\nu_m$ will have a value of,

$$I_\nu = \left[\frac{L_s}{4\pi\nu_m D^2}\right] \sim 10 \left[\frac{L_s}{10^{32}\,\mathrm{ergs}^{-1}}\right] \left[\frac{\nu}{10^{15}\,\mathrm{Hz}}\right]^{-1} \left[\frac{D}{100\,\mathrm{pc}}\right]^{-2} \mathrm{mJy}. \tag{3.14}$$

This implies that this luminosity may be hidden in the thermal spectrum of the K4-5 secondary star.

3.2.2 Particle acceleration through double layers in the magnetosphere

Another consequence of sheared magnetic fields is global field-aligned potential drops in the magnetosphere. Field-aligned currents $j_{\parallel}$ flow along the flux tubes in a global circuit in the magnetosphere. Accordingly, the shear in the propeller region is dissipated through the flux tubes. The magnetic field strength decreases with an increase in distance from the white dwarf, i.e., it is inversely proportional to the cube of the radius R, while the electron density is directly proportional to R increases towards the propeller region. Low electron density and strong magnetic fields close to the white dwarf imply an increase in plasma resistivity $\eta \propto T^{-3/2} ln(T^{3/2}/N_e^{1/2})$. Consequently, the field-aligned current $j_{\parallel}$ may reach a critical value $j_{crit} = eN_e f C_s$ [111] for powerful micro-instabilities to develop. Once the threshold of the field-aligned current j_{crit} is reached, anomalously high resistivity is realised in the region where strong double layers develop with large field-aligned potential drops $\Phi_{\parallel}$. The value of the potential drop in the double layer was estimated (e.g., [35, 111] through the ratio of the influx of electromagnetic (EM) Poynting flux into the double layer and the flux of charged particles from the double layer,

$$\Phi_{\parallel} = \left[\frac{\text{EM energy influx into the double layer}}{\text{Particle flux from the double layer}}\right]. \tag{3.15}$$

This potential drop can be written in a mathematical form as,

$$\Phi_{\parallel} = \left[\frac{B_\phi^2 V_A}{8\pi e N_e V_D}\right] \tag{3.16}$$

where N_e, V_A and $V_d = fC_s$ represent the electron density , Alfvén velocity and drift velocity respectively. Meintjes and de Jager [35] showed that

$$\beta \sim 10^{-16} \left[\frac{N_e}{10^6\,\mathrm{cm}^{-3}}\right] \left[\frac{T_{\mathrm{eff}}}{10^4\,\mathrm{K}}\right] \left[\frac{B_p}{10^6\,\mathrm{G}}\right]^{-2}. \tag{3.17}$$

The Alfvén velocity V_A approaches the speed of light where $\beta \ll 1$ and the electron densities in the magnetosphere having the values $N_e \simeq 10^6$ cm^{-3} [33]. These conditions are assumed to be applicable close to the white dwarf, with the resulting potential drops taking values of,

$$\Phi_{\parallel} \sim 300 \left[\frac{B_\phi}{1000\,\mathrm{G}}\right]^2 \left[\frac{N_e}{10^6\,\mathrm{cm}^{-3}}\right]^{-3/2} \left[\frac{T_{\mathrm{eff}}}{10^4\,\mathrm{K}}\right]^{-1/2} \text{Tera Volts} \tag{3.18}$$

It was argued [35] that in this region, the synchrotron losses are the ultimate energy limiting factor on electrons. It was then shown by equating the rate at which particles (e.g., electrons) gain energy to the synchrotron loss rate of the accelerator the electrons will reach a maximum energy of,

$$\varepsilon_{max} \leq 50 \left[\frac{B_m}{B_*}\right] \left[\frac{\Phi_{\parallel}}{300\,\mathrm{TeV}}\right]^{1/2} \left[\frac{l}{R_*}\right]^{-1} \mathrm{keV} \tag{3.19}$$

where it was assumed that an accelerator has the same size as the white dwarf [35]. This may have relevance to explain the observed Suzaku X-ray emission from AE Aqr.

Accelerated protons and ions are not affected by synchrotron losses. Hence, these particles reach the full energy of the accelerator. These energetic particles will interact with the ambient matter or influx of gas in the system. Accordingly, gamma-rays are produced through this particle-particle collision. Meintjes and de Jager [35] argued that the interaction time-scale τ_{pp} of an energetic proton or ion beams with the surrounding gas must be shorter than the duration of the Keplerian periods of the surrounding gas orbiting the accelerator. gamma-ray studies revealed a pulsed component that is consistent with Keplerian periods that are $P_K \sim 33.3$ s [6]. The correlation between the Keplerian and the pulsed period of observed data implies a lower limit to the gas densities inside the blobs of [35],

$$N_b > [cP_K\sigma_{pp}]^{-1} > 2 \times 10^{13} \left[\frac{\sigma_{p-p}}{50\,\mathrm{mb}}\right]^{-1} \left[\frac{P_K}{33.3\,\mathrm{s}}\right]^{-1} \mathrm{cm}^{-3} \tag{3.20}$$

where σ_{pp} is the cross section for particle-particle collisions. The cross section for a particle-particle is expressed in millibam (mb, where 1 mb $= 10^{-27}$ cm^2). The estimated blob densities of $N_b \sim 10^{16}$ cm^{-3} obtained from hard X-ray studies of, e.g., AM Herculis [112] correspond well with the minimum limit of target matter required to generate VHE gamma-ray pulsed emission at short periods (e.g., 33.3 s). Meintjes and de Jager [35] suggested that VHE pulsed emission from AE Aqr will be observed with periods $P_{TeV} \sim P_*/(1 - P_*/P_K)$ because the target matter is mostly located and restricted to the regions outside the co-rotation radius. They also used the concept of a double layer to explain the unique gamma-ray burst observed from this source. The double layers are assumed to form in high-micro-instability regions with high resistivity and high potential drops. As a result, very large electric fields are expected in these regions. In this framework the total double layer power ($P_{DL} = \int j \cdot E dV = (1/2)LI^2$) is converted to kinetic energy of particles, and subsequently TeV gamma-ray emission. It was assumed that the strongest potentials are produced close to the compact object [35] where the proton density is limited to $N_p \sim 10^6$ cm^{-3}, and the current of very energetic particles in the double layer is given by $j = eN_pc$. The luminosity of these relativistic protons was estimated at,

$$P_{DL} = (eN_pc\phi_{\parallel}d^2) \approx 10^{34} \left[\frac{N_p}{10^{12}\,\mathrm{cm}^{-3}}\right] \left[\frac{\Phi_{\parallel}}{10^{12}\,\mathrm{V}}\right] \left[\frac{d}{R_*}\right]^2 \mathrm{erg\,s}^{-1}. \tag{3.21}$$

This value is sufficiently large to explain the observed VHE gamma-ray burst luminosity [6]. In addition, this value matches the spin-down power, and in this framework, all the spin-down power is converted into the kinetic energy of very high energy particles, hence very high energy emission at high energies $E \geq 0.1$ TeV.

3.2.3 Pulsar-like particle acceleration

The propeller spin-down power of the white dwarf in AE Aqr, which is greater than the total multi-frequency emission, may imply that the spin-down power is most probably behind all or most of the multi-wavelength emission in AE Aqr. The discovery of hard X-rays with a flat power law spectrum analogous to pulsars with low-mass accretion, places AE Aqr in a similar category as rotation powered pulsars (e.g., [21]). Hence, pulsar-like particle acceleration is expected from this system. The spin-down is possibly the driving factor behind the generation of substantial electric fields along the magnetic field lines. The component of the electric field parallel to the magnetic field, e.g., [113, 114] is

$$E_{\parallel} = E_{AS}^{\parallel}\sqrt{2R/r}, \tag{3.22}$$

where $E_{AS}^{\parallel}$ is calculated as

$$\begin{aligned} E_{AS}^{\parallel} &= \frac{1}{8\sqrt{3}}\left(\frac{\Omega_* R}{c}\right)^{5/2} B_* \\ &= 10^4 \left(\frac{P}{33\,\mathrm{s}}\right)^{-\frac{5}{2}} \left(\frac{\mu_{33}}{10^{33}\,\mathrm{G\,cm}^3}\right) \left(\frac{R}{10^9\,\mathrm{cm}}\right)^{-\frac{1}{2}} \mathrm{Vm}^{-1} \\ &= 10^3 \left(\frac{P}{33\,\mathrm{s}}\right)^{-\frac{5}{2}} \left(\frac{\mu_{33}}{10^{33}\,\mathrm{G\,cm}^3}\right) r_{l,11}^{-\frac{1}{2}}\, \mathrm{Vm}^{-1}. \end{aligned} \tag{3.23}$$

This expression describes $E_{AS}^{\parallel}$ in the vicinity of the light cylinder radius, where μ_{33} is the magnetic moment of the white dwarf given in the units of $10^{33}\,\mathrm{G\,cm}^3$, and $P = 33$ s is the spin period of the white dwarf i n AE Aqr. The electric potential in the regions between the polar cap and the light cylinder is then given by:

$$\begin{aligned} V_{pc}(r) &= \int_R^r E_{\parallel} ds \\ &\simeq 2\times 10^{11} \left(\frac{P}{33\,\mathrm{s}}\right)^{-\frac{5}{2}} \left(\frac{\mu_{33}}{10^{33}\,\mathrm{G\,cm}^3}\right) \left(\frac{R}{10^9\,\mathrm{cm}}\right)^{\frac{1}{2}} \left[\left(\frac{r}{R}\right)^{\frac{1}{2}} - 1\right] \mathrm{V}. \end{aligned} \tag{3.24}$$

The electric potential varies with the distance from the white dwarf. Figure 3.2 shows this variation with distance normalized with respect to the light cylinder radius ($\eta = r/R_{lc}$), where $R_{lc} \approx 5$ ls (ls=light seconds). Close to the white dwarf's surface, the potential difference is zero($V = 0$), and the electric potential increases to orders of 1 Tera Volt at the light cylinder radius and beyond.

The pulsar-like acceleration requires a region with high magnetic fields and low plasma density. The propeller action in AE Aqr is ensuring a region of low density somewhere in the vicinity of the white dwarf. The mass transfer rate is very high compared to the mass accreted ($\kappa = \dot{M}_1/\dot{M}_2 \sim 10^{-3}$), implying that the density

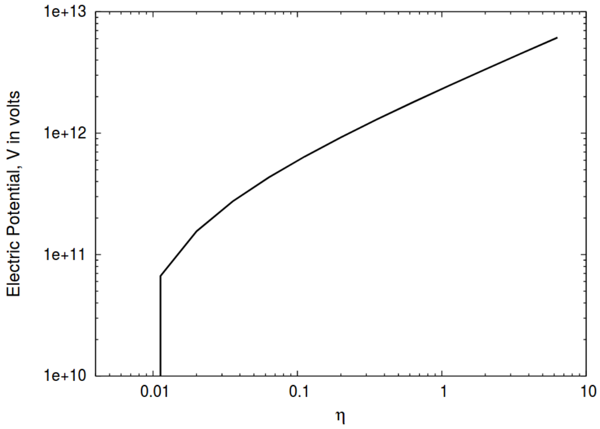

Figure 3.2: Variation of the electric potential as a function of normalized radius [18]

of the plasma close to the white dwarf may approach the Goldreich-Julian density ([115]), which is given by

$$n_{GJ} \simeq 2 \times 10^3 \left(\frac{B_*}{10^6}\right)\left(\frac{P}{33\,\mathrm{s}}\right)^{-1} \mathrm{cm}^{-3}, \tag{3.25}$$

where B_* is the white dwarf's surface field strength. The electrostatic shielding will not short-circuit electric fields in such a low plasma density, where the synchrotron losses and the ionization losses determine the effective acceleration of electrons.

Thermal electron density (n_p) free mean path is $\lambda_e = (1/n_p)(1/ln\Lambda)(\pi e^2/8\epsilon_0 E_e)^{-2}$, where $ln\Lambda$ is the Coulomb logarithm [$ln\Lambda \sim 10-20$ (e.g., [10])]. Meintjes, Oruru, and Odendaal [18] showed that thermal electrons with energy $E_{th} \sim 1$ keV with the plasma density n_p have mean free paths ranging between $\lambda_e \sim 10^6(n_p/10^{11}\ \mathrm{cm}^{-3})^{-1}$ cm - $10^{11}(n_p/10^6\ \mathrm{cm}^{-3})^{-1}$ cm. They also showed that the electrons in the thermal plasma with the electric field in excess of the Dreicer field, $E_D \sim 2 \times 10^{10}(N_e/T_{eff})$ statvolts cm^{-1} (e.g [35]), accelerate freely without encountering the hindering effects of particle-particle collisions. The Dreicer field upper limit for AE Aqr is of the order of

$$E_D \leq 0.1 \left(\frac{n_e}{10^{11}\,\mathrm{cm}^{-3}}\right)\left(\frac{T_{eff}}{10^7\,\mathrm{K}}\right)^{-1} \mathrm{V\ m}^{-1}, \tag{3.26}$$

where n_e is the particle density and T_{eff} is the effective temperature . They also showed that $\delta = E_{\|}/E_D \gg 10^4$. This result implies the effective acceleration of the whole electron population in the plasma.

3.3 Propeller and pulsar induced non-thermal signatures from radio to VHE emission

The magnetic propeller process and the accompanying particle acceleration have been discussed up to now since it is believed that the transient emission is linked to these processes. Refer to Appendix A for a detailed discussion of non-thermal mechanisms (e.g., synchrotron process). For the rest of this chapter, non-thermal signatures from radio to VHE emission associated with the magnetic propeller and particle acceleration will be briefly discussed.

3.3.1 Non-thermal Radio emission

Venter and Meintjes [34] proposed a model where Kelvin-Helmholtz instabilities play a significant role. They showed that the differential motion between the slow clumpy mass stream from the secondary star and the fast rotating magnetosphere would result in Kelvin-Helmholtz instabilities. The mixing of the gas stream with the magnetosphere will result in massive shearing of magnetic fields, perhaps triggering the tearing mode instability and resultant reconnection of magnetic fields which accelerates the trapped electrons to energies of $\sim 20\,\mathrm{MeV}$ in the presence of the magnetic field of the order of $\sim 400\,\mathrm{G}$. This process will result in the generation of magnetised bubbles, which will be flung out by the propeller mechanism. The spectrum of radio to mid-IR of AE Aqr in this frame is produced by the superposition of the emission from several blobs [34] (see Figure 3.3).

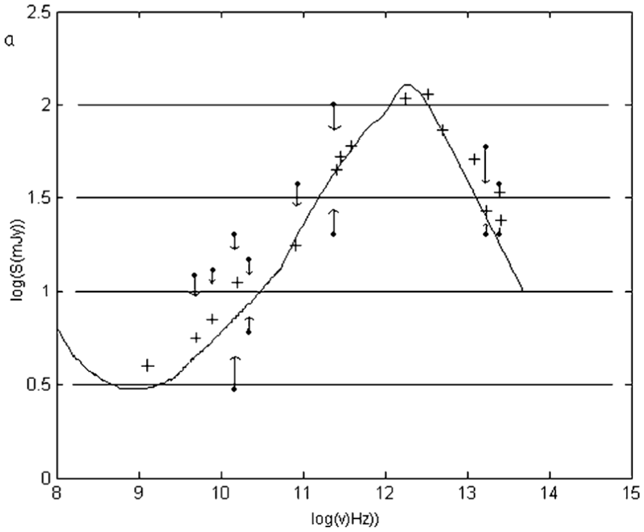

Figure 3.3: The simulated and observed spectrum of superposition of several (≥ 10) synchrotron emitting magnetised bubbles ($B_0 \geq 1000\,\mathrm{G}$) in different stages of evolution. [19]. See also Figure 2.10 for comparison.

However Abada-Simon et al., [62] suggested that the transient non-thermal radio emission may originate from the secondary star. Meintjes [116] later showed that this emission might originate from the secondary star's magnetospheric field, which is pumped continuously by the magnetosphere of the white dwarf or the ejected material which rams into the magnetic prominences stretching from the secondary star surface. The secondary star in cataclysmic variables can have large scale magnetospheric prominences or flux tubes that can stretch to the white dwarf in many instances [117]. On the other hand, it was shown [118] that the disturbances of the secondary star's magnetospheric tubes, even at a small scale, will result in magnetic field aligned potentials and currents, which are the zones for particle acceleration in regions of low conductivity. These potentials can reach values of [116],

$$\Phi_{\parallel} = \left[\frac{300(\triangle B_{\perp})^3}{64\pi e N_e^{3/2}\sqrt{4\pi kT}}\right] \geq 10 \text{ Mega Volts}, \tag{3.27}$$

where $\triangle B_{\perp} = B_0 \sim 1000\,\mathrm{G}$ is the average polar value of the magnetic field at the surface of the secondary star, $N_e = 10^{11}$ cm $^{-3}$ and $T = 10^5\,\mathrm{K}$. This can easily account for the relativistic electrons with $\gamma = 20$, which will result in the transient synchrotron emission to frequencies of the order of,

$$\nu \approx \frac{\gamma^2 eB}{2\pi m_e c} \sim 10^{12}\ \mathrm{Hz}\,. \tag{3.28}$$

Therefore the energetics associated with the processes discussed earlier can comfortably drive the transient non-thermal emission and explain the SED displayed in Figure 3.3.

3.3.2 Pulsar induced hard X-ray Emission

The particle acceleration in the magnetospheric field may be inhibited by other processes such as inverse Compton losses or synchrotron losses. Meintjes, Oruru, and Odendaal [18] showed that synchrotron losses inside the propeller zone limit electron energies to

$$\gamma_e = 10^5 \left(\frac{R_{prop}}{10^{10}\ \mathrm{cm}}\right)^{-1} \left(\frac{B_p}{130\ \mathrm{G}}\right)^{-2}, \tag{3.29}$$

where the propeller zone's magnetospheric field is given by B_p. The individual electrons with a Lorentz factor $\gamma \sim 10^5$ will radiate most of their energy with a frequency of,

$$\nu = 5 \times 10^{18} \left(\frac{B_p}{130\ \mathrm{G}}\right)^{-2} \left(\frac{\gamma_e}{10^5}\right)^{2}\ \mathrm{Hz}. \tag{3.30}$$

This value is compatible with the frequency of the observed hard X-ray emission discovered by the Suzaku satellite (see Figure 2.11 [10]). This hard X-ray emission has a calculated luminosity of $L_X \sim 5 \times 10^{29}$ erg s^{-1} which compares to 0.01% of the spin-down power. This conversion efficiency places AE Aqr in the same category of young rotation-powered pulsars in the energy range 2-10 keV [119].

3.3.3 Pulsar and burst-like VHE Gamma-ray Emission signatures

The pulsar-like acceleration can produce highly relativistic particles with a large Lorentz factor. These highly relativistic particles (i.e., electrons) in the presence of lower energy photons are an excellent ingredient for VHE gamma-ray production. Meintjes, Oruru, and Odendaal [18] showed that the pulsar-like activities are possible in the vicinity of the white dwarf and can result in highly relativistic electrons with a Lorentz factor of $\gamma \sim 10^5$, which provides an exciting possibility for high energy gamma-ray production by up-scattering of optical photons ($\epsilon \sim 1$ eV) produced by the K-type secondary star, or propeller expelled outflow, to high energies, i.e., the inverse Compton process. The inverse Compton process takes place in the Thompson limit for photons with frequencies [18]

$$\nu < 1.2 \times 10^{15} \left(\frac{\gamma}{10^5}\right)^{-1} \text{ Hz}, \tag{3.31}$$

which is compatible with the optical photons from the companion star (K3-5). They also calculated an upper limit for the possible gamma-ray energies generated in this limit as

$$\epsilon_\gamma = 0.2 \left(\frac{\gamma}{10^5}\right)^2 \left(\frac{\epsilon_{ph}}{5 \text{ eV}}\right) \text{ TeV}. \tag{3.32}$$

As a result of the propeller action, the region with sheared magnetic fields will generate field aligned currents (inductive currents) in the magnetosphere of the white dwarf. Double layers can result in induced circuits where there is low conductivity, i.e., where the gas density is low. The mechanism will take place near the white dwarf, and the potential generated in this region can be of the order of $\Phi \sim 300$ TV over short time scales (e.g., [35, 116]). The electron synchrotron losses in this region will be severe, limiting electron energies. Protons, which are not affected by synchrotron losses will obtain energies of the order of perhaps 1 TeV. These protons will have the luminosity estimated by equation 3.21. If the density of clumpy gas in this region is of the order of 10^{13} cm^{-3} (particle density inside the blob [112]), the collision of the clumpy gas and the protons and ion beams is possible which will result in the production of π° mesons which will decay into gamma-rays. The short burst-like gamma-ray signal may carry a periodic signature which will most probably be a beat period between the period of the accelerator white dwarf and the target matter, which can either be the surface layers of the secondary or the propeller ejected matter (see Figure 2.13, e.g., Meintjes et al., [12, 6];Bowden et al., [13])

Chapter 4

Radio emission from AE Aquarii

Introduction

AE Aqr is a unique source with multi-frequency characteristics from radio to possibly gamma-ray emission. The source exhibits pulsations in the optical waveband at or close to the white dwarf rotational period and its first harmonic (e.g., [5]). During flare episodes, quasi-periodic oscillations (QPOs) with periods slightly longer than the spin period (33.08 s) and the second pole (16.54 s) have been observed. The X-ray emission also reveals pulsed emission and quasi-periodic oscillations at the fundamental frequency (33.08 s) of the rotational period of the white dwarf (e.g., [82]). Studies of gamma-ray emission have also revealed unconfirmed pulsed emission close to the fundamental frequency and the first harmonic of the white dwarf using Cherenkov telescopes. More recently, consistent low-level pulsed emission was observed at the first harmonic using Fermi-LAT (e.g., [6]). No coherent pulsed radio emission from AE Aqr has been reported yet (e.g., [62]) at either the spin period or the period at the QPOs. Therefore, a new investigation of the nature of the radio emission will be performed using the most sensitive radio telescopes currently available, the MeerKAT telescope array. This telescope has discovered numerous radio galaxies since its commissioning. With its outstanding sensitivity, it is firmly believed that any possible low-level pulsed emission can be revealed from any weak source within its range.

This chapter presents the procedures used and results obtained during the investigation of the nature of the radio emission from AE Aqr utilising the highly sensitive MeerKAT radio telescope. The chapter is structured in the following format; A general discussion of the MeerKAT interferometer telescope will be presented together with its data products. A review of calibration processes required for radio data is given, to shed light on how the data of AE Aqr were calibrated. Imaging and deconvolution are also briefly discussed to put in context how the data were imaged. Barycentre correction and timing analysis are also reviewed since the periodic nature of the emission will be investigated. Lastly, an extended presentation of the results obtained and a discussion will be presented.

Figure 4.1: A photograph of MeerKAT receptors (courtesy SARAO)

4.1 The MeerKAT Interferometer Telescope

Karoo Array Telescope (KAT) was renamed MeerKAT (i.e., more of KAT)[1] after the South African government increased its budget to allow 64 interlinked receptors instead of 20 receptors proposed in the initial budget. The MeerKAT telescope is a radio telescope located in the Northern Cape province (Upper Karoo region) of South Africa. It is also known as the pathfinder or precursor for the Square Kilometer Array (SKA).

MeerKAT consists of 64 receptors with 48 located within a core region of 1 km in diameter centred at approximate coordinates ($30^\circ 42' 47.41''$ South and $21^\circ 26' 38.00''$ East). This configuration supports HI and pulsar science (e.g., [120, 121, 122, 123, 124]). The remaining 16 receptors are distributed in a spiral form outside the core with a maximum baseline of 8 km for any two receptors to enable higher angular resolution (e.g., [120, 125]). Figure 4.1 shows a diagram of some of the receptors of the MeerKAT telescope. Figure 4.2 (left) shows the distribution of the receptors of the entire array, and (right) shows the zoomed-in inside core receptors.

The MeerKAT receptors consist of an antenna positioner, a set of digitizers, and radio receivers, where the antenna positioner is a steerable dish resting on a pedestal. It consists of a 13.5 m effective diameter primary reflector with a 3.8 m diameter secondary reflector, cryogenically cooled receivers, feed horns, digitizers mounted on the feed indexer, support structures, and drive systems are all installed on the pedestal. The receptor is designed such that its components will not obstruct or interrupt incident electromagnetic signals (i.e., the design is known as the Offset Gregorian optical layout). This design ensures the rejection of the undesirable radio frequency interference from terrestrial radio transmitters and satellites. In addition, the thermal ground spillover noise is avoided in this set-up by the extra extension at the bottom of the secondary reflector. Figure 4.3 is a schematic diagram of the

---

[1] `http://www.ska.ac.za/wpcontent/uploads/2016/07/meerkat-fact-sheet-2016.pdf`

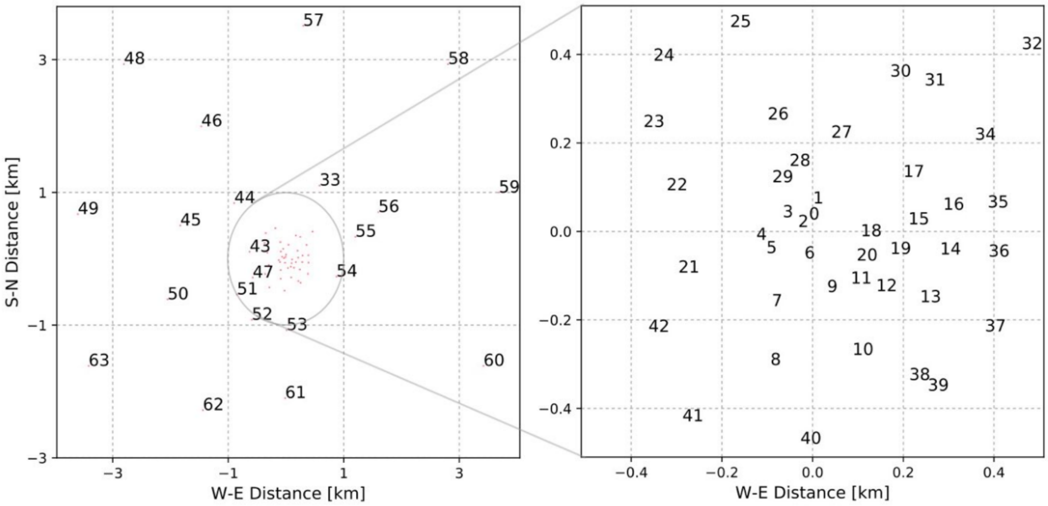

Figure 4.2: The (left) panel show the entire distribution of all antenna from M00 to M063, and (right) panel is a zoom-in of the core receptors [20]

MeerKAT receptor, which shows the components and their position on each receptor.

The majority of the MeerKAT antennas is installed with the Max-Plank S-Band (MP-SbS) receiving system, and each antenna consists of digitizers and other receivers on the receiver indexer. These recievers includes the UHF-band (580–1015 MHz) receiver, and L-band (900–1670 MHz) receiver (e.g., [120]). The indexer on each antenna allows automatic selection and positioning of the receiver based on the chosen frequency band. Each antenna on the MeerKAT array has a receiver front-end and the back-end system. The front-end system receives captured radio radiation, and transforms it to a measurable voltage signal. The cryogenic receivers, which form part of the receiver front-end, amplify the voltage to a measurable signal. In essence, the receiver front-end captures the electromagnetic signal, converts it to the equivalent radio frequency (RF) voltage, and amplifies and digitizes this voltage using the four digitizers, consisting of an electronic component, i.e, the analog to digital converter (ADC).

The digitized RF signal is transmitted from the front-end receiver to the back-end receiver system (correlator) using the standard Ethernet (1 m underground for thermal stability) network. The ethernet cables are also used to distribute time and frequencies signal reference to synchronize each digitizer's time and frequency on every receptor. The correlator integrates all the MeerKAT receptor coherent signals (voltage streams), aligning them to compensate for instrumental and geometric delays. The voltage signal is first divided into frequency channels, and phase-aligned per frequency channel before cross-correlation (X), and/or beamforming (B). A polyphase filterbank handles channelization in the "F-engine" processing nodes. The correlator "B-engine" performs beamforming of previously delayed, channelized, and reordered voltage signals from all receptors. It coherently integrates this voltage signal to create multiple narrow high sensitivity beams (tied-array beam) for fast transient and pulsar applications. Both F and B engines also handle both polarizations. The MeerTRAP (TRAnsients and Pulsars, [126, 127, 128]) back-end also has an essential feature, which makes it possible to observe simultaneously in two modes coherent and incoherent. The incoherent mode provides a larger field of view and lower sensitivity than the coherent observation, which has higher sensitivity and a lower field

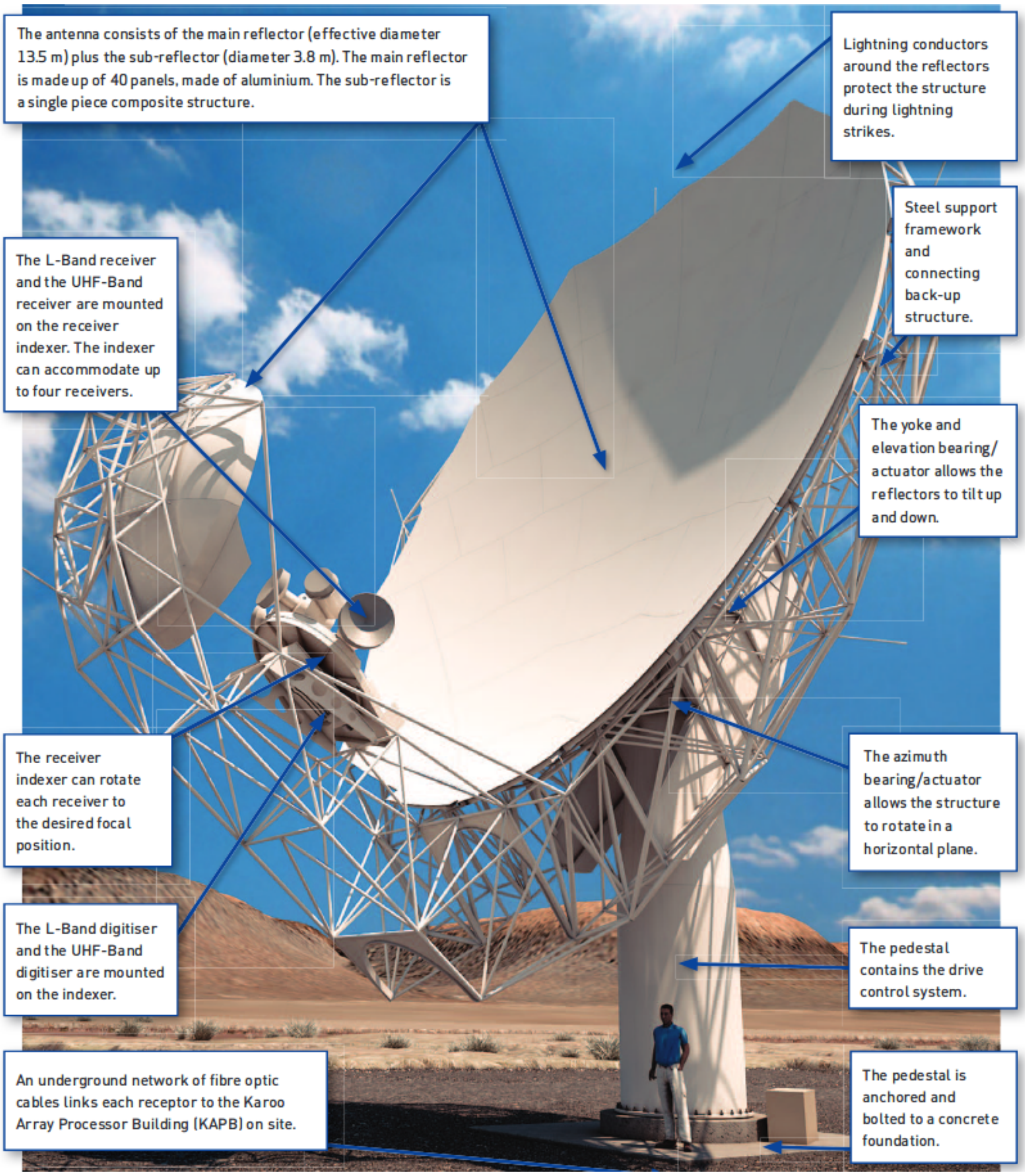

The antenna consists of the main reflector (effective diameter 13.5 m) plus the sub-reflector (diameter 3.8 m). The main reflector is made up of 40 panels, made of aluminium. The sub-reflector is a single piece composite structure.

Lightning conductors around the reflectors protect the structure during lightning strikes.

Steel support framework and connecting back-up structure.

The L-Band receiver and the UHF-Band receiver are mounted on the receiver indexer. The indexer can accommodate up to four receivers.

The yoke and elevation bearing/actuator allows the reflectors to tilt up and down.

The receiver indexer can rotate each receiver to the desired focal position.

The azimuth bearing/actuator allows the structure to rotate in a horizontal plane.

The L-Band digitiser and the UHF-Band digitiser are mounted on the indexer.

The pedestal contains the drive control system.

An underground network of fibre optic cables links each receptor to the Karoo Array Processor Building (KAPB) on site.

The pedestal is anchored and bolted to a concrete foundation.

Figure 4.3: The MeerKAT receptor schematic diagram

of view.

4.1.1 Data Products of the MeerKAT

The MeerKAT data products are stored in Hierarchical Data Format v5 (HDF5). The HDF5 system consists of a software library that accesses the HDF5 file format and manipulates them with programming languages. This software performs some initial flaggings on the raw data, i.e., edge truncation caused by bandpass and satellites. The resulting HDF5 raw data file will be transformed into a file called Measurement Set (MS), containing all essential information about the observed sources, used antennas, polarisation, frequency or spectral information, and the observation interval sets. This MS file stores information in tables and can be manipulated with most software to reduce the data and process the sky brightness with its parameters (i.e., data reduction). The data reduction and analysis processes in this study were performed using the CASA package. The reduction of radio data with CASA software will be discussed briefly in subsection 4.2.2. In the following section a general approach for radio data reduction and analysis is discussed.

4.2 Data Reduction and Analysis

Instrumental and atmospheric effects can corrupt and induce variations in the measured phase and amplitude of the visibility measured by an interferometer, which can obscure the natural variations of the target source. Therefore, it is imperative to reduce the magnitude of these errors through calibration processes before imaging and deconvolution [129]. In this section, data reduction, i.e., calibration processes, e.g., data editing (flagging), bandpass correction, and complex gain correction using Common Astronomy Software Application (CASA) are highlighted. For a formal discussion of these calibrations processes refer to calibration and editing by Fomalont and Perley [130, 129]. The initial procedure, before the application of the calibration process, is to first inspect the data for any bad sections as a result of radio frequency interference (RFI) or even system failure (e.g., telescope off-source data).

4.2.1 Data editing and flagging

Despite numerous techniques developed to avoid or mitigate bad data, e.g., removing of the RFI using reference antennas [131], mitigation of RFI using the spatial information and null directions, provided in the multi-feed systems (e.g., [132, 133, 134, 135]), and blanking out unlikely high values at high time resolutions (e.g., [133, 136, 137]), the observed data from the correlator always exhibit bad data, which require some further editing [136]. Therefore, it is imperative to investigate, edit and flag bad data from all observed data. Flagging involves removing parts of the spectrum with bad data, i.e., bad data is identified in frequency, time, and antenna space and eliminated in the final processing of the observed data. It is crucial to make sure that the astronomical data is not accidentally flagged as bad data [138].

Historically, the detection of RFI was through human visual inspection of the observed data. This process becomes increasingly impossible due to the massive volume of data available, and a large volume of observed data means many person-hours [139]. Consequently, algorithms that enable automatic RFI flagging were developed (e.g., Effelsberg Bonn HI Survey [140]). In this approach, the algorithms look for the characteristics of RFI in observed data and flag the identified parts. The recommended algorithm for MeerKAT data is the AOflagger developed by Offringa which implements multiple methods directed towards different characteristics of RFI [138]. This algorithm can detect different types of RFI with multiple characteristics.

4.2.2 Data reduction with CASA

CASA is a package developed by the National Radio Astronomy Observatory (NRAO) team to reduce the radio data. The CASA calibration package follows many philosophical approaches that involve mathematical models. It involves a complex set of

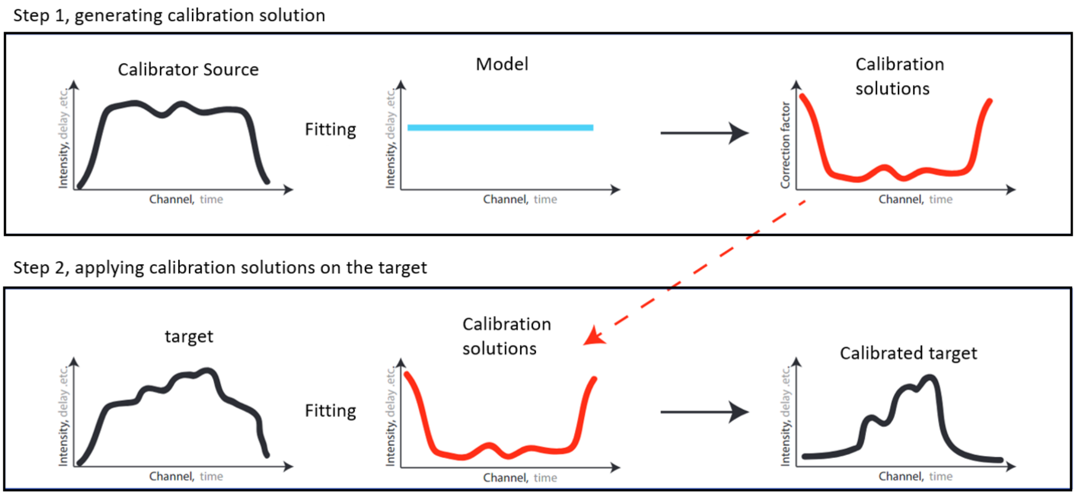

Figure 4.4: This is a general illustration of the process of calibration. The model and the obtained data of the calibration source are used to create calibration solutions.

steps that can follow one another in sequence or randomly, depending on the type of data. These steps include calibration of the model visibility, bandpass, gain, and polarization. For a detailed discussion of the reduction and calibration processes using CASA refer to CASA documentation[2].

In principle, calibration makes use of model visibilities for known sources that satisfies the properties of calibrator sources and compares them to the observed visibilities. The intrinsic properties of a known calibration source are used by the CASA packages to generate the model visibility. The CASA packages combine the model visibility and the observed visibility to generate the calibration solutions. These solutions are constructed by fitting the observed visibility data to the model visibility, and the resulting solutions are stored in a calibration table. The calibration process is performed on the target field by fitting the calibration solutions with the observed visibility of the target field (see illustration in Figure 4.4).

The CASA calibration tasks such as *gaincal* (complex gain), *blcal* (bandpass), and *polcal* (polarization) make use of the generated model of the calibrator source to generate a set of calibration solutions and store them in a caltable (calibration table). For example, the task *gaincal* is used to perform the antenna based delays by producing delay calibration tables, where the subsequent calibration such as complex gain, bandpass, and flux calibration will be applied. This task uses the reference antenna and the baselines to perform the delay calibration. Accordingly, a careful examination is needed when choosing a reference antenna. The reference antenna should not be involved in massively flagged baselines, as this could result in the loss of a vital section of the array.

4.2.3 Imaging and Deconvolution

There are several algorithms for non-linear techniques to perform deconvolution on radio data, e.g., Maximum Entropy Method (MEM, [141]) and CLEAN [142]. The non-linear deconvolution process aims to find a sensible model compatible with the

---

[2] https://casa.nrao.edu/casadocs

data. It requires a priori assumption of the model to pick probable (invisible) distributions to fill unmeasured sections of the Fourier space [3].

MEM finds the smoothest possible positive image within the noise level of the experiment. It fits the data by maximizing the entropy on the map. This algorithm is most suited for extended sources with extended smooth structures. The CLEAN deconvolution algorithm assumes that numerous points can represent the source in an otherwise empty field. The algorithm searches for these points, and subtracts a synthesized dirty beam from each of the identified corresponding points iteratively, starting with the brightest. The final clean image is then obtained by the sum of these point sources convolved with a theoretical Gaussian beam. André Offringa [143] developed the CLEAN algorithm WSClean version 2.6 (2017-01-20) released under the GPL version 3 used in this study.

This CLEAN algorithm splits the bandwidth into evenly spaced channels or subbands. Next, it creates a dirty and a point spread function (PSF) image for each subband through imaging of input channels with frequencies that fall within the subband frequency range. Then the image-based clean loop is initiated with a few modifications. First, the component awaiting cleaning is determined by searching for the highest peak in the image. Second, the component's spectral variation is obtained by measuring each sub-band flux at the highest peak position. Lastly, a polynomial or sinusoidal function can be fitted to the spectral measurements before subtracting the PSFs from the dirty images. The flux given by the fitted value obtained at every iteration is subtracted from each sub-band image. This method is called multi-frequency deconvolution or joined-channel deconvolution. This method's significance is seen in a decreased chance of selecting side lobes or noise peaks since the method uses the entire bandwidth to determine the position of clean components.

4.2.4 Barycentric correction and Timing analysis

Recent studies in X-ray and gamma-ray (e.g., [21, 15]) support the presence of a particle accelerator in AE Aqr. Studies have exhibited multiwavelength emission from AE Aqr, and periodic signals were confirmed at or near the rotational period of the white dwarf in some of the wavelength regimes. In this section, a general discussion is given on how the binary rotation, Earth's rotation and orbit, and a selection of other factors can affect a signal emitted from a pulsating system like AE Aqr. The short discussion is based on Ambrosino and Meddi's [144] paper and the studies conducted by Becker, Kramer, and Sesana [145]; refer to these authors for an in depth understanding.

In principle, the Earth-bound clock does not tick at a constant rate since the Earth does not satisfy the requirements for an ideal inertial reference frame. The clock ticking is affected by the Earth's spinning and its orbit about the Sun, with this phenomenon having a notable effect on timing analysis. Therefore following this line of thought, one encounters an inherent problem when searching for periodicity in a signal received from celestial objects. Accordingly, it is imperative to account for this problem when conducting timing data analysis to correct the periodic measurements, such as rotation periods of a compact object and orbital parameters. Since

---

[3] `https://web.njit.edu/~gary/728/Lecture6.html`, `https://science.nrao.edu/science/meetings/2014/14th-synthesis-imaging-workshop/lectures-files/wilner_siw2014.pdf`

the Earth is neither stationary nor moving in a straight path, a new reference frame must be chosen which satisfies these demands. The Solar System Barycentre (SSB), in comparison with the Earth, satisfies the requirements for inertial of the reference frame. Thus one can write the photon arrival time (TOAs) on the SSB from celestial objects as follows,

$$t_{SSB} = t_{obs} + t_{clk} + \Delta R_{\odot} + \Delta E_{\odot} + \Delta S_{\odot} + \Delta DM \tag{4.1}$$

where t_{SSB} is barycentre corrected photon arrival times, t_{obs} is the photon observed TOAs, t_{clk} constitute clock corrections, which convert universal time coordinated (UTC) to barycentric dynamical time (BDT). Apart from the factors mentioned above, many factors should be considered when conducting time analysis as indicated in equation 4.1, which includes the Roemer delay ($\Delta R_{\odot}$), Einstein delay ($\Delta E_{\odot}$), Shapiro delay ($\Delta S_{\odot}$), and the dispersion measure (ΔDM), which describes the integrated path length of the free electron along the line of sight.

BMJD (AstroPy)	BMJD (Time Utilities)	Difference
58539.206628872635	58539.206628868820	3.812×10^{-09}
58539.206652021676	58539.206652016845	4.831×10^{-09}
58539.206767766900	58539.206767763010	3.885×10^{-09}

Table 4.1: The barycentric corrected time calculated by Astropy and online Time utilities. AstroPy overestimate the barycentric correction by the values shown in column three.

Timing analysis requires that the corrections mentioned above should be done beforehand to quantify the periodic signal correctly. Therefore numerous software packages are developed to correct the arrival time to the barrycentre. Most of these software packages consider all the delays, clock corrections and the dispersion measure. In this study, the coordinates AstroPy package was used to correct the barycentre correction (converting UTC to BJD) before conducting time series analysis. The accuracy of this package was tested using the online Time Utilities [4]. Refer to Table 4.1 for a qualitative comparison of the accuracy of AstroPy versus online Time utilities.

4.2.5 Lomb-Scargle method (Time series analysis)

Time series analysis reveals hidden physical phenomenon in given astronomical data, i.e., the periodicity of the emission and an understanding of the physical processes behind the observed periodicity. In most cases, it will be apparent that the object's brightness varies with time but requires a unique technique to diagnose the presence of periodicity in the emission. The Lomb-Scargle periodogram is a good relevant technique used to detect the periodic component in irregularly sampled data. It integrates a number of techniques, such as: Fourier analysis, least squares, Bayesian probability theory, and bin based phase-folding. For a comprehensive discussion of Lomb-Scargle refer to these references ([146, 147, 148, 149, 150, 151, 152, 153]). The Lomb-Scargle method was implemented using the AstroPy package (astropy.time.series) in this study to analyze the radio data, where we seek to constrain and identify possible pulsed emission from AE Aqr.

---

[4] http://astroutils.astronomy.ohio-state.edu/time/

The Lomb-Scargle periodogram technique is a conventional algorithm for detecting and characterizing periodic unevenly sampled data. The technique is named after the developers Lomb [146] and Scargle [147]. The technique uses the least squares approach to calculate, test, and assign frequencies on given data to produce a power spectrum. A model is fitted to the data to each candidate frequency in the least square method, and the frequency that maximizes the likelihood will be assigned to that particular data. As a result, the periodogram will be generated from this process. The normalized periodogram for the Lomb-Scargle technique is,

$$P_x(\omega) = \frac{1}{2\sigma^2}\left[\frac{(\sum_i (x_i - \bar{x}) cos\omega(t_i - \tau))^2}{\sum_i cos^2\omega(t_i - \tau)} + \frac{(\sum_i (x_i - \bar{x}) sin\omega(t_i - \tau))^2}{\sum_i sin^2\omega(t_i - \tau)}\right] \tag{4.2}$$

where σ^2 is the variance, the average of the data is given by $\bar{x}$, and the lag τ time between measurements is also defined as,

$$\tau = \frac{1}{2\omega} tan^{-1}\left[\frac{\sum_i sin(2\omega t_i)}{\sum_i cos(2\omega t_i)}\right] \tag{4.3}$$

The AstroPy Lomb-Scargle periodogram uses four normalization algorithms, namely the standard, model, logarithmic, and power spectral density (PSD) normalization. From the Lomb-Scargle periodogram, pulse signals are indicated by peaks, which can result in interpreting peaks that arise from noise as a signal. Therefore, the noise level must be estimated to separate signal from noise, where the expression $P(\omega)$ becomes useful to separate signals from the spurious spectral peak due to noise. One can determine the maximum power $\langle Z(max) \rangle = \sum_{k=1}^{N} \frac{1}{k}$ [147] for a pure noise spectrum of N frequencies with discrete power. From this equation, a noise peak can be perceived as a signal if the false alarm probability is not computed in the absence of the actual signal. Thus for a power level $z_0 = -ln\left(1 - [1 - p_0]^{1/N}\right)$ considered as a signal, one can compute the probability p_0, which helps distinguish between false claim and positive detection. However, some spurious peaks can still pass the probability test since observation errors may also lead to power leakage from the true peaks, and aliases may also arise due to the presence of higher-frequency components. Accordingly, the best frequency does not always correspond to the highest peak.[5]

4.3 Observation, Reduction and Analysis of AE Aqr MeerKAT data

The MeerKAT telescope carried out an imaging observation of AE Aqr on 25 Feb 2019 at 04:57:48.5 UTC, and the observation lasted until 05:55:41.1 UTC. This observation was part of the CV component of ThunderKAT [154]. The observation was conducted with 61 antennas, which correspond to approximately 2016 baselines with the most extended baseline 8 km long. The observation frequency was centred at 1284 MHz with the correlator configured at 2 s integration time per each visibility sample with 4096 frequency channels sampling the entire L-Band of MeerKAT, which is 856 MHz wide, ranging from 900-1670 MHz. Each channel is 209 kHz wide.

---

[5] `https://docs.astropy.org/en/stable/timeseries/lombscargle.html`

The nova-like system AE Aqr was observed for a total of 45 minutes in three identical scans alongside the bandpass and flux calibrator source PKS B1934-638 (J1939-6342), which was observed for 5 mins at the onset of the observation, and the amplitude and phase calibrator PKS 2008-068 (J2011-0644) was observed for 2 mins continually three times throughout the entire observation (refer to Table 4.2).

Time (UTC)	Source Name	Property
04:57:48.5 - 05:02:48.4	J1939-6342	Bandpass and Flux Calibrator
05:03:38.4 - 05:18:38.0	AE Aqr	Target [Scan 1]
05:18:56.0 - 05:20:56.0	J2011-0644	Amplitude and Phase Calibrator
05:21:00.0 - 05:36:01.6	AE Aqr	Target [Scan 2]
05:36:19.6 - 05:38:19.5	J2011-0644	Amplitude and Phase Calibrator
05:38:23.5 - 05:53:25.1	AE Aqr	Target [Scan 3]
05:53:43.1 - 05:55:41.1	J2011-0644	Amplitude and Phase Calibrator

Table 4.2: The observation time range for calibration sources and the target source, AE Aqr.

The reduction of MeeKAT data of AE Aqr was conducted using the CASA package, as briefly discussed below, but following the general routine discussed earlier in section 4.2. Bandpass, flux density, and delay corrections were determined using the flux and bandpass calibrator source, while the time-dependent complex gains corrections were determined using the phase calibrator source.

The amplitude and phase of the data were first edited, e.g., flagging before calibration. The latest AOFlagger algorithm was used, which implements multiple methods directed towards different characteristics of RFI [138]. This algorithm detects different types of RFI with multiple characteristics. Following editing and flagging, 8:1 frequency averaging was applied to the data with time averaging using the integration time (2 s). Further data reduction was performed using the Inter-University Institute for Data Intensive Astronomy (IDIA) data reduction pipeline, which implements the reduction in the following steps.

The flux density calibrator source J1939-6342, which has a high signal-to-noise ratio, was used to calibrate antenna-based gain and bandpass. The task *setjy* sets the flux density, the spectral index, and the reference frequency of the calibrator source. Note that these parameters are obtained from the catalog, and the task *setjy* makes use of these parameters to create the calibration model. The bandpass instrumental response is determined using the task *gaincal*, which performs the initial set of phase-only corrections and antenna-based delay corrections. These initial phase and delay corrections are performed on the flux density calibrator source J1939-6342, using channel 265 and 390 since they were least affected by RFI, and the signal to noise ratio was set at minimum 5 σ. Following the bandpass instrumental responses calculation for these two channels, the solutions were applied to all channels. Finally, the bandpass corrections were determined using the task *bandpass*, applying the phase, and delay corrections.

The complex gain calibration solutions were determined using both the phase calibrator source J2011-0644 and the flux density calibrator source J1939-6342. The phase calibrator source model was generated using the parameters flux density spectral index and reference frequency, making use of the task *setjy*. The complex gain corrections were solved on the phase calibrator source using the task *gaincal*, applying the bandpass corrections. In the same approach taken on the phase calibrator, the complex gain corrections were solved on the flux density calibrator source. Lastly, before applying the corrections, the phase calibrator's complex gain solutions are scaled with the known flux of the flux density calibrator using the task *fluxscale*.

Finally, the correction solutions, i.e., antenna-based gain, bandpass, and the complex gain, were applied to the calibrator sources and, most importantly, on target source (AE Aqr). The $flagdata$ task was used to flag the data of the target source since the flagging performed early was directed at the calibration sources. Further averaging of the target source after applying all the calibration was performed using the *split* task.

4.3.1 Imaging and flux measurements

The imaging process was performed using *wsclean version* 2.6 [143], an algorithm compatible with CASA. This clean algorithm follows the processes highlighted earlier in section 4.2.3 of this chapter. Deconvolution was conducted using the clean multi-frequency algorithm, and eight channels (sub-bands) were used to produce the entire epoch's image (of size 8192×8192), where these eight bands were further used to investigate the sky's apparent spectral variations across the band. The clean multi-frequency algorithm uses *-joinchannels* flag to join the sub-bands results to produce an average image, where the average flux will be extracted. Deconvolution process termination was handled using *-auto-threshold* = 0.3, *auto-masking* = 0.5, and terminated after 30 000 clean iterations, where the end of each iteration is governed by *-mgain* = 0.80. The visibility data were gridded and weighted using the Briggs method with a robust parameter of -0.3 to reduce the point spread function's sidelobes. The weighting function brings out features on various angular scales from the same visibility sample. The resulting synthesized beam had a 7.92 arc seconds major axis and a 5.47 arc seconds minor axis, with a position angle of 58.61°. The CASA *split* task was used to split the measurement set file using the time domain into multiple measurement set files of short intervals, 2 seconds, 4 seconds, 6 seconds, 8 seconds and 10 seconds to search for potential short time scale variability. These short interval measurement set files were imaged using the same processes with three channels, and a smaller image size was produced for each measurement set file.

The flux measurements of AE Aqr from the whole observation image was conducted using the python source finder software PyBDSF[6], and the measurements were confirmed using CASA task $imfit$[7]. Flux measurements from multiple images was conducted using the $imfit$ tasks. Both PyBDSF and $imfit$ make use of a square aperture centred on the target source. The root-mean-square (rms) flux density was also determined on the target region but not including it. In cases where the rms was less than the noise around the target, the flux density was re-measured using a bigger aperture. This scenario is usually brought up by calibration errors and unsuccessful sampling of *uv*-plane coverage. The light curves were finally produced from flux points measured from multiple images.

---

[6] `https://www.astron.nl/citt/pybdsf/.`

[7] `https://casa.nrao.edu/docs/taskref/imfit-task.html.`

4.3.2 Search for periodic emission

Timing analysis was performed on each barycentre corrected radio light curves produced using the imaging techniques. The barycentric time corrections were performed using a package in AstroPy as highlighted earlier in section 4.2.4. The timing analysis procedures utilized the Lomb-Scargle method available in AstroPy version 3.6.0. The Nyquist frequency for each light curve was avoided by performing the Lomb-Scargle analysis on frequencies with a minimum frequency above the Nyquist frequency, i.e., setting a frequency range of $0.02 < f < 0.1$ Hz. This frequency range encompasses the expected fundamental F_0 and the first harmonic $2F_0$ frequencies.

4.4 Results

The L-band short observation of AE Aqr with the MeerKAT telescope resulted in the first detection of this source by this telescope (see Figure 4.5). The nova-like system was detected at 1.284 GHz with a peak flux density of 2.64 ± 0.07 mJy and rms noise level of 0.04 mJy. The spectral variation and the periodic nature of radio emission from AE Aqr was studied using the L-band data from the MeerKAT telescope. The nature of the spectral variation, together with the evidence of possible pulsed radio emission from AE Aqr is presented in the following sections.

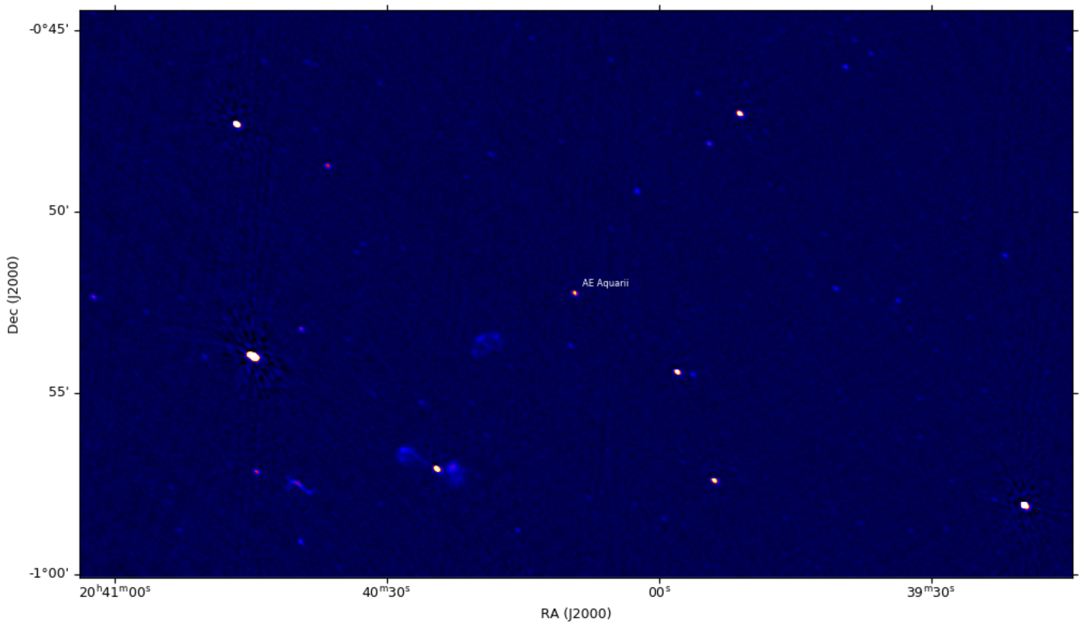

Figure 4.5: The radio sky map of AE Aqr produced from the L-band of MeerKAT data.

4.4.1 Radio spectrum

To produce the spectrum of AE Aqr the data was divided into five channels, and the entire observation was also divided into 30 seconds sections where flux was extracted. Extracted flux was plotted as a function of frequency see the left panel of Figure 4.6. In each channel, the measured flux is averaged to produce a single flux point for each channel, where the error for each data point is the standard deviation of the mean (see right panel of Figure 4.6). The average flux measurements for each of the five channels are listed in Table 4.3. The time averaged spectrum obtained in this study characterize the emission as non-thermal synchrotron emission, which reveal a power law spectrum with spectral index $\alpha = -0.87 \pm 0.10$ and $p = 2.74 \pm 0.79$, and p is the energy spectral index of the electron spectrum.

Frequency (GHz)	Average Flux Density (mJy)
0.941	4.82 ± 0.08
1.112	4.48 ± 0.08
1.284	3.95 ± 0.13
1.454	3.52 ± 0.08
1.626	2.98 ± 0.06

Table 4.3: Summary of the MeerKAT flux measurements of AE Aqr conducted in this study.

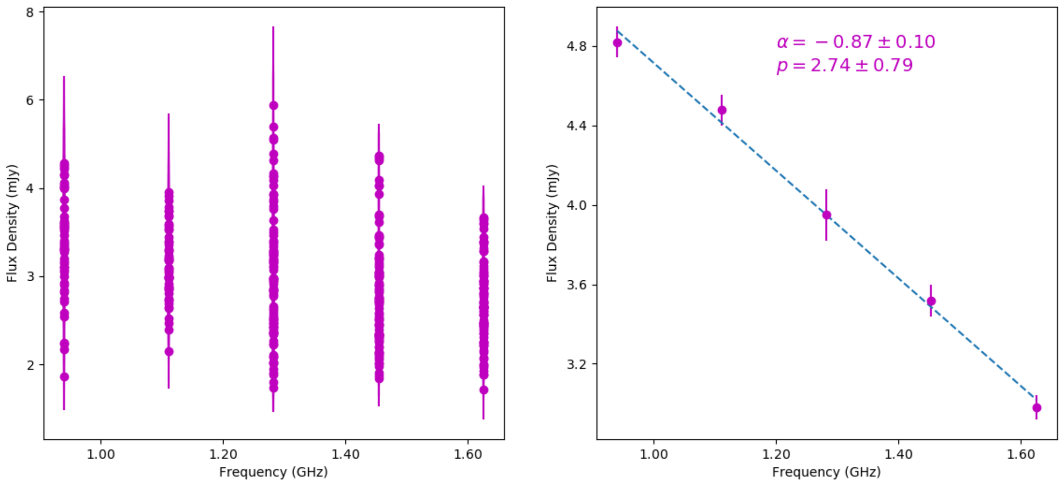

Figure 4.6: The left panel show data points extracted for each time bin in each channel. The right panel show the average of flux measured in each channel.

The average flux density measured from this study was plotted together with flux density obtained in the literature to quantify the flux levels measured by the MeerKAT in relation to flux points measured by a other telescopes (see Figure 4.7). The green solid circles in the insert are average radio and mm fluxes observed using VLA, the James Clark Maxwell Telescope (JCMT), Infrared Astronomical Satellite (IRAS), ISOPHOT, AND Institut de Radioastronomie Millimétrique (IRAM, e.g., [9, 78]). Some of these fluxes are plotted as green solid circles in the main figure.

4.4.2 Pulsed radio emission

The light curves generated in this study fall within 0.363-0.382 orbital phases calculated using the ephemeris (MJD 49280.92222) with an orbital period ($P_{orb} = 9.8797327$ hr) [155], where the superior conjunction of the white dwarf is at phase zero (0.0). The light curves produced for each lower channel (lc_0000, 856-1140 MHz), middle channel (lc_0001, 1140-1426 MHz), upper channel (lc_0002, 1426-1712 MHz), and the entire L-band for each binning are presented with the Lomb-Scargle pulse profiles. The light curves are presented first before their corresponding pulse profiles. The light curves are presented in ascending order of the bin size used, i.e., 2, 4, 6,

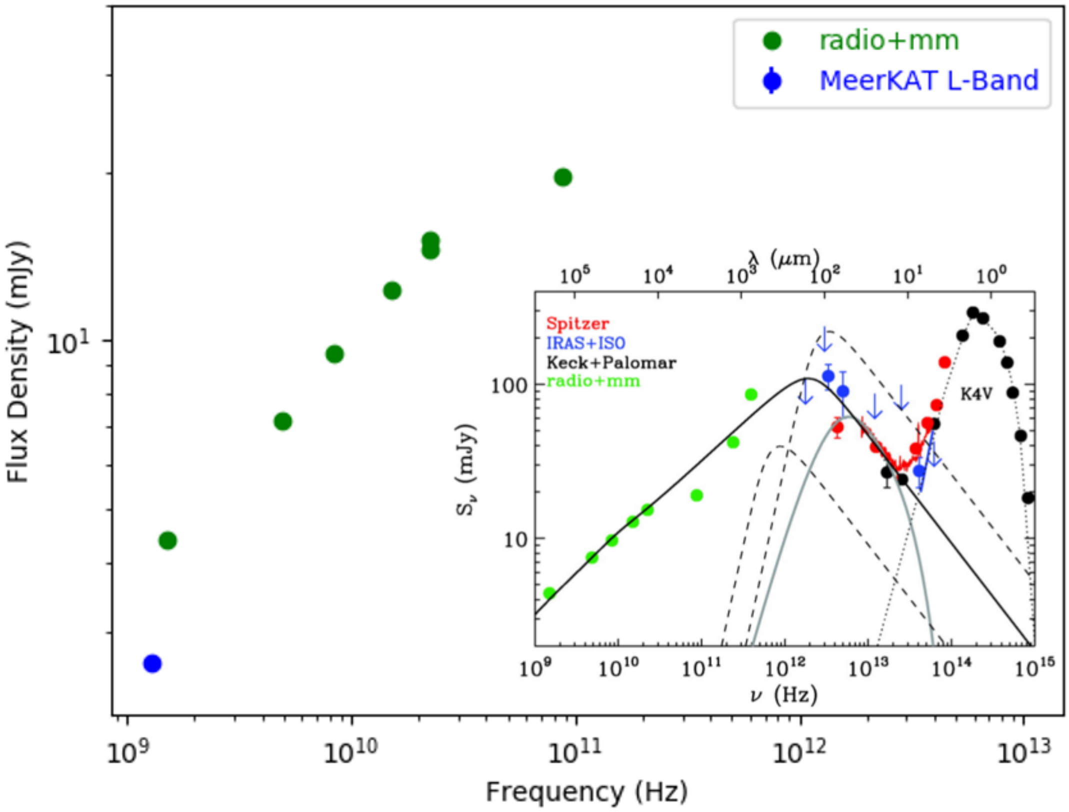

Figure 4.7: The flux density measured from the MeerKAT data is indicated by blue diamonds and the rest was obtained from the literature, insert figure refer to Dubas et al.,[9].

8, and 10 seconds correspond to Figures 4.8, 4.10, 4.12, 4.15, and 4.18 in that order. The periodograms Figure 4.9, 4.11, 4.13, 4.16, and 4.19 for each light curve are presented after each corresponding light curve. Next the stacked periodograms for the three channels as well as the three scans, together with the periodogram for the first scan of lower channel are shown with lower channel noise distribution in Figure 4.14, 4.17, and 4.20. The noise distribution is indicated by a blue line, and any point above this line implies the presence of pulsed signal in the data. Some periodograms revealed weak pulses at or near the rotational period (33 s) of the white dwarf in AE Aqr. The lower channels shows the most significant peaks at or near the frequency (F_0 = 0.030229 Hz) of the white dwarf's rotational period. These periodograms with substantial significant pulses, which are produced from the same binning but different channels are stacked together to improve signal to noise of the pulsations. A stacked Lomb-Scargle power is produced by incoherently adding the Lomb-Scargle power of periodograms of choice [156].

The Lomb-Scargle periodograms of AE Aqr MeerKAT L-band data revealed indications of pulsed emission. Amongst all the bin size used, the Lomb-Scargle periodic search of the 8 seconds binning revealed more compelling results as presented in Figure 4.16 and Figure 4.17. The entire L-band (see Figure4.16 (a)) manifested the strongest signal pulsed at (P $\sim$ 33.08 s). It is also significant that the lower channel contribute a greater fraction of the detected pulsed signal Figure 4.16 (b), while (c) the middle and the (d) upper channel display random, pulsation signatures. The 8 seconds binned data also revealed the most significant stacked pulse profile for the various (a) channels and (b) scan, performed to improve signal to noise of the pulsations (Figure 4.17). It has been observed that the power of the 33.08 s pulse fades

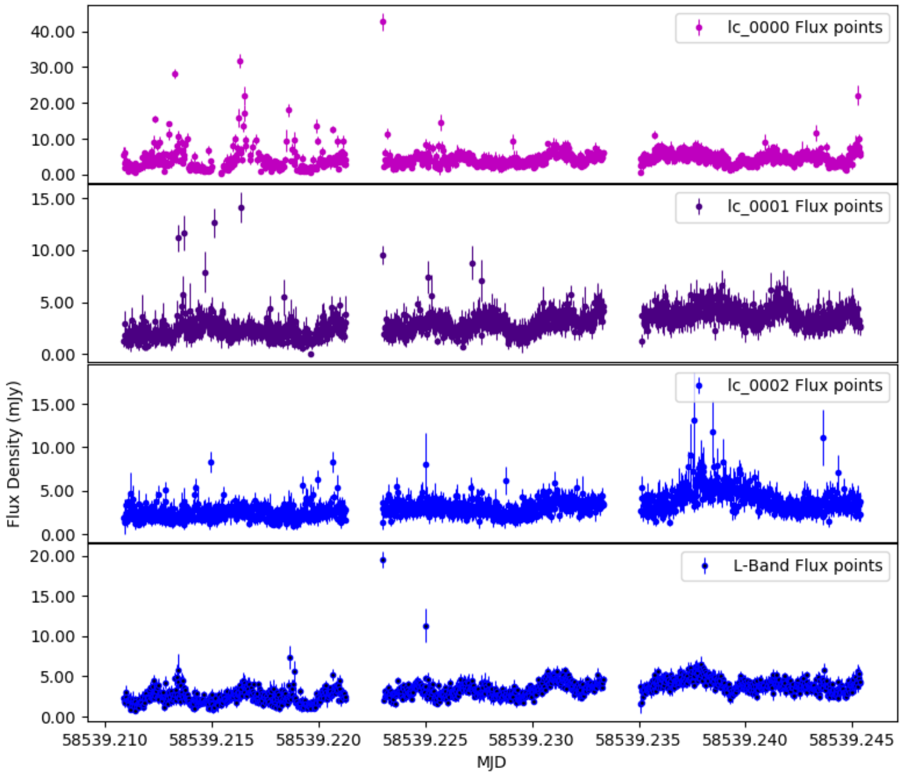

Figure 4.8: Two seconds binning lightcurves from top to bottom: lower channel 856-1140 MHz (lc_0000), middle 1140-1426 MHz (lc_0001), upper 1426-1712 MHz(lc_0002) and the entire L-band plotted at the bottom.

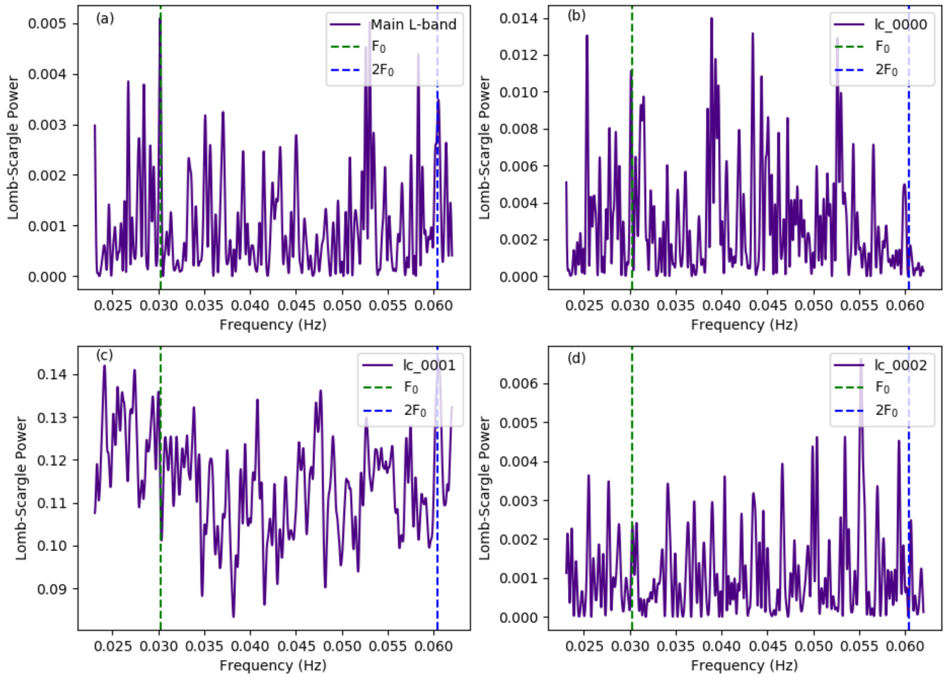

Figure 4.9: Periodograms produced from two seconds binned data, (a) L-band, (b) lower, (c) middle, and (d) upper channels, plotted over a wide frequency range that includes the fundamental frequency and first harmonic indicated by vertical lines.

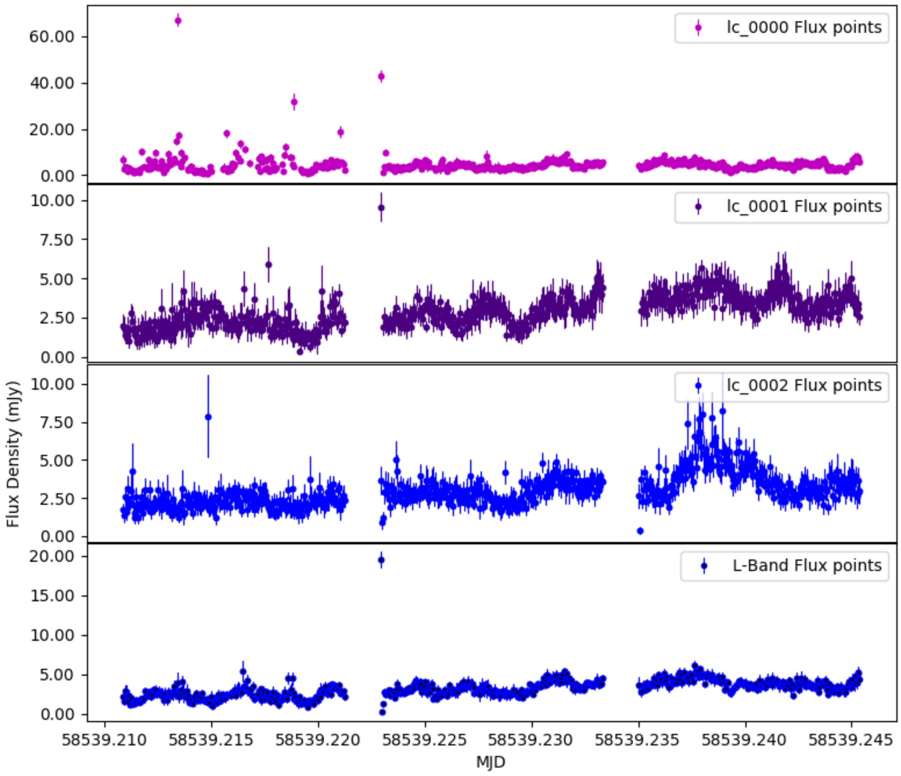

Figure 4.10: Four seconds binning lightcurves from top to bottom: lower channel 856-1140 MHz (lc_0000), middle 1140-1426 MHz (lc_0001), upper 1426-1712 MHz(lc_0002) and the entire L-band plotted at the bottom.

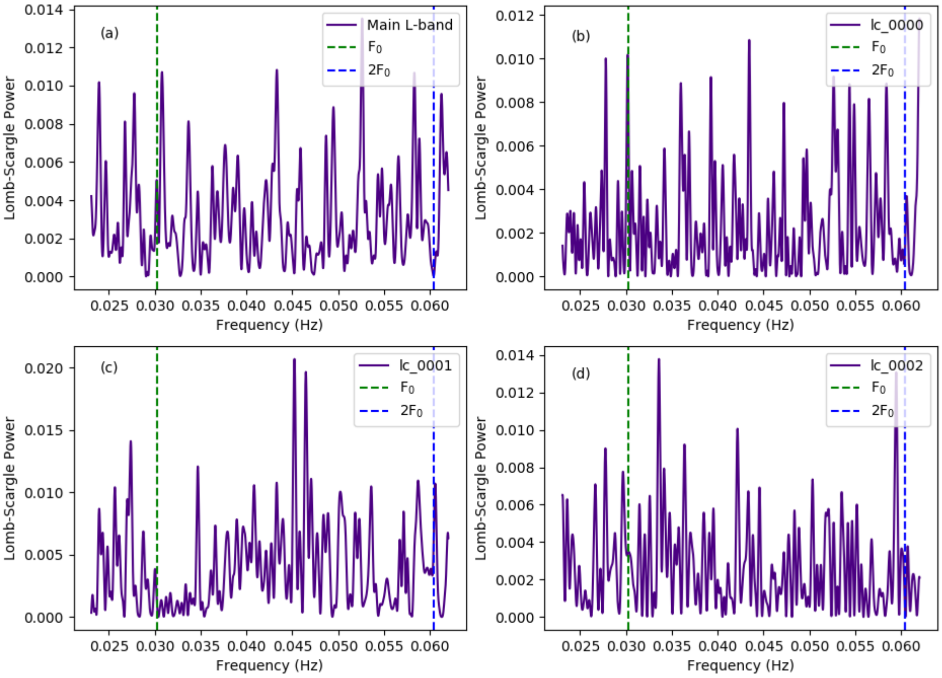

Figure 4.11: Periodograms produced from four seconds binned data, (a) L-band, (b) lower, (c) middle, and (d) upper channels, plotted over a wide frequency range that includes the fundamental frequency and first harmonic indicated by vertical lines.

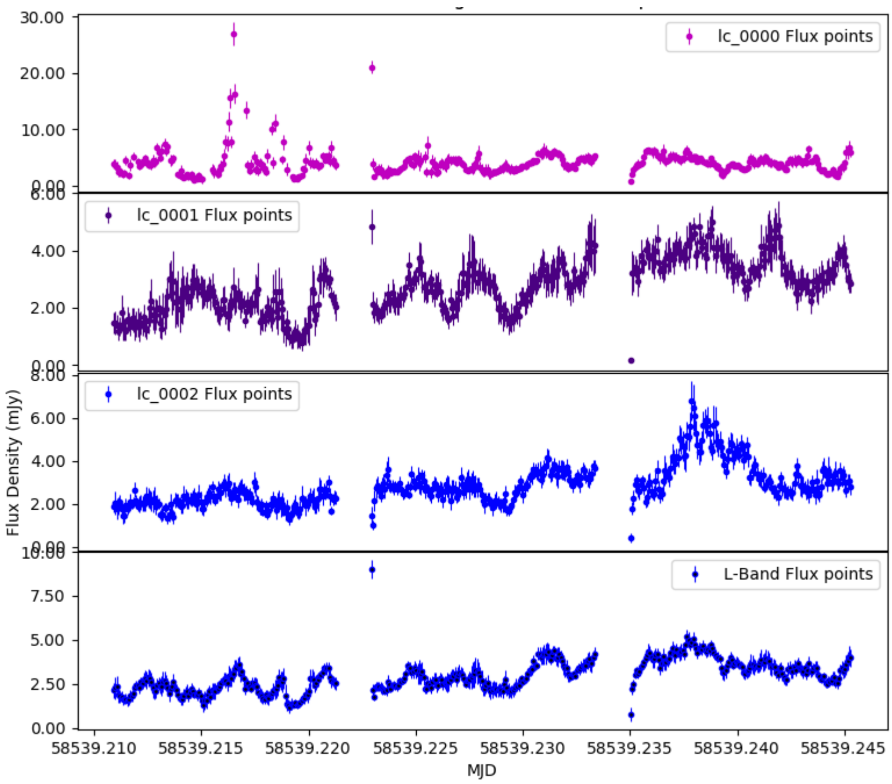

Figure 4.12: Six seconds binning lightcurves from top to bottom: lower channel 856-1140 MHz (lc_0000), middle 1140-1426 MHz (lc_0001), upper 1426-1712 MHz(lc_0002) and the entire L-band plotted at the bottom.

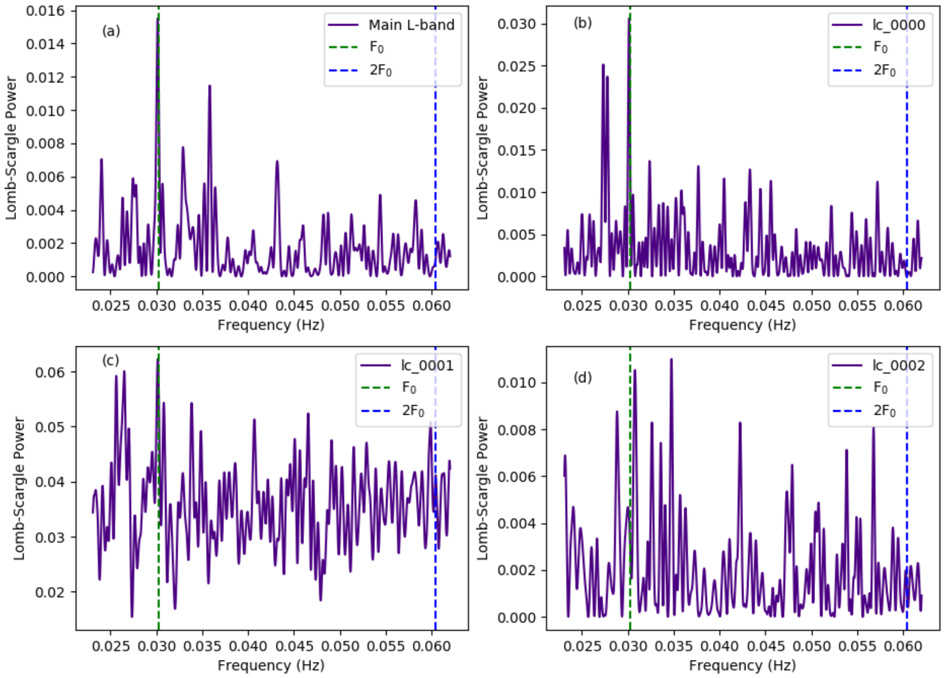

Figure 4.13: Periodograms produced from six seconds binned data, (a) L-band, (b) lower, (c) middle, and (d) upper channels, plotted over a wide frequency range that includes the fundamental frequency and first harmonic indicated by vertical lines.

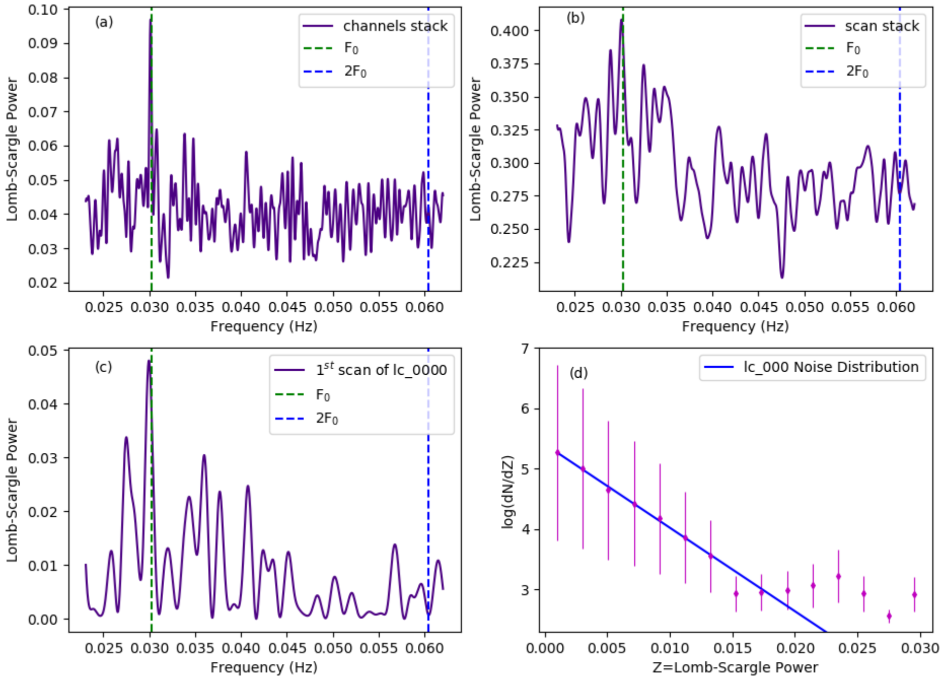

Figure 4.14: (a) Stacked lc_0000, lc_0001, lc_0002 power spectrum (b) stacked power spectrum for scans 1, 2, and 3 [all channels], (c) power spectrum corresponding to the lower channel of the first scan, and (d) the noise distribution of the 6 seconds binned data for the lower channel.

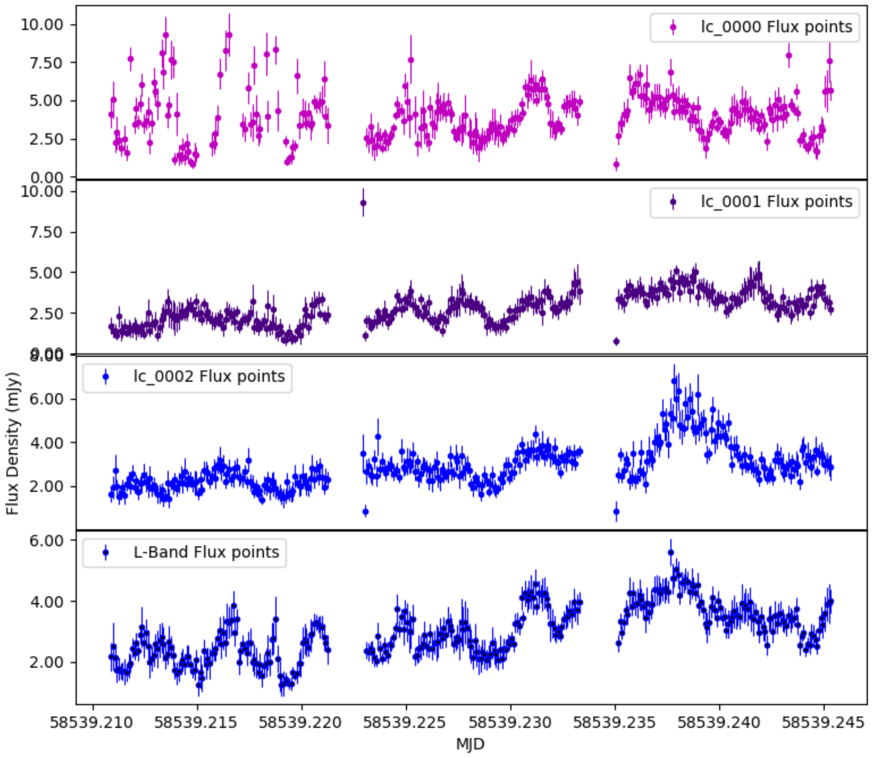

Figure 4.15: Eight seconds binning lightcurves from top to bottom: lower channel 856-1140 MHz (lc_0000), middle 1140-1426 MHz (lc_0001), upper 1426-1712 MHz(lc_0002) and the entire L-band plotted at the bottom.

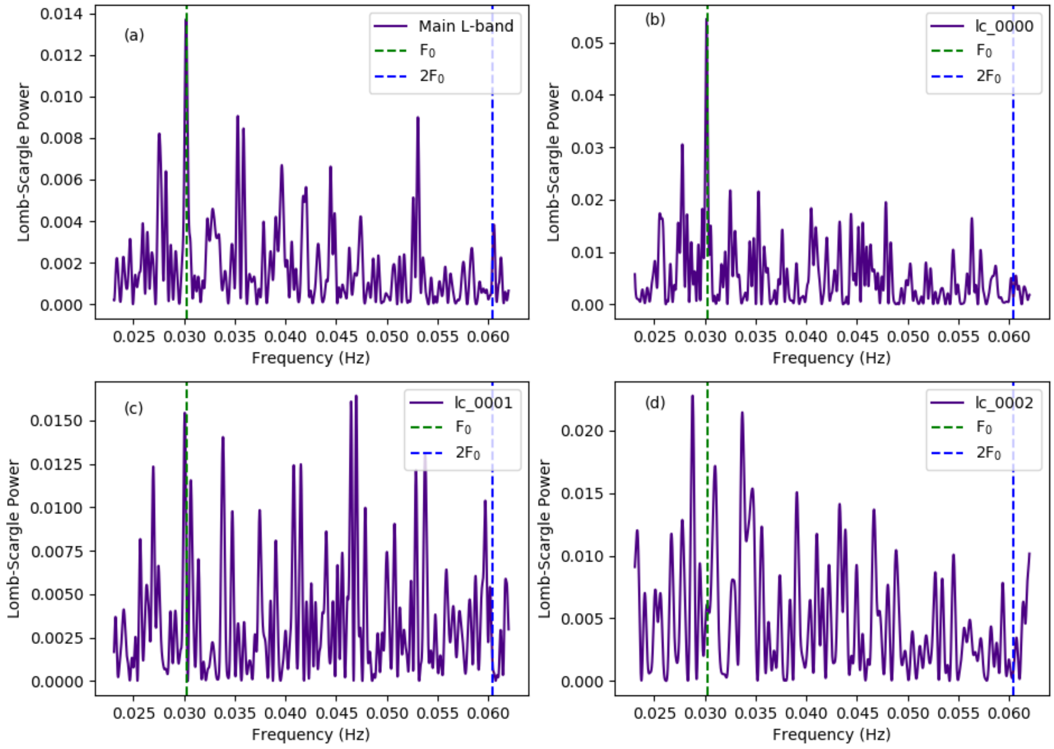

Figure 4.16: Periodograms produced from eight seconds binned data, (a) L-band, (b) lower, (c) middle, and (d) upper channels, plotted over a wide frequency range that includes the fundamental frequency and first harmonic indicated by vertical lines.

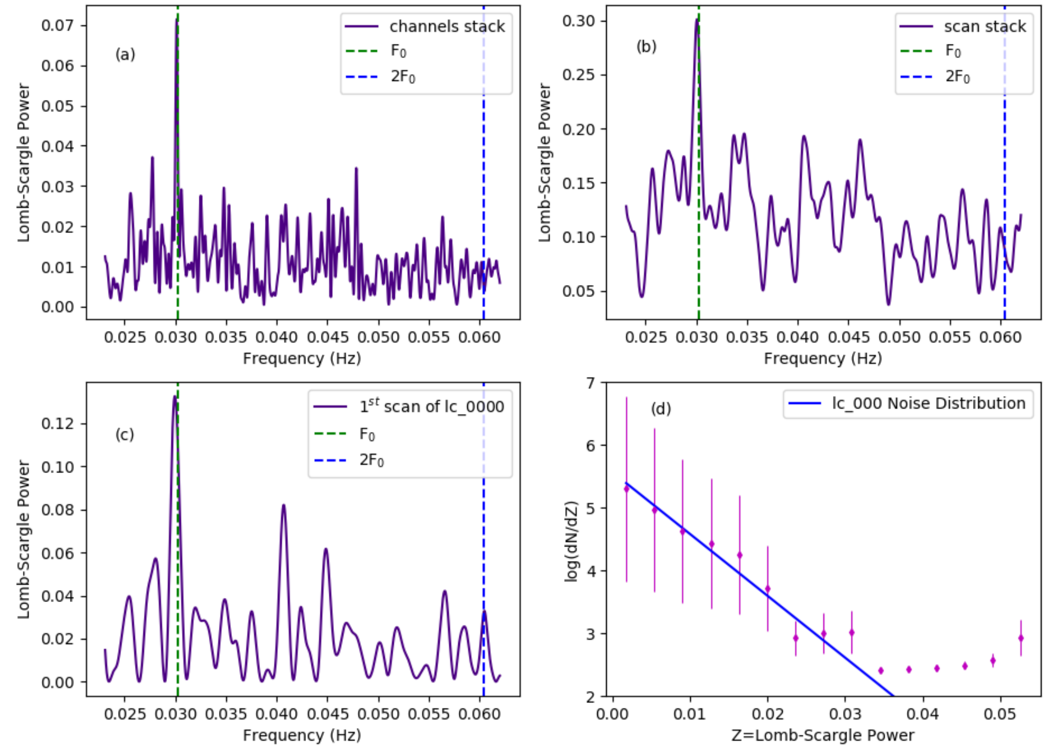

Figure 4.17: (a) Stacked lc_0000, lc_0001, lc_0002 power spectrum (b) stacked power spectrum for scans 1, 2, and 3 [all channels], (c) power spectrum corresponding to the lower channel of the first scan, and (d) the noise distribution of the 8 seconds binned data for the lower channel.

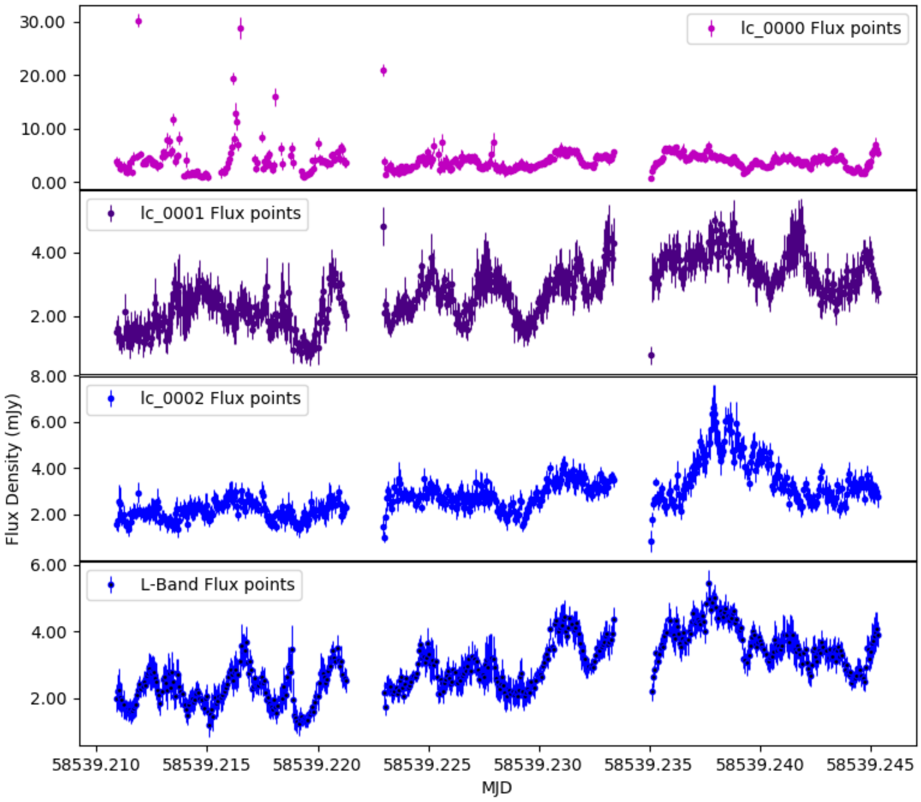

Figure 4.18: Ten seconds binning lightcurves from top to bottom: lower channel 856-1140 MHz (lc_0000), middle 1140-1426 MHz (lc_0001), upper 1426-1712 MHz(lc_0002) and the entire L-band plotted at the bottom.

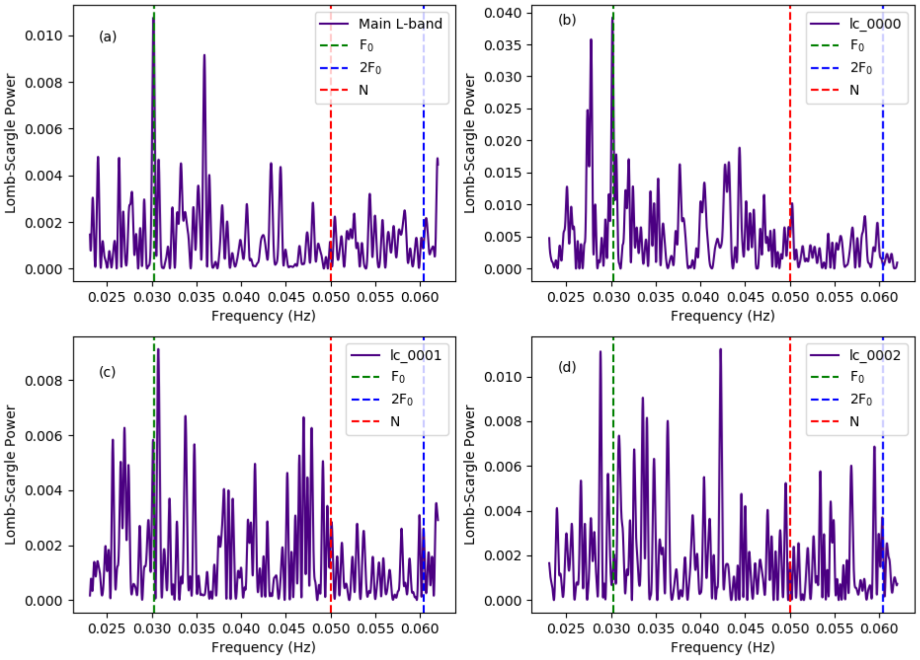

Figure 4.19: Periodograms produced from ten seconds binned data, (a) L-band, (b) lower, (c) middle, and (d) upper channels, plotted over a wide frequency range that includes the fundamental frequency and first harmonic indicated by vertical lines. Nyquist (N) frequency for the 10 seconds binned date is 0.05 Hz, and so no information can reliably be extracted for frequencies above 0.05 Hz i.e., $2F_0$ due to aliasing.

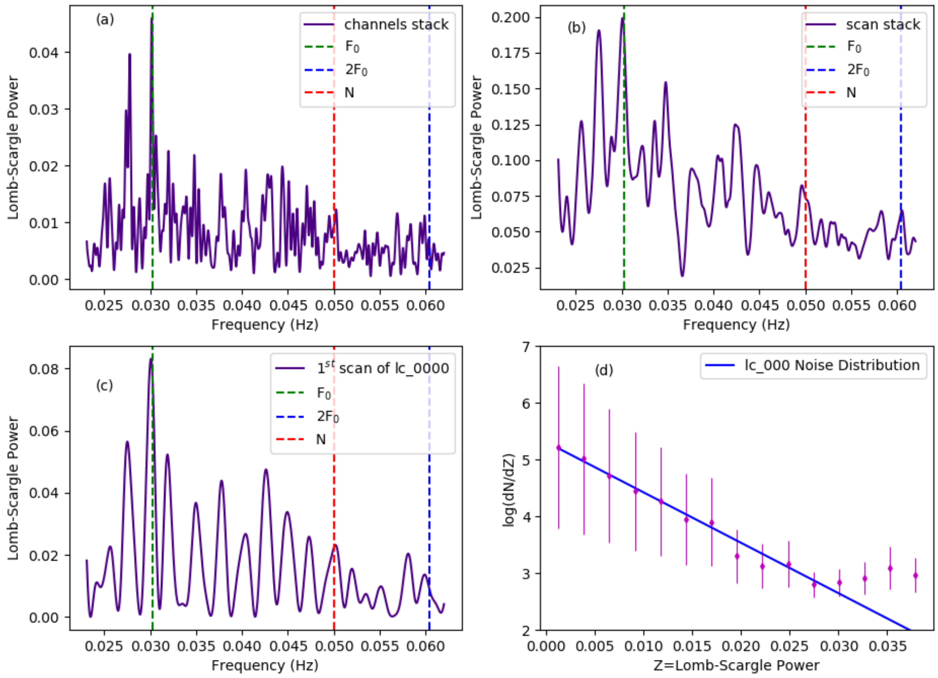

Figure 4.20: (a) Stacked lc_0000, lc_0001, lc_0002 power spectrum (b) stacked power spectrum for scans 1, 2, and 3 [all channels], (c) power spectrum corresponding to the lower channel of the first scan, and (d) the noise distribution of the 10 seconds binned data for the lower channel. Nyquist (N) frequency for the 10 seconds binned date is 0.05 Hz, and so no information can reliably be extracted for frequencies above 0.05 Hz i.e., $2F_0$ due to aliasing.

away if the binning time reduces, similarly the 10 seconds binning yielded less significant results than the 8 seconds binning. The 8 seconds bin data is more significant because four bin values fit inside the spin period, while for the 10 seconds bins, only three bin values are available per period. Thus giving a greater cumulative effect in terms of the greater resolution at 8 seconds bins. The periodic signal period was measured from 6, 8, and 10 seconds periodograms Table 4.4. These periods are close to the rotational period of the white dwarf in AE Aqr but slightly redshifted, and the average value of 6, 8, and 10 seconds of the L-band given in Table 4.4 is 33.13 ± 0.02 s.

Binning (s)	1^{st} lc_0000	lc_0000	L-band
6	33.36 s	33.18 s	33.16 s
8	33.37 s	33.15 s	33.11 s
10	33.24 s	33.15 s	33.11 s

Table 4.4: The period of the pulsed radio emission measured from the first scan of the lower channel, lower channel, and the entire L-band.

4.5 Discussion

We have discovered optically thin non-thermal pulsed radio emission from AE Aqr in the L-band MeerKAT data. This is the first time pulsed emission is detected in the radio waveband. Flux variation is observed in lower, middle and upper bands. However, at 33.08 s the lower section of the L-band exhibits stronger pulsed emission signatures than the middle and upper sections. This may perhaps indicate that there are two processes responsible for the measured radio emission from AE Aqr from $\sim$ 1 GHz to $\sim$ 1000 GHz. At higher frequencies of the L-band, the pulsed emission is dominated by the signal that does not exhibit any periodic emission. All three scans of the entire observation were investigated for periodic emission, and amongst all three scans split into the lower, middle, and upper subbands, a more significant signal was confined on the lower channel of the first scan. This can explain why it is impossible to detect strong pulsed signal from the combined dataset. The moving averages and other more robust methods were applied to the light curves to improve the pulsation signatures from the data, but the results were less compelling.

From the light curve, it can be clearly seen that the flux levels were varying rapidly and increases from the onset of the observation. The pulsed emission manifested more in the first scan than the entire lower channel. This strengthen the idea that the radio emission measured from AE Aqr is produced by two different processes, where the pulsed emission component exhibits a transient nature, which was only strong in the first section of the data. It is possible that the periodic emission is present in all scans, but the non-periodic emission overshadows it.

The spectral variation of radio emission from AE Aqr on the MeerKAT telescope's L-band exhibits the emission that can be characterized by a power law model. But the observed variability of AE Aqr over the entire radio spectrum is explained in terms of the superposition [30] of expanding optically thick synchrotron clouds [31]. The spectral behaviour of AE Aqr shown in insert of Figure 4.7 is accumulated flux measurements, i.e., average flux measured over a long period of time. The data of AE Aqr was interpreted in terms of a van der Laan process (ν^{α}), which presents a cumulative spectrum or a time-average spectrum. The spectral behaviour of the flux measured from the MeerKAT significantly differs from the flux measured by other telescopes as presented in Figure 4.7. One-hour data revealed more information in terms of the nature of emission of AE Aqr. The results of the short observation proved that the MeerKAT telescope is so far the best instrument to observe sources like AE Aqr.

Nevertheless, the radio emission measured by the MeerKAT telescope significantly differ from the measurements made by other telescope. Firstly it exhibits signatures of pulsed emission at or near the fundamental frequency of the white dwarf and secondly the spectrum resemble a power law distribution. The proposed radio emission models for AE Aqr may not be adequate to explain the properties revealed by the MeerKAT radio data of AE Aqr. However, the pulsar-like synchrotron mechanism may be the best mechanism to explain the measurements made through the MeerKAT telescope. The pulsed emission detected in the lower frequency bands with oscillations close to 33.08 s period and a power law spectrum strengthen the possibility of a pulsar-like process. In a way it confirms a pulsar-like synchrotron mechanism since the data clearly show a power law spectrum that may imply a pulsar-like synchrotron emission process, where emission is revealed at the spin period of the white dwarf. It can either be a pure pulsar-like emission of electrons accelerating away from the polar cap region or the magnetosphere of the white dwarf that can either pump the secondary magnetic field or even the mass flow from the secondary star and produce a periodic effect. The pulsed emission detected in this study strengthen the notion that at the lower frequency end around 1 GHz more of the pulsar emission is revealed whilst at higher frequencies the cumulative effect of radiation from blobs ejected by the propeller mechanism may dominate the emission, thus overwhelming the pulsar emission. The hard X-ray spectrum above 10 keV measured by the Suzaku satellite revealed possible non-thermal emission analogous to young rotational-powered pulsars. In the frame of a pulsar-like process, the process responsible for Suzaku hard X-ray emission, is perhaps the same process responsible for radio emission measured in this study.

Chapter 5

Search for gamma-ray emission using Fermi-LAT Data

Introduction

The search for pulsed gamma-ray emission using the Fermi Large Area Telescope (Fermi-LAT) pass 7 data revealed low-level but consistent pulsed emission at the first harmonic (16.54 s) of the spin period (33.08 s) of the white dwarf in AE Aqr [16]. Together with the results reported in the 90's of intermittent pulsed burst-like gamma-ray emission [12, 6, 22] and the detected hard X-rays [10, 21], which could be modelled as non-thermal emission by a power law model, has motivated this study. Accordingly, a re-analysis was conducted utilising the pass 8 data, an upgraded dataset and analysis toolkit with more inclusive selection criteria and an improved galactic diffuse gamma-ray emission model.

This chapter is structured as follows, a brief discussion of the Fermi telescope followed by a presentation of the standard data analysis process for unbinned and binned analyses using Fermi science tools. The results from the standard analysis processes will be presented, including a discussion of the significance of the results and we present a possible new approach to analyse transient sources with non-significant results under standard techniques. This new method and results will be described, including a discussion of how burst-like and pulsed gamma-ray emission in the Fermi-LAT pass 8 data were detected for AE Aqr.

5.1 The Fermi Large Area Telescope

The Fermi Gamma-ray Space Telescope was launched by NASA on 11 June 2008 into a low earth orbit (LEO) at an altitude of 550 km. Fermi-LAT is the primary instrument on the Fermi Gamma-ray Space Telescope, formerly known as the Gamma-ray Large Area Space Telescope (GLAST). The Fermi-LAT is in constant survey mode, and covers the whole gamma-ray sky every 3 h. It has a large field of view of 2.4 sr at 1 GeV, about 20 % of the sky. The corresponding energy sensitivity is between 0.1 - 500 GeV. The point spread function (PSF) is about 68 % containment radius. Fermi-LAT data access, tutorials, and software tools can be accessed through Fermi at ASDC (Fermi at ASDC [1]) and Fermi Science Support Centre at HEASARC [2]. Abdo

---

[1] `http://fermi.asdc.asi.it/`

[2] `http://fermi.gsfc.nasa.gov/ssc/`

et al., [157] and Ackermann et al., [158] describe the in-flight calibration of the Fermi-LAT. Refer to Atwood et al., [159] for an in-depth discussion of the Fermi-LAT instrumentation and technical specifications. The next paragraph is a brief discussion of the improvements done on the pass 7 reprocessed dataset to produce the pass 8 dataset.

Pass 8 provides the new version of the LAT data, which is the improved version of the pass 7 reprocessed data. The entire dataset of the mission is reprocessed, including the upgraded event reconstruction, a broader energy range, an increased effective area, and better energy measurements. Pass 8 allows the user to select a subset of the events if necessary, to improve analysis results since the quality of measurements for both energy and position have been re-evaluated. The Fermitools are also adjusted to support the new data and all the changes. Contrary to pass 6, pass 7, and pass 7 reprocessed, where the focus was primarily on reducing the uncertainties in the response functions of the instrument, pass 8 brings in a significant change in the event-level reconstruction. In other words, pass 8 is a complete revision of the entire analysis chain that yields significant gains in the performance of the instrument. The introduction of pass 8 was aimed at reducing the error in the energy measurement that results from the instrumental pile-up away from the gamma-ray shower, i.e., ghost events, and its results show a substantial improvement in this regard. The tracker reconstruction of pass 7 data resulted in various problems that led to loss of events. Problems include i.e., increased complexity, which often ends in mislabelling of gamma-ray events leading them to be classfied as background, loss of events that fail to reconstruct, and some of the events also transfer from the core of the Point-Spread Function (PSF) to the tails due to tracks poorly reconstructed. The pass 8 reconstruction approach addresses these problems through tree-based tracking, which examines the conversion in the tracker at the origin of a shower and tries to model this process by connecting hits into tree-like structures. In pass 7, the events that have tracks with no energy deposits in the calorimeter were eliminated, but with the latest development, these events are considered, since the minimum selection cut for energy deposited in the calorimeter was removed. Consequently, the number of events detected by pass 8 exceeds those detected by pass7 (for more information on pass 8 data, see discussion in Atwood et al., [160]). The increase in the effective area resulted in a corresponding rise in absolute background levels. However, despite the increase in background levels, the signal-to-background ratios have also improved, improving the point source sensitivity overall energy ranges of the LAT instrument.

5.1.1 Fermi data products

Two essential fits files are extracted from the LAT data; the photon file and the spacecraft file. The photon file comprises information necessary for science analysis, such as the event's energy, the quality of the event reconstruction, and the position. On the other hand, the spacecraft file gives the information of where the LAT was pointing, i.e., it consists of the position of the spacecraft and corresponding time (in 30 s intervals) of its orientation. The LAT data also have an extended file, which has the same photon data as the photon file along with supplementary photons with more relaxed cuts. This file is not important when conducting an analysis using Fermi science tools.

5.2 Fermi Data analysis of AE Aqr

In this study, the Fermi-LAT archived gamma-ray data observed between 2008-08-04 at 15:43:36 and 2020-03-25 at 05:21:17 were considered. The analysis was undertaken using the Fermi Science Tools software packages (v11r0p5) installed with Anaconda python package. We used the P8R3_SOURCE_V2_v1 set of response functions and selected corresponding source−class events, event class (evclass=128) and FRONT+BACK event type (evtype=3). Analysis photons were collected from a 10° region of interest (ROI) with its centre at AE Aqr (RA=310.038°, DEC= -0.8708° *epoch* J2000), which was chosen to account for the PSF of the LAT instrument [159, 160]. The zenith angle cut was set at 90 degrees to prevent contamination by photons produced from cosmic-ray interaction with the atmosphere. Binned and unbinned maximum likelihood analyses were performed on the energy range 0.1-500 GeV using the *gtlike/pyLikelihood* routine. Sources within 20° of the ROI from the fourth catalog of Fermi-LAT (4FGL), the instrumental background, and the diffuse galactic and extragalactic isotropic emission model (gll_iem_v07.fits) [161], as well as the source of interest, were included in the spectral model file. The analysis of AE Aqr was undertaken making use of a power law and the spectral model for pulsars,i.e., a power law with the exponential-cutoff2 (see equation 5.1 and 5.2).

The power law model has three prominent parameters which include the spectral index (γ) which controls the hardness of the source, the flux value known as the prefactor normalisation (N_o), which scales the brightness of the observed source, and the energy scale (E_o). Thus, the power law distribution of photons takes the following mathematical form,

$$\frac{dN}{dE} = N_o \left[\frac{E}{E_o}\right]^{\gamma} \tag{5.1}$$

The power law with super-exponential cut-off2 is one of the spectral models that describe gamma-ray emission from a pulsar-like system. It shares features with a power law spectral model , but it has an additional factor (terms ar additive), the super-exponential term (see equation 5.2).

$$\frac{dN}{dE} = N_o \left(\frac{E}{E_o}\right)^{\gamma_1} e^{-aE^{\gamma_2}} \tag{5.2}$$

where the parameters of this spectral model have the same meaning as in the power law spectral model but this model also includes the γ_2 index and the exponential factor a.

Sources were added to an eXtensible Markup Language (XML) file (the spectral model file) from the fits file of the 4FGL catalog, making use of the python module (make4FGLxml.py). The isotropic component (IRFs) and diffuse galactic emission were included in the spectral model file in the same manner. Many features can be considered to constrain the spectral model, i.e., fixing or freeing parameters using features such as significance, the variability of the source, the radius, and PSF as the deciding factors. The default value for significance (5 σ) was used to freeze[3] out any source with significance less than the limit value. The PSF set to **TRUE** forced all sources to be modelled as point sources including the extended sources,

---

[3] When a source parameter is frozen or fixed it will not be optimised. The value of the parameter will not change during the fitting process

the radius limit was set to an absolute maximum radius of 15 °. This radius marks the maximum distance from the ROI centre beyond which all parameters should be fixed. Even norms or prefactor of variable sources will be fixed beyond this radius. The source under consideration (AE Aqr) was added to the XML manually with the models mentioned earlier. The log(likelihood) analysis fit the data to a given model [162]. Therefore, the spectral model and all other precomputed likelihood files were used to optimize and fit the observed data.

The significance of gamma-ray emission from AE Aqr was estimated using the test statistic (TS). The TS is equivalent to the ratio of -2log(likelihood) (see discussion Appendix B) with and without the source, i.e.,

$$TS = -2log\left(\frac{L_{max,0}}{L_{max,1}}\right) \tag{5.3}$$

where $L_{max,0}$ determines the value of the maximum likelihood of a model without an additional source known as the null hypothesis and $L_{max,1}$ determines the value of the maximum likelihood of a model with an additional source at a given location. The significance of gamma-ray emission is determined by taking the square root of the TS, i.e., $\sigma = \sqrt{TS}$ [162].

5.2.1 Binned log(likelihood)

The approach described above was used for an initial exploratory analysis, and the source of interest was insignificant with a TS of zero. Therefore, before performing the binned log(likelihood), all appropriate parameters in the XML file for every source within 10 ° were freed. Then data were fitted to model parameters that were first optimized and fitted with the MINUIT (refer to Appendix B) algorithm and re-optimized and re-fitted with the NEWMINUIT optimizer to improve the fit statistics. The fit converged with some sources having bad statistics, e.g., negative test statistics. The fit parameters were saved to the output XML. The model map and the residual map were produced using the output fitted model to inspect sources not correctly modelled. The fit quality was also investigated visually through the counts' spectrum (see Figure 5.1), which shows counts distribution as a function of energy for each source in the model. From the model map and residual map (Figure 5.2) sources not correctly modelled were identified and set free in the XML file, including the instrumental background model, diffuse galactic emission model and sources within 5° from the centre of the ROI. Then the data were optimized and fitted again with MINUIT and then NEWMINUIT. The residual map must be flat showing no excess positive or negative counts. If the model of the source overestimates the counts for a certain region or source the residual map will have negative excess counts or vice versa, e.g., the region of 4FGL J2025.6-0735 was overestimated. Since the significance of a faint source is dependent on the fit of the bright sources in the ROI, the process of re-optimization and refitting was repeated on the successive modified XML file until all sources were correctly modelled.

The final fit on the final model was conducted to measure the photon flux or upper limits, likelihood TS and the predicted counts (Npred). Unfortunately the search yielded no significant gamma-ray signature, therefore the upper limits were calculated for binned likelihood analysis.

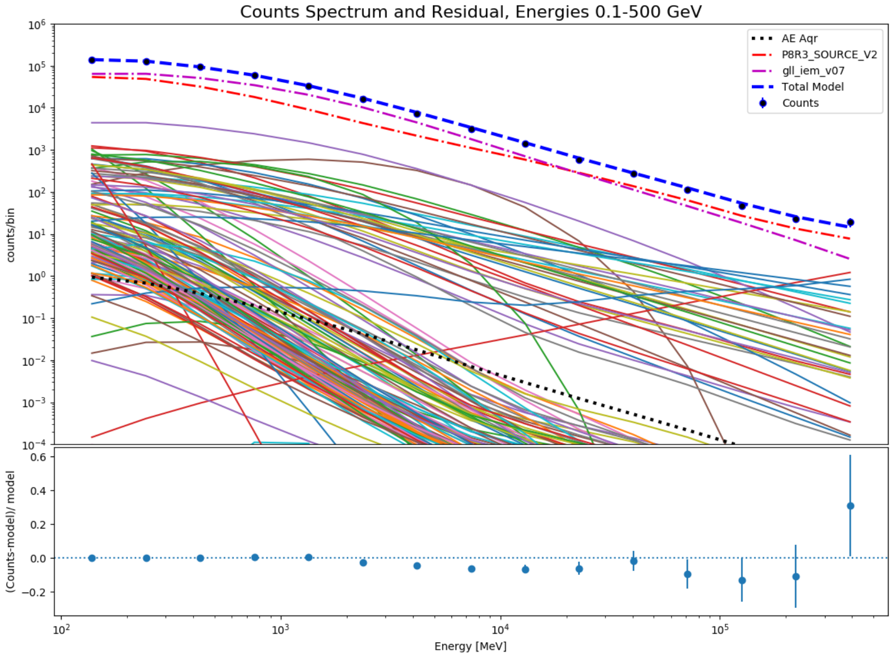

Figure 5.1: The counts spectrum is the cumulative model for all source spectra in the region included in the analysis.

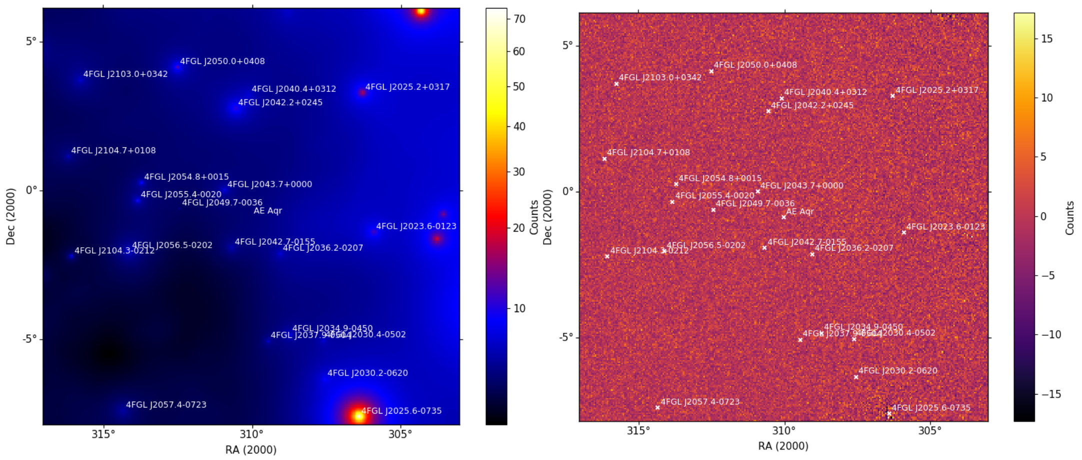

Figure 5.2: The model map (left) and the residual map (right). Inspecting the residual map shows that the counts for some regions were overestimated or underestimated.

5.2.2 Unbinned log(likelihood)

Unbinned log(likelihood) was performed on the entire period of the dataset to produce the best spectral model. Since the process requires high-performance computations, and it consumes more time than binned, an iterative approach was used at this stage. With a lot of free parameters, the process takes longer to finish. Therefore to reduce the number of parameters in the spectral model, the XML file was generated using the standard approach with the deciding factors set as described earlier (see section 5.2) but with significance set at a limit of 120 σ to reduce the number of free parameters in the model to ensure the tools will work correctly. The resulting spectral model had 11 free parameters, including power law parameters for AE Aqr. The optimization and fitting were conducted, producing a model with new parameters for free sources. Some bright sources in the model were set free, but to maintain a minimum number of free parameters newly modelled sources were fixed. This method was repeated until all sufficiently bright sources in the ROI were modelled. Note that the normalization and prefactor of the isotropic model and the diffuse galactic emission model were allowed to vary at each succeeding optimisation and fitting.

5.2.3 TS and Residual Maps

In addition to binned and unbinned log(likelihood), a further significance test was done through the production of the test statistic maps. Test statistic and residual maps were generated for the region 80×80 pixels centered on AE Aqr with a bin step of 0.1 degrees/pixel with stereographic (STG) projection [163], using the *gttsmaps* routine, which generates a TS map for each source component in the model centred at each spatial bin. The method calculates the likelihood TS for each bin using equation 5.3, where the likelihood is maximized at each grid point on the sky. In other words, the point source is iteratively fitted at each grid of the entire specified region. This method helps to find unmodelled, new, and fainter sources, which will then show on the local maxima of the map.

The *gtlike* output model file was again edited, all sources' parameters were frozen including the prefactor or norm of the diffuse sources. This will make the *gttsmap* skip the process of refitting the entire model at every point on the grid. Running *gttsmap* with this setting produces a residual map. TS maps are only sensitive to a positive deviation with respect to the model. We check whether there is any excess at the coordinates of AE Aqr by running the *gttsmaps* with AE Aqr excluded from the output source model and all the parameters frozen including the galactic sources. These processes were performed for both binned and unbinned analyses.

5.3 Results for the search for gamma-ray emission using standard binned and unbinned analyses techniques

The binned and unbinned analyses performed using the standard technique for the entire period of the analysis resulted in no detection of any significant gamma-ray radiation at the region of AE Aqr. The threshold of source detection requires a source to have a statistical significance above 5 σ, which corresponds to a test statistic of 25. Since the statistical significance of the source under consideration is significantly below the threshold, the upper limits were calculated at a 95 % confidence level both for unbinned and binned analyses. The upper limit (UL) results and other statistics from this analysis are listed in Table 5.1.

The likelihood model map shows all sources that were included in the fit, and it provides a visual aspect of fitted sub-models. Figure 5.3 compares the raw data to the fitted data. The accuracy of the fit is investigated by a residual map, which is the residual between the raw data map and the model map. Residual maps can show both positive and negative deviations. In the case where the sub-models assume the

	unbinned		binned	
Energies	0.1-500 GeV	1-500 GeV	0.1-500 GeV	1-500 Gev
Test statistic	0.9331	-0.00021	0.1197	2.24
Predicted Counts	234.469	0.0084	6.436	257.24
UL (ph.cm^{-2}s^{-1})	4.01 $\times 10^{-9}$	3.36 $\times 10^{-9}$	6.77 $\times 10^{-9}$	5.54 $\times 10^{-9}$

Table 5.1: Binned and unbinned log(likelihood) analyses results.

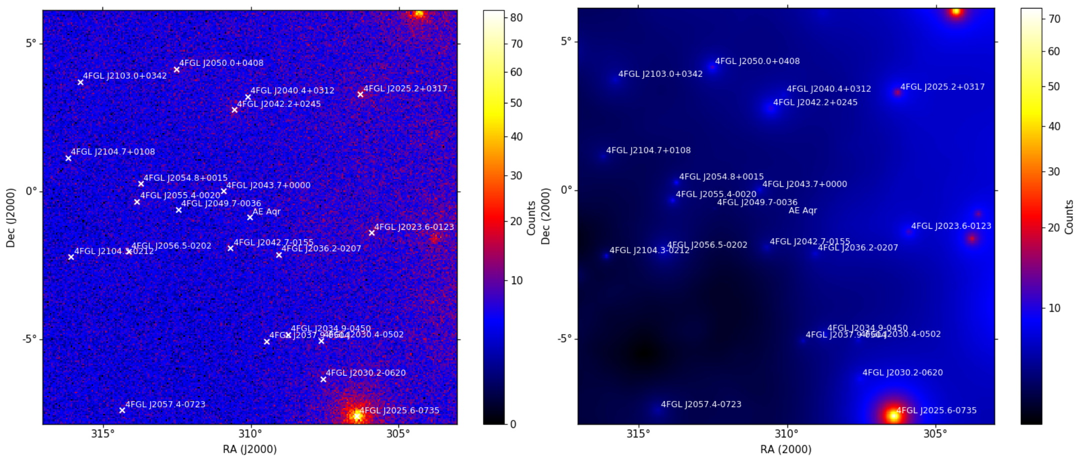

Figure 5.3: Counts or raw data map (left) is the data sum of detected counts at a given grid location, a model map (right).

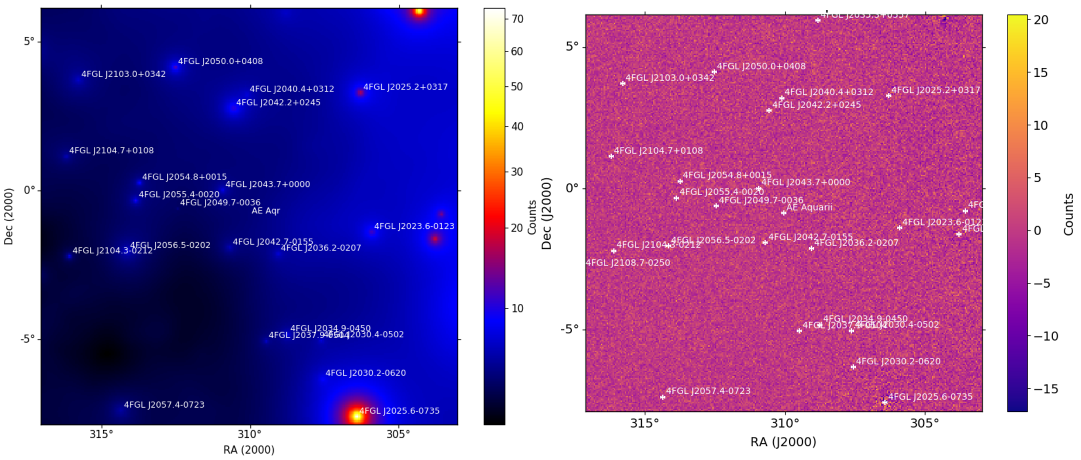

Figure 5.4: The model map (left) displays the distribution of predicted counts for each source included in the model and the residual map (right), checks the correctness of the model.

observed data, the entire map will be flat with significance values around zero (see Figure 5.4).

Further review of the significance of the source was accomplished through the production of diagnostic TS maps. The resulting TS maps for both analyses are shown in Figure 5.5 . The right panel of Figure 5.5 are the residual maps, which shows no signs of any gamma-ray activity in the region of AE Aqr. If there is a new source not included in the catalog or any source excluded from the model the two maps will be different on the region of the source. In principle when producing the TS map the

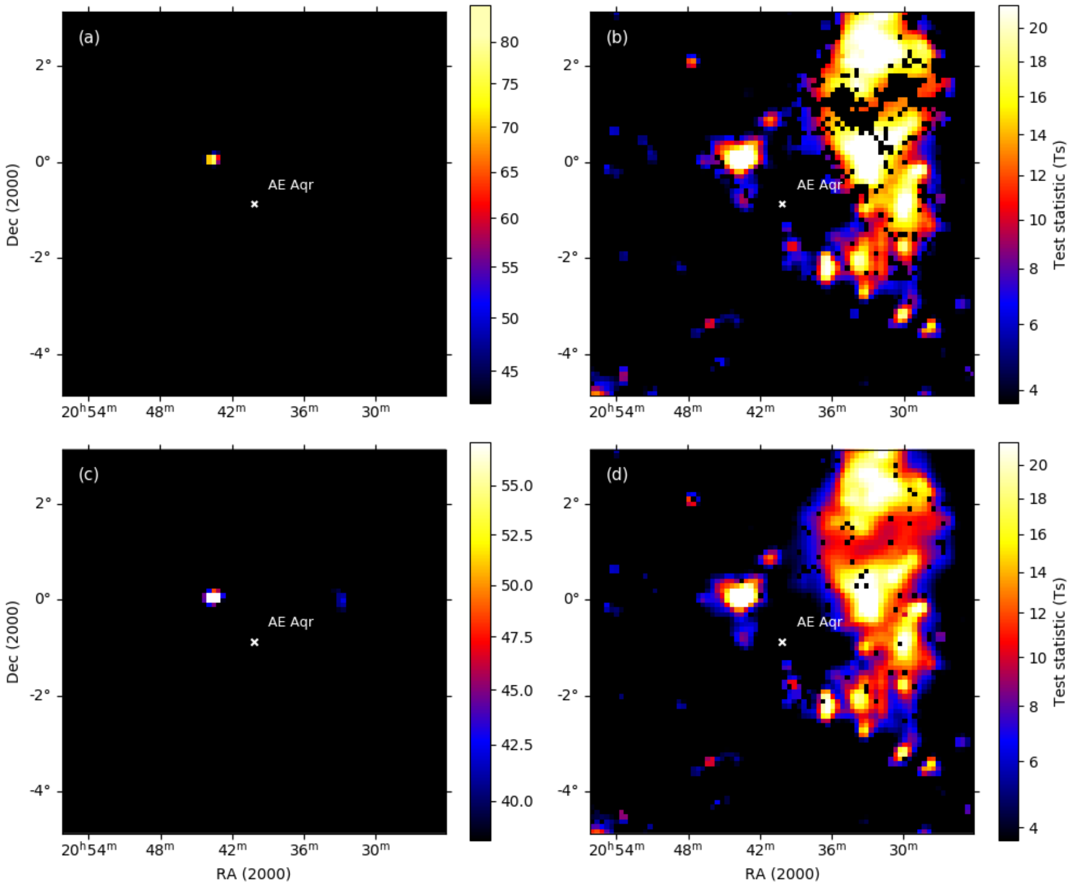

Figure 5.5: Top: Binned TS maps (left) and residual maps (right), were both generated with 100 × 100 pixels with a bin step size of 0.1 for the entire period of the dataset. Bottom: Unbinned TS maps (left) and residual maps (right), were both generated with 100 × 100 pixels with a bin step size of 0.1 for the entire period of the dataset.

source of consideration is intentionally omitted from the model to check for its significance. The absence of a point-like source at the position of AE Aqr in the TS map may be due to the Fermi standard analysis technique not being effective enough to detect short period burst-like emission from faint sources.

5.4 Search for transient emission from AE Aqr

The standard binned and unbinned analyses techniques resulted in no detection of gamma-ray emission from AE Aqr. Therefore, to further investigate for any possible emission, the data were investigated for transient gamma-ray emission. To search for transient gamma-ray emission an unbinned log(likelihood) analysis was conducted at selected bin periods that included the periods contemporary to optical flares observed by Zamanov et al., [164] and van Heerden [15]. This approach aimed to check for any gamma-ray emission that correlates with optical flares. It was reported by Meintjes et al., [6] that gamma-ray emission is likely to be detected at or just before the onset of the optical flaring. Thus the selected bin periods for unbinned log(likelihood) analysis were chosen to incorporate each optical flare. Observations have also shown that AE Aqr has very short flares that range from minutes to a few

Flare	T-start (UTC)	T-end (UTC)
1	2010 Jun 02 at 23:18:14.400	2010 Jun 03 at 01:00:00.000
2	2010 Jun 07 at 23:18:14.400	2010 Jun 08 at 01:00:00.000
3	2010 Jun 17 at 22:35:11.040	2010 Jun 18 at 01:28:53.200
4	2010 Jun 25 at 22:04:04.800	2010 Jun 26 at 02:50:11.282
5	2010 Jul 16 at 20:13:29.280	2010 Jul 17 at 01:11:37.016
6	2010 Jul 28 at 19:36:54.720	2010 Jul 28 at 19:36:54.720
7	2010 Aug 20 at 17:17:48.480	2010 Aug 20 at 23:39:02.343
8	2010 Sep 03 at 16:44:58.560	2010 Sep 03 at 22:15:08.669
9	2011 Aug 07 at 17:13:12.000	2011 Aug 08 at 00:24:16.364
10	2011 Aug 08 at 17:17:22.560	2011 Aug 09 at 00:02:55.966
11	2011 Aug 10 at 17:02:24.000	2011 Aug 10 at 23:44:05.079
12	2011 Aug 11 at 16:55:12.000	2011 Aug 11 at 23:26:21.315
13	2011 Aug 19 at 17:05:08.160	2011 Aug 19 at 23:21:58.234
14	2011 Aug 24 at 16:47:34.080	2011 Aug 24 at 23:04:18.656
15	2011 Aug 25 at 16:50:52.800	2011 Aug 25 at 23:04:38.588
16	2011 Aug 26 at 16:58:04.800	2011 Aug 26 at 22:32:46.422
17	2012 May 16 at 23:57:24.480	2012 May 17 at 04:05:47.546
18	2012 May 19 at 02:37:14.880	2012 May 19 at 04:13:38.052
19	2012 May 21 at 02:30:54.720	2012 May 21 at 04:16:13.783
20	2012 May 22 at 02:01:58.080	2012 May 22 at 04:01:51.408
21	2012 May 23 at 01:55:03.360	2012 May 23 at 04:00:16.906
22	2012 May 25 at 02:08:09.600	2012 May 25 at 04:00:03.631
23	2012 May 27 at 01:45:50.400	2012 May 27 at 04:00:06.916
24	2012 May 29 at 01:42:48.960	2012 May 29 at 04:11:05.913
25	2013 Apr 12 at 02:58:33.600	2013 Apr 12 at 03:37:35.165
26	2013 Apr 13 at 03:15:50.400	2013 Apr 13 at 03:38:45.693
27	2013 Apr 14 at 03:40:19.403	2013 Apr 15 at 00:00:00.000

Table 5.2: T-start and T-end marks the beginning and the end of the analysis period.

hours (e.g., [5]). Therefore, it is difficult to search for the variability of low-level transient source using Fermi-LAT dataset.

Zamanov et al., [164] reported strong short time optical flaring between 10^{th} and 16^{th} of August 2011. Refer to Table 5.2 for Fermi LAT periods that coincide with optical flares observed by Van Heerden [15] considered in this study. The analysis was performed for the period that incorporates each entire observation. Since it is difficult to get the best spectral model that describes the data on a single day analysis, the previously optimized spectral model was again used at this point.

The search for transient gamma-ray emission from the Fermi-LAT dataset for periods that coincide with optical flares resulted in a TS that ranges between $0 - 2$, which is insignificant according to the Fermi detection limit. The significance was further investigated using the TS maps, which also revealed no excess gamma-ray emission.

To further search for transient gamma-ray emission, the final spectral model was used to produce a characteristic light curve over the entire dataset with the time axis set to 14 days per bin. Since gamma-rays from AE Aqr reported in the 90's are sporadic burst-like emission, we searched for time bins that have a sufficient significance. On the other hand, we also aimed to investigate the upper limit flux variations.

The light curve revealed that in the data there exist periods with excess significance. Further investigations were pursued through unbinned log(likelihood) analysis on the time bins with significance above 1 σ (see Figure 5.6).

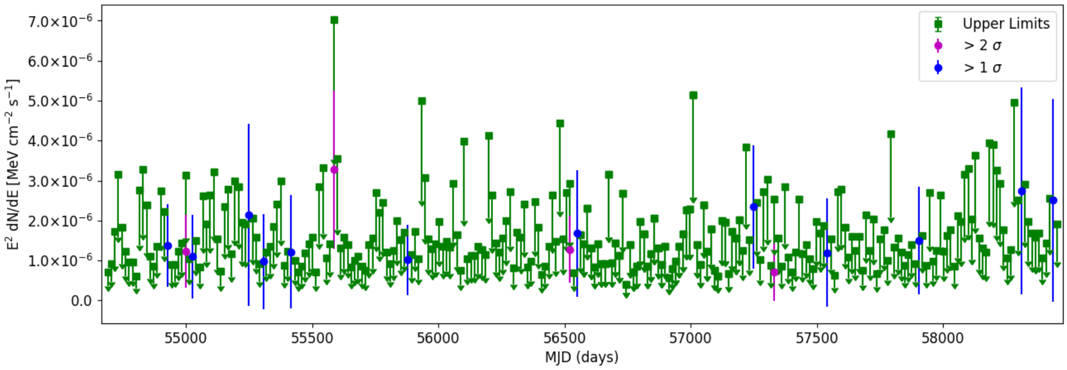

Figure 5.6: The light curve of AE Aqr produced for the energy range 0.1-500 GeV for the entire period of the dataset. Blue circle (1 σ) and magenta circle (2 σ) correspond to periods where good convergence was obtained. Green squares represent upper limits.

Further likelihood analysis for the selected periods that had significance values above 1 σ resulted in improved significance with TS ranging between $4 - 12$. Again a further test for significance was done through the production of test statistic maps, i.e., TS and residual maps. Only a few selected maps resulting from this analysis are shown in Figure 5.7 for selected periods with significance above 2 σ. The TS maps generated for these selected periods revealed indications of gamma-ray emission at the region of AE Aqr. Thus further investigation was conducted by generating spectral points presented in the following section.

5.4.1 Spectral Energy Distribution

The spectral energy distribution (SED) for time bins with significance over 2 σ was generated using the standard techniques of unbinned processes. The standard energy bins for a decade is ten energy bins, where as in this study, 12 energy bins were used since the narrower the energy bin, the closer a photon is associated with its original characteristics. The SED was computed to check the model accuracy and the contribution of each energy bin to the average calculated significance. The computed flux spectral points generated as a function of energy are shown on the left-hand panel of Figure 5.8, and the corresponding TS for each energy bin is shown on the right-hand panel.

5.4.2 Search for Pulsations

Pulsed optical and X-ray emission has been detected at $F_0 = 30.23$ mHz, the fundamental frequency with emission pulsation spread over the frequency interval $\sim 29.9 - 30.0$ mHz. These short frequency pulsed emissions were explained in terms of the propeller-driven emission since the interaction of the magnetosphere, and the mass flow takes place outside the co-rotation radius of the white dwarf. In the early

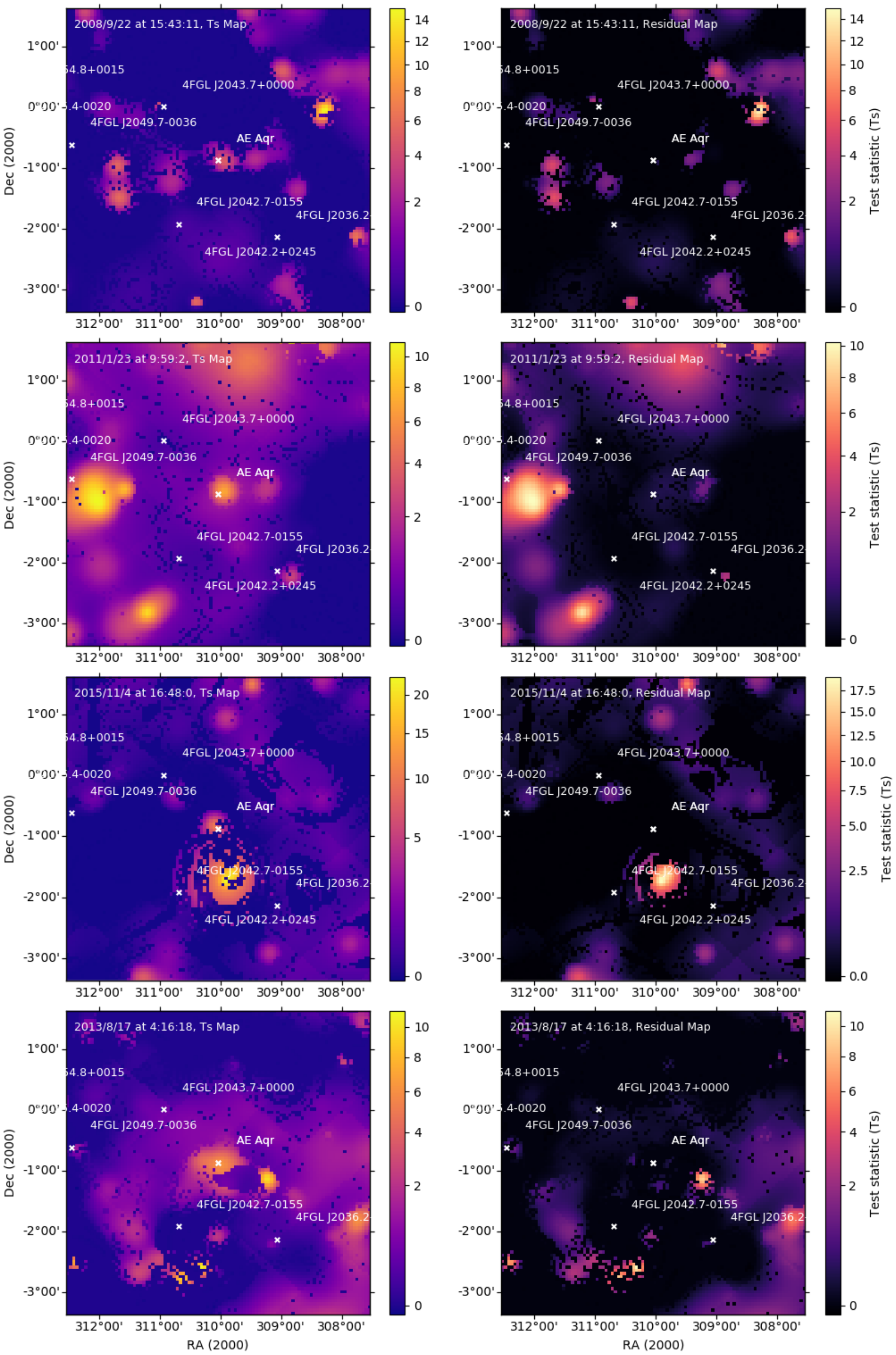

Figure 5.7: TS maps (left panel) and residual maps (right panel), were both generated with 60 × 60 pixels with a bin step size of 0.1 for periods with significance above 2 σ.

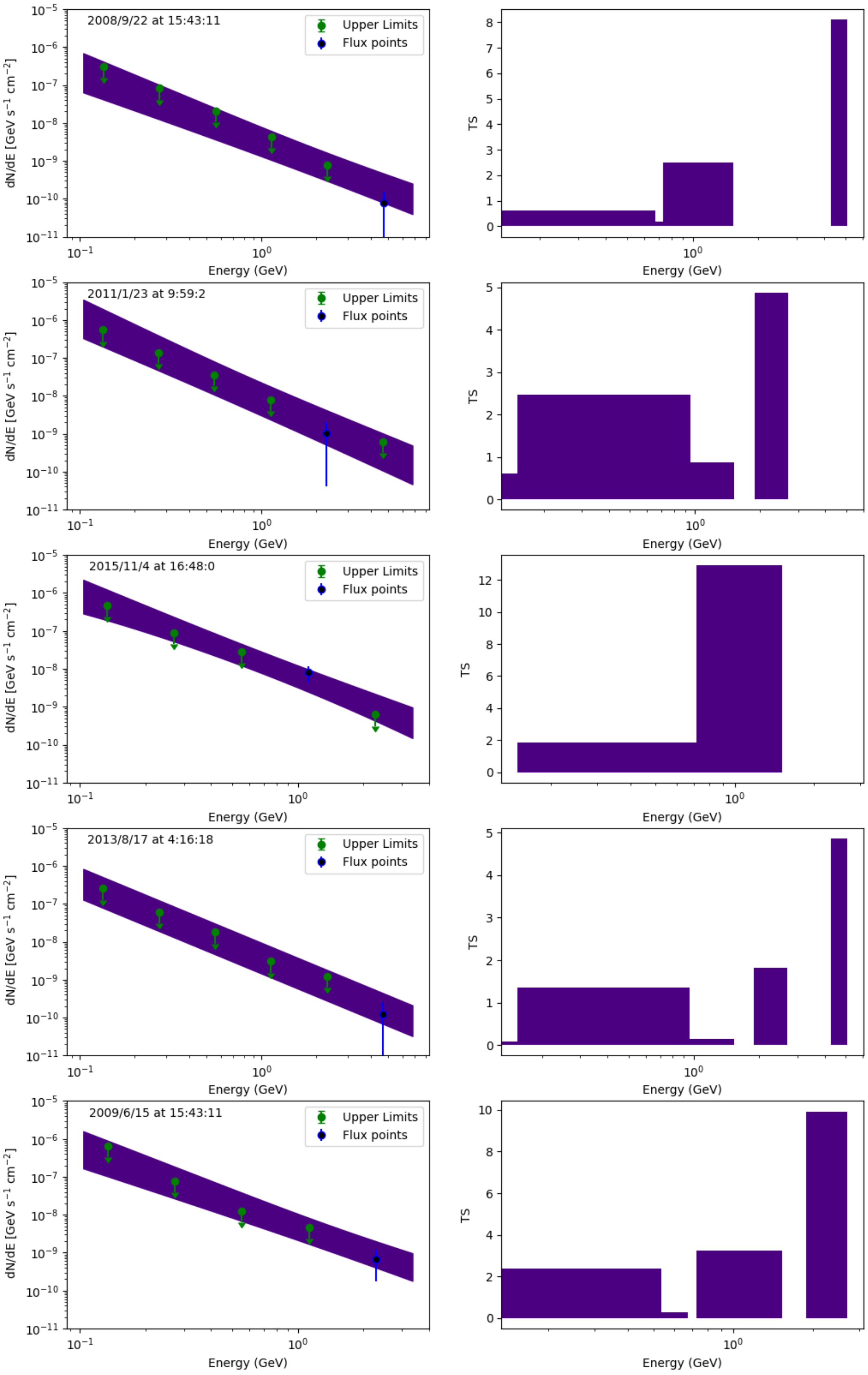

Figure 5.8: The spectral energy distribution plots (left panel) and the corresponding bar chart of TS distribution of the source's significance over the entire analysis energy ranges (right panel), generated for periods that have significance above 2 σ.

90's (e.g., [6]) pulsed higher energy emission was also detected at these frequencies. The correlation between VHE gamma-ray and optical emission was also confirmed at 30 mHz. Episodic emission at $F_1 = 2F_0$, the first harmonic was also reported.

The Fermi Science Tools software packages (v10r0p5) is not eligible for the so-called blind search, fortunately our case is feasible since the rotational period of the white dwarf is known, and evidence of the detected pulse frequency is available. The periodic search was performed using *gtpsearch* and *gtpphase* routines. Python scripts were developed to use these tools effectively. The *gtpsearch* supports numerous test statistics techniques of timing analysis, for example, the Chi-squared, H, Z-squared, Z-squared with N, and the Rayleigh test used in this study. Only light-curve time bin periods with significance above 2 σ and the time bin periods that coincide with optical flares were considered.

The routine makes use of the coordinates of the source of interest to calculate the barycentric correction. It also uses the spacecraft file to perform the barycentric correction, the demodulation of binary to the arrival time of each photon. The ephemeris of AE Aqr used to conduct this analysis were obtained from Jian et al., [96]. The source ephemeris parameters were manually added on this, and the next step since the source does not have a database file. The GTIs files for the selected periods were used as the input (event) file along with the spacecraft file. The spin or pulse period search was performed first with the central frequency set on or near the fundamental frequency or the first harmonic. The number of separate trials were set in such a way that the frequency base is wide enough to cover the red-shifted frequency peaks. If the peak appears between $29.9 - 30.0$ mHz the process was repeated with the central frequency set to the frequency with the highest Rayleigh test statistics.

Each peak within the red-shifted range, as observed in the optical band, was tested for periodicity using the *gtpphase* routine, which generates the pulse phase light curve points. The routine adds a PULSE_PHASE column to the event file. It computes the pulse phase for each photon's arrival time, and writes these computed pulse phase values to the PULSE_PHASE column. The same event files and spacecraft used on *gtpsearch* is also used on this step with the central frequency or period set to the observed frequency with the highest test statistics in the previous step. A sinusoidal shape in the light curve indicates the episodic nature of the detected photons.

The results that show more significant indications of pulsed emission from the search for periodic emission are shown in Figure 5.9, where the pulse profiles are on the left side panel and the pulse phase light curves are on the right panel. The pulse profile and the pulse phase light curve presented in this figure are 14-day periods selected sections of the data with positive TS value. Some pulsed power appears near or at the rotation period of the white dwarf in AE Aqr. And some of the accompanying pulse phase light curves revealed the periodic nature of the collected photons. The maximum Rayleigh statistic $2nR^2$ [165] from the 14-day data is $2nR^2 = 13.8$, which corresponds to a probability for chance occurrence of $Pr = e^{-nR^2} \approx 10^{-3}$ [166]. Noticeable from the phase distribution of the 33.08 s pulse is an indication of a double pulse which signifies pulsed power also at 16.54 s.

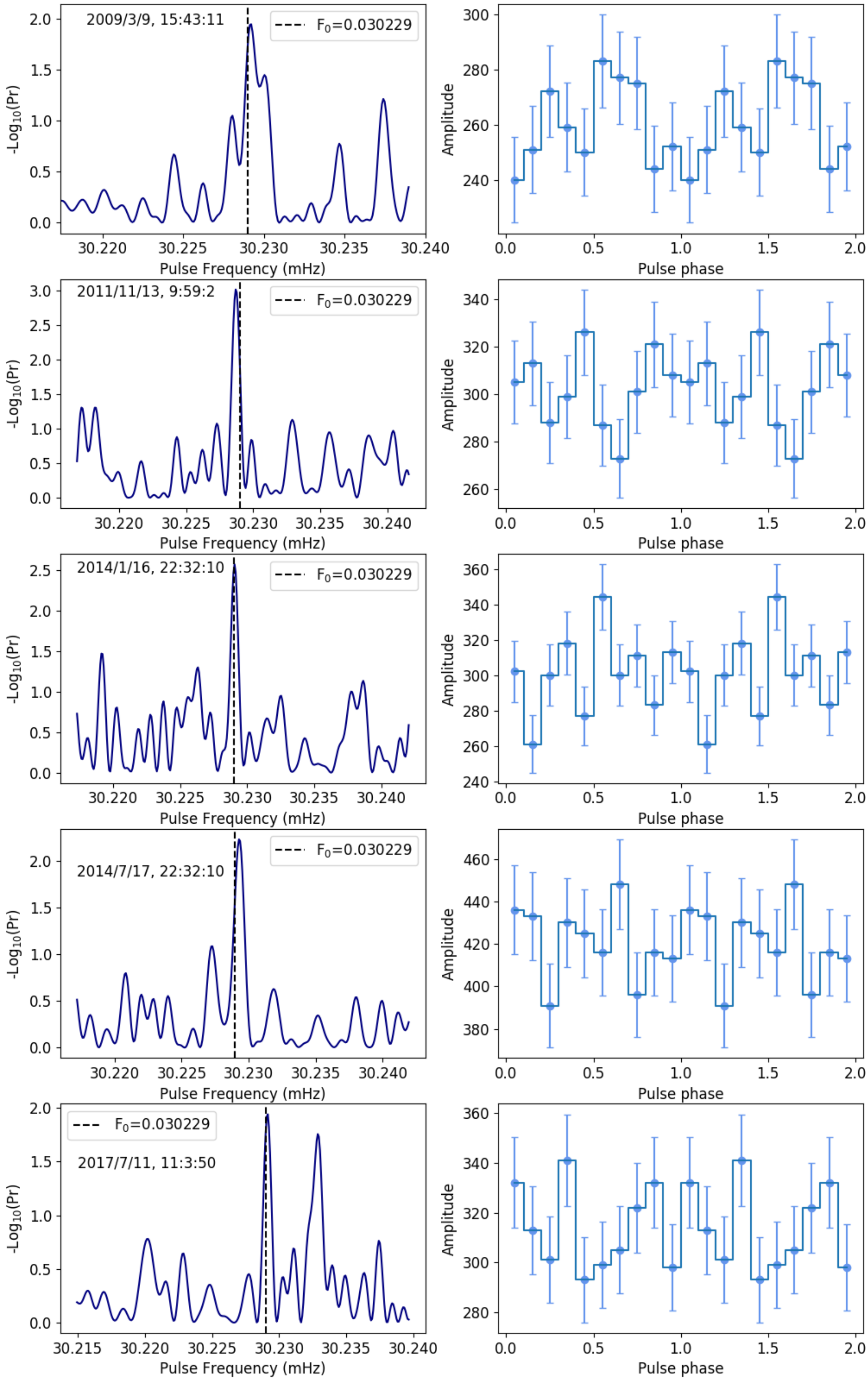

Figure 5.9: Pulsed power spectrum (left panel) and the phase distribution (right panel) of the 33 s pulse with respect to the ephemeris for periods with significance above 2 σ.

5.4.3 Detection of gamma-ray emission from AE Aqr

In the previous section, indications of positive detection have manifested in some of the 14-day width time bins, and the Rayleigh test results in those sections support the idea of classifying AE Aqr as a low-level pulsed gamma−ray source, since there was some indication of emission modulated at or near the rotational period of the white dwarf in AE Aqr. It is difficult to detect AE Aqr with a smaller telescope such as the Fermi-LAT since AE Aqr is a transient source. However, the advantage with the Fermi telescope is that we have a very long data baseline of about ~ 11 years, which makes it possible to detect emission from weak sources that emit sporadically at a low-level but continuously. It should be possible to get a measurable signal with a binned analysis technique if a steady source that emits at a low and steady rate over an extended period is considered. AE Aqr does not fit in this category because it emits aperiodic transient (burst-like) emission making it impossible to predict its radiation emission pattern, which complicates it tremendously. A long baseline is still an advantage if data selection processes are refined. Since the Fermi-LAT standard data selection for binned and unbinned analysis techniques yields no significant results, our guess is bad data was also considered during the analysis. We, therefore, applied a more selective filtering process for the data selection. We only selected periods with positive likelihood test statistics in the entire length of the Fermi-LAT dataset for unbinned and binned analyses. Only the data selection process was altered at this stage of the analysis, where the filtering process was performed as before but only selecting periods with positive test statistics. Binned and unbinned analyses were again performed using the same technique described in the data analysis section.

	Unbinned		Binned	
	value	error	value	error
Prefactor	1.52×10^{-11}	2.27×10^{-12}	1.62×10^{-11}	2.24×10^{-12}
Index	2.45	0.14	2.54	0.12
Scale	808.325		808.325	
Npred	2152.5		2018.7	
TS	223.916		220.162	
Flux ph/cm^2/s	1.76×10^{-8}	4.14×10^{-9}	2.97×10^{-8}	3.10×10^{-9}

Table 5.3: The statistics of gamma-ray emission presented here were measured from the data filtered using selective filtering techniques. Flux levels for the entire energy range and the whole observation period measured using the binned analysis technique complements the results obtained through the unbinned analysis. Even though there seems to be a significant difference between the predicted counts (Npred) from both techniques, the test statistics are fairly comparable.

A re-analysis of Fermi-LAT data for the past 11 years employing the data filtered employing the selective filtering technique resulted in positive detection of AE Aqr with a $\sqrt{TS} \simeq 14\ \sigma$ significance for both binned and unbinned analyses (see listed statistics in Table 5.3). As we predicted, summing up periods with positive test statistics should yield positive detection, the transient source was detected with flux levels comparable to the flux levels predicted in the literature. We firmly believe that with more constrained data filtering the results can improve. They can also improve when more data are obtained.

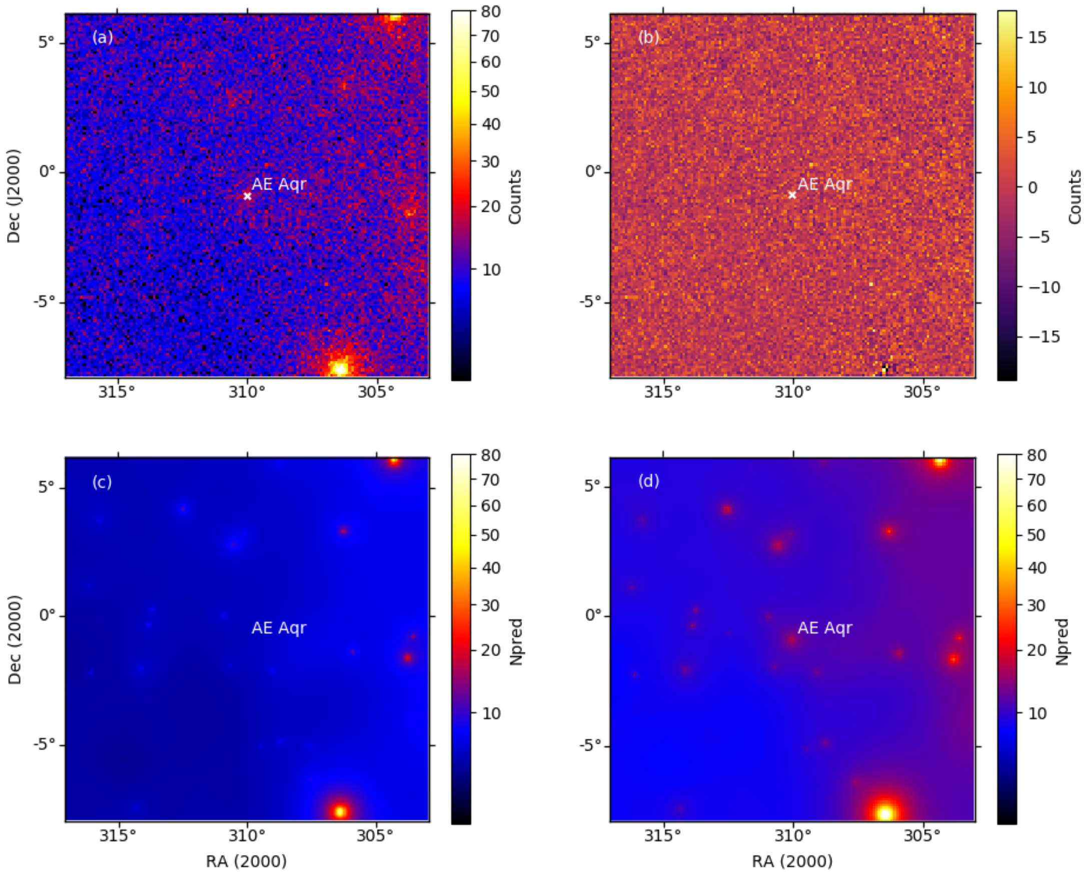

Figure 5.10: A map of counts (a) for the entire energy range and the whole observation period produced with the data filtered using the advanced techniques reveals significant counts at the location of AE Aqr. A residual map (b) is relatively flat across the entire region of interest, implying a good fit. The model map (c) produced from the data filtered using the standard techniques shows no indication of a point-like source at the location of AE Aqr. In contrast, the model map (d) produced from the data filtered with advanced techniques exhibits a point-like feature at the location of AE Aqr.

The binned analysis is usually accompanied by the model map and its residual map generated from the counts map and model map (see Figure 5.10). A counts map produced from good data of good time intervals revealed indications of possible emissions at the location of AE Aqr. Good data in this scenario are data that were found to have a positive gamma-ray excess. The model map is a map that shows all the sources included in the final fit and the predicted counts for each source. The model map produced earlier did not reveal any gamma-ray excess at the region of AE Aqr. Comparing the model map produced from the data filtered using the standard way to the model map produced from the data filtered using the selective method shows a considerable difference. The newly generated model map shows a point-like source at the location of AE Aqr, and the residual map is flat across the whole map, implying a good fit. In this case, the model map and the residual map reveal that the model closely resembles the observed data.

The significance of the detection of AE Aqr was further reviewed through diagnostic plots, the residual, and the TS maps (see Figure 5.11). The maps of the ROI generated through unbinned and binned analyses for the entire energy range using newly selected data strengthen the results obtained from both analyses. The residual map

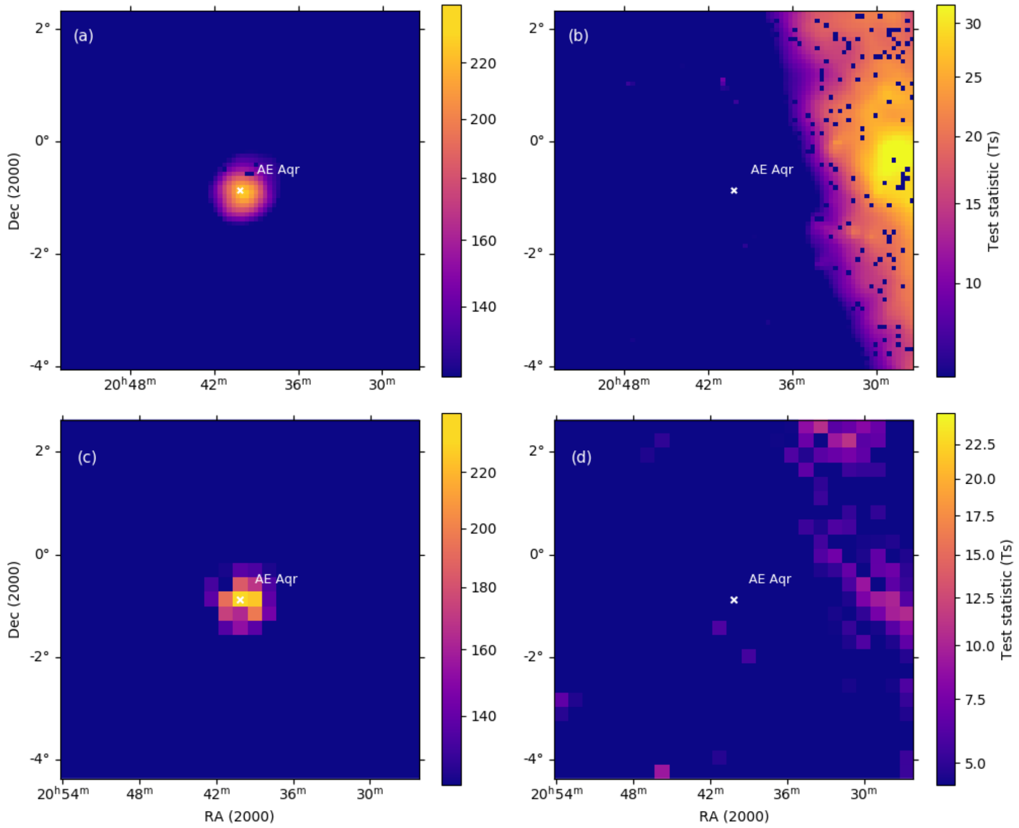

Figure 5.11: The diagnostic maps presented here are generated from the data filtered using the refined technique. The TS map (a) binned and (c) unbinned is produced with AE Aqr intentionally left out from the model to check whether a point-like feature will appear at the region of AE Aqr. Normatively, the residual maps both binned (b) and unbinned (d) are supposed to have no excess emission if all ROI significant sources and the background emission are correctly modelled.

shows traces of excess gamma-rays, which resemble gamma-rays from background emission. The residual map does not show any point-like source excess emission, implying that no source was accidentally omitted from both analyses. The map generated without the model of AE Aqr exhibits a point-like source at the location of AE Aqr. The excess emission of gamma-rays at the location of AE Aqr has a TS value that corresponds well with the value obtained from both analyses.

The analysis was extended to investigate the nature of the newly measured higher energy emission. The investigation was conducted through measurements of flux and significance of each energy bin to quantitatively and qualitatively compare the contribution and significance of each energy bin. Figure 5.12 show plots of measured fluxes and their statistical significance indicated as TS values for both binned and unbinned analyses. The entire energy range was divided into ten logarithmic energy bins to search for the contribution of each energy bin. Both binned and unbinned analyses reveal that the measured significance comes from the energy range between 0.1-10 GeV, with the greatest significance measured at energy bins above 1 GeV. In both binned and unbinned, some energy bins have significance in excess of 5 σ. The threshold for detection for each energy bin was set at $\sqrt{TS} = 2\ \sigma$. All energy bins with the measurable excess gamma-rays from binned analysis resulted as flux points with two energy bins above 0.7 GeV having 5 σ detection (see Table 5.5). The best fit of the binned spectral flux points above 2 σ is a power law with a photon

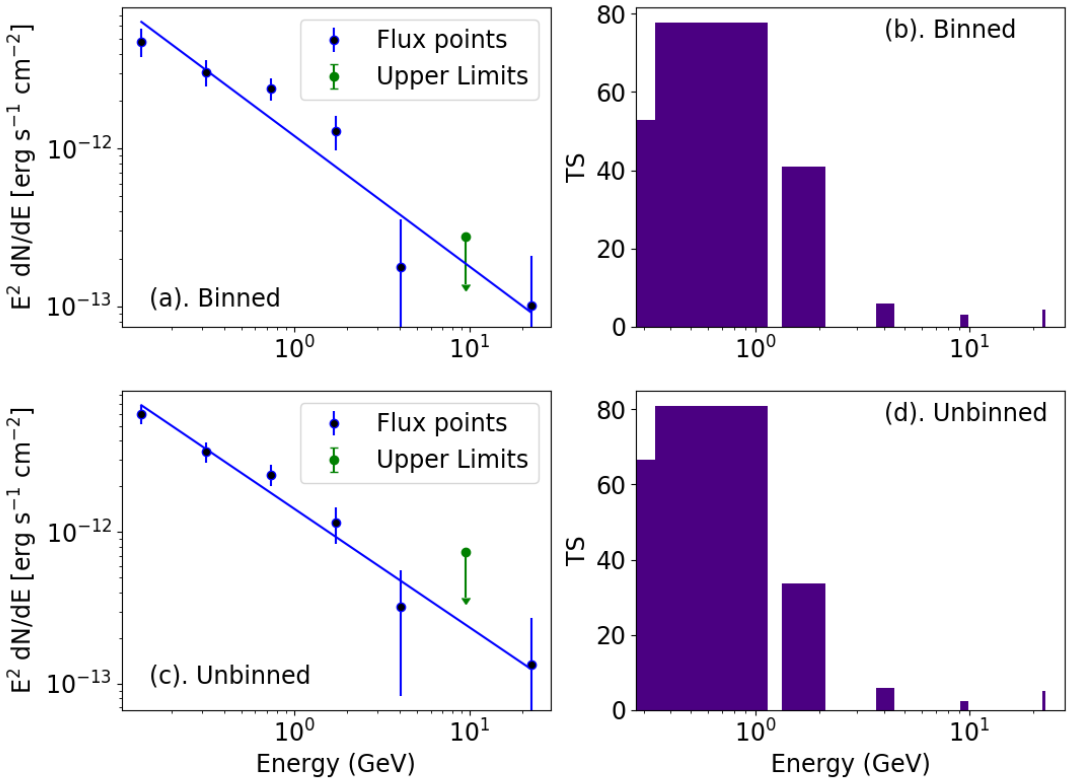

Figure 5.12: The spectral energy distribution plots for the energy range 0.1−500 GeV and the entire observation period (more than a decade), where (a) is generated through binned analysis from the data filtered using the refined filtering techniques, and (c) is an unbinned analysis result. The corresponding significance distributed as a function of energy for each energy bin with measurable signal (b) binned and (d) unbinned reveals that AE Aqr emits more significant emission (e.g., above 5 σ) in energy bins between 1-5 GeV.

index $\Gamma = 1.93$. Four of seven energy bins with measurable signal from unbinned analysis were considered significant, with a single energy bin above 1 GeV having its significance in excess of 6 σ (see Table 5.4). These four flux points could be modelled with a power law model with a spectral index $\Gamma \sim 2.034$

Energy	dN/dE	dN/dE$_{Error}$	E^{2}dN/dE	E^{2}dN/dE$_{Error}$	TS
GeV	ph / (cm2 GeV s)		erg / (cm2 s)		
0.13	2.05×10^{-07}	2.92×10^{-08}	5.98×10^{-12}	8.52×10^{-13}	55.7
0.32	2.11×10^{-08}	3.23×10^{-09}	3.39×10^{-12}	5.17×10^{-13}	66.7
0.74	2.72×10^{-09}	4.25×10^{-10}	2.20×10^{-12}	3.74×10^{-13}	80.9
1.74	2.38×10^{-10}	6.40×10^{-11}	1.15×10^{-12}	3.09×10^{-13}	33.7
4.07	1.21×10^{-11}	8.92×10^{-12}	3.20×10^{-13}	2.37×10^{-13}	5.86
9.54	5.05×10^{-12}		7.36×10^{-13}		2.35
22.4	1.67×10^{-13}	1.71×10^{-13}	1.34×10^{-13}	1.37×10^{-13}	5.00

Table 5.4: Periods with significance greater than average for the entire dataset were merged and an unbinned analysis was conducted. Ten energy bins for the entire energy range were used to produce the spectral points. Energy bins with TS greater than 4 were considered as spectral points. Photon flux and energy flux was calculated for each energy bin.

Energy	dN/dE	dN/dE_{Error}	E^2dN/dE	E^2dN/dE_{Error}	TS
GeV	ph / (cm2 GeV s)		erg / (cm2 s)		
0.13	1.64×10^{-07}	3.41×10^{-08}	4.77×10^{-12}	9.96×10^{-13}	35.79
0.32	1.91×10^{-08}	3.61×10^{-09}	3.06×10^{-12}	5.78×10^{-13}	52.95
0.74	2.74×10^{-09}	4.42×10^{-10}	2.41×10^{-12}	3.89×10^{-13}	77.74
1.73	2.67×10^{-10}	6.65×10^{-11}	1.29×10^{-12}	3.21×10^{-13}	40.90
4.07	6.63×10^{-12}	6.84×10^{-12}	1.76×10^{-13}	1.82×10^{-13}	6.043
9.53	1.90×10^{-12}		2.77×10^{-13}		3.232
22.4	1.25×10^{-13}	1.34×10^{-13}	1.01×10^{-13}	1.07×10^{-13}	4.487

Table 5.5: Periods with significance greater than average for the entire dataset were selected and merged to conduct binned analysis. Ten energy bins for the entire energy range were used to produce the spectral points. Energy bins with TS greater than 4 were considered as spectral points. Photon flux and energy flux was calculated for each energy bin.

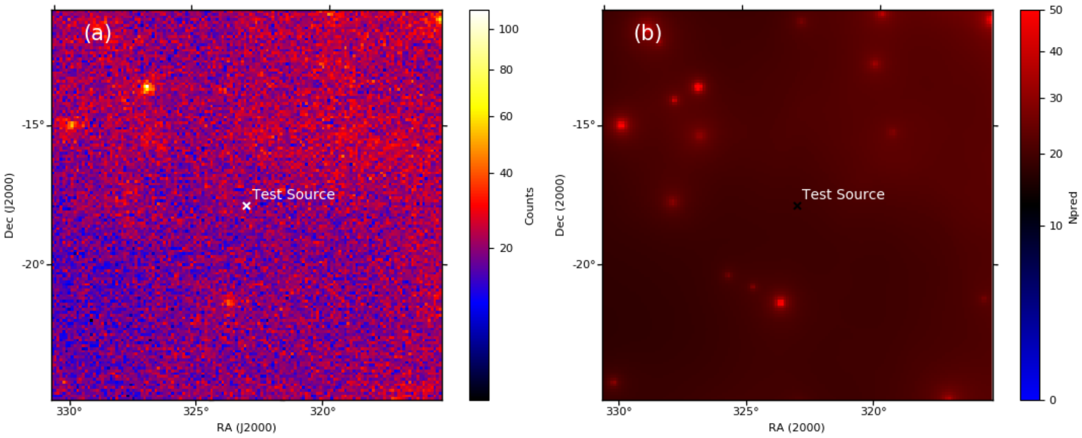

Figure 5.13: The counts map of the test source display a high background emission and at the coordinates of the test source no gamma-ray excess have been revealed on the model map.

5.4.4 Testing the selective (refined) filtering technique on a test source

The refined filtering technique was tested by placing a fictitious point source at coordinates RA = 323° and DEC = -18° ($\sim$ 20°). The location is selected because it is free of any detected gamma-ray source, and is far from influence of gamma-ray activities involved at the location of AE Aqr. The method and procedures applied on AE Aqr were also applied at the test source. The light curve produced from the point source had sections with TS values more than that obtained on AE Aqr's light curve. At this point one could have concluded that the gamma-ray emission measured for AE Aqr is just background gamma-ray emission. The doubts were cleared after running binned likelihood tests using the advanced filtered data which resulted in no detection of any excess gamma-rays above the background emission. The highest test statistics measured for the test source using binned likelihood technique was 0.1.

The counts map produced for the test source show that most of the emission in the region is dominated by the background emission. At the coordinates of the test source the emission was flat like other areas dominated by background emission. The region of the test source and the region of AE Aqr resemble each other when applying the standard way of filtering, but there is a difference after applying

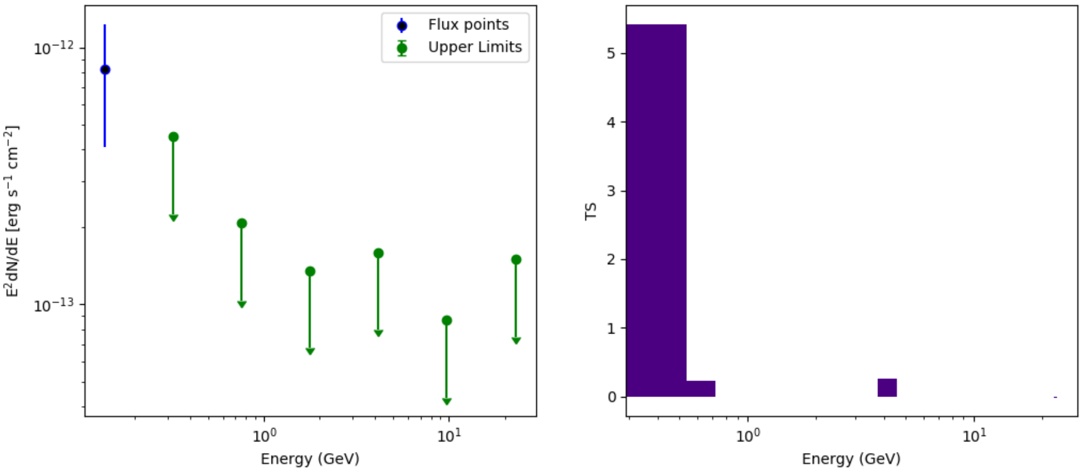

Figure 5.14: SED analysis of the test source only resulted in upper with the highest possible emission at the lowest energy bin.

the refined filtering technique on the data. The model map generated exhibited no gamma-ray predicted counts at the location of the test source (see Figure 5.13). The TS map produced was just like the residual map without any excess emission at the location of the test source. The spectral analysis revealed that there is no gamma-ray source at the test source position except background emission (see Figure 5.14). The results obtained for the test source strengthen the credibility of the method used to detect gamma-ray emission from the nova-like AE Aqr.

5.4.5 Detection of pulsed gamma-ray emission from AE Aqr

The system did not reveal any excess emission above the background emission when standard techniques for binned and unbinned analyses were conducted on the Fermi-LAT pass 8 data centred on AE Aqr. However seeing that selected 14-day data bins revealed pulsed gamma-ray emission at or near the rotational period, motivated us to look for other alternatives to search for emission, since the assumption was that AE Aqr's long term cumulative flux levels are lower than the background emission. There are however, indications that the system might emit short burst-like pulsed emission intermittently. The refined filtering technique was applied to the Fermi-LAT data to search for stronger transient gamma-ray emission. Subsequently, transient gamma-ray emission from the nova-like AE Aqr was detected with both unbinned and binned analysis techniques. The detection of gamma-ray emission led to a deeper search for pulsed emission. Now the entire observation period was used to search for pulsed gamma-ray emission including the periods that did not have positive likelihood test statistics. The events data files were split into smaller data sections, i.e., 3 minutes, 5 minutes, and 10 minutes data sections, before applying the good time intervals and periodic search process. As stated, the underlying idea is that the source has revealed very short rapid flares in optical wavebands and signatures of gamma-rays reported in the early 90s that followed similar characteristics. Therefore, by following the same analogy a search for pulsed gamma-ray emission might be revealed.

The search for pulsed emission from the Fermi-LAT pass 8 dataset using the Rayleigh test from the Fermi Science Tools software packages (v10r0p5) revealed 10 minutes

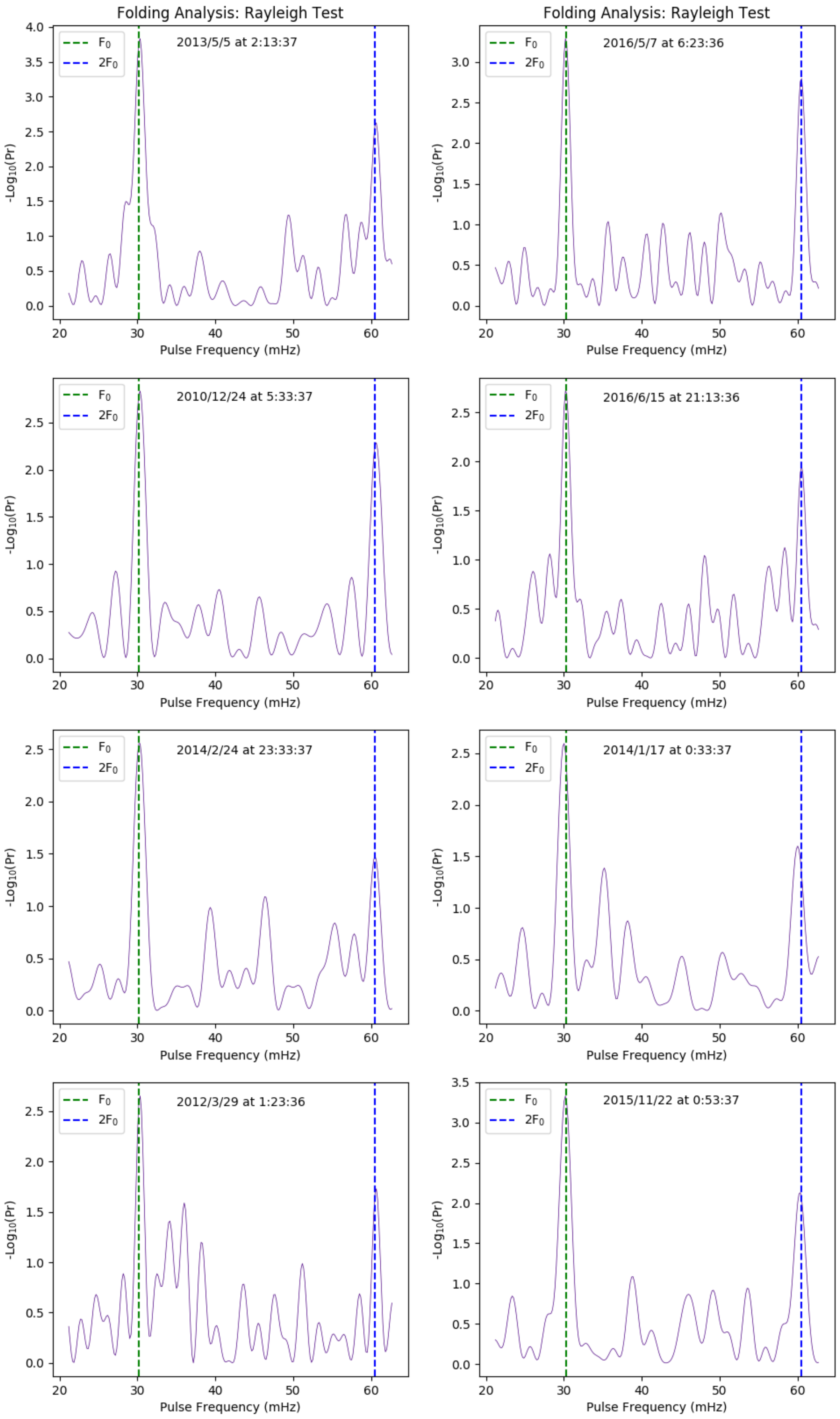

Figure 5.15: The pulse profiles of AE Aqr showing the pulses at or near the fundamental frequency and the first harmonic.

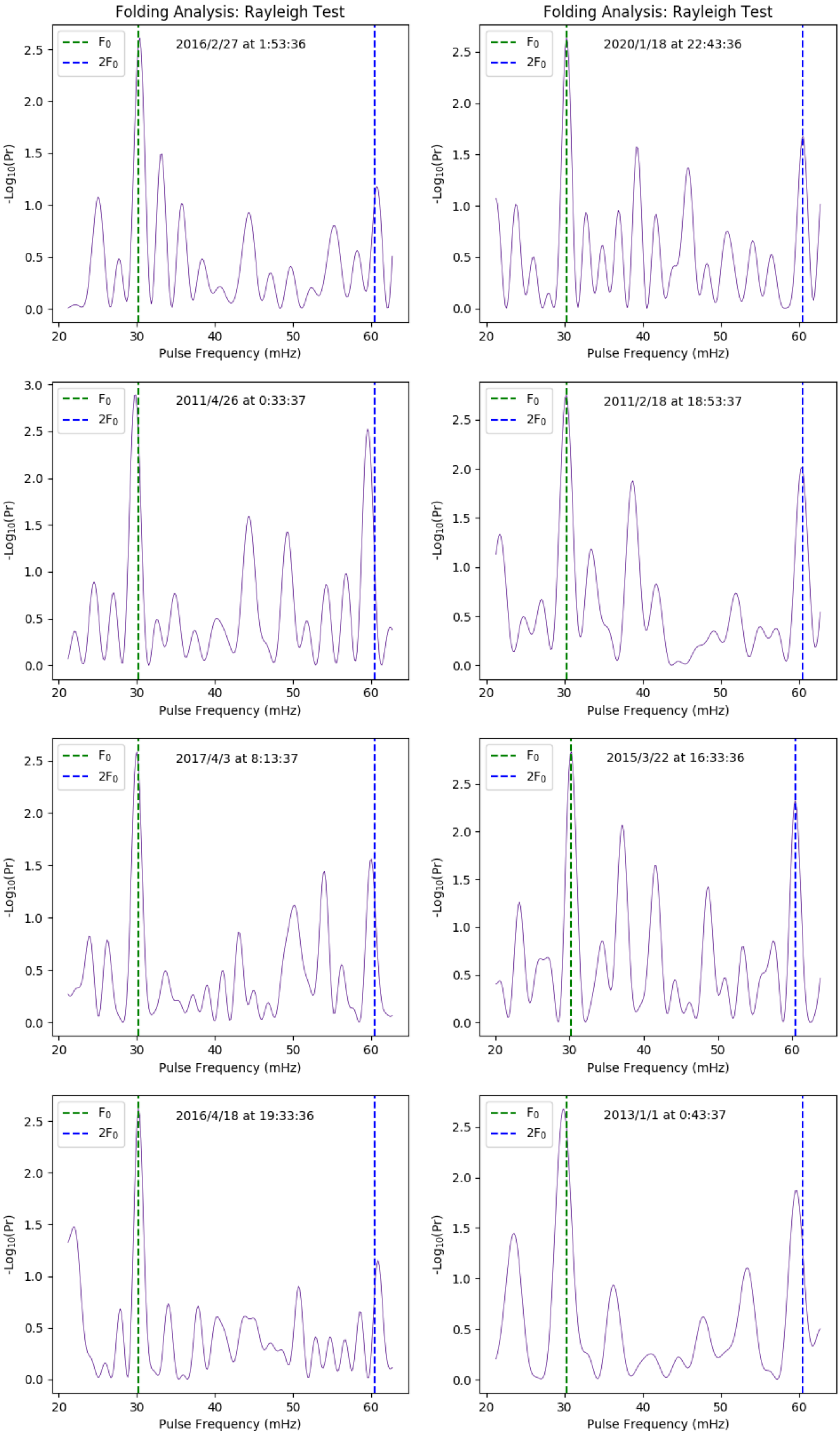

Figure 5.16: The pulse profiles of AE Aqr showing the pulses at or near the fundamental frequency and the first harmonic.

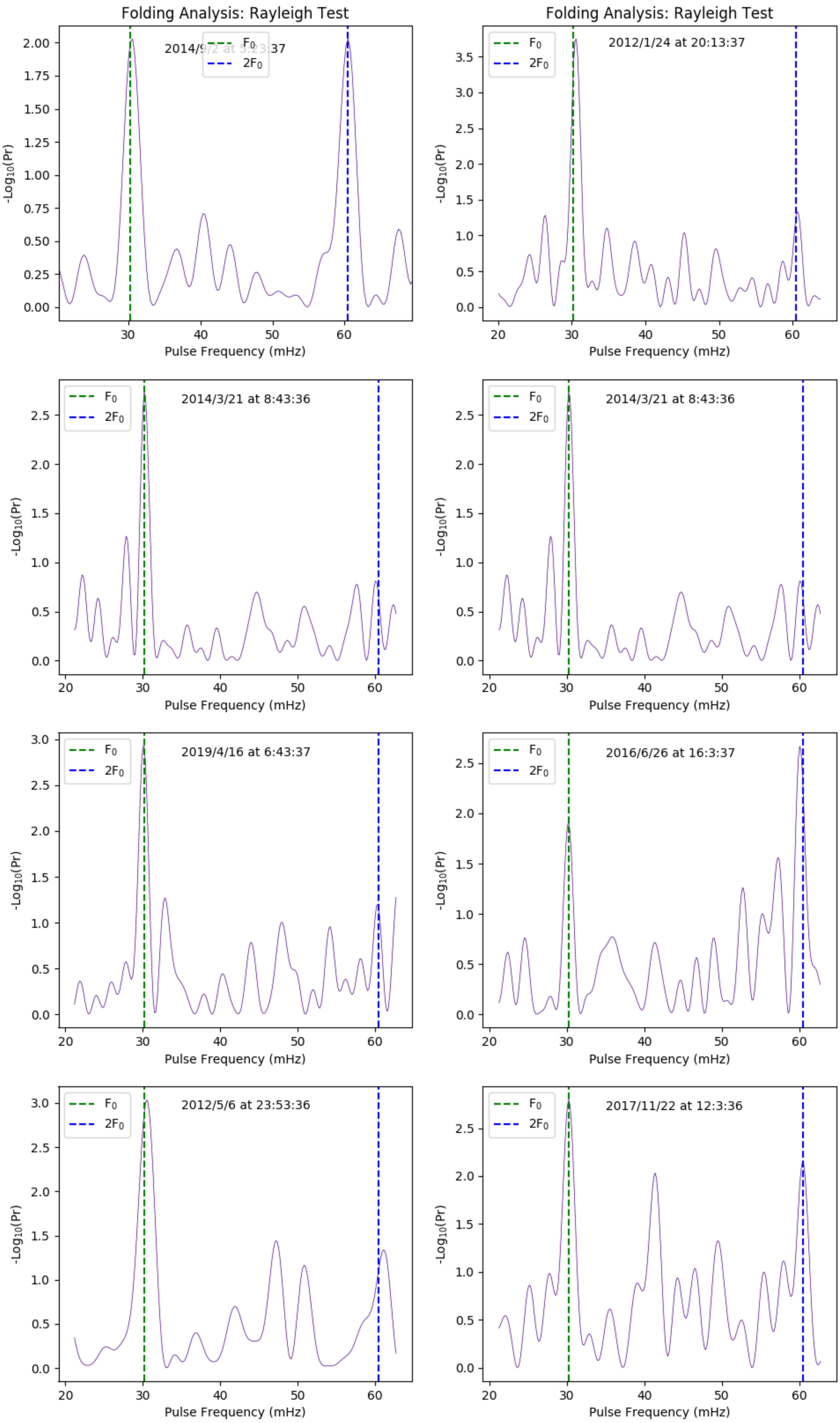

Figure 5.17: The pulse profiles of AE Aqr showing the pulses at or near the fundamental frequency and the first harmonic.

time bins displaying pulsed emission at both the fundamental frequency and the first harmonic. The evidence of pulsed emission is presented in this section (see Figure 5.15 to 5.17). The search was performed using 3 minutes, 5 minutes and 10 minutes data sections but the results presented in this section are from the 10 minutes data sections. Photons considered for analysis are collected within a radius of 10 degrees from AE Aqr to account for the PSF. The standard way requires that the radius be small, but this has the consequence of losing a greater percentage of photons, especially if the source in question is a weak gamma-ray source.

Nonetheless, the expectation was to find strong periodic signal evidence in three and five minutes data sections, however, strong signals at both the fundamental and the first harmonic are more defined in the 10 minutes data sections. The highest Rayleigh power obtained from the 10 minutes data section is $2nR^2 = 17.56$, which correspond to a chance probability of $\sim 10^{-4}$. The technique was tested for technical errors by running the same process on the test source a distant away from AE Aqr. The test source used is a fictitious point-like source or a real gamma-ray point-like source at 2 degrees, 3 degrees, 5 degrees, 8 degrees, 10 degrees and 15 degrees away from AE Aqr. Thus, the periodicity of photons within 15 degrees of AE Aqr was investigated using a point-like source at various positions away from AE Aqr to investigate the behaviour of the measured pulsed emission. To visually inspect how the pulsed signal varies with angular distance from AE Aqr, we selected the epochs (2013/5/5 at 2:13:37), (2016/5/7 at 6:23:36), (2010/12/24 at 5:33:37) and (2016/6/15 at 21:13:36) which correspond to the first four pulse profiles in Figure 5.15, and we conducted the Rayleigh test at different angular distances to produce pulse profiles in Figure 5.18 and Figure 5.19. The results showed a gradual decline of -log(Pr) as the angular distance from AE Aqr increases (see Figure 5.18 and 5.19). This shows that choosing a 10 degrees radius was a good choice. Even though the Rayleigh power at 8 degrees has significantly decreased there is still pulsed emission signature at a low-level.

The search for periodicity is always associated with oversampling, thus the statistical penalties must be introduced when determining the significance of each mode of periodic emission. The concept of independent frequency spacing is imperative when searching for periodicity. Independent Fourier spacing (IFS) as defined by de Jager [167] in the period range is 1 IFS $= P^2/T$ and in the frequency range is 1 IFS $= 1/T$, where T and P represent the observation time and search period respectively. IFS is interpreted as the consecutive testing for periodicity at k frequencies or periods with inter-spacing $\geq$ 1 IFS with any test for uniformity equivalent to a periodicity search using k independent trials. The true chance probability is

$$Pr = 1 - (1 - p)^k, \tag{5.4}$$

if the smallest probability (p) is obtained for uniformity from k independent trials. This expression reduces to $Pr \sim kp$ for very small values of p, with $k = n$IFS $= T(F_2 - F_1)$, the statistical penalty for oversampling, where T is the observation period and $(F_2 - F_1)$ is the covered frequency range. The true probability after introducing a factor of 2 for oversampling is $Pr \sim 2kp$.

The technique of stacking is useful to distinguish between erroneous detection and signal. If n observations are conducted at a given frequency ν, the chance probabilities $Pr_i^\nu, i = 1, ..., n$ may be integrated incoherently [156] to get a more significant pulsed signal at the cost of phase information. The technique sums up all power

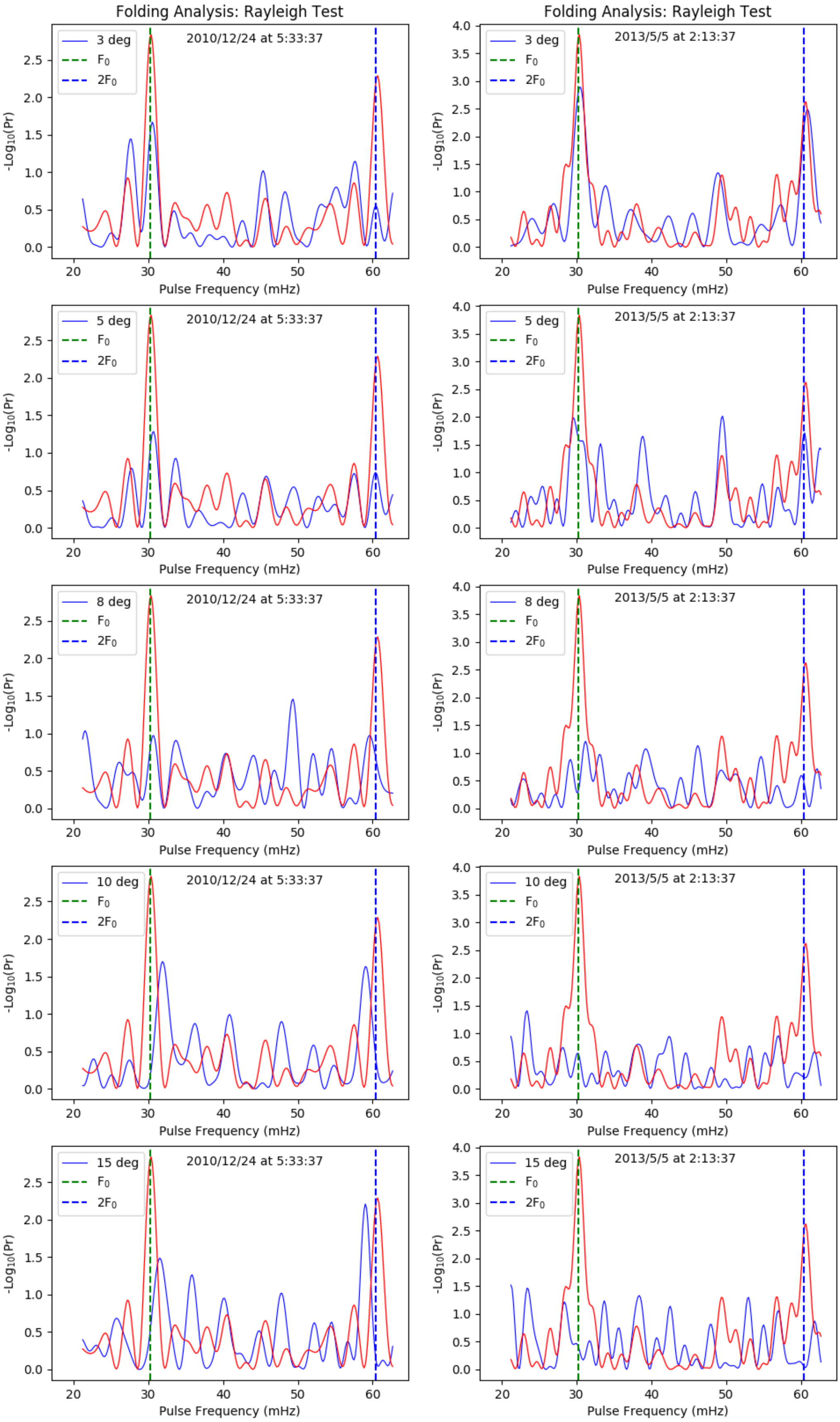

Figure 5.18: The left panel pulse profiles are produced from the epoch (2013/5/5 at 2:13:37), where the red pulse profile is for AE Aqr and the blue pulse profile represent a test source at different radii. The right panel are pulse profiles produced from the epoch (2016/5/7 at 6:23:36). The results show a gradual reduction in power for the test source relative to distance.

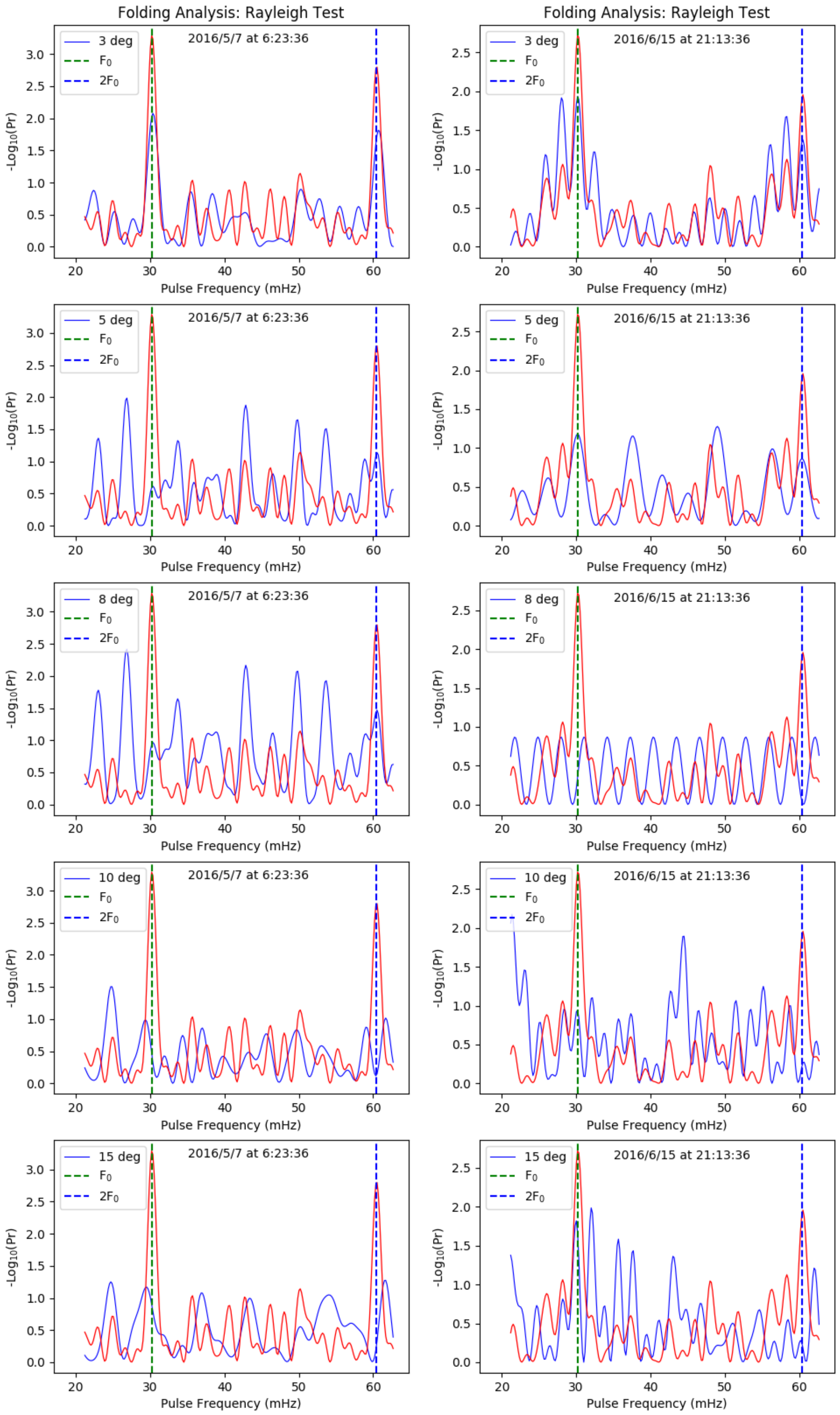

Figure 5.19: The left panel pulse profiles are produced from the epoch (2010/12/24 at 5:33:37), where the red pulse profile is for AE Aqr and the blue pulse profile represent a test source at different radii. The right panel are pulse profiles produced from the epoch (2016/6/15 at 21:13:36). The results show a gradual reduction in power for the test source relative to distance.

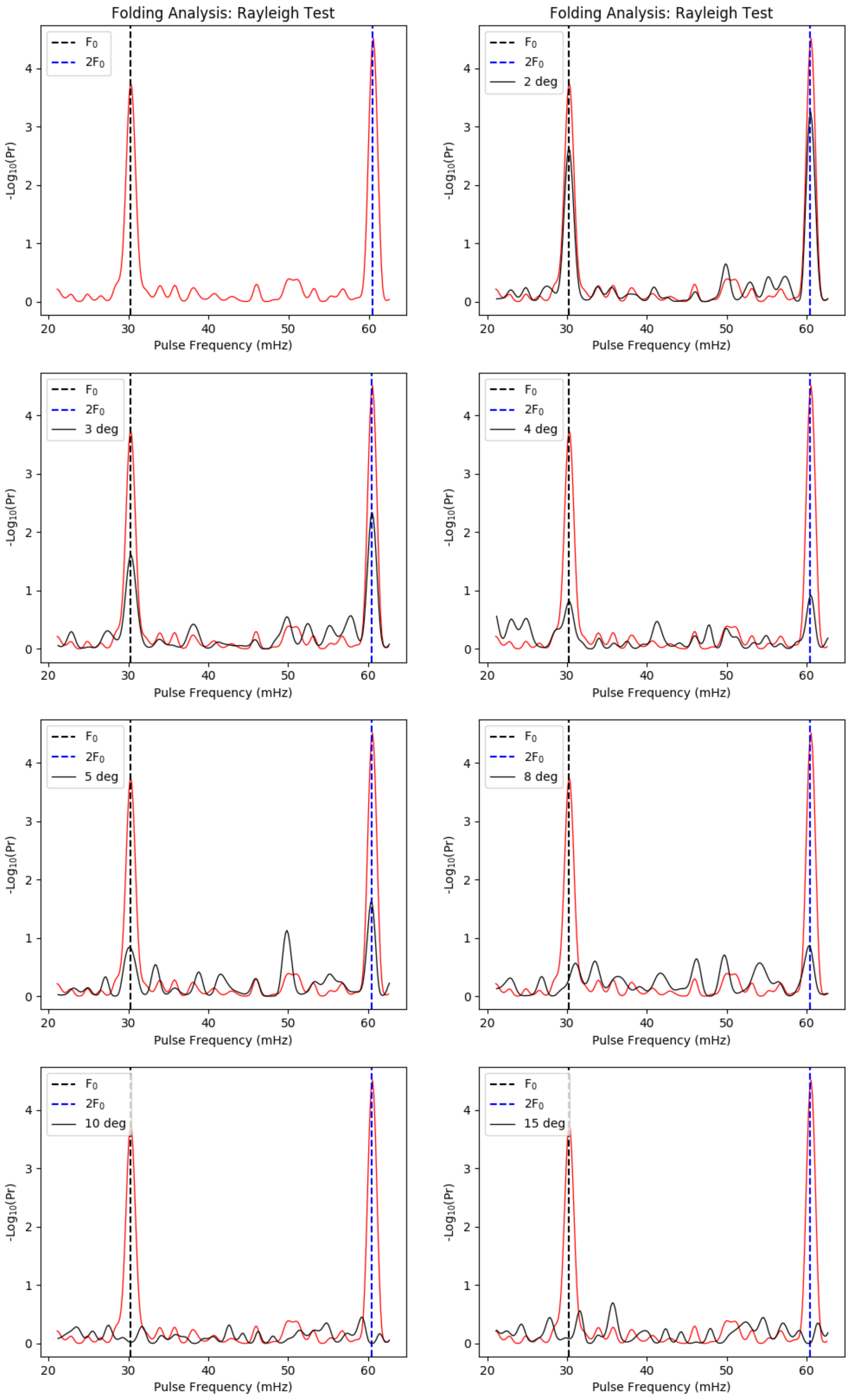

Figure 5.20: The stacked Rayleigh test pulse profiles of AE Aqr showing the pulses at or near the fundamental frequency and the first harmonic. The plot also includes stacked Rayleigh test power results for the test source placed at different radii, which manifest a gradual decline with increasing angular distance.

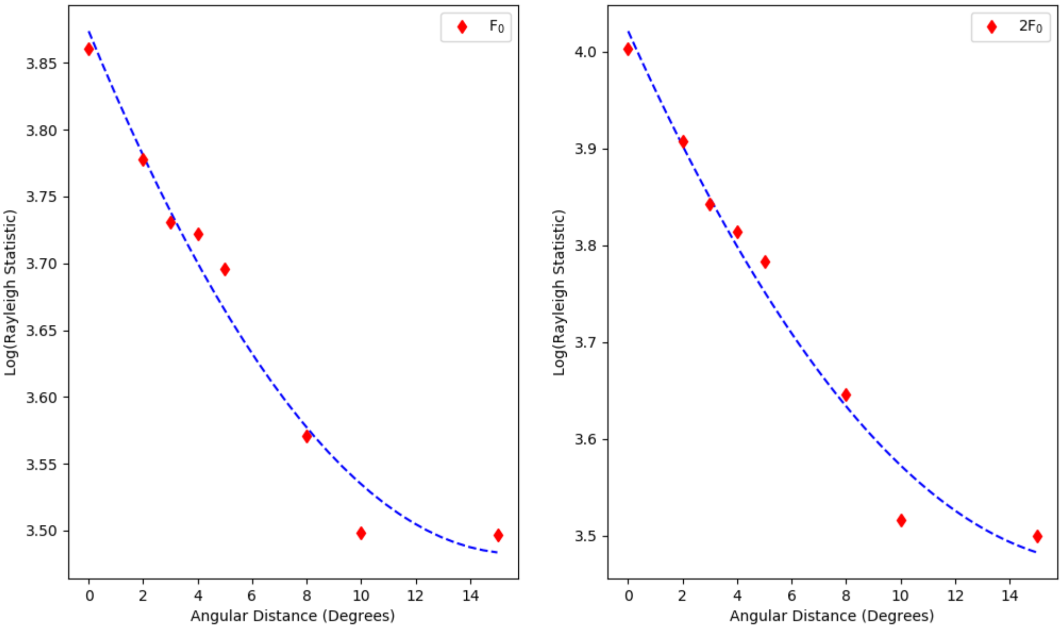

Figure 5.21: The Rayleigh Statistic as function of angular distance reveal a gradual decline.

with same frequencies, to obtain a statistic which follows a χ^2 distribution with $2n$ degrees of freedom in the absence of a signal. The chance probability of the final power spectrum is calculated from the equation of the χ^2 distribution,

$$\chi^2_{2n}(\nu) = -2\sum_{i=1}^{n} ln(Pr_i^{\nu}). \tag{5.5}$$

The technique assumes that each observation consists of a weak signal that contributes to a more significant detection. Therefore, observations with significance that can result in the improvement of the overall significance should be used. Therefore, all Rayleigh power spectra with Rayleigh power $2nR^2 > 13.9$ (>3 σ) at either the fundamental frequency or the first harmonic for the entire mission were stacked together to produce a more significant power spectrum (see Figure 5.20). Equal weight was allocated to each selected power spectrum and the statistical penalty Equation 5.4 to the probability of $\chi^2_{2n}(\nu)$ distribution. The stacked power spectrum for AE Aqr and the stacked power spectrum of test point sources positioned at 2 degrees, 3 degrees, 4 degrees, 5 degrees, 8 degrees, 10, degrees, and 15 degrees were plotted together to compare the signal strength.

The Rayleigh statistic at both the fundamental (33.08 s) and the first harmonic (16.54 s) that result after conducting the Rayleigh test when AE Aqr is at the centre and when the centre is shifted to various positions were plotted as a function of angular distance (see Figure 5.21). The Rayleigh statistic of the stacked spectra in Figure 5.20 were used to analyse how Rayleigh power is related to the angular distance. The results confirm that the signal strength of the pulsed emission at both 33.08 s and 16.54 s is centred at the coordinates of AE Aqr.

While there are several methods to investigate white noise structure on pulse profile data, we plotted log(dN/dZ) as a function of the Rayleigh statistic (Z). The white noise in the data follows an inverse linear trend, while points that do not follow the

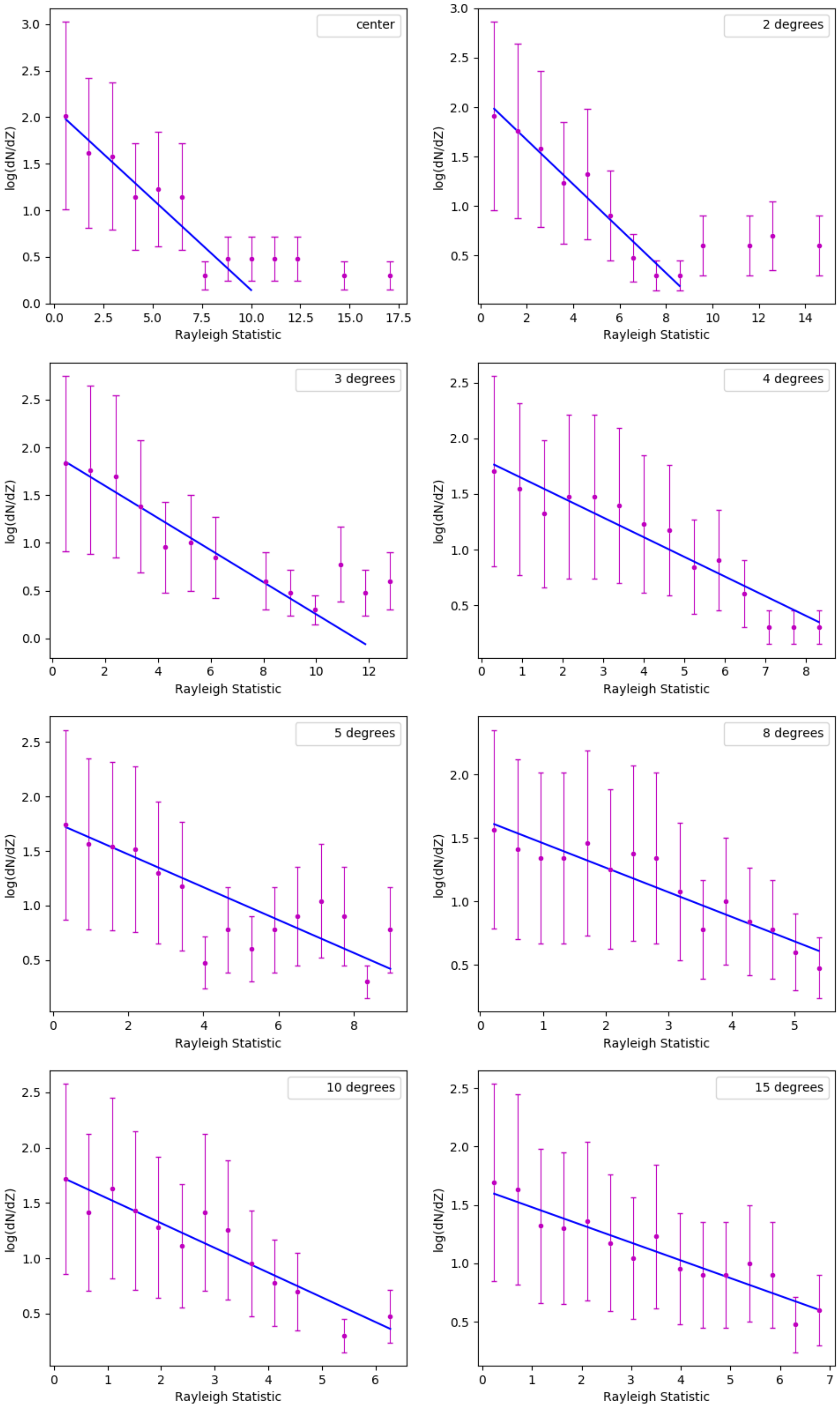

Figure 5.22: The noise distribution is represented by the straight line and Z is the Rayleigh statistic. The first top plot on the left panel is the noise distribution produced from the spectrum of AE Aqr followed by other noise distribution at various angular distance. The white noise plot for AE Aqr has more points that deviates from the inverse linear distribution.

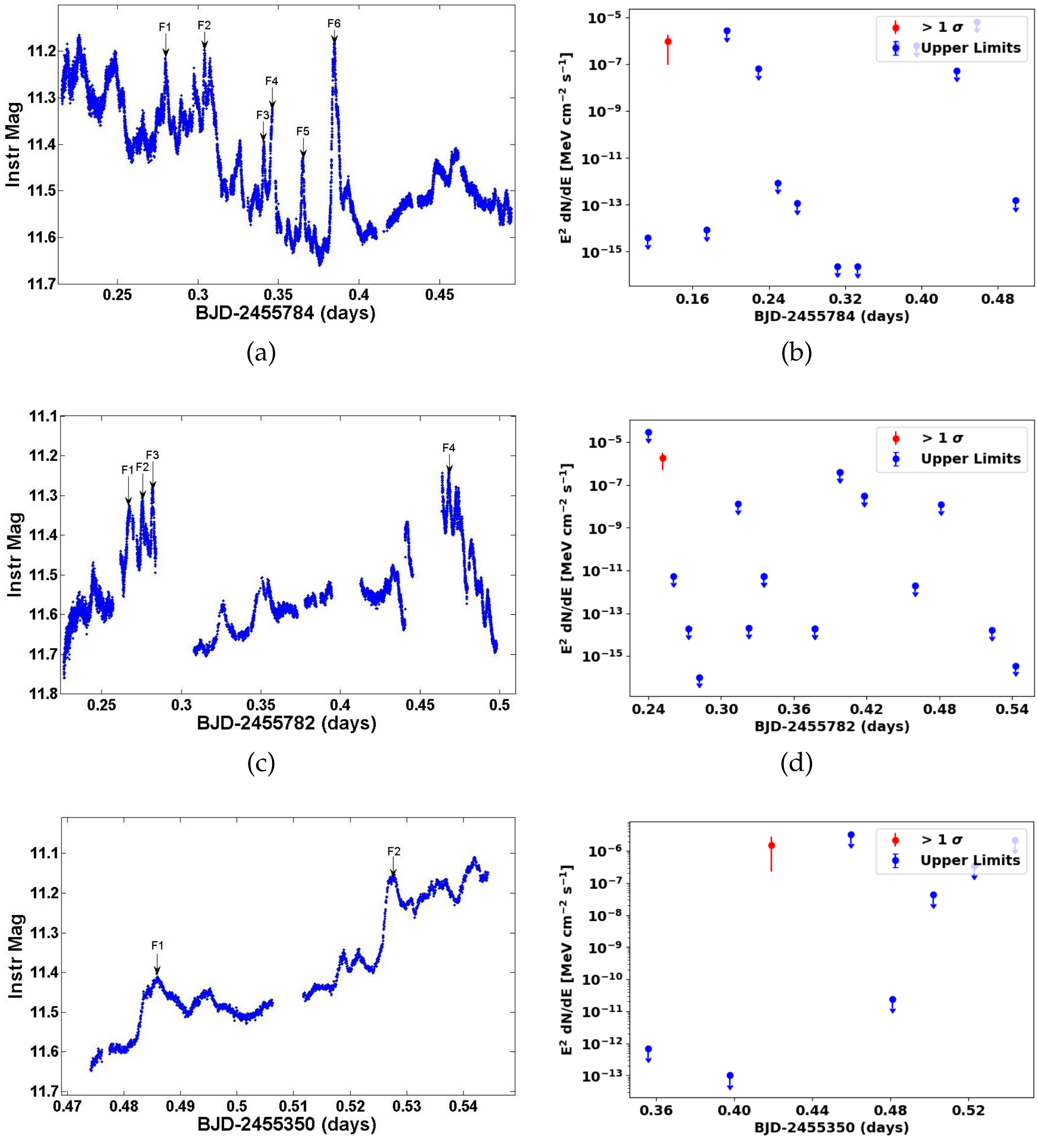

(a) (b)

(c) (d)

(e) (f)

Figure 5.23: Some of the optical light curves (a), (c), and (e) observed by Van Heerden [16] used to search for the counterpart in VHE gamma-rays. The corresponding light curves (b), (d), and (f) from the Fermi-LAT data revealed possible time stamps that correlate with the optical flares when the source emits pulsed gamma-rays. These gamma-ray light curves revealed good convergence at periods just before a huge flare and some of these periods correspond to a power spectrum that exhibit pulsations at or close to the rotational frequency and the first harmonic. Panel (b) corresponds to 2011/8/10 power spectra and panels (d) & (f) correspond to 2011/8/8 and 2010/6/2 respectively.

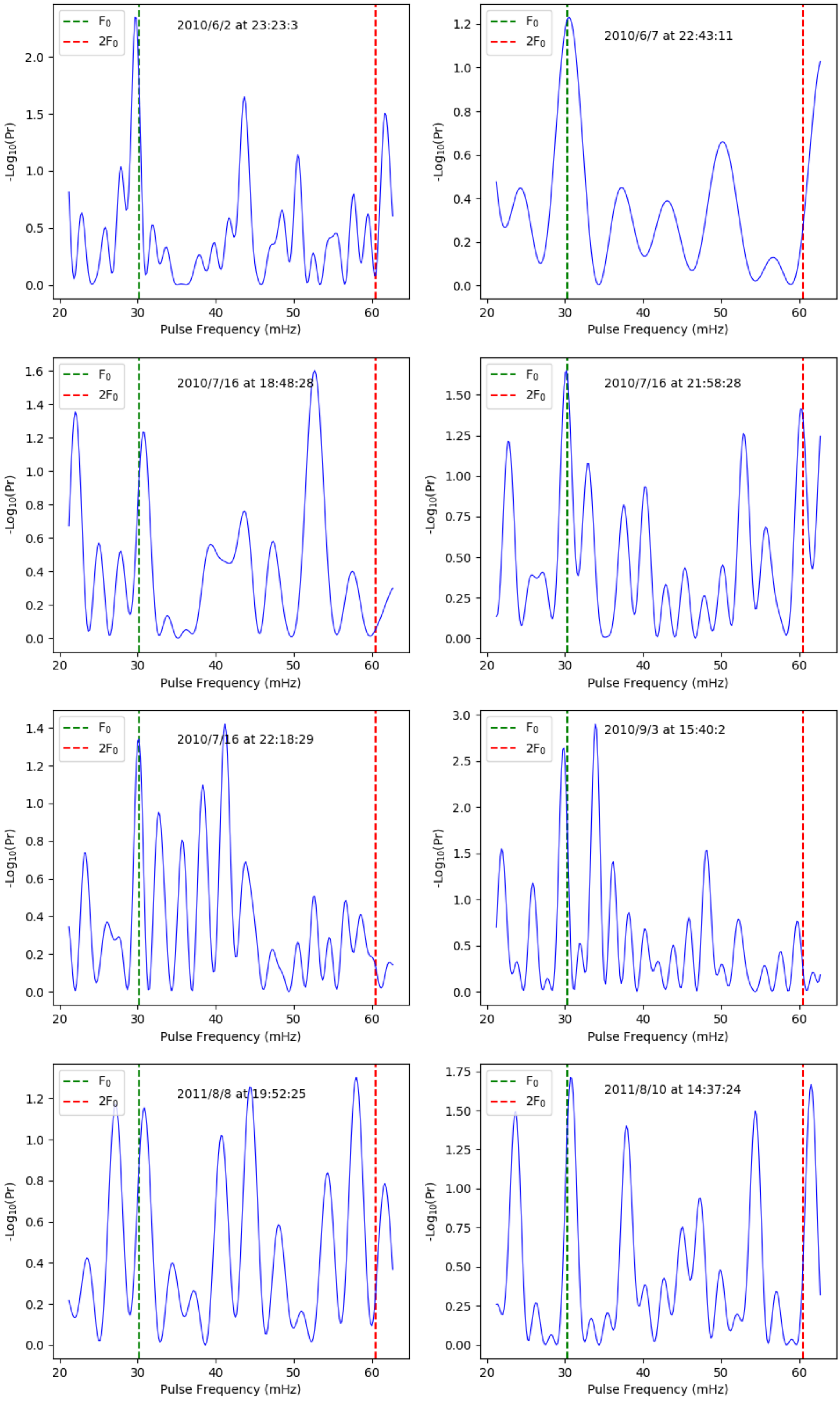

Figure 5.24: The pulse profiles of AE Aqr produced by the Rayleigh test folding analysis technique from the Fermi data that coincide with optical light curves [16] revealed pulses at or near the fundamental frequency and the first harmonic.

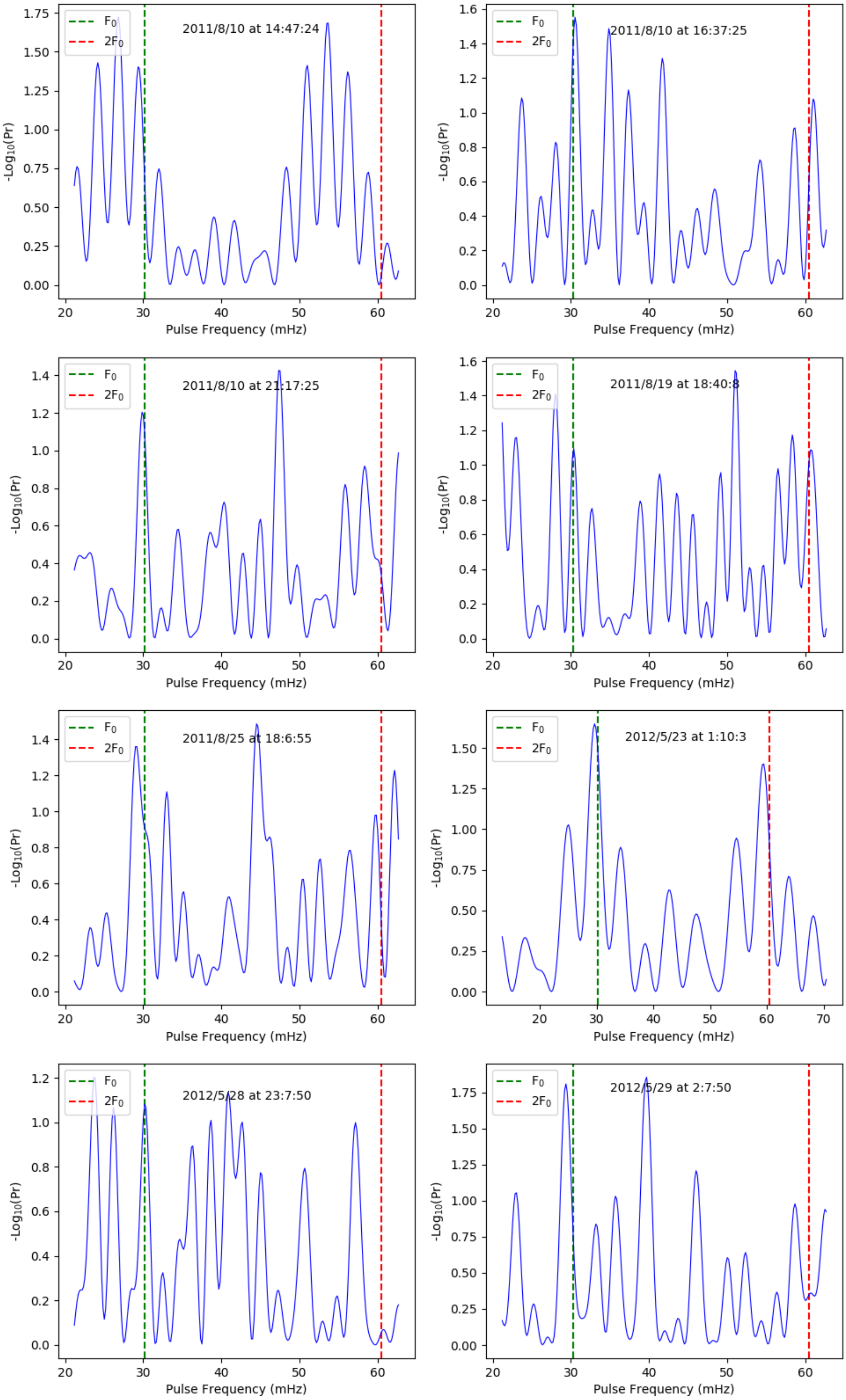
2011/8/10 at 14:47:24

2011/8/10 at 16:37:25

2011/8/10 at 21:17:25

2011/8/19 at 18:40:8

2011/8/25 at 18:6:55

2012/5/23 at 1:10:3

2012/5/28 at 23:7:50

2012/5/29 at 2:7:50

Figure 5.25: The pulse profiles of AE Aqr produced by the Rayleigh test folding analysis technique from the Fermi data that coincide with optical light curves [16] revealed pulses at or near the fundamental frequency and the first harmonic.

Observation date	Fundamental period (P)	First harmonic period (P_2)
2013/5/5 at 2:13:37	32.94	16.52
2016/5/7 at 6:23:36	33.12	16.52
2010/12/24 at 5:33:37	32.94	16.52
2016/6/15 at 21:13:36	33.12	16.52
2014/2/24 at 23:33:37	33.12	16.52
2014/1/17 at 0:33:37	33.31	16.66
2012/3/29 at 1:23:36	32.94	16.52
2015/11/22 at 0:53:37	33.13	16.57

Table 5.6: The periodic of gamma-ray pulse period, P the fundaments period and P_2 the first period for dates that corresponds to power spectra in Figure 5.15

trend will imply the data's pulse signal presence. We construct the noise distribution from the stacked spectrum centred at AE Aqr and various angular distances to visually investigate how the noise distribution varies with angular distance from AE Aqr. For the spectra used at this stage, refer to Figure 5.20. The white noise distribution graphs confirm that the pulsed gamma-ray emission is centred at the coordinates of AE Aqr since Figure 5.22 reveals that the pulsed signal vanishes as the angular distance increases from AE Aqr. The noise distribution plot produced for the spectrum at the centre has more points that deviate from the trend line than the noise distribution plot from spectra, e.g., 2 degrees away from the centre.

The periods of the periodic gamma-ray emission were measured from the power spectra in Figure 5.15. These measured periods are presented in Table 5.6 are close to the fundamental (33.08 s) and first harmonic (16.54 s) periods but slightly red-shifted (e.g., [6]). However, the average value calculated for the fundamental period is 33.08 ± 0.05 s and the first harmonic average is 16.54 ± 0.02 s. These values match with periods of the optical emission presented by Patterson [5].

One of the final analysis processes was to compare optical characteristics with corresponding gamma-ray events. Some of the optical observations [16] that were conducted on AE Aqr since the Fermi-LAT mission started were therefore used to search for coincident pulsed gamma-rays. Fermi gamma-ray data sections that coincide with the optical observation were selected such that the length of each dataset overlaps the length of each optical flare since burst-like gamma-ray emissions might be expected at the onset or during an optical flare. An attempt to produce gamma-ray light curves with 30 mins bin size was done. Since AE Aqr is a faint source it is very difficult to produce a gamma-ray light curve. Therefore, only flux points that have significance above 1 σ were regarded as flux points, and upper limits flux were considered for the timebin with flux below 2 σ (see Figure 5.23).

To search for periodic emission on these light curves an ROI of 10 degrees was used. The search for periodic gamma-ray emission resulted in indications of gamma-ray emission from AE Aqr for some of the data sections that coincide with the optical emission (see Figure 5.24 and 5.25). Pulses at the fundamental frequency and the first harmonic are not as clear as in other periodograms presented earlier. Some of the periodic search results imply that some of gamma-ray events took place just before violent optical flares. This phenomenon was not strongly observed in most of the optical flares. The technique of stacking was again applied at the corresponding Rayleigh power spectra to reveal a possible signal at either fundamental or first

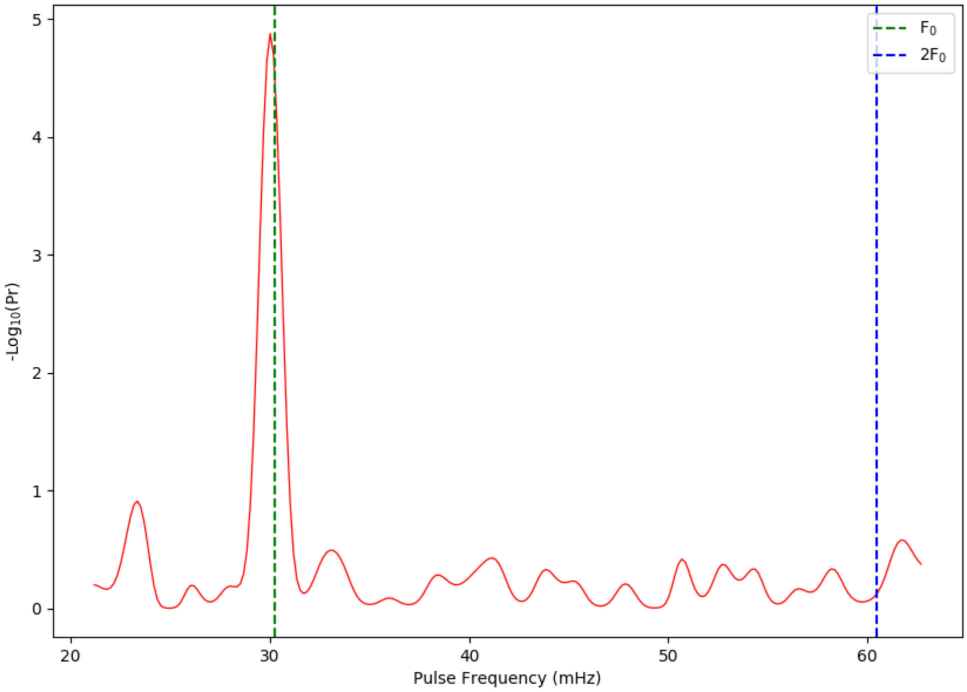

Figure 5.26: Stacked FFT's of the periods that coincides with the optical flares [15] showing a pulse near the fundamental frequency.

harmonic. The result after applying the statistical penalty Equation 5.4 to the probabilities of $\chi^2_{2n}(\nu)$ distribution revealed a strong signal at the fundamental frequency (33.08 s) (see Figure 5.26).

5.5 The updated broadband SED and discussion of results

The search for gamma-ray emission using more than a decade of data resulted in the detection of pulsed gamma-ray emission from AE Aqr. Gamma-ray emission was detected at $\sim 14\,\sigma$ through unbinned and binned analysis techniques. AE Aqr can be categorised as a low-level transient gamma-ray source. The search for gamma-ray emission at shorter periods resulted in no detection of any gamma-ray emission. However, refined filtering of the entire dataset resulted in the detection of gamma-ray emission. To detect pulsed emission one should dissect the entire dataset into smaller sections. In addition the sections that correspond to the optical light curve observed by Van Heerden [16] also imply that the gamma-ray emission from AE Aqr consists of a pulsed component.

The nature of the measured signal was further investigated to see whether the pulsed emission corresponds to burst-like events observed in the past. Sections that have more significant pulses at or near the fundamental frequency and the first harmonic were selected to run unbinned and binned likelihood analyses. It was expected that these sections would have a high corresponding TS, Npred and flux levels but the results were less compelling. The likelihood TS is the ratio between the likelihood without a source and the likelihood with a source added, thus, these results are consistent since the significance of the source increases with more good data gathered. Therefore, an analysis conducted on the filtered data using the refined filtering techniques, i.e., selecting all sections on the entire data with significance above 2 σ

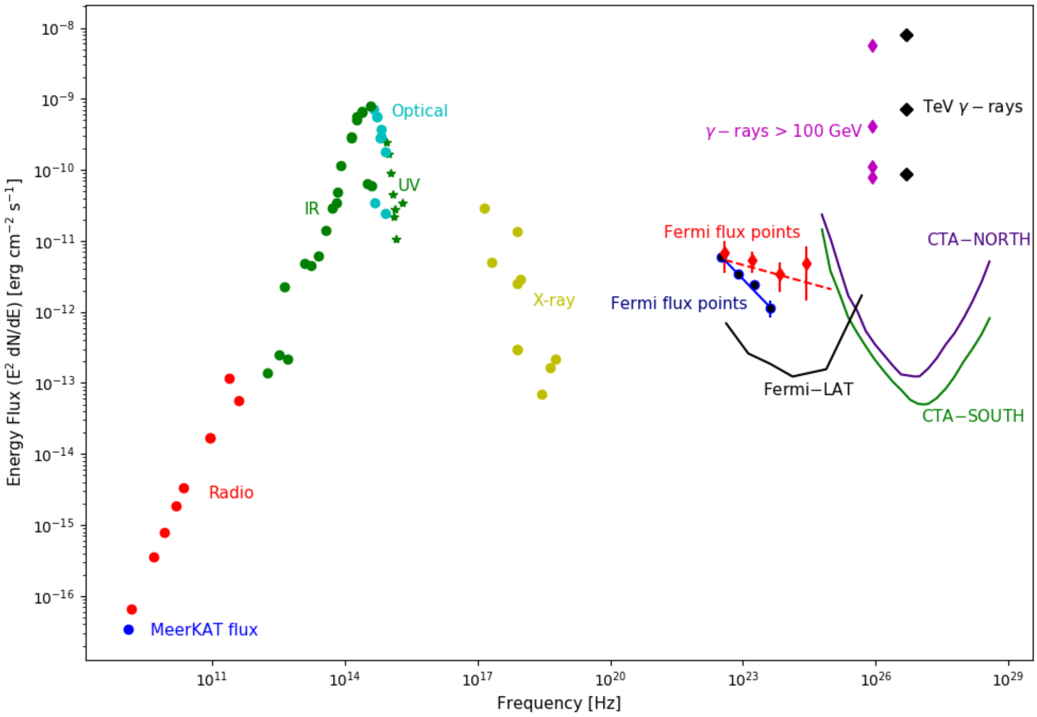

Figure 5.27: The updated broadband SED from radio to very high energy emission from AE Aqr (e.g., [21]). The flux points measured in this study are indicated by navy-blue circles including CTA, and Fermi−LAT sensitivity curves. The gamma−ray flux levels around 100 GeV are burst−like events detected by the Durham group [22] and the TeV gamma−ray flux levels were transient burst−like events detected with the Nooitgedacht Mk I Cherenkov telescope[6]. Both groups reported these events contemporaneously in the late 1980s and early 1990s, see Oruru and Meintjes [21] (and references therein) for a discussion.

resulted in high flux levels compared to when all sections with positive TS were selected. This choice was made under the assumption that sections with high TS tend to produce good pulse spectra. Thus these sections with significance above 2 σ could be associated with burst-like events. The SED analysis conducted on the 2 σ filtered data indicate a harder gamma-ray spectrum than TS>0 filtered data. A fit through flux points measured from a $TS > 0$ refined filtered dataset exhibit a power law spectrum with an index $p \sim 2.2$. These spectral points were added to the broadband SED in Figure 5.27. The flux points of a 2 σ refined filtered dataset are indicated by red diamonds. The extrapolated model shows that the emission from AE Aqr could be above the detection limit of both CTA north and south.

Lastly, we checked the occurrence of the burst-like events that have pulsed signal with significance over 2 σ. We aimed to establish the re-occurrence of these events for future follow-up observations with more sensitive telescopes like CTA. The duty cycle (DC) of pulsed signal from AE Aqr was calculated as follows;

$$\mathrm{DC} = \left[\frac{\text{Total 10 mins bins with Rayleigh Statistic} > 2\sigma}{\text{Total 10 min bins with GTIs over the entire dataset}}\right] = \frac{1508}{185420} \sim 1\%. \quad (5.6)$$

The observed DC from the Fermi-LAT data is very small and is comparable to that estimated ($\sim$ 10 %) by Meintjes et al., [6] but it is larger than what was obtained ($\sim$ 0.2 %) by Bowden et al., [13]. Using the 10 minutes sections with Rayleigh statistic

$> 2\ \sigma$ and the total 10 minutes from the entire dataset the DC is ~ 0.28 %. The approach considers the entire dataset; it ignores the fact that in some periods, the telescope was pointing away from the region of AE Aqr.

Data sections that display transient events reveal AE Aqr in both binned and unbinned and residual maps (see Figure 5.7 and 5.11), with a significance of ~ 9 as indicated in Table 5.3. Periodic analysis and stacking of power spectra revealed a clear indication of pulsed emission at both the spin frequency and first harmonic. A control analysis revealed that the power at fundamental frequency and the first harmonic fades away in region of the sky that are taken for control analysis (see Figure 5.20). It was also shown that the gamma-ray spectra of the flaring periods are constantly harder than the overall spectrum, which predicts flux levels above the CTA threshold.

Chapter 6

Discussion and Conclusion

The aim of this study was the search for pulsed radio and gamma-ray emission from the nova-like variable AE Aqr using MeerKAT and Fermi-LAT data. Since no indication of pulsed radio emission was detected from AE Aqr in the past our aim was to establish whether the sensitivity of the MeerKAT telescope can reveal indications of pulsed emission. On the other hand low-level pulsed gamma-ray emission was seen using the Fermi-LAT pass 7 dataset [16]. We therefore aimed to investigate the presence of pulsed emission since the data together with the analysis software have been improved in the pass 8 dataset. The findings from this study will be presented in the next sections starting with results obtained from the MeerKAT data.

The analysis of the short observation of AE Aqr resulted in the first detection of this source by the MeerKAT telescope using the L-band. The nova-like system was detected at a peak flux density of 2.64 ± 0.0659 mJy with rms noise level at 0.04 mJy. The radio emission variability from AE Aqr was also investigated using the MeerKAT radio data, and pulsed radio emission was discovered. Pulsations were detected at a low-level at the white dwarf's rotational period (33.08 s), but a further investigation resulted in no indication of any pulsations at the first harmonic (16.54 s). Dissecting the data revealed that the greatest contribution of these pulsations were detected at lower L-band frequencies and at the onset of the flare event. No pulsations were significant at the peak of the flare-like event. The non-thermal characteristics of the radio emission were also confirmed in this study with a spectrum that assumes a power law model. The spectral variation studies revealed an optically thin spectrum with a power law spectral index of $\alpha = -0.87$ and electron energy index of $p = 2.74$. The power law spectrum observed in the MeerKAT data seems to be unrelated to the overall radio spectrum up to $\sim$ 1000 GHz, which can be explained as the net emission from a superposition of optically thick synchrotron clouds in terms of a van der Laan process. Therefore, a correlation between the MeerKAT data and observations at higher frequencies will be an interesting topic for in-depth follow-up studies.

Gamma-ray emission from AE Aqr was investigated using an $\sim$ 11-year baseline of the archived upgraded Fermi-LAT pass 8 dataset, which offers more inclusive selection criteria, and an improved galactic diffuse gamma-ray emission model. The standard binned and unbinned analyses techniques performed with the latest Fermi Science Tools software packages (v11r0p5) installed with Conda resulted in a non-detection of any significant gamma-ray excess in the region of AE Aqr. An analysis with a more constrained model also revealed no indications of any gamma-ray excess at the region of AE Aqr. A search for transient burst-like gamma-ray events was conducted to further investigate any possible gamma-ray activities at the location of

AE Aqr. Selected bin periods that included the periods contemporaneous to optical flares were used to search for transient gamma-ray emission using the standard unbinned analysis technique. This approach aimed at investigating the presence of any gamma-ray emission that correlates with optical flares since the likelihood of gamma-ray emission from AE Aqr is expected at or just before the onset of the optical flaring [6]. This search also resulted in no detection of gamma-ray emission from AE Aqr. The search for transient gamma-ray emission was advanced by searching for flaring activity in the gamma-ray dataset. This was achieved through a characteristic light curve produced for the entire dataset with the time axis set to 14 days per bin. The search for time bins that have a sufficient gamma-ray activity revealed several time bins with significance in excess of 2 σ. Further investigation pursued through unbinned analysis on these time bins revealed more evidence of sporadic burst-like events. The diagnostic sky map plots generated for these selected time bins also display excess gamma-ray emission at the region of AE Aqr.

A search for pulsed gamma-ray emission was conducted using the entire 11-year Fermi-LAT dataset and the periods that are contemporaneous with previously observed optical flares resulted in no significant indication of any pulsed emission. However, there is evidence of pulsed emission from some time bins that have excess significance (2 σ). The search for pulsations in the time bins with excess significance resulted in some profiles with strong pulsed power appearing within the range 29.9-30.23 mHz (33.08-33.45 s). Some of the accompanying pulse phase light curves folded with 33.08 s rotation period clearly display the periodic nature of the collected photons. The maximum Rayleigh statistic detected from these data sections is $2nR^2 = 13.8$, which corresponds to a probability for chance occurrence of $Pr = e^{-nR^2} \approx 10^{-3}$ [166]. The phase distribution of the 33.08 s period indicates a double pulse which implies pulsed power also at the first harmonic (16.54 s).

The above mentioned results motivated a further search of sporadic burst-like gamma-ray emission from AE Aqr. The refined or a more selective filtering was applied on the $\sim$ 11-year Fermi-LAT dataset to investigate evidence of possible transient emission from this source. Using the refined filtered data AE Aqr was detected with a significance of $\sim$ 14 σ utilising both binned and unbinned analysis techniques. The gamma-ray spectral variation observed in the refined filtered data revealed a spectrum that can be fitted with a power law model with an index of $\sim$ 2. More refined filtering revealed evidence of spectral hardening above the galactic gamma-ray emission, which is unrelated to AE Aqr.

The search for pulsed gamma-ray emission was also advanced to further investigate the presence of stronger pulsations. Instead of using the refined filtered dataset, the entire dataset ($\sim$ 11 years) was divided into 10 minute sections. The search conducted for periodic emission within these sections revealed a stronger pulsed signal close to or at the fundamental frequency (33.08 s) and the first harmonic (16.54 s). We showed in a control analysis that the pulsations decrease systematically further away from the source of interest in regions that extend up to 15 degrees. The stacking of pulsed periodograms (FFTs) with significance above 3 σ reveal pulsed emission from both poles with significance above 5 σ after introducing statistical penalties that result from oversampling. However, this significance may or should not be considered as the overall significance of AE Aqr since a smaller sample of the entire dataset is chosen to demonstrate pulsed emission from both poles. Noticeable from the stacked periodogram is a strong pulse at the first harmonic, which mimics the optical pulsed signal (e.g., [12, 5]. The search was again extended to periods that are contemporaneous to observed optical flares. The results show indications of pulsed signal within the noise level. However, stacking of the periodograms of these periods revealed a pulsed signal with a significance over 4 σ at the fundamental period (33.08 s) after applying the statistical penalties of oversampling.

The pulsed radio and gamma-ray emission reported in this study conform to earlier reports of pulsed non-thermal emission before or during flares. This seem to suggest the switch-on of a particle acceleration mechanism that may be associated with enhanced mass transfer from the secondary star with associated enhanced propeller ejection of matter from the white dwarf's magnetosphere. The pulsed gamma-ray power spectra, when stacked, revealed clear evidence of particle acceleration from two polar zones [33.08 s, 16.54 s], resulting in a double pulse. The question that begs for an answer is why the radio emission shows only 33.08 s pulsed emission with a non-thermal signature while the gamma-ray emission seems to be driven from both poles of the fast rotating white dwarf. It was suggested that the transient non-thermal radio emission may originate from the secondary star. A model which supports this notion revealed that this emission might originate from the secondary star's magnetospheric field, which is pumped continuously by the magnetosphere of the fast rotating white dwarf.

The pulsed gamma-rays, on the other hand, may be the result of proton and ion beams accelerated from both polar cap regions which interact with the propeller-ejected material from the magnetosphere. Previous studies also suggest the existence of a circumbinary reservoir of ejected material that can act as a target for accelerated particles, with associated gamma-ray production through π^0 decay. Additionally, there is clear evidence of spectral hardening during active periods which could result in detectable emission with more sensitive Cherenkov telescopes like the CTA.

In conclusion, the results presented in this study confirm the enigmatic nature of AE Aqr as a source of non-thermal emission from radio to gamma-ray energies. Our analysis methodology in both radio and gamma-ray regimes also suggests that special care needs to be taken to isolate regions of enhanced activity for analysis to search for pulsed emission signatures. Since the duty cycle is very low, ranging between 0.2-1 % (depending on the definition), it complicates the search with ground-based Cherenkov telescopes. It is proposed that follow-up studies with Fermi-LAT continue and also for continuous 1-2 h nightly observations with H.E.S.S. or CTA be conducted, which may increase the chance for detection given the regular flaring activity displayed by the source. Periodic phenomena may reveal itself when periodograms of observations are stacked.

Bibliography

[1] Schmidt G D 1999 *Annapolis Workshop on Magnetic Cataclysmic Variables* vol 157 p 207

[2] Cropper M 1990 *Space Science Reviews* **54** 195–295

[3] Frank J, King A, Raine D *et al.* 2002 *Accretion power in astrophysics* (Cambridge university press)

[4] Patterson J 1994 *Publications of the Astronomical Society of the Pacific* **106** 209

[5] Patterson J 1979 *The Astrophysical Journal* **234** 978–992

[6] Meintjes P, De Jager O, Raubenheimer B, Nel H, North A, Buckley D and Koen C 1994 *The Astrophysical Journal* **434** 292–305

[7] Wynn G A, King A R and Horne K 1997 *Monthly Notices of the Royal Astronomical Society* **286** 436–446

[8] Bookbinder J and Lamb D 1987 *The Astrophysical Journal* **323** L131–L135

[9] Dubus G, Taam R E, Hull C, Watson D M and Mauerhan J C 2007 *The Astrophysical Journal* **663** 516

[10] Terada Y, Hayashi T, Ishida M, Mukai K, Dotani T, Okada S, Nakamura R, Naik S, Bamba A and Makishima K 2008 *Publications of the Astronomical Society of Japan* **60** 387–397

[11] Brink C, Cheng S, de Jager C, Meintjies J, Nel I, North R, Raubenheimer C and van der Walt J 1990 *International Cosmic Ray Conference* vol 2 p 283

[12] Meintjes P J 1992 *Simultaneous optical and TeV gamma-ray observations of the cataclysmic variable AE Aquarii* Ph.D. thesis

[13] Bowden C, Bradbury S, Chadwick P, Dickinson J, Dipper N, Edwards P, Lincoln E, McComb T, Orford K, Rayner S *et al.* 1992 *Astroparticle Physics* **1** 47–59

[14] Bednarek W, Blanch O, Cortina J, de Oña Wilhelmi E, Hadasch D, López-Coto R, López-Oramas A, Munar-Adrover P, Paredes J, Pérez-Torres M *et al.* 2017 *AIP Conference Proceedings* vol 1792 (AIP Publishing LLC) p 040016

[15] Van Heerden H J 2015 *A search for pulsed high-energy non-thermal emission from the nova-like variable system AE Aquarii* Ph.D. thesis University of the Free State

[16] van Heerden H J and Meintjes P J 2015 *Mem. Soc. Astron. Ital.* **86** 111

[17] Wynn G and King A 1995 *Monthly Notices of the Royal Astronomical Society* **275** 9–21

[18] Meintjes P, Oruru B and Odendaal A 2012 *Memorie della Societa Astronomica Italiana* **83** 643

[19] Meintjes P and Venter L 2003 *Monthly Notices of the Royal Astronomical Society* **341** 891–900

[20] Asad K, Girard J, de Villers M, Lehmensiek R, Ansah-Narh T, Iheanetu K, Smirnov O, Santos M, Jonas J, de Villiers D *et al.* 2019 *arXiv preprint arXiv:1904.07155*

[21] Oruru B and Meintjes P 2012 *Monthly Notices of the Royal Astronomical Society* **421** 1557–1568

[22] Chadwick P, Dickinson J, Dickinson M, Dipper N, Holder J, McComb T, Orford K, Rayner S, Roberts I, Roberts M D *et al.* 1995 *Astroparticle Physics* **4** 99–111

[23] Ghisellini G 2013 *Radiative processes in high energy astrophysics* vol 873 (Springer)

[24] Zinner E 1938 *Astronomische Nachrichten* **265** 345–352

[25] Joy A H 1954 *The Astrophysical Journal* **120** 377

[26] Crawford J A and Kraft R P 1956 *The Astrophysical Journal* **123** 44

[27] Chincarini G and Walker M 1981 *Astronomy and Astrophysics* **104** 24–32

[28] Meintjes P and Venter L 2005 *Monthly Notices of the Royal Astronomical Society* **360** 573–582

[29] Van Paradijs J, Kraakman H and van Amerongen S 1989 *Astronomy and Astrophysics Supplement Series* **79** 205–215

[30] Bastian T, Dulk G and Chanmugam G 1988 *The Astrophysical Journal* **324** 431–440

[31] Van der Laan H 1963 *Monthly Notices of the Royal Astronomical Society* **126** 535–552

[32] Bastian T, Beasley A and Bookbinder J 1996 *The Astrophysical Journal* **461** 1016

[33] Eracleous M and Horne K 1996 *The Astrophysical Journal* **471** 427

[34] Venter L and Meintjes P 2006 *Monthly Notices of the Royal Astronomical Society* **366** 557–565

[35] Meintjes P and De Jager O 2000 *Monthly Notices of the Royal Astronomical Society* **311** 611–620

[36] Meintjes P J 1989 *Simultaneous optical and TeV gamma-ray observations of the cataclysmic variable AE Aquarii* Ph.D. thesis

[37] Meintjes P, Raubenheimer B, De Jager O, Brink C, Nel H, North A, Van Urk G and Visser B 1992 *The Astrophysical Journal* **401** 325–336

[38] Meintjes P, Odendaal A and van Heerden H 2015 *Acta Polytechnica CTU Proceedings* **2** 86–89

[39] Knigge C, Baraffe I and Patterson J 2011 *The Astrophysical Journal Supplement Series* **194** 28

[40] Warner B 1995 *Cataclysmic Variable Stars, Cambridge University Press, Cambridge*

[41] Ritter H 2012 *Memorie della Societa Astronomica Italiana* **83** 505

[42] Aungwerojwit A, Gänsicke B, Rodríguez-Gil P, Hagen H J, Harlaftis E, Papadimitriou C, Lehto H, Araujo-Betancor S, Heber U, Fried R *et al.* 2005 *Astronomy & Astrophysics* **443** 995–1005

[43] Abada-Simon M, Mouchet M, Aubier M, Barrett P, de Jager O, de Martino D and Ramsay G 1999 *The Universe as Seen by ISO* vol 427 p 257

[44] Hellier C 2001 *Cataclysmic Variable Stars-how and why they vary* (Springer Science & Business Media)

[45] Ramsay G and Cropper M 2004 *Monthly Notices of the Royal Astronomical Society* **347** 497–507

[46] Kuijpers J and Pringle J 1982 *A&A* **114** L4

[47] Chanmugam G and Ray A 1984 *The Astrophysical Journal* **285** 252–257

[48] Schneider D and Young P 1980 *The Astrophysical Journal* **238** 946–954

[49] Burnard D, Arons J and Lea S 1983 *The Astrophysical Journal* **266** 175–187

[50] Hellier C, Beardmore A and Buckley D A 1998 *Monthly Notices of the Royal Astronomical Society* **299** 851–854

[51] Norton A, Butters O, Parker T and Wynn G 2008 *The Astrophysical Journal* **672** 524

[52] Patterson J, Thorstensen J R, Vanmunster T, Fried R E, Martin B, Campbell T, Robertson J, Kemp J, Messier D and Armstrong E 2004 *Publications of the Astronomical Society of the Pacific* **116** 516

[53] Hellier C, Wynn G A and Buckley D A 2002 *Monthly Notices of the Royal Astronomical Society* **333** 84–92

[54] Hellier C 2002 *arXiv preprint astro-ph/0201475*

[55] Southworth J, Gänsicke B, Marsh T, De Martino D and Aungwerojwit A 2007 *Monthly Notices of the Royal Astronomical Society* **378** 635–640

[56] Warner B and Wickramasinghe D T 1991 *Monthly Notices of the Royal Astronomical Society* **248** 370–376

[57] Canalle J and Opher R 1997 *Astronomical Time Series* (Springer) pp 223–226

[58] Bath G, Evans W and Pringle J 1974 *Monthly Notices of the Royal Astronomical Society* **166** 113–121

[59] Choi C S, Dotani T and Agrawal P 1999 *The Astrophysical Journal* **525** 399

[60] Itoh K, Okada S, Ishida M and Kunieda H 2006 *The Astrophysical Journal* **639** 397

[61] Welsh W F, Horne K and Oke J 1993 *The Astrophysical Journal* **406** 229–239

[62] Abada-Simon M, Bastian T S, Horne K, Robinson E and Bookbinder J A 1995 *Magnetic Cataclysmic Variables* vol 85 p 355

[63] Schenker K, King A, Kolb U, Wynn G and Zhang Z 2002 *Monthly Notices of the Royal Astronomical Society* **337** 1105–1112

[64] De Jager O 1991 *International Cosmic Ray Conference* vol 2 pp 16–1

[65] Meintjes P 2002 *Monthly Notices of the Royal Astronomical Society* **336** 265–275

[66] Robinson E L, Shafter A W and Balachandran S 1991 *The Astrophysical Journal* **374** 298–306

[67] De Jager O and Meintjes P 1993 *Astronomy and Astrophysics* **268** L1–L4

[68] De Jager O, Meintjes P, O'Donoghue D and Robinson E 1994 *Monthly Notices of the Royal Astronomical Society* **267** 577–588

[69] Hamada T and Salpeter E 1961 *The Astrophysical Journal* **134** 683

[70] Friedjung M 1997 *New Astronomy* **2** 319–322

[71] Friedjung M 2006 *Journal of the American Association of Variable Star Observers (JAAVSO)* **35** 137–140

[72] Eracleous M, Horne K, Robinson E L, Zhang E H, Marsh T R and Wood J H 1994 *The Astrophysical Journal* **433** 313–331

[73] Welsh W F, Horne K and Gomer R 1995 *Monthly Notices of the Royal Astronomical Society* **275** 649–670

[74] Beskrovnaya N, Ikhsanov N, Bruch A and Shakhovskoy N 1996 *Astronomy and Astrophysics* **307** 840–848

[75] Welsh W F, Horne K and Gomer R 1998 *Monthly Notices of the Royal Astronomical Society* **298** 285–302

[76] Mouchet M, Casares J, Harlaftis E, Emannelsen I, Martinez-Pais P I and Olsen O 1995 *Magnetic Cataclysmic Variables* vol 85 p 359

[77] Abada-Simon M, Lecacheux A, Bastian T S, Bookbinder J A and Dulk G A 1993 *The Astrophysical Journal* **406** 692–700

[78] Abada-Simon M, Casares J, Evans A, Eyres S, Fender R, Garrington S, De Jager O, Kuno N, Martínez-Pais I, De Martino D *et al.* 2005 *Astronomy & Astrophysics* **433** 1063–1077

[79] Tanzi E G, Chincarini G and Tarenghi M 1981 *Publications of the Astronomical Society of the Pacific* **93** 68

[80] Bastian T, Beasley A and Bookbinder J 1996 *Radio Emission from the Stars and the Sun* vol 93 p 185

[81] Kuijpers J, Fletcher L, AbadaSimon M, Horne K, Raadu M, Ramsay G and Steeghs D 1997

[82] Patterson J, Branch D, Chincarini G and Robinson E 1980 *The Astrophysical Journal* **240** L133–L136

[83] Eracleous M, Halpern J and Patterson J 1991 *The Astrophysical Journal* **382** 290–300

[84] Clayton K and Osborne J 1995 *Magnetic Cataclysmic Variables* vol 85 p 379

[85] Reinsch K, Beuermann K, Hanusch H and Thomas H C 1995 *Magnetic Cataclysmic Variables* vol 85 p 115

[86] Mauche C W 2006 *Monthly Notices of the Royal Astronomical Society* **369** 1983–1987

[87] Terada Y, Ishida M, Mukai K, Makishima K, Dotani T, Gallo L, Naik S, Hayashi T, Okada S, Nakamura R *et al.* 2007 *The Obscured Universe. Proceedings of the VI INTEGRAL Workshop* vol 622 p 521

[88] Koyama K, Tsunemi H, Dotani T, Bautz M W, Hayashida K, Tsuru T G, Matsumoto H, Ogawara Y, Ricker G R, Doty J *et al.* 2007 *Publications of the Astronomical Society of Japan* **59** S23–S33

[89] Takahashi T, Abe K, Endo M, Endo Y, Ezoe Y, Fukazawa Y, Hamaya M, Hirakuri S, Hong S, Horii M *et al.* 2007 *Publications of the Astronomical Society of Japan* **59** S35–S51

[90] Kitaguchi T, An H, Rana V R, Kaspi V M, Gotthelf E V, Harrison F A, Boggs S E, Christensen F E, Craig W W, Hailey C J *et al.* 2015 *THE THIRTEENTH MARCEL GROSSMANN MEETING: On Recent Developments in Theoretical and Experimental General Relativity, Astrophysics and Relativistic Field Theories* (World Scientific) pp 2443–2446

[91] Ryspaeva E 2017 *Journal of Physics: Conference Series* vol 798 (IOP Publishing) p 012001

[92] Lang M, Akerloff C, Carter-Lewis D, Cawley M, Chantell M, Colombo E, Connaghton V, Fegan D, Fennell S, Gaidos J, Hillas A, Kerrick A, Kertzman M, Lamb R, Meyer D, Reynolds P, Rovero A, Sembroski G, Schubnell M and Weeekes T 1995 *International Cosmic Ray Conference* vol 2 p 378

[93] Colombo E, Lang M, Gillanders G and Moriarty P 1997 *International Cosmic Ray Conference* vol 3 p 225

[94] Lang M, Buckley J, Carter-Lewis D, Catanese M, Cawley M, Colombo E, Connaughton V, Fegan D, Finley J, Gaidos J *et al.* 1998 *Astroparticle Physics* **9** 203–211

[95] Sidro N, Cortina J, Mauche C, de Oña E, Rico J and Torres D 2008 *Proceedings of the 30th International Cosmic Ray Conference* vol 2 p 715

[96] Li J, Torres D F, Rea N, de Ona Wilhelmi E, Papitto A, Hou X and Mauche C W 2016 *The Astrophysical Journal* **832** 35

[97] Ghosh P and Lamb F K 1991 *Neutron Stars: Theory and Observation* (Springer) pp 363–444

[98] Wang Y M and Robertson J 1985 *Astronomy and Astrophysics* **151** 361–371

[99] Holman G D 1985 *Symposium-International Astronomical Union* vol 107 (Cambridge University Press) pp 191–196

[100] Priest E R 1981 *Solar flare magnetohydrodynamics* (Gordon & Breach, New York)

[101] Aly J and Kuijpers J 1990 *Astronomy and Astrophysics* **227** 473–482

[102] Svestka Z 1976 *Solar Flares* (Reidel, Dordrecht)

[103] Parker E N 1979 *Cosmical magnetic fields: Their origin and their activity* (Oxford : Clarendon Press ; New York : Oxford University Press)

[104] Lesch H 1991 *Astronomy and Astrophysics* **245** 48–56

[105] Setti G 1976 *NATO Advanced Science Institutes (ASI) Series C* vol 28

[106] Biskamp D 1988 *Lecture Notes in Physics (eds. K. Meisenheimer & HJ Röser), Springer Berlin* **279**

[107] Benz A O and Oss R V 1994 *Solar Physics* **154** 203–204

[108] Haerendel G 1994 Particle acceleration from field aligned potential droms

[109] Dreicer H 1959 *Physical Review* **115** 238

[110] Abada-Simon M, Mouchet M, Aubier M, Barrett P, De Jager O, De Martino D, Ramsay G and SP-427 E 1998 (ESA)

[111] Haerendel G 1994 *International Astronomical Union Colloquium* vol 142 (Cambridge University Press) pp 765–774

[112] Beardmore A and Osborne J 1997 *Monthly Notices of the Royal Astronomical Society* **290** 145–159

[113] Ikhsanov N R and Biermann P 2006 *Astronomy & Astrophysics* **445** 305–312

[114] Arons J and Scharlemann E T 1979 *The Astrophysical Journal* **231** 854–879

[115] Goldreich P and Julian W H 1969 *The Astrophysical Journal* **157** 869

[116] Meintjes P 2017 *The Golden Age of Cataclysmic Variables and Related Objects-III* vol 255 (SISSA Medialab) p 007

[117] Meintjes P and Jurua E 2006 *Monthly Notices of the Royal Astronomical Society* **372** 1279–1288

[118] Venter L and Meintjes P 2007 *Monthly Notices of the Royal Astronomical Society* **378** 681–690

[119] Becker W and Trümper J 1997 *Astronomy & Astrophysics* **236**

[120] Qwabe N S and Deane R P 2018 *14th European VLBI Network Symposium & Users Meeting (EVN 2018)* p 145

[121] Rotich Kipnoo E K, Gamatham R R, Leitch A W, Gibbon T B, Malan S, Kriel H and Kapp F 2017 *South African Journal of Science* **113** 1–4

[122] Camilo F 2018 *Nature Astronomy* **2** 594–594

[123] Kramer M, Menten K, Barr E, Karuppusamy R, Kasemann C, Klein B, Ros E, Wieching G and Wucknitz O 2018 *MeerKAT Science: On the Pathway to the SKA* vol 277 (SISSA Medialab) p 003

[124] Camilo F, Scholz P, Serylak M, Buchner S, Merryfield M, Kaspi V, Archibald R, Bailes M, Jameson A, Van Straten W *et al.* 2018 *The Astrophysical Journal* **856** 180

[125] Booth R, de Blok W, Jonas J and Fanaroff B 2009 *http://www. ska. ac. za/temp/rfp_meerkat. pdf* **99** 107–111

[126] Stappers B 2016 *Proc. Sci.(MeerKAT2016)* **10**

[127] Caleb M, Stappers B, Abbott T, Barr E, Bezuidenhout M, Buchner S, Burgay M, Chen W, Cognard I, Driessen L *et al.* 2020 *Monthly Notices of the Royal Astronomical Society* **496** 4565–4573

[128] Sanidas S, Caleb M, Driessen L, Morello V, Rajwade K and Stappers B W 2017 *Proceedings of the International Astronomical Union* **13** 406–407

[129] Taylor G B, Carilli C L and Perley R A 1999 *Synthesis Imaging in Radio Astronomy II* vol 180

[130] Fomalont E B and Perley R A 1999 *Synthesis imaging in radio astronomy II* vol 180 p 79

[131] Barnbaum C and Bradley R F 1998 *The astronomical journal* **116** 2598

[132] Ellingson S W and Hampson G A 2002 *IEEE Transactions on Antennas and Propagation* **50** 25–30

[133] Leshem A, van der Veen A J and Boonstra A J 2000 *The Astrophysical Journal Supplement Series* **131** 355

[134] Smolders B and Hampson G 2002 *IEEE Antennas and Propagation Magazine* **44** 13–22

[135] Kocz J, Briggs F and Reynolds J 2010 *The Astronomical Journal* **140** 2086

[136] Baan W, Fridman P and Millenaar R 2004 *The Astronomical Journal* **128** 933

[137] Niamsuwan N, Johnson J T and Ellingson S W 2005 *Radio Science* **40**

[138] Offringa A R, van de Gronde J J and Roerdink J B T M 2012 *A&A* **539**(A95)

[139] Fridman P and Baan W 2001 *Astronomy & Astrophysics* **378** 327–344

[140] Winkel B, Kalberla P, Kerp J and Flöer L 2010 *The Astrophysical Journal Supplement Series* **188** 488

[141] Gull S F and Daniell G J 1978 *Nature* **272** 686–690

[142] Högbom J 1974 *Astronomy and Astrophysics Supplement Series* **15** 417

[143] Offringa A and Smirnov O 2017 *Monthly Notices of the Royal Astronomical Society* **471** 301–316

[144] Ambrosino F and Meddi F 2017 *Photon Counting-Fundamentals and Applications* (IntechOpen)

[145] Becker W, Kramer M and Sesana A 2018 *Space Science Reviews* **214** 30

[146] Lomb N R 1976 *Astrophysics and space science* **39** 447–462

[147] Scargle J D 1982 *The Astrophysical Journal* **263** 835–853

[148] Press W H and Rybicki G B 1989 *The Astrophysical Journal* **338** 277–280

[149] VanderPlas J T and Ivezic Ž 2015 *The Astrophysical Journal* **812** 18

[150] Baluev R V 2008 *Monthly Notices of the Royal Astronomical Society* **385** 1279–1285

[151] Palmer D M 2009 *The Astrophysical Journal* **695** 496

[152] Zechmeister M and Kürster M 2009 *Astronomy & Astrophysics* **496** 577–584

[153] VanderPlas J T 2018 *The Astrophysical Journal Supplement Series* **236** 16

[154] Woudt P A, Fender R, Corbel S, Coriat M, Daigne F, Falcke H, Girard J, Heywood I, Horesh A *et al.* 2018 *Proceedings of MeerKAT Science: On the Pathway to the SKA — PoS(MeerKAT2016)* vol 277 p 013

[155] Casares J, Mouchet M, Martinez-Pais I and Harlaftis E 1996 *Monthly Notices of the Royal Astronomical Society* **282** 182–190

[156] Eadie W T, Drijard D and James F E 1971 *Statistical methods in experimental physics* (Amsterdam: North-Holland)

[157] Abdo A, Ackermann M, Ajello M, Asano K, Atwood W B, Axelsson M, Baldini L, Ballet J, Barbiellini G, Baring M G *et al.* 2009 *The Astrophysical Journal Letters* **706** L138

[158] Ackermann M, Ajello M, Albert A, Allafort A, Atwood W, Axelsson M, Baldini L, Ballet J, Barbiellini G, Bastieri D *et al.* 2012 *The Astrophysical Journal Supplement Series* **203** 4

[159] Atwood W, Abdo A A, Ackermann M, Althouse W, Anderson B, Axelsson M, Baldini L, Ballet J, Band D, Barbiellini G *et al.* 2009 *The Astrophysical Journal* **697** 1071

[160] Atwood W, Albert A, Baldini L, Tinivella M, Bregeon J, Pesce-Rollins M, Sgrò C, Bruel P, Charles E, Drlica-Wagner A *et al.* 2013 *arXiv preprint arXiv:1303.3514*

[161] Acero F, Ackermann M, Ajello M, Albert A, Baldini L, Ballet J, Barbiellini G, Bastieri D, Bellazzini R, Bissaldi E *et al.* 2016 *The Astrophysical Journal* **223** 26

[162] Mattox J R, Bertsch D, Chiang J, Dingus B, Digel S, Esposito J, Fierro J, Hartman R, Hunter S, Kanbach G *et al.* 1996 *The Astrophysical Journal* **461** 396

[163] Calabretta M R and Greisen E W 2002 *Astronomy & Astrophysics* **395** 1077–1122

[164] Zamanov R, Latev G, Stoyanov K, Boeva S, Spassov B and Tsvetkov S 2012 *Astronomische Nachrichten* **333** 736–743

[165] Mardia K 1972 *Statistics of directional data* (New York: Academic Press)

[166] Madzime S T, Meintjes P, Singh K K and van Heerden H 2020 *Proceedings of 7th Annual Conference on High Energy Astrophysics in Southern Africa — PoS(HEASA2019)* vol 371 p 051

[167] De Jager O 1987 *The analysis and interpretation of VHE gamma ray measurements* Ph.D. thesis

[168] Irwin J A 2007 *Astrophysics: decoding the cosmos* (John Wiley & Sons)

[169] Rybicki G B and Lightman A P 2008 *Radiative processes in astrophysics* (John Wiley & Sons)

[170] Longair M S 1992 *High energy astrophysics. Vol. 1: Particles, photons and their detection*

Appendix A

Radiation Processes

Introduction

AE Aqr exhibits multi-wavelength emission powered by a number of different processes, both thermal and non-thermal. Therefore the most likely and relevant thermal and non-thermal radiation processes related to AE Aqr will be reviewed in this chapter in order to give a basis for the theoretical outline within which this study can be assessed. This study focuses mainly on searching for GeV gamma-rays from Fermi-LAT data and radio emission from the MeerKAT telescope. Hence we discuss the possible production mechanism accompanying radio emission, soft and observed hard gamma-ray [6]. Several processes are responsible for the production of radio emission and VHE gamma-rays, but in this study, the focus is on synchrotron, inverse Compton, synchrotron self-Compton, and pion decay. The magnetic field of a magnetised source can be inferred using its radiation. Hence cyclotron radiation is discussed to give a framework within which the magnetic fields of AE Aqr can be quantified. The radiation produced through synchrotron processes is signified by linear polarization. Therefore, the intrinsic polarization of synchrotron radiation will also briefly be reviewed in this chapter.

A.1 Cyclotron radiation

Cyclotron radiation is a thermal radiation process also perceived as non-relativistic synchrotron radiation, since the mechanisms are analogous with a difference in the particle velocity and the strength of the magnetic fields. Both processes are produced by a particle moving in a magnetic field.

A particle (e.g., electron) moving with non-relativistic energy ($v \ll c$) in a uniform static magnetic field produces radiation at low frequencies with the associated observed sinusoidal electric field. The observed transformed electric field E(t) gives only one frequency peak, the fundamental frequency. This fundamental frequency of emission is equal to the gyration frequency of the spiraling particle around the magnetic field (see Figure A.1). The observation of the radiation emission from a charged particle trapped in the magnetic field confirms the magnetic field's presence, its strength, and perhaps its orientation.

A charged particle q moving at a non-relativistic velocity v, in the presence of the magnetic field B experiences the Lorentz force,

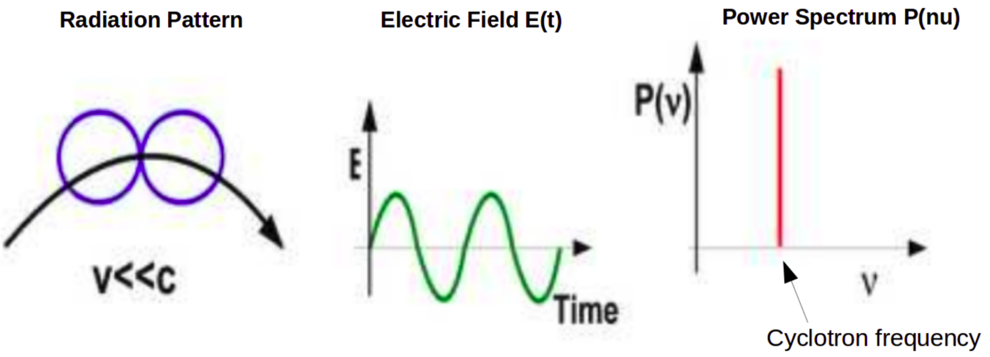

Figure A.1: Cyclotron dipole radiation pattern (left panel), transformed electric field (middle panel), with the corresponding power spectrum (right) with all its power concentrated at the fundamental frequency [23, page 68].

$$F = q\left[\frac{v}{c} \times B\right] \tag{A.1}$$

The parallel component of the velocity to the magnetic field is not affected by the field. Thus it remains constant, which is not the case for the perpendicular component $v_\perp = v\sin\phi$. In this case, the Lorentz force is only described by the perpendicular velocity component. The direction of the Lorentz force F, magnetic field B, and velocity of the particle v are always orthogonal, and their relationship is expressed as,

$$F = \frac{qv}{c} Bsin\phi = \frac{qv}{c} B_\perp \tag{A.2}$$

The magnitude of this force greatly depends on the pitch angle ϕ, the angle between v and B, where the magnetic field is described by the perpendicular component $B_\perp = Bsin\phi$. The particle is forced to move in a circular path (helical motion) around the magnetic field lines if the angle between the charged particle's velocity and the magnetic field is arbitrary between $0 - 180°$. When the angle is $90°$ the particle experiences the maximum force at $\sin\phi = 1$. On the other hand, the particle experiences no force if $\phi = 0°$ or $\phi = 180°$, i.e., when the direction of the velocity of the particle is parallel to the magnetic field, the particle will remain undisturbed. The charged particle has a helical motion described by equation A.1, which can also take the following form,

$$\frac{d^2\mathbf{x}}{dt^2} = -\frac{q}{mc}\frac{d\mathbf{x}}{dt} \times B \tag{A.3}$$

with B describing a constant uniform magnetic field. In the rectangular coordinate system, if we choose the field line to point in the direction of the z axis, the general solutions of this equation of motion are given by

$$x = x_0 + Acos(w_c t + \psi) \tag{A.4}$$
$$y = y_0 + Acos(w_c t + \psi) \tag{A.5}$$
$$z = z_0 + v_\parallel t \tag{A.6}$$

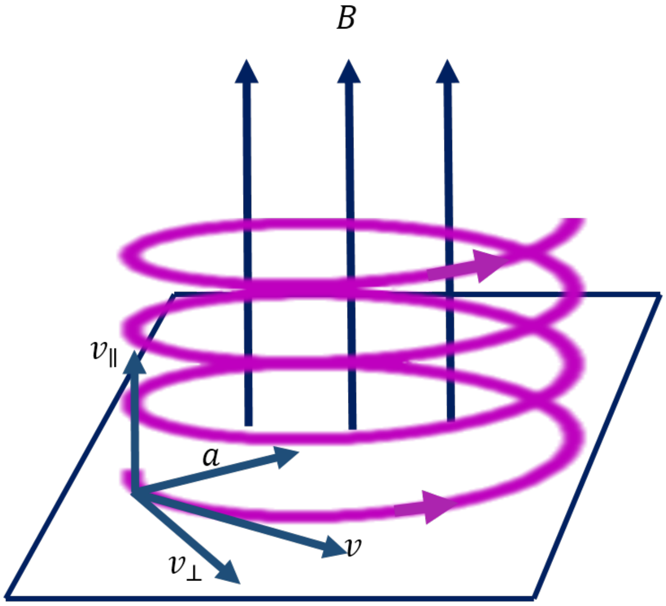

Figure A.2: The schematic diagram of a particle in helical motion about the magnetic field lines. The acceleration vector of the particle is directed inwards towards the centre.

where x_0, y_0, z_0, A, ψ, and $v_{\|}$ are six constants of integration and w_c is the cyclotron frequency. For helical motion A is the radius of the orbit in the x-y plane , superimposed on a uniform motion along the z axis.

The centripetal force balances the Lorentz force and directs the particle to spiral in a helical motion around the field lines (see Figure A.2). Therefore, the expression of the gyration radius (gyroradius) is determined by equating the Lorentz force with the centripetal force,

$$\begin{aligned} F &= \frac{qv}{c} B_{\perp} = m \frac{v_{\perp}^2}{r_0} \\ r_0 &= m \frac{v_{\perp} c}{qB} = \frac{v_{\perp} T}{2\pi} = \frac{v_{\perp}}{2\pi \nu_0} \end{aligned} \tag{A.7}$$

The gyroradius expression can now be employed to find the period of a gyrating particle. The period $T = 1/\nu_0$ of the gyrating particle does not depend on the size of the orbit, and it is constant for a constant magnetic field, where ν_0 is the gyrofrequency. From the expression for the gyroradius, one can write gyrofrequency as a function of the magnetic field, the speed of light c, and the mass of the particle as,

$$\nu_0 = \frac{qB}{2\pi mc} \tag{A.8}$$

This gyrofrequency expression above can be reduced to the following expression if the particle is an electron,

$$\left[\frac{\nu_0}{MHz}\right] = \frac{eB}{2\pi m_e c} = 2.8 \left[\frac{B}{Gauss}\right] \tag{A.9}$$

When a trapped particle loops around the field line over the gyration period, its speed is expected to change. The change of direction is associated with the particle acceleration. Conservation of energy and momentum requires that a particle in this orientation must accelerate and speed up. Conversely, its speed may stay the same while the radius enlarges, which is not the case in this scenario. Instead, the particle loses its energy through radiation, i.e., it radiates in all directions (cyclotron radiation) in a dipole pattern moving along the helical path. The resulting frequency of radiation from a gyrating particle is equal to the gyrofrequency $\nu_0 = w_c$ (cyclotron frequency or Larmor frequency).

The gyrofrequency is independent of the velocity of the particle for non-relativistic velocities. Thus, the gyrofrequency is independent of the kinetic energy of the charged particle $(E_k) = \frac{1}{2}mv^2$. If the magnetic field strength is constant, all electrons in the ambient will emit with the same frequency despite their different velocities. Even though particles with different velocities will have different gyro-radii, the radiation frequency will be the same for non-relativistic particles subjected to the same magnetic field strength. This characteristic feature provides a unique way to quantize the magnetic field since the radiation frequency is single-valued or monochromatic. The technique is not always useful since the cyclotron frequency must be higher than the plasma frequency for radiation to escape. Only objects with low electron density or strong magnetic fields, i.e., higher than 3.5 G can produce emission detectable from the ground because of the Earth's $\approx$ 10 MHZ ionospheric cutoff (for a detailed discussion see [168, page 259]).

It was mentioned earlier that all non-relativistic particles in the same magnetic field strength emit at the same (fundamental) frequency. Weaker harmonics will accompany the fundamental frequency at multiples of the fundamental frequency for hotter gases or relativistic particles with a non-thermal distribution (see Figure A.3). Since particles of different velocities emit at the same gyro-frequency, observation of multiple spectral lines at the fundamental frequency and harmonics helps confirm that the emission is actually due to cyclotron processes. Some objects may have varying magnetic fields, which may result in a continuum spectrum, or the magnetic field may vary significantly within the region under observation, which may have a couple of fundamental cyclotron frequencies for each field line.

A.1.1 Total power emitted by cyclotron radiation

If a charged particle is accelerated, and is observed in a reference frame where its velocity is less compared to the speed of light $v \ll c$, then in that coordinate frame, the acceleration field becomes [169, page 84],

$$\bar{E}(\bar{r}, t) = \frac{q}{c}\left[\frac{\bar{n} \times [(\bar{n} - \bar{\beta}) \times \dot{\bar{\beta}}]}{R[1 - \bar{\beta} \cdot \bar{n}]^3}\right] \tag{A.10}$$

This equation A.10 describes the acceleration field at a retarded position and time. If $\beta = \frac{v}{c}$ approaches zero the field reduces to,

$$\bar{E}(\bar{r}, t) = \frac{q}{c}\left[\frac{\bar{n} \times (\bar{n} \times \dot{\bar{\beta}})}{R}\right] \tag{A.11}$$

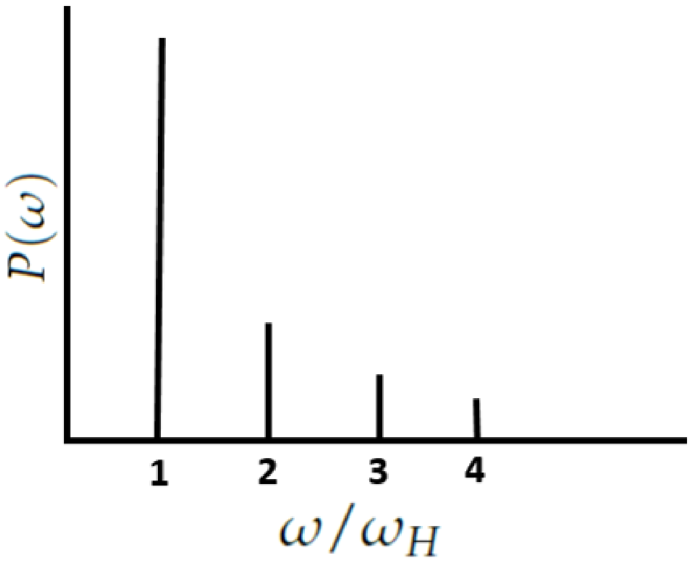

Figure A.3: The power spectra of cyclotron radiation with the fundamental frequency and multiple harmonics.

and

$$\bar{B}(\bar{r},t) = \bar{n} \times \bar{E}(\bar{r},t) \tag{A.12}$$

where $\bar{n}$, $\bar{E}(\bar{r},t)$ the electric field and $\bar{B}(\bar{r},t)$ the magnetic field are all perpendicular to each other. The instantaneous energy flux is given by by the Poynting flux vector. Substituting the acceleration field expression and the magnetic field equation A.12 and applying the back-cab rule, the resulting expression is the Poynting flux expressed as a function of the electric field, i.e., it is described by the square magnitude of $\bar{E}(\bar{r},t)$.

$$\begin{aligned} \bar{S} &= \frac{c}{4\pi}[\bar{E}(\bar{r},t) \times \bar{B}(\bar{r},t)] = \frac{c}{4\pi}\left[\bar{E}(\bar{r},t) \times (\bar{n} \times \bar{E}(\bar{r},t))\right] \\ S &= \frac{c}{4\pi}E(\bar{r},t)^2 \end{aligned} \tag{A.13}$$

The acceleration radiation field equation A.11 reduces to the following expression since $\bar{n} \perp (\bar{n} \times \dot{\bar{\beta}})$ and $|\bar{n}|^2 = 1$,

$$E(\bar{r},t) = \frac{q|\dot{\bar{\beta}}|sin\theta}{Rc} \tag{A.14}$$

Substituting the simplified acceleration radiation field A.14 into the Poynting flux equation result in,

$$\begin{aligned} S &= \frac{c}{4\pi}E(\bar{r},t)^2 \\ S &= \frac{q^2}{4\pi R^2 c^3}a^2 sin^2\theta = \frac{dw}{dAdt} \end{aligned} \tag{A.15}$$

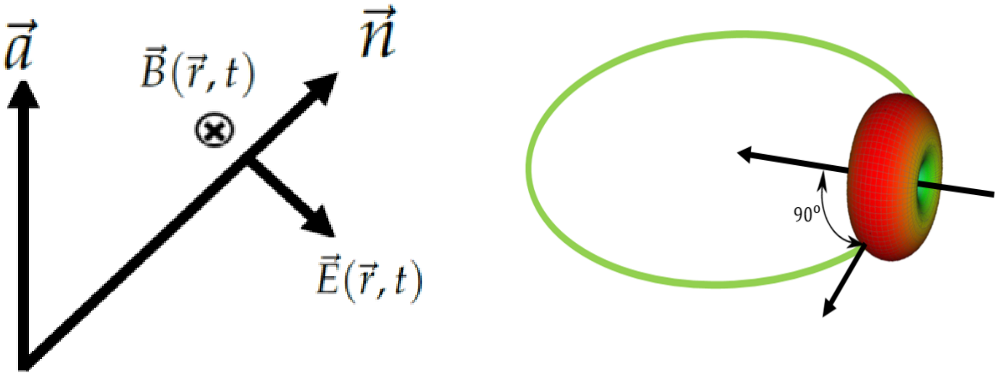

Figure A.4: The acceleration vector of a non relativistic particle in the presence of magnetic and electric field (left), and the resulting dipole radiation pattern (right).

Now we can evaluate the energy flux by writing the Poynting flux equation A.15 into a more descriptive emission coefficient form,

$$\begin{aligned} S &= \frac{dw}{dAdt} = \frac{dw}{R^2 d\Omega dt} \\ \frac{dw}{dt} &= \frac{q^2}{4\pi c^3} a^2 sin^2\theta d\Omega \end{aligned} \tag{A.16}$$

The energy Poynting flux is along the direction of $\bar{n}$, where θ is the angle between acceleration and $\bar{n}$. The total power radiated isotropically is obtained by integrating equation dw/dt over the entire solid angle $d\Omega$,

$$\begin{aligned} P &= \int_\Omega \left(\frac{dw}{dt}\right) d\Omega = \int_\Omega \left(\frac{q^2}{4\pi c^3} a^2 sin^2\theta\right) d\Omega \\ &= \frac{q^2}{4\pi c^3} a^2 \int_0^\pi sin^3\theta d\theta \int_0^{2\pi} d\phi \\ &= \frac{2}{3}\frac{q^2 a^2}{c^3} \end{aligned} \tag{A.17}$$

The result of equation A.17 is a general formula for charged particles moving with non relativistic speeds and is known as the Larmor formula. The power emitted is propotional to the square of the acceleration and the charge of the particle. Investigating equation A.16, a clear characteristic dipole pattern $dw/d\Omega dt \propto sin^2\theta$ is observed as shown in Figure A.4.

It is also clear that the maximum radiation is emitted perpendicular to the electric field and the acceleration, with no radiation emitted along the direction of acceleration. The acceleration vector component of the particle always points to the centre of the circle for particles in a circular motion about the field lines, and the electric field vector of the emitted radiation will be in the same direction of the acceleration as seen by a distant observer.

Polarization is another crucial feature of radiative emission from magnetised plasmas. For cyclotron emission, if the observer is in the direction of the field line, the E field will rotate with time, giving circularly polarised emission while if the observer's line of sight is perpendicular to the electric field, E field will oscillate linearly (like a dipole) resulting in linear polarization. Elliptical polarization will result if the observer is viewing from an intermediate angle (e.g., [168, page 258] [169, page 85]).

A.2 Synchrotron Radiation

Many astrophysical sources are magnetised and contain relativistic leptons (electrons and positrons). Magnetic fields and relativistic leptons are the main ingredients of synchrotron radiation. The driving mechanism behind this is the Lorentz force. Similar to the cyclotron mechanism, the Lorentz force will cause a particle to gyrate about the field line. The main difference is that the particle in the synchrotron mechanism is moving with relativistic velocity. Hence synchrotron radiation is known as relativistic cyclotron radiation. The mass of a particle moving with relativistic velocity is higher than the rest mass by a factor $\gamma = 1/\sqrt{1 - v/c}$, also known as the Lorentz factor. The only force acting on the particle is the Lorentz force since there is no electric field,

$$F_L = \frac{d}{dt}(\gamma m v) = \frac{q}{c} v \times B \tag{A.18}$$

To extract more information from this expression, velocity components are introduced in the expression as follows,

$$\frac{d}{dt}(v_\perp + v_\parallel) = \frac{q}{\gamma m c}(v_\perp + v_\parallel) \times B \tag{A.19}$$

The parallel component of the Lorentz force is insignificant for ϕ approaching zero, therefore falls away. This implies that there is no acceleration along the magnetic field ($dv_\parallel / dt = 0$). The velocity is constant and normal to the acceleration, which means the solution for the above expression is a uniform circular motion. The synchrotron radiation from the electron spiralling about the magnetic field lines can be determined using the orthogonal acceleration component,

$$a_\perp = \frac{d}{dt}(v_\perp) = \frac{q v_\perp B}{\gamma m c} \tag{A.20}$$

These equations are derived following the assumption that the synchrotron losses are insignificant during one revolution about a magnetic field line. Now from this acceleration expression one can derive the Larmor radius of the particle's orbit, since the particle in a circular orbit has the expression of the acceleration $a_\perp = v_\perp^2 / r_L$,

$$r_L = \frac{\gamma m c v_\perp}{qB} = \frac{\gamma m c v sin\phi}{qB} \tag{A.21}$$

where the fundamental frequency ν_B (gyration frequency) is the inverse of time required to complete one orbit, $T_{gyr} = 2\pi r_L / v_\perp$,

$$\nu_B = \frac{1}{T_{gyr}} = \frac{qB}{2\pi\gamma mc} = \frac{qB}{2\pi E} \tag{A.22}$$

Unlike cyclotron gyrofrequency, the synchrotron gyrofrequency depends on the energy of the charged particle. Since the Lorentz factor γ can be very large, the synchrotron gyroradius is larger than the cyclotron gyroradius, which implies that the synchrotron gyrofrequency is much lower than the cyclotron frequency.

A.2.1 Total energy losses of a single particle

The power emitted in electromagnetic radiation by non-relativistic charged particles is according to the Larmor formula, (see equation A.17). This is not the case for particles moving with relativistic velocities since the power depends on the charged particle's acceleration. Accordingly, the transformation of acceleration to the rest frame is necessary in order to evaluate the relativistic power correctly. The results of acceleration transformation between the rest and lab frame are shown in equation A.23 and A.24.

$$a_{\|} = \gamma^3 a_{\|} \tag{A.23}$$

$$a_{\perp} = \gamma^2 a_{\perp} \tag{A.24}$$

The transformation is applied twice on the parallel component, since the perpendicular displacement is invariant. Also note that the emitted power is Lorentz invariant. Therefore the power in the rest frame can be written as,

$$\begin{aligned} P = P' &= \frac{2q^2}{3c_3}[a_{\|}'^2 + a_{\perp}'^2] \\ &= \frac{2q^2}{3c_3}\gamma^2[\gamma^2 a_{\|}^2 + a_{\perp}^2] \end{aligned} \tag{A.25}$$

The parallel component's contribution is negligible and will be ignored for the rest of the calculations since the velocity of a relativistic particle is always close to the speed of light. This implies that one cannot accelerate the particle in the direction of the velocity, i.e., the parallel component. However, with a modest magnetic field, one can firmly bend the direction of motion and have a significant perpendicular acceleration $a_{\|} \ll a_{\perp}$. Substituting equation A.20 and A.24 into the equation of power ignoring the parallel component gives,

$$\begin{aligned} P &= \frac{2q^2}{3c^3}\gamma^4 \frac{q^2B^2}{\gamma^2 m^2 c^2} v_{\perp}^2 \\ &= \frac{2q^2}{3}\gamma^2 \left(\frac{q^2}{m^2c^4}\right) cB^2 \frac{v^2}{c^2} sin^2\phi \end{aligned} \tag{A.26}$$

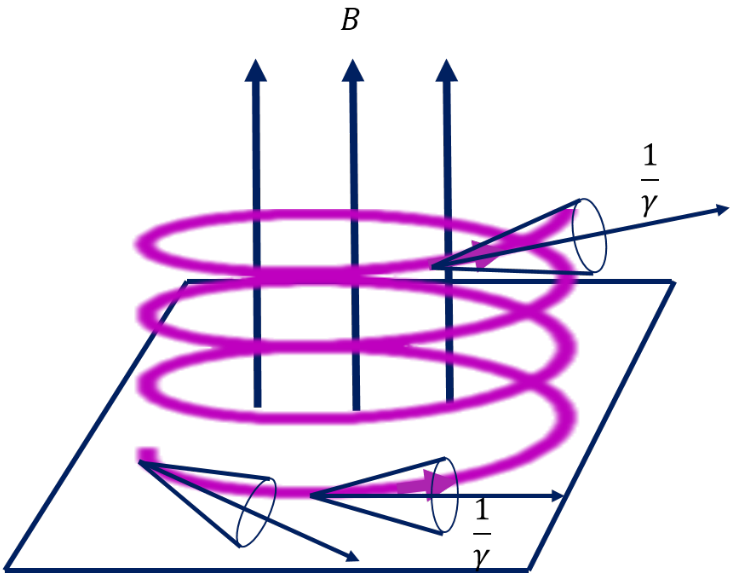

Figure A.5: Radiative emission from a relativistic particle in the presence of a strong magnetic field is beamed into a conical shape solid angle as viewed by a distant observer.

Nevertheless, in the case of an isotropic distribution of the velocities it is imperative to average the equation of power over all angles of a given speed $\beta = v/c$. Averaging the term $\sin^2\phi$ over the solid angle gives 2/3, which simplifies the equation to describe the power emitted by electron synchrotron radiation to

$$P = \left(\frac{2}{3}\right)^2 \gamma^2 r_0^2 c B^2 \beta^2 \tag{A.27}$$

where $r_0 = \left(q^2/m^2c^4\right)$ is the classical gyration radius with $q = e$ the electron charge, and $\beta = v/c$. The power equation can also be written in a more convenient form with physical parameters as,

$$P = \frac{4}{3}\gamma^2 r_0^2 \sigma_T c \beta^2 U_B \tag{A.28}$$

where $\sigma_T = 8\pi r_0^2/3$ is the Thompson cross section and $U_B = B^2/8\pi$ represent the magnetic energy density.

A.2.2 Spectrum of synchrotron Radiation

The synchrotron radiation power of an electron is boosted by a factor γ^2, with its distribution varying with angle. The observer in the rest frame sees emission over a wide angle, conversely a distant observer sees emission beamed into a narrow cone (see Figure A.5). The radiation cone has a solid angle twice the angle $sin\phi \sim 1/\gamma$.

The radiation observed is associated with time Δt_e for each revolution with the radiation cone pointing in the observer's direction. The time over which the cone sweeps across the observer is short compared to the gyration period. As a result, brief repeated pulses of emission are observed. The synchrotron spectrum requires a conversion from a time to a frequency domain, with the effect of the Doppler shift also considered, since the emission is only observed when the particle sweeps through the observer's line of sight. The electron will beam radiation towards the observer for time Δt_e related to the distance AB/v,

$$\begin{aligned}\Delta t_e &= \frac{AB}{v} = \frac{1}{v}\left(r_L\frac{2}{\gamma}\right) = \frac{1}{v}\left[\frac{\gamma m_0 c^2 \beta sin\phi}{eB}\right]\frac{2}{\gamma} \\ &= \frac{2m_0 c}{eB} = \frac{1}{\pi}\left(\frac{2\pi m_0 c}{eB}\right) = \frac{1}{\pi}\frac{1}{\nu_0} \\ &= \frac{2}{2\pi}\frac{1}{\gamma\nu_B}\end{aligned} \tag{A.29}$$

The observer can measure the change in time between the arrival of the pulse emitted between positions A and B, where A and B are the start and end of the path length (arc) between which the radiation will be beamed in a cone directed in the observer's line of sight. This is achieved by using the time aberration relationship that connects the emitted pulse, and the Doppler-shifted received pulse,

$$\begin{aligned}\Delta t_{AB} &= \frac{\Delta t_e^{'}}{\delta D} = \gamma(1-\beta cos\phi)\left(\frac{\Delta t_e}{\gamma}\right) \\ &= (1-\beta cos\phi)\Delta t_e = (1-\beta)\Delta t_e \\ &= \frac{1-\beta)(1+\beta)}{(1+\beta)}\Delta t_e = \frac{(1-\beta^2)}{(1+\beta)}\Delta t_e \\ &= \frac{1}{\gamma^2}\left(\frac{1}{1+\beta}\right)\Delta t_e \approx \frac{1}{2\gamma^2}\Delta t_e \approx \frac{1}{2\gamma^2}\left[\frac{2}{2\pi}\frac{1}{\gamma\nu_B}\right] \\ &\approx \left[\frac{1}{2\pi\gamma^3\nu_B}\right]\end{aligned} \tag{A.30}$$

The change in time Δt_{AB} between pulses emitted at A and B is derived making use of the equation A.29 assuming that β approaches 1, where $\delta D = \gamma(1-\beta cos\phi)$ is the Doppler factor, and the rest and moving frame time is evaluated by $\Delta t_e^{'} = \frac{\Delta t_e}{\gamma}$. The inverse of Δt_A is the typical synchrotron angular frequency ω.

$$\begin{aligned}\omega &= 2\pi\nu_s \approx \frac{1}{\Delta t_A} \\ \nu_s &= \frac{1}{2\pi\Delta t_A} \approx \frac{1}{2\pi}\frac{1}{\left[\frac{1}{2\pi\gamma^3\nu_B}\right]} = \gamma^3\nu_B\end{aligned} \tag{A.31}$$

A particle is expected to emit most of its power at the characteristic synchrotron frequency ν_s. This frequency is greater than the fundamental synchrotron frequency ν_B by a factor γ^3 and the gyration frequency ν_0 for non relativistic particle by a factor γ^2,

$$\nu_s \approx \gamma^3\left(\frac{\nu_L}{\gamma}\right) = \gamma^2\left(\frac{eB}{2\pi m_0 c}\right) = \gamma^2\nu_0 \tag{A.32}$$

The power per unit frequency per unit angle emitted by a relativistic electron is given by the following expression,

$$P_s(\nu, \gamma, \phi) = \frac{\sqrt{3}e^3 B sin\phi}{m_e c^2} F\left(\frac{\nu}{\nu_c}\right) \tag{A.33}$$

The critical frequency ν_c is the maximum frequency above which there is negligible emission. It is derived from the flux expression, see result of equation A.34. Hence, flux as a function of frequency is obtained by integrating the power expression over the emission pattern,

$$\begin{aligned} F\left(\frac{\nu}{\nu_c}\right) &= \frac{\nu}{\nu_c}\int_{\frac{\nu}{\nu_c}}^{\infty} K_{5/3}(y)dy \\ \nu_c &= \frac{3}{2}\nu_s sin\phi \\ \nu_c &= \frac{3}{2}\gamma^2\left(\frac{eB}{2\pi m_0 c}\right) sin\phi \\ \nu_c &= 4.2\gamma^2\left[\frac{B_\perp}{Gauss}\right] \end{aligned} \tag{A.34}$$

The critical frequency is a few order of magnitudes greater than the fundamental synchrotron frequency ν_B, and most of the energy is emitted at a frequency $\nu_{max} = 0.29\ \nu_c$. Therefore the synchrotron radiation forms a broad-band continuous spectrum that peaks at ν_{max}, since the fundamental frequency is extremely low, and its harmonics are closely spaced (see Fig: A.6). Given enough relativistic particles, even small magnetic fields can produce observable synchrotron radiation since synchrotron frequencies are much greater than the plasma frequency [168, page 265]

The work done so far focuses only on the radiation spectrum of one particle, now the focus is shifted towards an ensemble of particles. It should be remembered that synchrotron radiation is non-thermal, and the relativistic particle velocities do not follow a Maxwellian distribution. The relativistic particles consist of the electron component of the cosmic rays. Thus, the most probable particle distribution in higher energy astrophysics is the power law ,

$$N(\gamma) = K\gamma^{-p} \tag{A.35}$$

where $N(\gamma)$ is the number of cosmic-ray electrons per unit interval of electron energy per unit volume, p is the energy spectral index of cosmic-ray electrons, and K is a constant.

Since the relativistic particles are assumed to have a power law distribution, one can obtain the synchrotron emissivity produced by particles that possess anisotropic velocity distribution,

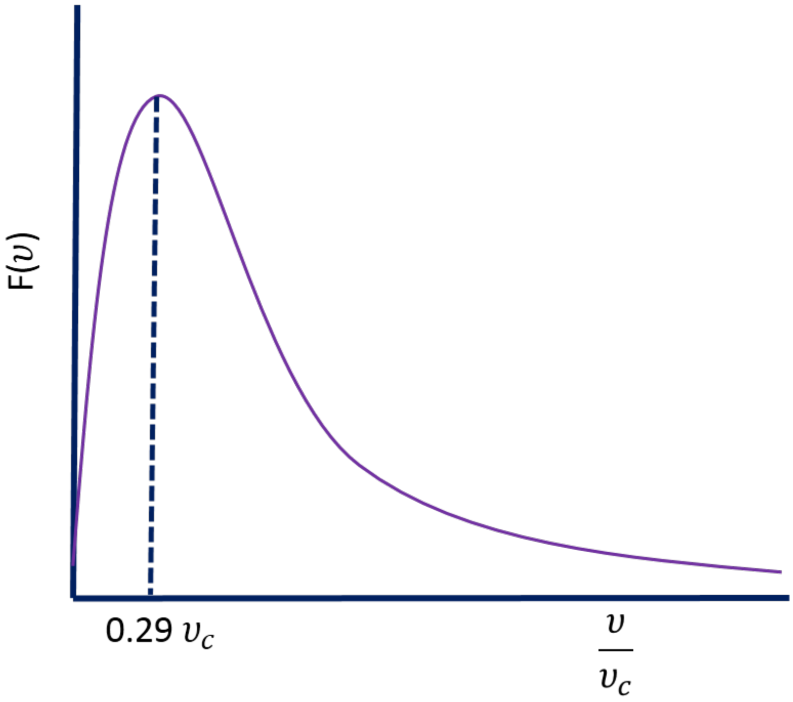

Figure A.6: Synchrotron spectrum showing the characteristic peak emission at 0.29 ν_c

$$
\begin{aligned}
\varepsilon_s(\nu,\phi) &= \frac{1}{4\pi}\int_{\gamma min}^{\gamma max} N(\gamma)P_s(\nu,\gamma,\phi)d\gamma \\
\varepsilon_s(\nu,\phi) &= \frac{1}{4\pi}\int_{\gamma min}^{\gamma max} K\gamma^{-P}\frac{\sqrt{3}e^3 B sin\phi}{m_e c^2}F\left(\frac{\nu}{\nu_c}\right)d\gamma
\end{aligned}
\tag{A.36}
$$

but it is also known that the critical frequency is given by,

$$
\begin{aligned}
\nu_c &= \frac{3}{2}\gamma^2\left(\frac{eB}{2\pi m_0 c}\right) sin\phi \\
\frac{\nu_c}{\nu} &= \frac{3}{2}\frac{\gamma^2}{\nu}\left(\frac{eB}{2\pi m_0 c}\right) sin\phi
\end{aligned}
\tag{A.37}
$$

Rearranging this expression and solving for γ

$$
\begin{aligned}
\gamma &= \left(\frac{\nu}{\nu_c}\right)^{-\frac{1}{2}}\nu^{\frac{1}{2}}\left(\frac{4\pi m_e c}{3eB}\right)^{\frac{1}{2}} sin^{-\frac{1}{2}}\phi \\
|d\gamma| &= \frac{1}{2}\nu^{\frac{1}{2}}\left(\frac{4\pi m_e c}{3eB}\right)^{\frac{1}{2}} sin^{-\frac{1}{2}}\phi\frac{1}{2}\left(\frac{\nu}{\nu_c}\right)^{-\frac{3}{2}} d\left(\frac{\nu}{\nu_c}\right)
\end{aligned}
\tag{A.38}
$$

where $\nu_c = \nu_c(\gamma)$, and it is assumed that the spectrum is contained in $F\left(\frac{\nu}{\nu_c}\right)$ implying that $d\gamma = d\left(\frac{\nu}{\nu_c}\right)$. The emissivity equation A.36 is simplified using the expression for γ and the infinitesimal expression of γ (equation A.38),

$$\begin{aligned}
\varepsilon_s(\nu,\phi) &= \frac{K}{4\pi}\left(\frac{4\pi m_e c}{3e}\right)^{-\frac{p-1}{2}} sin^{\frac{p+1}{2}}\phi \left(\frac{\sqrt{3}e^3}{m_e c^2}\right)\left[B^{\frac{p+1}{2}}\nu^{-\frac{p-1}{2}}\right] \\
&\times \int_{\gamma min}^{\gamma max} F\left(\frac{\nu}{\nu_c}\right)\left(\frac{\nu}{\nu_c}\right)^{\frac{p-3}{2}} d\left(\frac{\nu}{\nu_c}\right) \\
\varepsilon_s(\nu,\phi) &= const \times B^{\left(\frac{p+1}{2}\right)}\nu^{-\left(\frac{p-1}{2}\right)} \\
&= const \times B^{\left(\frac{p+1}{2}\right)}\nu^{-\alpha}
\end{aligned} \tag{A.39}$$

where $\alpha = \frac{p-1}{2}$ is the spectral index which is related to the energy spectral index of particles p, e.g., the cosmic ray electron distribution index. Thus, there exists a strong relationship between the energy of the electron and the frequency of a radiated photon.

The synchrotron emission from some sources can easily be detected but from other sources it is a hard task. The question is: what are the factors that control the extent of synchrotron emission? The synchrotron flux of a homogeneous and thin source with volume V$\sim R^3$ can be derived at a distance d_L making use of the synchrotron emissivity (equation A.39),

$$\begin{aligned}
F_s(\nu) &\approx \frac{L_s(\nu)}{4\pi d_L^2} = \frac{4\pi\varepsilon_s(\nu)V}{4\pi d_L^2} = const \times B^{\frac{p+1}{2}}\nu^{-\frac{p-1}{2}} \times \frac{R^3}{d_L} \\
&\propto B^{\frac{p+1}{2}}\nu^{-\frac{p-1}{2}} \times \frac{R^3}{d_L} = \left(\frac{R}{d_L}\right)^2 \nu^{-\alpha}B^{1+\alpha}R \\
&\propto \theta_s^2\nu^{-\alpha}B^{1+\alpha}R
\end{aligned} \tag{A.40}$$

This result shows that the emission depends on both magnetic field strength and the particle density (which forms part of the normalization), where θ_s is the angular radius of the source. It is possible to determine the frequency spectral index α if the source is observed at two different frequencies, hence the energy spectral index of the cosmic ray electrons p.

A.2.3 Synchrotron Absorption

Since emission processes have their absorption counterpart, synchrotron radiation is not unique in this regard, but its emission is through relativistic electrons. As mentioned earlier, the relativistic particles do not obey the Maxwellian distribution. Therefore the same principles for an optically thick black-body radiation source can not be applied. Fortunately, equilibrium between thermal particles ($\sim kT$) and the population of relativistic electrons ($\sim \gamma m_0 c^2$) inside a plasma is expected,

$$\begin{aligned} kT &\sim \gamma m_0 c^2 \\ &\sim \left(\frac{\nu}{\nu_c}\right)^{1/2} m_0 c^2 \end{aligned} \tag{A.41}$$

thus, photons in the limit $h\nu \ll kT$ will be absorbed. In this limit, the Rayleigh and Jean law is used to describe the specific intensity of particles with low frequency,

$$\begin{aligned} I_\nu &= 2kT_b\frac{v^2}{c^2} = 2[\gamma m_0 c^2]\frac{v^2}{c^2} = 2\left[\left(\frac{\nu}{\nu_c}\right)^{1/2} m_0 c^2\right]\frac{v^2}{c^2} \\ &= \frac{2m_0c^2}{c^2}\nu_L^{-1/2}\nu^{5/2} \\ &\propto B^{-1/2}\nu^{5/2} \end{aligned} \tag{A.42}$$

So the typical synchrotron spectrum for some sources is made up of both a optically thick part $h\nu \ll kT$ and the optically thin $h\nu \gg kT$. The synchrotron flux of the optically thick part $h\nu \ll kT$ is evaluated by equation,

$$\begin{aligned} F_s(\nu) &\approx I_\nu \theta_s^2 \\ &\propto B^{-1/2}\theta_s^2\nu^{5/2} \end{aligned} \tag{A.43}$$

and for the optically thin is evaluated by equation,

$$F_s(\nu) \propto \theta_s^2 \nu^{-\alpha} B^{1+\alpha} R \tag{A.44}$$

Inferring from the equation of optically thick emission, it is clear that at low frequency, the spectrum increases with the frequency obeying a power law distribution with a slope of 5/2, which is the case for an optically thick medium. When the frequency exceeds the plasma frequency, the medium becomes optically thin, here the slope becomes negative, and the spectrum decreases with increasing frequency with a slope of $-\alpha$. It is advised to compute the optically thick and thin emission of the synchrotron spectrum separately. The perpendicular magnetic field can be determined when an optically thick source is observed. The perpendicular magnetic field, on average, is approximately equal to the magnetic field of the source. A point to note is, not all sources can be observed on the optically thick part since the frequency of the optically thick emission of some sources will be too low for detection. Therefore, the alternative is to observe the optically thin frequencies, which also has its challenges since the emission is dependent on magnetic field strength and the particle density (normalization constant). To evaluate the particle density, the energy contained in the relativistic gas and the associated magnetic field must be determined, which is not an easy task. However, synchrotron radiation is linearly polarized. Therefore, one can investigate the origin of synchrotron radiation through polarization studies since synchrotron emission is intrinsically polarized for electromagnetic fields that are uniform in direction [168, page 270]

A.2.4 Polarization of Synchrotron radiation.

Radiation from synchrotron sources is intrinsically polarized because the acceleration is perpendicular to the magnetic field, where the magnetic field has a coherent structure over large scales. It should be noted that radiation from a single particle is elliptically polarized. However, the total radiation observed from a source derives from particles with a distribution that varies smoothly with the pitch angle. Therefore, net polarization will be linear since the elliptical components will cancel out. Instead of using the intensity we can describe the radiation using its power per unit frequency $P_\perp(\nu)$ and $P_\parallel(\nu)$ as shown by equation A.46 and A.45, respectively [169, page 180,181]. These radiation power components are perpendicular and parallel to the projection of the magnetic field on the plane of the sky (see Figure A.7).

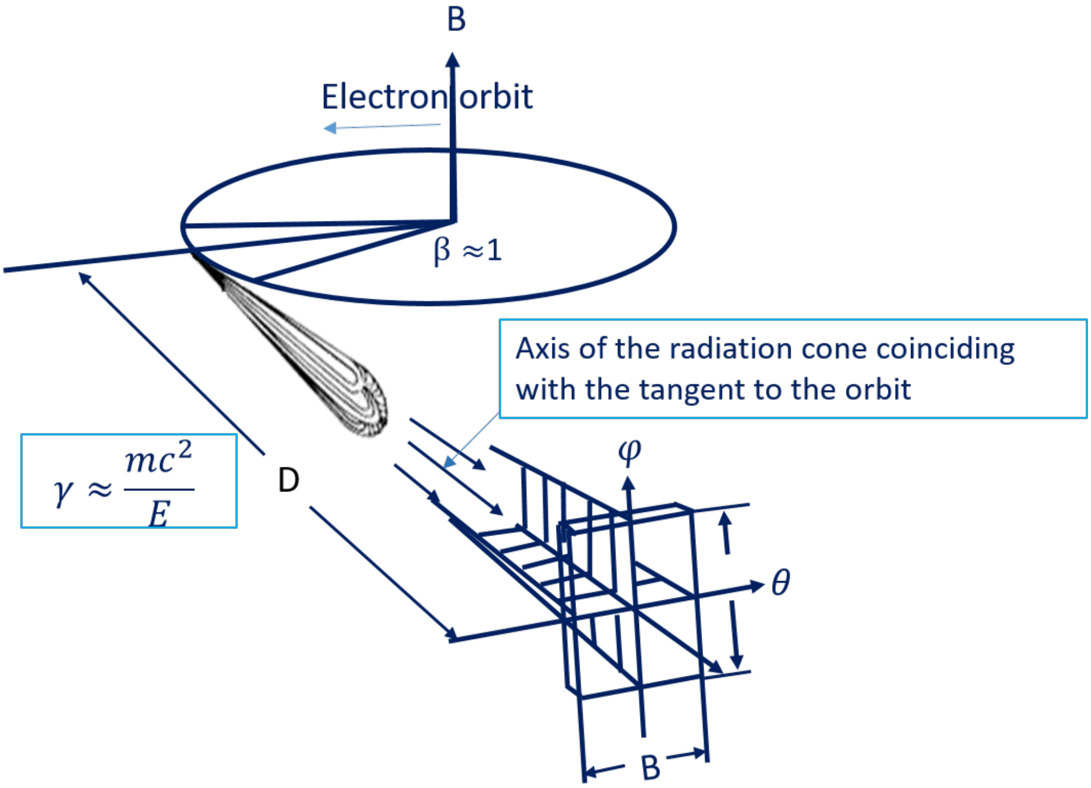

Figure A.7: synchrotron radiation polarization

$$P_\parallel(\nu) = \frac{\sqrt{3}}{16\pi^2}\frac{e^3 B sin\phi}{m}\left[F\left(\frac{\nu}{\nu_c}\right) - G\left(\frac{\nu}{\nu_c}\right)\right] \tag{A.45}$$

$$P_\perp(\nu) = \frac{\sqrt{3}}{16\pi^2}\frac{e^3 B sin\phi}{m}\left[F\left(\frac{\nu}{\nu_c}\right) + G\left(\frac{\nu}{\nu_c}\right)\right] \tag{A.46}$$

where

$$F\left(\frac{\nu}{\nu_c}\right) = \frac{\nu}{\nu_c}\int_{\frac{\nu}{\nu_c}}^{\infty} K_{5/3}(y)dy \tag{A.47}$$

with $K_{5/3}(y)$ the modified Bessel function and

$$G\left(\frac{\nu}{\nu_c}\right) = \frac{\nu}{\nu_c} K_{2/3}\left(\frac{\nu}{\nu_c}\right) \tag{A.48}$$

The plane waves polarization is evaluated using a relationship between maximum and minimum intensity,

$$\Pi = \frac{I_{max} - I_{min}}{I_{max} + I_{min}} \tag{A.49}$$

It only applies for plane waves, and if used for circular or elliptical, it will underestimate the degree of polarization. Since a large potion of the power is emitted in the perpendicular direction the perpendicular power will replace I_{max} and the parallel power will take the I_{min}. Substituting A.45 and A.46 into A.49 the result is the degree of linear polarization of synchrotron radiation equation A.50.

$$\Pi = \frac{P_\perp - P_\parallel}{P_\perp + P_\parallel} = \frac{G\left(\frac{\nu}{\nu_c}\right)}{F\left(\frac{\nu}{\nu_c}\right)} \tag{A.50}$$

If the particle energy distribution assumes a power law, integrating over γ gives the polarization

$$\begin{aligned}\Pi &= \frac{\int_0^\infty G\left(\frac{\nu}{\nu_c}\right)\gamma^{-p} d\gamma}{\int_0^\infty F\left(\frac{\nu}{\nu_c}\right)\gamma^{-p} d\gamma} = \frac{\int_0^\infty G\left(x\right) x^{\frac{p-3}{2}} dx}{\int_0^\infty F\left(x\right) x^{\frac{p-3}{2}} dx} \\ &= \frac{p+1}{p+\frac{7}{3}}\end{aligned} \tag{A.51}$$

Detection of linear polarization from radiation is evidence for the existence of a synchrotron mechanism in any astrophysical environments. Such environment are also known to be sites of relativistic particles, for example, supernova remnants.

A.3 Inverse Compton Radiation

The Inverse-Compton scattering is an inverse process of the Compton scattering. With Compton scattering, unlike Thompson scattering that occurs in the classical regime, quantum effects are taken into account. We see quantum effects in two ways, one within the kinematics of the scattering process and the other within the change of the cross-sections (discussion of these processes follows from Rybicki & Lightman [169, Chapter 7] and Ghisellini [23, Chapter 5]). The photon possesses the relativistic momentum ($h\nu/c$) and energy ($h\nu$), which give rise to the kinematic quantum effects. Scattering in the Thompson limit is elastic because the charge does not recoil contrary to the Compton scattering where the collision is inelastic with the incident photon energy being more than the energy of the scattered photon ($\epsilon_i \neq \epsilon_f$).

A.3.1 Compton scattering

The phenomenon where a scattered photon loses some of its energy to a stationary electron is known as Compton scattering. During the collision, the photon will give away part of its energy to the stationary electron, which will recoil with a kinetic energy that matches the energy lost by a photon. The assumption is that the photon that collides is the same photon that scatters, but in reality, the photon energy is absorbed by the electron, and a new photon with lower energy is emitted. As a result, the photon will have a longer wavelength since part of the energy of the absorbed photon was transformed into kinetic energy of the electron.

Considering a scenario where the incident and scattered photon have frequency ν, the shift in wavelength can be determined using the four-momenta vector, working in the momentum space because momentum is a vector quantity that incorporates magnitude and direction. Before and after the collision, momentum is conserved in both the mutually perpendicular directions. The momentum conservation law requires that momentum in all particles or bodies involved in the collision be conserved. The initial and final momentum of the photon and electron in four-momenta,

$$\vec{P}_\gamma + \vec{P}_e = \vec{P}'_\gamma + \vec{P}'_e \tag{A.52}$$

where subscripts γ and e stands for a photon and an electron respectively and the prime represents the final four-momenta, rearranging and squaring will get the following expression,

$$\vec{P}_\gamma^2 + \vec{P}_e^2 + \vec{P}_\gamma'^2 + 2\vec{P}_\gamma \cdot \vec{P}_e - 2\vec{P}_\gamma \cdot \vec{P}'_\gamma - 2\vec{P}_e \cdot \vec{P}'_\gamma = \vec{P}_e'^2 \tag{A.53}$$

The four-momentum vector for a particle is $\vec{P}_\gamma = (\frac{\epsilon}{c}, \vec{p})$ where $\vec{p}$ is the simple momentum. Squaring this expression gives $P^2 = \frac{\epsilon^2}{c^2} - p^2 = m^2c^2$ since it is an invariant quantity. Therefore substitute this result into the expression of the four-momenta results,

$$m_\gamma^2 c^2 + m_e^2 c^2 + 2\vec{P}_\gamma \cdot \vec{P}_e - 2\vec{P}_\gamma \cdot \vec{P}'_\gamma - 2\vec{P}_e \cdot \vec{P}'_\gamma = m_e^2 c^2 \tag{A.54}$$

where the term $m_\gamma^2 c^2$ is dropped from the expression since a photon does not have rest mass,

$$\vec{P}_\gamma \cdot \vec{P}_e = \vec{P}_\gamma \cdot \vec{P}'_\gamma + \vec{P}_e \cdot \vec{P}'_\gamma \tag{A.55}$$

Now to simplify this expression, the four-momenta of a photon $\vec{P}_\gamma = (\frac{h\nu}{c}, \frac{h\nu}{c}\hat{k}_1)$ and an electron four-momenta $\vec{P}_e = (\frac{mc^2}{c}, 0)$ is used. The general dot product of four-momenta of identical particles is given as $\vec{P}_1 \cdot \vec{P}_1 = (\frac{\epsilon_1}{c}\frac{\epsilon_1}{c} - \vec{p} \cdot \vec{p})$. The shift in wavelength is obtained by substituting these expressions into the expression A.55,

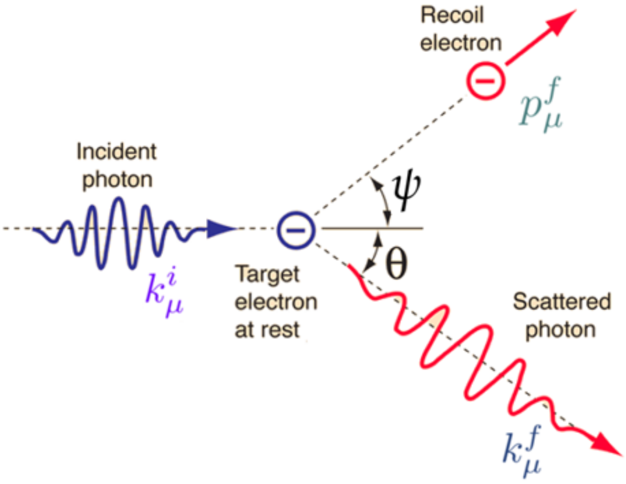

Figure A.8: The Compton effect is the scattering of a photon by an electron. Momentum and energy are conserved in such an incident. Therefore, the scattered photon has a reduced frequency (longer wavelength) as compared to the incident photon.

$$\begin{aligned}
\left[\frac{h\nu}{c},\frac{h\nu}{c}\hat{k}_1\right]\cdot\left[\frac{mc^2}{c},0\right] &= \left[\frac{h\nu}{c}\frac{h\nu^{'}}{c}-\frac{h\nu}{c}\frac{h\nu^{'}}{c}\hat{k}_\mu^i\cdot\hat{k}_\mu^f\right]+\left[\frac{h\nu^{'}}{c},\frac{h\nu^{'}}{c}\hat{k}_\mu^i\right]\cdot\left[\frac{mc^2}{c},0\right]\\
\frac{h\nu}{c}mc &= \frac{h\nu}{c}\frac{h\nu^{'}}{c}(1-cos\theta)+\frac{h\nu^{'}}{c}mc\\
\frac{1}{\lambda} &= \frac{1}{\lambda}\frac{1}{\lambda^{'}}\frac{h}{mc}(1-cos\theta)+\frac{1}{\lambda^{'}}\\
\lambda^{'} &= \lambda+\frac{h}{mc}(1-cos\theta)\\
\Delta\lambda &= \lambda_c(1-cos\theta)
\end{aligned}\tag{A.56}$$

where $\hat{k}_\mu^i\cdot\hat{k}_\mu^f = cos\theta$, and θ is the angle between the direction of the incident $\hat{k}_\mu^i$ and the scattered $\hat{k}_\mu^f$ photon (see Figure A.8). The Compton shift wavelength $\Delta\lambda = \lambda^{'}-\lambda$ varies with direction of the scattered photon and the Compton wavelength $\lambda_c = \frac{h}{mc}$ of the scattering particle. The scattering is nearly elastic when $\lambda \gg \lambda_c$ (i.e., $h\nu \ll mc^2$). Under this circumstance, it can be assumed that the photon energy remains the same before and after the collision.

A.3.2 Inverse Compton scattering

In Compton scattering a stationary electron interacts with a photon in motion. What will happen when both electron and photon are in motion with approximately the same kinetic energy? In a case where both photon and electron are in motion, and the electron's kinetic energy is comparable to the energy of the photon, the collision results in transfer of energy to the photon, a scenario known as inverse Compton scattering. In simple terms inverse Compton scattering is the reverse process of Compton scattering. It occurs when the electron possesses relativistic energies higher than the photon, which makes it possible for the energy to be transferred from the relativistic electron to the photon. This mechanism is seen in the accretion disks of black holes, AGN, pulsars, and peculiar white dwarfs. The inverse Compton mechanism is effective in the production of higher energy gamma-rays through up scattering of lower energy photons.

Inverse Compton scattering can be evaluated in two regimes, in the Thomson and Klein-Nishina limit. These categories follow the energy of the incident photon in the electron rest frame. If the energy of the photon is greater than the rest mass of an electron the process is in the Klein-Nishina regime,

$$x^{'} = \frac{h\nu^{'}}{m_0c^2} > 1 \tag{A.57}$$

and Thomson for vice versa

$$x^{'} = \frac{h\nu^{'}}{m_0c^2} < 1 \tag{A.58}$$

The lab frame energy limits for both regimes can be evaluated by considering ultra-relativistic electrons and the energy of the incoming photon in the rest frame ($K^{'}$) of the electron. An observer in the co-moving frame will see the frequency of the incoming photons Doppler boosted by the Doppler factor $\delta_D = 1/\gamma(1-\beta cos\theta^{'})$,

$$\begin{aligned} \nu^{'} &= \delta_D \nu_{em} = \frac{\nu_{em}}{\gamma(1-\beta cos\theta^{'})} \\ \nu^{'} &= \frac{\nu_{em}}{\gamma(1-\beta^2)} \\ \nu^{'} &= \gamma\nu_{em} \end{aligned} \tag{A.59}$$

Thus, the observer in the rest frame measures a frequency boosted by the Lorentz factor $\gamma = (1-\beta^2)^{1/2}$. In the expression above $\nu^{'}$ is the frequency in the electron rest frame ($K^{'}$) and in this frame $cos\theta^{'} \rightarrow \beta = v/c$, where $\theta^{'}$ is the angle between the incoming photon direction and the direction of the electron's velocity. Thus in the electron co-moving frame the incident photon within the aberration angle $\theta^{'} \leq 1/\gamma$ will be Doppler boosted. Substituting A.59 into A.57 gives an inequality expression for the energy in the lab compared to the rest mass of the electron in the Klein-Nishina regime,

$$h\nu_{em} > \frac{m_0c^2}{\gamma} \tag{A.60}$$

Also substituting A.59 into A.58 gives an inequality expression for the energy in the lab compared to the rest mass of the electron in the Thomson regime

$$h\nu_{em} < \frac{m_0c^2}{\gamma} \tag{A.61}$$

These results can help to determine the regime in which the scattering takes place. The frequency for the scattered photon in the lab frame for the Klein-Nishina regime is given by $\nu_{em} > m_0c^2/\gamma h$ and in the Thomson limit $\nu_{em} < m_0c^2/\gamma h$.

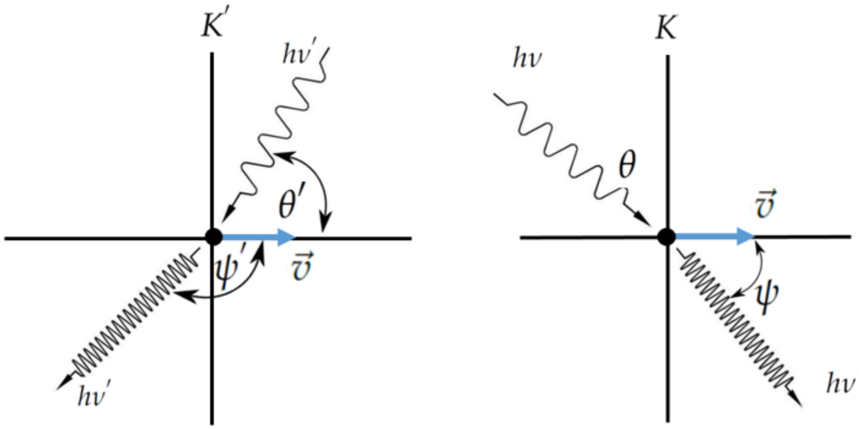

Figure A.9: The geometry of inverse Compton scattering in K and $K^{'}$ reference frames, wherein K frame the electron is considered to be stationary.

A.3.3 Inverse Compton energy transfer

The energy of the incoming photon in the $K^{'}$ frame can be evaluated using the frequency relationship between the lab frame K and electron rest frame $K^{'}$. Both the photon and the electron are in motion, thus to simplify the derivation a fixed frame is considered. Hence, a fixed reference frame is utilised to evaluate the angles between the incoming photon and the relativistic electron, which is assumed to be moving in the x-direction. The following transformation is performed (see Figure A.9). An observer in the $K^{'}$ frame will see a photon with frequency,

$$\begin{aligned}
\nu^{'} &= \frac{\nu_{em}}{\gamma(1-\beta cos\theta')} = \frac{\nu_{em}}{\gamma(1+\beta cos(\pi-\theta'))} = \frac{\nu_{em}}{\gamma(1+\beta cos\psi')} \\
\nu^{'} &= \frac{\nu_{em}}{\gamma\left(1+\beta\left[\frac{cos\psi-\beta}{1-\beta cos\psi}\right]\right)} = \frac{(1-\beta cos\psi)\nu_{em}}{\gamma(1-\beta^{2})} \\
\nu^{'} &= \gamma(1-\beta cos\psi)\nu_{em}
\end{aligned} \tag{A.62}$$

making use of the aberration formula $cos\psi^{'} = \frac{cos\psi-\beta}{1-\beta cos\psi}$ where ψ is the angle between the electron velocity and the incoming photon in the lab system, $\psi^{'} = \pi - \theta^{'}$ and ν_{em} is the frequency of the emitted photon. Therefore the energy of the system can be written,

$$\begin{aligned}
\epsilon^{'} &= h\nu^{'} \\
h\nu^{'} &= \gamma(1-\beta cos\psi)h\nu_{em} \\
\frac{h\nu^{'}}{m_0c^2} &= \gamma(1-\beta cos\psi)\frac{h\nu_{em}}{m_0c^2} \\
x^{'} &= \gamma(1-\beta cos\psi)x
\end{aligned} \tag{A.63}$$

The consistency of this formula can be verified using equations A.59 and A.62. In the $K^{'}$ frame the incoming photon approaches the observer within an angle $sin\theta^{'} \sim 1/\gamma$

and $cos\theta^{'} \sim \beta$. The corresponding angle for $sin\theta^{'} \sim 1/\gamma$ in the K frame is given by solving A.59 and A.62 to get $cos\psi = 0$ which gives $\psi = \pi/2$. Therefore the incoming photons with angles $\psi = \pi/2$ in the co-moving reference frame will have angles $sin\theta^{'} \sim 1/\gamma$. Considering a case where $\theta^{'} \rightarrow 0°$ in $K^{'}$ frame the frequency in the rest frame can be written,

$$\begin{aligned} \nu^{'} &= \frac{\nu_{em}}{\gamma(1-\beta cos\theta^{'})} = \frac{\nu_{em}}{\gamma(1-\beta)} = \frac{(1+\beta)\nu_{em}}{\gamma(1-\beta^2} \\ \nu^{'} &= \gamma(1+\beta)\nu_{em} \end{aligned} \tag{A.64}$$

solving A.62 and A.64 gives $cos\psi = -1$, i.e., $\psi = 180°$. This result implies that photons interact with the electron right from the front in the K frame as well, but now just expressed in terms of $\psi = 180°$.

A.3.4 Inverse Compton scattering energy

Considering energy scattered in the Thomson regime, a convenient way to handle inverse Compton scattering is to evaluate the process in the co-moving reference frame. The scattering process is elastic in the Thompson limit $x^{'} = h\nu^{'}/m_0c^2 < 1$ which means in the $K^{'}$ frame the energy of the incoming photon $x^{'}$ is equal to the energy of the scattered photon $x_1^{'}$ regardless of the angle. The angle between the scattered photon and the electron velocity is $\psi_1^{'}$. The scattered radiation pattern maps the cross-section of a peanut. The energy of the scattered photon in the lab frame can be evaluated by transforming the scattered energy $x_1^{'}$ and the angle $\psi_1^{'}$ in the rest frame $K^{'}$ using the Doppler factor $\delta_D = 1/\gamma(1-\beta cos\psi_1)$.

$$\begin{aligned} x_1 &= \frac{h\nu_1}{m_0c^2} = \delta_D\frac{h\nu_1^{'}}{m_0c^2} \\ x_1 &= \delta_D x_1^{'} = \frac{1}{\gamma(1-\beta cos\psi_1)}x_1^{'} = \frac{1}{\gamma\left(1-\beta\left[\frac{\beta+cos\psi_1^{'}}{1+\beta cos\psi_1^{'}}\right]\right)}x_1^{'} \\ x_1 &= \frac{1+\beta cos\psi_1^{'}}{\gamma(1-\beta^2)}x_1^{'} \\ x_1 &= \gamma(1+\beta cos\psi_1^{'})x_1^{'} \end{aligned} \tag{A.65}$$

Here the aberration formula $cos\psi_1 = (\beta + cos\psi_1^{'})/(1+\beta cos\psi_1^{'})$ is used to simplify and express the scattered energy in the K frame in terms of the $K^{'}$ quantities. The goal is to transform all the quantities and express the scattered energy in the lab frame quantities. This is achieved by making use of $cos\psi_1^{'} = (\beta + cos\psi_1)/(1+\beta cos\psi_1)$ to transform back to the initial expression in the previous expression and substitute $x^{'} = \gamma(1-\beta cos\psi)x$ (equation A.63). The result is the scattered energy expressed in lab frame quantities,

$$\begin{aligned}
x_1 &= \frac{1}{\gamma(1-\beta cos\psi_1)}x_1^{'} \\
x_1 &= \frac{1}{\gamma(1-\beta cos\psi_1)}\gamma(1-\beta cos\psi)x \\
x_1 &= \frac{(1-\beta cos\psi)}{(1-\beta cos\psi_1)}x
\end{aligned} \tag{A.66}$$

Finally, the relationship between the scattered energy and the energy of the incoming photon is expressed in K frame quantities only. Now the maximum and minimum energy transfer can be derived. The maximum energy transfer from electron to the scattered photon is attained when the collision is head-on, and the photon is scattered in the opposite direction from its initial direction. It was shown that when incoming photons approach with an angle of $\psi = 180^\circ$ the scattered photon will have an angle $\psi_1 = 0^\circ$. Substituting these conditions into the expression of the scattered energy in the lab frame gives the maximum energy expression,

$$\begin{aligned}
x_{1,max} &= \frac{(1-\beta cos\psi)}{(1-\beta cos\psi_1)}x = \frac{(1-\beta cos(\pi))}{(1-\beta cos(0))}x = \frac{(1+\beta)}{(1-\beta)}x \\
&= \frac{(1+\beta)(1+\beta)}{(1-\beta)(1+\beta)}x = \gamma^2(1+\beta)^2 x \\
&= 4\gamma^2 x
\end{aligned} \tag{A.67}$$

This expression is only valid when $\beta \to 1$, i.e., $\gamma \gg 1$. The minimum energy transfer from the electron to the scattered photon is obtained when the collision is head to tail. The incoming photon approaches the electron from behind with an angle $\psi = 0^\circ$ and scatters in the opposite direction with an angle $\psi_1 = \pi^\circ$ relative to the electron velocity. Applying these conditions on the expression A.66 gives the minimum energy transfer from the electron,

$$\begin{aligned}
x_{1,min} &= \frac{(1-\beta cos(0))}{(1-\beta cos(\pi))}x = \frac{(1-\beta)}{(1+\beta)}x \\
&= \frac{(1-\beta)(1+\beta)}{(1+\beta)(1+\beta)}x = \frac{1}{\gamma^2(1+\beta)^2}x \\
&= \frac{1}{4\gamma^2}x
\end{aligned} \tag{A.68}$$

This minimum energy transfer expression is only valid when $\beta \to 1$, i.e., $\gamma \gg 1$. The photons are scattered into a cone with respect to the observer in the K where the observer sees all photons within an angle $sin\psi_1 = 1/\gamma$, with a corresponding angle of $cos\psi_1 = \beta$ with energy transfer expression,

$$\begin{aligned} x_1 &= \frac{(1-\beta cos\psi)}{(1-\beta^2)}x \\ &= \gamma^2(1-\beta cos\psi)x \end{aligned} \tag{A.69}$$

This expression evaluates the radiation transfer beamed into a cone, for an angle of $\psi = 0$ the expression reduces to $x_1 = x/(1+\beta)$; for an angle of $\psi = \pi/2$ it becomes $x_1 = \gamma^2 x$ and $x_1 = x/(1-\beta)$ for an angle $\psi = \pi$. The average energy expression after the scattering of an isotropic distribution of incoming photons by ultra-relativistic electrons with speeds approaching the speed of light can also be derived. The first step is to determine the energy density of the background photons as perceived by the observer in the $K^{'}$ frame. The brightness is related to the energy density $u_\nu(\Omega) = I_\nu/c$. Therefore the total energy density in the lab frame is given by,

$$\begin{aligned} U &= \int \left[\int \frac{1}{c} I_\nu d\nu\right] d\Omega \\ U &= \frac{1}{c}\int I d\Omega \end{aligned} \tag{A.70}$$

The lab quantities are transformed to the co-moving frame to determine the energy density measured by an observer in the $K^{'}$ frame. The solid angle is given by $d\Omega^{'} = d\phi^{'} sin\theta^{'} d\theta^{'}$. The angle $\phi^{'}$ is invariant since it is in the plane orthogonal to the motion of relativistic particles and ambient photons so $d\phi^{'} = d\phi$ but $sin\theta^{'} d\theta^{'}$ within the angles $\theta^{'} = [0, 1/\gamma]$ will be replaced with $-dcos\theta^{'}$ within the bounds $cos\theta^{'} = [1, -1]$. The observer in the $K^{'}$ frame will measure the energy density,

$$\begin{aligned} U^{'} &= \frac{1}{c}\int I^{'} d\Omega^{'} \\ &= \frac{1}{c}\int_0^{2\pi} d\phi \int_\beta^1 I^{'} dcos\theta^{'} \\ &= \frac{2\pi}{c}\int_{-1}^1 I^{'} dcos\theta^{'} \end{aligned} \tag{A.71}$$

The observer in the $K^{'}$ frame sees the intensity of the photons as $I^{'} = \delta_D^{'4} I$. Substituting this expression into equation A.71 and integrating gives the expression that describes the energy density in the co-moving frame,

$$\begin{aligned}
U^{'} &= \frac{2\pi}{c}\int_{-1}^{1}\delta_{D}^{'4} I dcos\theta^{'} \\
U^{'} &= \frac{2\pi I}{c}\int_{-1}^{1}\frac{1}{[\gamma(1-\beta cos\theta^{'})]^{4}}dcos\theta^{'} \\
U^{'} &= \frac{2\pi I}{\gamma^{4}c}\int_{-1}^{1}\left[1-\beta cos\theta^{'}\right]^{-4}dcos\theta^{'}.
\end{aligned} \tag{A.72}$$

Through inspection it is clear that $d/dcos\theta^{'}(1-\beta cos\theta^{'})^{-3} = 3\beta(1-\beta cos\theta^{'})^{-4}$. The solution of the energy density integral $\int(1-\beta cos\theta^{'})^{-4}$ is $1/[3\beta(1-\beta cos\theta^{'})^{3}]$. Therefore, the energy density in the co-moving frame is given by,

$$\begin{aligned}
U^{'} &= \frac{2\pi I}{\gamma^{4}c}\left[\frac{1}{3\beta\left(1-\beta cos\theta^{'}\right)^{3}}\right]_{-1}^{1} \\
U^{'} &= \frac{4}{3}\gamma^{2}\left[\frac{4\pi I}{c}\right] \\
U^{'} &= \frac{4}{3}\gamma^{2}U_{iso}
\end{aligned} \tag{A.73}$$

where U_{iso} is the isotropic energy density distribution. Therefore, the average scattered energy of an electron is determined from the expression describing the energy density in the co-moving frame of the electron. The observer in the $K^{'}$ frame will see energy density $U^{'} = N^{'}\langle\epsilon^{'}\rangle/(V^{'})$ and $U_{iso} = N\langle\epsilon\rangle/V$ where $N^{'}$ and N are the number of photons in the $K^{'}$ and K frame respectively, only valid for electron velocities approaching the speed of light, i.e., $\beta \rightarrow 1$. Inserting these results into the equation A.73 gives,

$$\begin{aligned}
\frac{N^{'}\langle\epsilon^{'}\rangle}{V^{'}} &= \frac{4}{3}\gamma^{2}\frac{N\langle\epsilon\rangle}{V} \\
\frac{\langle\epsilon^{'}\rangle}{\langle\epsilon\rangle} &= \frac{4}{3}\gamma^{2}\frac{V^{'}}{V}
\end{aligned} \tag{A.74}$$

where the number of photons observed in the $K^{'}$ and K frames are the same, i.e., $N^{'} = N$. The volume in the co-moving frame is related to the volume in the lab frame $V^{'} = A^{'}l^{'} = A\gamma l$,i.e., $\gamma = \frac{V^{'}}{V}$. In the $K^{'}$ frame the electron scatters the photon elastically in the Thomson limit $\langle\epsilon^{'}\rangle = \langle\epsilon_{1}^{'}\rangle$, inserting these results into equation A.74 gives,

$$\frac{\langle\epsilon_{1}^{'}\rangle}{\langle\epsilon\rangle} = \frac{4}{3}\gamma^{2}\gamma \tag{A.75}$$

Averaging the system's energy equation A.63, the system's energy reduces to $\langle \epsilon_1^{'} \rangle = \gamma(1 - \beta \langle cos\psi \rangle)\langle \epsilon_1 \rangle$ which further reduces to $\langle \epsilon_1^{'} \rangle = \gamma \langle \epsilon_1 \rangle$ since $\langle cos\psi \rangle = 0$. Inserting these results into equation A.75, the result is the photon's average energy after collision and scattering,

$$\langle \epsilon_1 \rangle = \frac{4}{3}\gamma^2 \langle \epsilon \rangle \tag{A.76}$$

This equation is the average energy of the up-scattered photon, and from it the average frequency of the up-scattered photon is deduced as,

$$\begin{aligned} h\langle \nu_1 \rangle &= \frac{4}{3}\gamma^2 h \langle \nu \rangle \\ \langle \nu_1 \rangle &= \frac{4}{3}\gamma^2 \langle \nu \rangle \end{aligned} \tag{A.77}$$

A.3.5 Inverse Compton single electron Power

The derivation of the inverse Compton power the non-relativistic case is first considered. Through Thomson scattering, the electric field of the incident electromagnetic radiation will accelerate the electron if the Poynting flux of the incoming plane wave on the electron is,

$$\vec{S} = \frac{c}{4\pi}\vec{E} \times \vec{B} = \frac{c}{4\pi}|\vec{E}|^2 \tag{A.78}$$

where $\vec{B}$ and $\vec{E}$ are the magnetic and electric field respectively. According to the Larmor equation the accelerated electron will radiate a photon with a frequency the same as the absorbed photon, i.e., the part of the incoming radiation will be scattered with no net energy transfer between the electron and the radiation. The scattered radiation power is the product of the absolute Poynting flux and the Thomson cross section $\sigma_T \equiv \frac{8\pi}{3}\left(\frac{e^2}{m_e c^2}\right) \approx 6.65 \times 10^{-25}$ cm^2, defined by the following equation,

$$P = |\vec{S}|\sigma_T \tag{A.79}$$

More precisely, the electron absorbs from the incoming wave the amount of power passing through the Thomson cross-section area and emit the radiation with the same power spreading it over a doughnut-shaped pattern described by the Larmor equation. Writing the scattered power in terms of the Thomson scattering and the energy density of the incident radiation,

$$P_{B\_field} = \sigma_T c U_{ph} \tag{A.80}$$

where U_{ph} is the total energy density of the background photon field (the incoming radiation) defined as $U_{ph} = |\vec{S}|/c$. This is the background field power that contributes to the inverse Compton scattering power.

To calculate the inverse Compton scattering total loss rate the rate of scattering in the K frame quantities for each electron is determined, i.e., the rate of scattering per electron for one direction in the photon distribution is defined as,

$$\frac{dN}{dt} = \int \sigma_T v_{rel} n(\epsilon) d\epsilon \tag{A.81}$$

where $v_{rel} = c(1 - \beta cos\psi)$ is the relative velocity between the incident photon and the electron and ψ is the angle between the incident photon and the velocity of the electron with $\beta = v/c$ where v is the velocity of the electron and $n(\epsilon)$ is the photon number density with energy $\epsilon = h\nu$, i.e.,

$$\frac{dN}{dt} = \int \sigma_T c(1 - \beta cos\psi) n(\epsilon) d\epsilon \tag{A.82}$$

It can be seen that the number or the rate of scattering between the incident photon and the electron is $dN/dt \propto (1 - \beta cos\psi)$. This means there is no scattering if the angle between the incoming photon and the electron approach zero, and the speed of the electron approaches the speed of light $\beta \to 1$. This implies that the optical depth will be significantly reduced, and the electrons move in the same direction. The power contained in the scattered radiation is the product of the energy of the scattered photon ϵ_1 and the rate of scattering,

$$\frac{d\epsilon_\gamma}{dt} = \epsilon_1 \frac{dN}{dt} \tag{A.83}$$

Since $x = \epsilon/(m_0 c^2)$, it implies that the energy can also be written as $x_1 = \epsilon_1/(m_0 c^2)$, i.e., $\epsilon_1 = \epsilon(1 - \beta cos\psi)/(1 - \beta cos\psi_1)$. Therefore the power in the scattering radiation becomes

$$\begin{aligned} \frac{d\epsilon_\gamma}{dt} &= \epsilon_1 \int \sigma_T c(1 - \beta cos\psi) n(\epsilon) d\epsilon \\ &= \int \sigma_T c(1 - \beta cos\psi) \epsilon \frac{(1 - \beta cos\psi)}{(1 - \beta cos\psi_1)} n(\epsilon) d\epsilon \\ &= \int \sigma_T c\epsilon \frac{(1 - \beta cos\psi)^2}{(1 - \beta cos\psi_1)} n(\epsilon) d\epsilon \end{aligned} \tag{A.84}$$

The observer in the K frame will see the photons scattered into a forward cone with half angle $sin\psi_1 = 1/\gamma$, i.e., $cos\psi_1 = \beta$. Accordingly, relativistic electrons radiation in scattering power will reduce to,

$$\begin{aligned}\frac{d\epsilon_\gamma}{dt} &= \int \sigma_T c\epsilon \frac{(1-\beta cos\psi)^2}{(1-\beta^2)} n(\epsilon) d\epsilon \\ &= \sigma_T c\epsilon\gamma^2 \int (1-\beta cos\psi)^2 n(\epsilon) d\epsilon\end{aligned} \tag{A.85}$$

The quantity $(1-\beta cos\psi)^2 = (1-2\beta cos\psi + \beta cos^2\psi)$ is averaged over the solid angle, i.e., $\langle cos\psi\rangle = 0$ and $\langle cos^2\psi\rangle = 1/3$ since an isotropic distribution of incident photons is assumed. Therefore the quantity $(1-\beta cos\psi)^2$ will become $(1+\frac{\beta^2}{3})$. Thus, the power of the scattered radiation is,

$$\begin{aligned}\left\langle \frac{d\epsilon_\gamma}{dt} \right\rangle &= \sigma_T c\gamma^2 \int (1-2\beta\langle cos\psi\rangle + \beta\langle cos^2\rangle\psi)\epsilon n(\epsilon) d\epsilon \\ &= \left(1+\frac{\beta^2}{3}\right)\sigma_T c\gamma^2 \times \int \epsilon n(\epsilon) d\epsilon \\ &= \left(1+\frac{\beta^2}{3}\right)\sigma_T c\gamma^2 \times U_{ph} \\ &= \left(1+\frac{\beta^2}{3}\right)\sigma_T c\gamma^2 \times \epsilon_{ph} n_{ph} \\ &= \left[\left(1+\frac{\beta^2}{3}\right)\gamma^2\epsilon_{ph}\right] \times \left[\sigma_T c n_{ph}\right]\end{aligned} \tag{A.86}$$

where from this expression it is clear that $\left[\left(1+\frac{\beta^2}{3}\right)\gamma^2\epsilon_{ph}\right] = \left[\frac{4}{3}\gamma^2\epsilon_{ph}\right] = \epsilon_1$ for electrons moving with relativistic speeds ($\beta \rightarrow 1$) and the remaining factor in the expression is the rate at which the energy is changing. This is the total power of the scattered radiation. The expression contains the already existing background photon field power equation A.80 and the inverse Compton power. Thus to probe only the inverse Compton power one should subtract the background field power.

$$\begin{aligned}P_{IC} &= \left\langle \frac{d\epsilon_\gamma}{dt} \right\rangle - P_{B\_field} \\ &= \left(1+\frac{\beta^2}{3}\right)\sigma_T c\gamma^2 U_{ph} - \sigma_T c U_{ph} \\ &= \gamma^2 c\sigma_T U_{ph} + \frac{\gamma^2\beta^2}{3} c\sigma_T U_{ph} - c\sigma_T U_{ph} \\ &= \frac{c\sigma_T U_{ph}}{1-\beta^2} + \frac{\frac{1}{3}\beta^2 c\sigma_T U_{ph}}{1-\beta^2} - \frac{1-\beta^2}{1-\beta^2} c\sigma_T U_{ph} \\ &= \frac{4}{3}\gamma^2\beta^2 c\sigma_T U_{ph}\end{aligned} \tag{A.87}$$

This result shows that if the speed of ambient electrons approaches the speed of light, the total power contained in the scattered radiation is dominated by the inverse

Compton power, i.e., the contribution of the background power is insignificant. This has some similarity to the power of the synchrotron radiation

$$P_{syn} = \frac{4}{3}\gamma^2\beta^2 c\sigma_T U_{mag} \tag{A.88}$$

Thus when the electrons moving with speeds close to the speed of light are in a region with both magnetic and radiation energy densities, these electrons will radiate through inverse Compton scattering and synchrotron mechanisms. In this case, the ratio of the power produced by each process is,

$$\frac{P_{syn}}{P_{IC}} = \frac{U_{mag}}{U_{ph}} \tag{A.89}$$

At low-frequencies electrons can absorb and radiate synchrotron radiation. Thus synchrotron cooling of relativistic electrons can also manifest in the heating of the thermal plasma through absorption processes. At high-frequencies scattering takes place in the Klein Nishina regime, i.e., cooling and scattering are less due to a smaller cross-section.

The focus has been on photons with an isotropic distribution. How do relativistic electrons and anisotropic photons behave? In the first case, the photons which come mainly from the front and back are considered. The gamma-ray production rate equation A.85 is employed here all quantities are kept constant except for the term that depends on direction. The resulting power is given by,

$$\begin{aligned}\frac{d\epsilon_\gamma}{dt} &= \int \sigma_T c\epsilon \frac{(1-\beta cos\psi)^2}{(1-\beta^2)} n(\epsilon)d\epsilon \\ \frac{d\epsilon_\gamma}{dt} &= \left[\sigma_T c\gamma^2 \int \epsilon n(\epsilon)d\epsilon\right](1-\beta cos\psi)^2 \\ P_\gamma(\mu) &= \frac{d\epsilon_\gamma(\mu)}{dt} = \kappa(1-\beta\mu)^2\end{aligned} \tag{A.90}$$

where $\mu = cos\psi$ and $\kappa = \left[\sigma_T c\gamma^2 \int \epsilon n(\epsilon)d\epsilon\right]$. The power expression above expressed as a function of angle is integrated to find its dependence on angles,

$$\begin{aligned}\int P_\gamma(\mu)d\mu &= \kappa\int(1-\beta\mu)^2 d\mu \\ P_\gamma &= \kappa\int(1-\beta\mu)^2 d\mu\end{aligned} \tag{A.91}$$

The resulting power expression is handy to express and find the contribution of photons from different directions. Photon fields mainly from the front will approach within an angle $\psi = [\frac{\pi}{2}, \pi]$ which translates to $\mu = [0, -1]$, and photons from the back with angular bounds $\psi = [0, \frac{\pi}{2}]$ and corresponding bounds $\mu = [1, 0]$. The ratio between the gamma-ray produced from photons from the front and photons from the back is ,

$$\begin{aligned}\frac{P_\gamma(up)}{P_\gamma(down)} &= \frac{2\kappa\int_{-1}^{0}(1-\beta\mu)^2 d\mu}{2\kappa\int_{0}^{1}(1-\beta\mu)^2 d\mu} \\ &= \frac{\left[\mu-\beta\mu+\beta^2\frac{\mu^3}{3}\right]_{-1}^{0}}{\left[\mu-\beta\mu+\beta^2\frac{\mu^3}{3}\right]_{0}^{1}} = 7\end{aligned} \tag{A.92}$$

The expression is valid only for an electron moving with relativistic speeds $\beta \rightarrow 1$. All the radiation is assumed to be produced along the electron's velocity vector. The scattering with the up-stream photons is seven times higher than with the photons coming from the back. A comparison of photon fields from the side and the front is,

$$\frac{P_\gamma(up)}{P_\gamma(side)} = \frac{2\kappa\int_{-1}^{0}(1-\beta\mu)^2 d\mu}{\kappa\int_{-1}^{1}(1-\beta\mu)^2 d\mu} = \frac{7}{4} \tag{A.93}$$

A.3.6 Single scattering spectra of inverse Compton

The inverse Compton scattering spectra depend on both the electron energy distribution and the incident spectrum. Fortunately, the general spectrum is obtained by simply averaging the entire distribution of electrons and photons. It is assumed that the electrons are traversing a region where the ambient photon energy density is given by U_{ph} and these photons are monochromatic. Accordingly, the energy (or frequency) of the photons can be non-dimensionalized, $x = h\nu/(m_e c^2)$. In the rest frame of the electrons, it is assumed that electrons are at rest with photons that appear to approach from the front within a half-angle $1/\gamma$. These photons will have a typical frequency $\nu^{'} = \gamma\nu_{em}$, which is double the frequency of photons that approaches precisely head-on. This expression is obtained by averaging equation A.62

$$\begin{aligned}\langle\nu^{'}\rangle &= \gamma(1-\beta\langle cos\psi\rangle)\langle\nu_{em}\rangle \\ \langle\nu^{'}\rangle &= \gamma\nu_{em}\end{aligned} \tag{A.94}$$

The scattering in the $K^{'}$ frame appear to occur in the Thomson regime which means the frequency of the incident photon will be equal to the frequency of the scattered photon ($\nu_1^{'} = \nu^{'}$). The angular pattern of the scattered radiation follows that of the Thomson cross section peanut shape spatial distribution. All photons in $K^{'}$ scattered within the half sphere $\psi_1^{'} \leq \frac{\pi}{2}$ will have angles viewed from the K frame $sin\psi_1$ with corresponding angle $cos\psi_1 = \beta$. These conditions were already applied to the scattered energy expression equation A.66 in the K frame and the resulting expression $x_1 = \gamma^2(1-\beta cos\psi)x$ equation A.69, if averaged over the solid angle gives,

$$\begin{aligned}\langle x_1\rangle &= \gamma^2(1-\beta\langle cos\psi\rangle)\langle x\rangle \\ \langle x_1\rangle &= \gamma^2 x \\ \langle \nu_1\rangle &= \gamma^2 \nu\end{aligned} \tag{A.95}$$

As expected the inverse Compton scattering boosts the ambient photon field by a factor $\gamma^{'}$. The photons' average energy was calculated earlier (photon spectrum) (see equation A.76).

A.3.7 Many electrons spectrum

The spectrum of a single electron is peaked, and it was shown that the up-scattered photons have boosted frequency with a factor γ^2. There is some similarity that exists between this spectrum and the synchrotron case. Thus, the expression for the inverse Compton emissivity is obtained in the same way as in the synchrotron case. It is assumed that relativistic electrons are distributed with a power law distribution. It is known that the number density of electrons $N(\gamma)$ within $[\gamma, \gamma + d\gamma]$ is equal to the number density of electrons $N(\epsilon)$ within $[\epsilon, \epsilon + d\epsilon]$. Thus,

$$N(\epsilon) = \frac{dN}{d\epsilon} = k_2\epsilon^{-p} = k_1\gamma^{-p} = N(\gamma) \tag{A.96}$$

An isotropic distribution of electrons is assumed, and to simplify the case an isotropic distribution of seed electrons and monochromatic frequency emission is also assumed. Using the average scattered frequency equation A.77 the expression for γ is,

$$\begin{aligned}\nu_{IC} &= \frac{4}{3}\gamma^2\nu_0 \\ \gamma &= \left[\frac{3}{4}\frac{\nu_{IC}}{\nu_0}\right]^{1/2}\end{aligned} \tag{A.97}$$

Differentiating γ with respect to the inverse Compton scattering frequency ν_{IC} gives,

$$\left|\frac{d\gamma}{d\nu_{IC}}\right| = \frac{\nu_{IC}^{-1/2}}{2}\left[\frac{3}{4\nu_0}\right]^{1/2} \tag{A.98}$$

The electrons within the energy bounds $[\gamma, \gamma + d\gamma]$ will transfer their power into radiation with frequencies between $[\nu, \nu + d\nu]$. Now the inverse Compton emissivity is written as,

$$\begin{aligned}\varepsilon_{IC}(\nu_{IC})d\nu_{IC} &= \frac{1}{4\pi}N(\gamma)P_{IC}(\gamma)d\gamma \\ \varepsilon_{IC}(\nu_{IC}) &= \frac{1}{4\pi}N(\gamma)P_{IC}(\gamma)\frac{d\gamma}{d\nu_{IC}}\end{aligned} \tag{A.99}$$

where $N(\gamma) = K\gamma^{-p}$, substituting this expression and equation A.87, A.97 and A.98 into equation A.99 gives the emissivity expression of inverse Compton scattering,

$$\begin{aligned}\varepsilon_{IC}(\nu_{IC}) &= \frac{1}{4\pi}K\left[\frac{3}{4}\frac{\nu_{IC}}{\nu_0}\right]^{1/2-p}\left[\frac{4}{3}\left(\frac{3}{4}\frac{\nu_{IC}}{\nu_0}\right)\beta^2 c\sigma_T U_{ph}\right]\left[\frac{\nu_{IC}^{-1/2}}{2}\left(\frac{3}{4\nu_0}\right)^{1/2}\right] \\ \varepsilon_{IC}(\nu_{IC}) &= \frac{K}{4\pi}\frac{\left(\frac{4}{3}\right)^{-\left(\frac{p-1}{2}\right)}}{2}\beta^2 c\sigma_T\frac{U_{ph}}{\nu_0}\left(\frac{\nu_{IC}}{\nu_0}\right)^{-\left(\frac{p-1}{2}\right)}\end{aligned} \tag{A.100}$$

From this expression it is clear that the inverse Compton emissivity is proportional to frequency, i.e., $\varepsilon_{IC}(\nu_{IC}) \propto \left(\frac{\nu_{IC}}{\nu_0}\right)^{-\alpha}$ where $\alpha = \left(\frac{p-1}{2}\right)$ is the spectral index. It is also possible to express the emissivity of inverse Compton scattering as a function of photon energy as follows,

$$\begin{aligned}\varepsilon_{IC}(\nu_{IC}) &= \frac{d\epsilon}{dVdtd\Omega d\nu} \\ \frac{\varepsilon_{IC}(\nu_{IC})}{h} &= \frac{d\epsilon}{dVdtd\Omega d(h\nu)} \\ \varepsilon_{IC}(h\nu_{IC}) &= \frac{1}{h}\times\frac{R}{R}\times\frac{K}{4\pi}\frac{\left(\frac{4}{3}\right)^{-\left(\frac{p-1}{2}\right)}}{2}\beta^2 c\sigma_T\frac{U_{ph}}{\nu_0}\left(\frac{\nu_{IC}}{\nu_0}\right)^{-\left(\frac{p-1}{2}\right)} \\ \varepsilon_{IC}(h\nu_{IC}) &= \frac{1}{4\pi}\frac{\left(\frac{4}{3}\right)^{-\left(\frac{p-1}{2}\right)}}{2}\frac{\tau_{IC}}{R/C}\beta^2\frac{U_{ph}}{h\nu 0}\left(\frac{\nu_{IC}}{\nu_0}\right)^{-\left(\frac{p-1}{2}\right)}\end{aligned} \tag{A.101}$$

where $\tau_{IC} = Kc\sigma_T$. For $\tau_{IC} < 1$ the optical depth represents the fraction of the seed photon density $\frac{U_{ph}}{h\nu_0} = \frac{nh\nu_0}{h\nu_0 h\nu_0} = n$ cm $^{-3}$ undergoing inverse Compton scattering in a time R/C with $\nu_{IC}/\nu_0 \sim \gamma^2$ the average gain in energy per scatter. This analysis is based on the assumption of monochromatic seed photons , one can also consider a case where the seed photons are not monochromatic.

A.3.8 Cooling Time and Compactness

The cooling time for inverse Compton scattering emission can be determined as follows,

$$\begin{aligned}t_{IC} &= \frac{\epsilon}{P_{IC}(\gamma)} = \frac{\gamma m_0 c^2}{\frac{4}{3}\sigma_T c\gamma^2\beta^2 U_{ph}} \\ t_{IC} &= \frac{3m_0c^2}{4\sigma_T\gamma U_{ph}}\end{aligned} \tag{A.102}$$

This expression describes the situation of the relativistic electrons. The cooling time expression allows one to introduce an important parameter called the compactness parameter, which is the ratio between the luminosity L of a source and its radius R. There exists a relationship between energy density U_{ph} and luminosity since there is a link between flux F and energy density $F = I\Delta\Omega = U_{ph}c$. Expressing the energy density in terms of flux but remembering that flux is given by,

$$\begin{aligned} F &= \frac{L}{4\pi R^2} = U_{ph}c \\ U_{ph} &= \frac{L}{4\pi R^2 c} \end{aligned} \tag{A.103}$$

This expression of the energy density is valid outside the source, at distance R from the source's center. In this instance, the denominator $4\pi R^2 c = 4\pi R^2(l_{ph}/\Delta t)$ is the volume of the shell traversed by the source radiation in one second. However, inside a homogeneous source a better way to determine the energy density is to determine the average time needed for a photon to cross the source, where for an optical thin source $t_{esc} = \frac{3}{4}\frac{R}{c}$, i.e., $t_{esc} \leq \frac{R}{c}$. This implies that the photons that do manage to escape the source are not produced at the centre. Therefore from the formalism it can be shown that,

$$\begin{aligned} U_{ph} &= \left(\frac{L}{V} \times \Delta t_{esc}\right) = \frac{L}{\frac{4}{3}\pi R^2} \times \frac{3}{4}\frac{R}{c} \\ &= \frac{9}{4}\frac{L}{4\pi R^2 c} \end{aligned} \tag{A.104}$$

The resulting energy density is $\frac{9}{4}$ greater than the energy density determined in the equation A.103, which is the energy density where photons can escape. However, substituting the expression for the photon energy density equation A.103 into the expression for the cooling time equation A.102, the compactness parameter is introduced,

$$\begin{aligned} t_{IC} &= \frac{3\gamma m_0 c^2}{4\sigma_T c\gamma\left[\frac{L}{4\pi R^2 c}\right]} = \frac{3\pi m_e c^3 R}{\sigma_T \gamma L}\frac{R}{c} \\ \frac{t_{IC}}{\frac{R}{c}} &= \frac{3\pi}{\gamma} \times \frac{1}{l} \end{aligned} \tag{A.105}$$

The compactness parameter is defined as $l = \frac{\sigma_T L}{m_e c^3 R}$. It is clear that this parameter depends on the luminosity and radius, i.e., $l \propto \frac{L}{R}$. This parameter can help to deduce whether inverse Compton cooling is the dominant processing in cooling the ambient electrons. The inverse Compton is dominant when $l > 1$. When this condition is met, even electrons with low energy will cool through the inverse Compton process. Through the compactness parameter, the optical depth can be determined, and the mean free path. Therefore, it is possible to check the occurrence of photon-photon collisions, which may lead to the production of electron-positron pairs. Gamma-ray photons are destroyed by photon-photon collisions if the compactness parameter is much greater than unity. The source will not emit VHE-TEV gamma-rays, since their annihilation would result in substantial flux of positron and electrons within the region of the source.

A.4 Synchrotron Self-Compton

Magnetised plasmas filled with relativistic electrons are perfect sites for Synchrotron Self-Compton processes (SSC). The relativistic electrons in these plasmas will fill the region with photons through the synchrotron radiation processes. These synchrotron photons will be boosted (up-scattered) to higher energies when they interact with relativistic electrons. This process is called synchrotron self-Compton process (see Figure A.10). In this process, the electrons do work twice, producing the synchrotron photons and scattering these photons up to the higher energies.

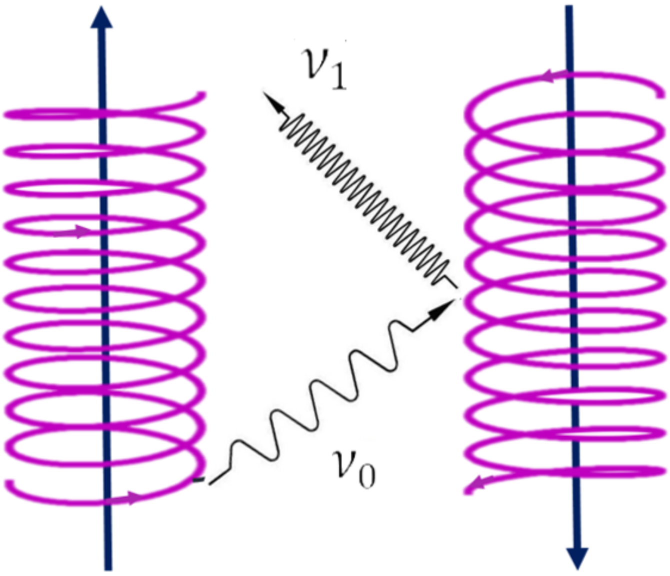

Figure A.10: A schematic diagram showing the electrons working twice first to produce synchrotron photon ν_0 and secondly scatter these photons up to higher energy photon ν_1. The purple coils represents the electron following helical motion around the magnetic field indicated by blue arrows.

A.4.1 SSC emissivity

The significance of this process is high for systems with high relativistic electron density, high magnetic field energy density, and photon density. If the relativistic electrons take a power law distribution, the SSC flux is expected to scale as the quadratic electron density K^2. This expectation follows the fact that the electron works twice. The emissivity of inverse Compton radiation is given by equation [23, page 92],

$$\varepsilon_c(\nu_c) = \frac{1}{4\pi}\frac{(4/2)^{\alpha}}{2}\frac{\tau_c}{R/c}\nu_c^{-\alpha}\int_{\nu min}^{\nu max}\frac{U_r(\nu)}{\nu}\nu^{\alpha}d\nu \tag{A.106}$$

Since it is assumed that photons are produced by synchrotron emitting electrons, the appropriate expression for the synchrotron radiation energy density is substituted,

$$\begin{aligned} U_s(\nu) &= \frac{L_\nu(ergs^{-1}Hz^{-1})}{V} \times t_{esc} = \frac{L_\nu}{V} \times \left(\frac{3R}{4c}\right) = \frac{L_\nu}{4\pi V} \times 4\pi \left(\frac{3R}{4c}\right) \\ &= \varepsilon_\nu(s) \times 4\pi \left(\frac{3R}{4c}\right) \end{aligned} \tag{A.107}$$

where V is the volume of the source, and the factor $3R/4c$ is the average photon source-crossing time. For a simple power law, the synchrotron emissivity can be written as $\varepsilon_s(\nu) = \varepsilon_{s,0}\nu^{-\alpha}$. Substituting equation A.107 into A.106, the result is the SSC emissivity,

$$\begin{aligned} \varepsilon_{SSC}(\nu_c) &= \frac{1}{4\pi}\frac{(4/2)^\alpha}{2}\frac{\tau_c}{R/c}\nu_c^{-\alpha}\int_{\nu min}^{\nu max}\frac{\varepsilon_\nu(s) \times 4\pi\left(\frac{3R}{4c}\right)}{\nu}\nu^\alpha d\nu \\ &= \frac{(4/2)^{\alpha-1}}{2}\tau_c \varepsilon_{s,0}\nu_c^{-\alpha}\int_{\nu min}^{\nu max}\frac{d\nu}{\nu} \end{aligned} \tag{A.108}$$

The term $\varepsilon_{s,0}\nu_c^{-\alpha} = \varepsilon_s(\nu_{IC})$ is the synchrotron emissivity at inverse Compton scattering frequencies. Therefore, equation A.108, after integrating, gives the following expression,

$$\begin{aligned} \varepsilon_{SSC}(\nu_{IC}) &= \frac{(4/2)^{\alpha-1}}{2}\tau_c \varepsilon_{s,0}\nu_c^{-\alpha} ln\Lambda \\ &= \frac{(4/2)^{\alpha-1}}{2}\tau_c \varepsilon_s(\nu_{IC}) ln\Lambda \end{aligned} \tag{A.109}$$

Substituting the optical depth $\tau_c = R\sigma_T K$, and the synchrotron emissivity $\varepsilon_s(\nu,\phi) = \varepsilon_s(\nu_{IC}) \propto KB^{1+\alpha}\nu_{IC}^{-\alpha}$ (equation A.39) into the SSC emissivity expression A.109 it is clear that the emissivity of the SSC scales as a quadratic.

$$\begin{aligned} \varepsilon_{SSC}(\nu_{IC}) &\propto \tau_c \varepsilon_{s,0}\nu_c^{-\alpha} ln\Lambda \\ &\propto R\sigma_T KKB^{1+\alpha}\nu_{IC}^{-\alpha} \\ &\propto K^2 \end{aligned} \tag{A.110}$$

Using the results of equation A.109, the ratio between the synchrotron and SSC emissivity flux can be estimated by the following expression,

$$\frac{\varepsilon_{SSC}(\nu_{IC})}{\varepsilon_s(\nu_{IC})} \sim \tau_c ln\Lambda \tag{A.111}$$

Figure A.11 gives a summary of the activities of SSC radiation, which show different slopes. The frequency part ν on the νF_ν is behind the different slopes shown on the

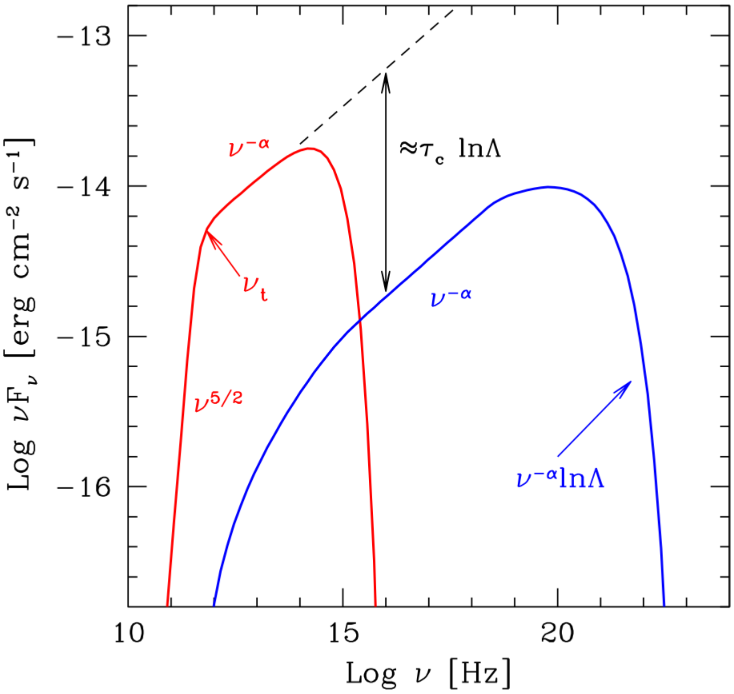

Figure A.11: The spectrum of Synchrotron Self-Compton, shown in the plane of νF_ν as a function of ν [23, page 105-106].

plot. If one is confident that the spectrum of a particular source is generated by the mechanism of synchrotron Self-Compton then it is possible to estimate parameters of the source such as the magnetic field [23, page 105-106].

A.5 Pion production

In this section a brief discussion of pion production is highlighted. For a detailed discussion of pion production refer to Longair ([170, page 292-293, 503]). Highly relativistic protons and nuclei in astrophysical shocks where charged particles are accelerated to higher energies, such as AGN, supernovae and possibly nova environments, produce gamma-rays through a chain process. If these particles move through a non-relativistic ambient medium, or through an intense radiation field they suffer losses through collisions with nuclei (N) or photons (γ). Pion production will result if these collisions occur above a certain threshold in reactions like ,

$$\begin{aligned} p + \gamma &\rightarrow p + \pi^o \\ p + N &\rightarrow p + N + \pi^o \end{aligned} \tag{A.112}$$

The production of pions always has a threshold, i.e., the incoming proton has to have a minimum energy for the reaction to take place. In this section the $p - \gamma$ and $p - p$ interactions are investigated. This reaction near threshold proceeds via a short lived resonance particle $\Delta^+(1232)$ with mass 1232 MeV.

A.5.1 Particle-Photon Pion Production

The reaction looks like the following,

$$p + \gamma \Rightarrow \Delta^{+}(1232) \Rightarrow \begin{cases} p^{+} + \pi^{o} & \textit{neutral pion production} \\ n + \pi^{+} & \textit{charged pion production} \end{cases}$$

The conversation law in the four-vector energy momentum can be expressed in a single equation as in equation A.113,

$$p^{Y} + q^{Y} = p_{\Delta}^{Y} = p^{2Y} + Q^{Y} = S^{Y} \tag{A.113}$$

where the four-momentum of the particles involved are

$$\begin{aligned} Proton : p^{Y} &= \gamma_{p} m_{p} c \begin{pmatrix} 1 \\ \beta_{p} \end{pmatrix} \\ Photon : p_{\gamma}^{Y} &= \frac{\epsilon_{ph}}{c} \begin{pmatrix} 1 \\ k \end{pmatrix} \\ Pion : p_{\pi}^{Y} & \gamma_{\pi} m_{\pi} c \begin{pmatrix} 1 \\ \beta_{\pi} \end{pmatrix} \end{aligned} \tag{A.114}$$

The Lorentz invariant length squared of this four-vector yields the relation.

$$\begin{aligned} p^{2} &= \eta_{00} p^{0} p^{0} + \eta_{11} p^{1} p^{1} + \eta_{22} p^{2} p^{2} + \eta_{33} p^{3} p^{3} \\ &= (p^{0})^{2} - (p^{1})^{2} - (p^{2})^{2} - (p^{3})^{2} \\ &= \left(\frac{\epsilon}{c}\right)^{2} - \left[(p^{1})^{2} + (p^{2})^{2} + (p^{3})^{2}\right] \\ &= \left(\frac{\epsilon}{c}\right)^{2} - |\bar{p}|^{2} \\ &= m_{0}^{2} c^{2} \end{aligned} \tag{A.115}$$

Since the total four-momentum before and after the collision is the same, a Lorentz invariant conserved quantity is defined, i.e., the total four-momentum squared,

$$\begin{aligned} s^{2} &= (\bar{p} + \bar{q})^{2} \\ &= (\bar{p} + \bar{q}) \cdot (\bar{p} + \bar{q}) \\ &= (\bar{p'} + \bar{Q}) \cdot (\bar{p'} + \bar{Q}) \end{aligned} \tag{A.116}$$

The momentum and energy conversation together imply that s^{2} does not change in the reaction, thus $s_{before}^{2} = s_{after}^{2}$, In the case where Δ-resonance dominates, the production process are $s^{2} = p_{\Delta}^{2} = m_{0}^{2} c^{2}$. Using the scalar product of two four vectors $\bar{A} \cdot \bar{B} = A^{\circ} B^{\circ} - \bar{A} \cdot \bar{B}$, it can be shown that the invariant quantity s^{2} before and after reactions is written as follows, making use of this information and equation A.115,

$$
\begin{aligned}
s^2_{before} &= (\bar{p}+\bar{q})\cdot(\bar{p}+\bar{q}) \\
&= \bar{p}\cdot\bar{p} + 2\bar{p}\cdot\bar{q} + \bar{q}\cdot\bar{q} \\
&= \left(\frac{\epsilon}{c}\right)^2 - |\bar{p}|^2 + 2\left(\frac{\epsilon_p\epsilon_{ph}}{c^2} - (\bar{p}\cdot\bar{q})\right) + 0 \\
&= m_p c^2 + 2\left(\frac{\epsilon_p\epsilon_{ph}}{c^2} - (\bar{p}\cdot\bar{q})\right)
\end{aligned}
\tag{A.117}
$$

For the reaction to proceed the threshold condition must be $s^2_{before} = m_0^2c^2$, using this condition and the equation A.117 gives,

$$
\left(\frac{\epsilon_p\epsilon_{ph}}{c^2} - (\bar{p}\cdot\bar{q})\right) \geq \frac{(m_\Delta^2 - m_p^2)c^2}{2}
\tag{A.118}
$$

For ultra-relativistic protons $\bar{p}\cdot\bar{q} = \epsilon_p\epsilon_{ph}cos\theta$, since $\epsilon_p \sim p_c \Rightarrow \bar{p} = \epsilon/c\bar{\beta}_p$ and the photon momentum is $\bar{q} = \epsilon_{ph}/c\hat{k}$, the condition on the equation A.118 becomes

$$
\epsilon_p \geq \frac{\frac{1}{2}(m_\Delta^2 - m_p^2)c^4}{4\epsilon_{ph}(1 - cos\theta)}
\tag{A.119}
$$

The maximum energy transfer occurs through head to head collisions when the angle $\theta \to \pi$, and thus the threshold condition can be written as,

$$
\epsilon_p \geq \frac{\frac{1}{2}(m_\Delta^2 - m_p^2)c^4}{4\epsilon_{ph}}
\tag{A.120}
$$

A.5.2 Pion production through proton-proton collisions

In this section a discussion of the inelastic collisions between particles in the co-moving is frame given. Using equation A.115 the total four-momentum $p_{tot}\cdot p_{tot} = p'_{tot}\cdot p'_{tot}$ in the co-moving,

$$
\begin{aligned}
\left(\frac{\epsilon^2_{tot}}{c^2}\right) - |p_{tot}|^2 &= \left(\frac{\epsilon'^2_{tot}}{c^2}\right) - |p'_{tot}|^2 \\
\left(\frac{\epsilon'^2_{tot}}{c^2}\right) &= \left(\frac{\epsilon^2_{tot}}{c^2}\right) - |p_{tot}|^2
\end{aligned}
\tag{A.121}
$$

since total momentum after the collision in the co-moving frame is zero. Simplifying the equation for the total four-momentum the total energy in the co-moving frame is obtained,

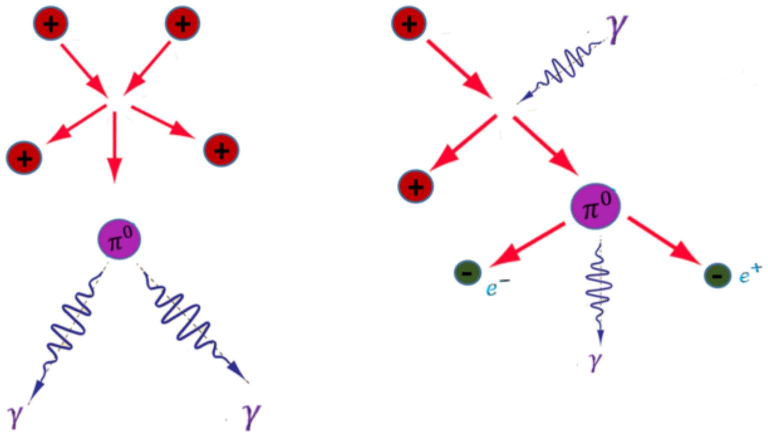

Figure A.12: Schematic diagram of neutral pion production and decay

$$\begin{aligned}
\epsilon'^2_{tot} &= \epsilon^2_{tot} - |p_{tot}|^2 c^2 \\
\epsilon'^2_{tot} &= \epsilon^2_{tot} - [p_1^2 c^2 + p_2^2 c^2] \\
\epsilon'^2_{tot} &= \epsilon^2_{tot} - p_1^2 c^2 \\
\epsilon'^2_{tot} &= \epsilon^2_{tot} - \epsilon_1^2 + m_1^2 c^4 \\
\epsilon'^2_{tot} &= (\epsilon_1 + m_2^2 c^2)^2 - \epsilon_1^2 + m_1^2 c^4
\end{aligned} \tag{A.122}$$

After the collision the net kinetic energy in the co-moving frame is zero. This implies that any residual energy will be instrumental in the creation of a particle with mass Δm,

$$\epsilon'^2_{tot} = [m_1 c^2 + m_2 c^2 + \Delta m c^2]^2 \tag{A.123}$$

solving equation A.122 and A.123 for ϵ_1 gives,

$$\epsilon_1 = m_1 c^2 + \frac{m_1 \Delta m}{m_2} c^2 + \Delta m c^2 + \frac{\Delta m^2}{2 m_2} c^2 \tag{A.124}$$

but $\epsilon_1 = T_1 + m_1 c^2$, thus the kinetic energy in the lab frame is,

$$T_1 = \Delta m c^2 \left[1 + \frac{m_1}{m_2} + \frac{\Delta m}{2 m_2} \right] \tag{A.125}$$

This is the lab frame kinetic energy required to produce an extra particle with rest mass Δm. Therefore the threshold energy for pion production through $p + p \rightarrow p + p + \pi^o$ is given by equation A.126,

$$\begin{aligned}
\epsilon_{tot} &= m_p c^2 + T_1 \\
&= m_p c^2 + \Delta m c^2 \left[1 + \frac{m_1}{m_2} + \frac{\Delta m}{2 m_2} \right]
\end{aligned} \tag{A.126}$$

A.5.3 Pion Decay

Collision of a proton and nucleus or a photon produces a charged or neutral pion. The neutral pion π^o, is highly unstable and has a very short life span $1.78 \times 10^{-16}\ s$, thus they decay to produce two gamma-ray photons (see Figure A.12 for a schematic diagram of the processes from the production of the pion and it's decay, to the emission of gamma-rays).

There are cases where the neutral pion will decay into a positron, an electron and a gamma-ray photon, the summary of the probability of occurrence is given by,

$$\pi^o \rightarrow \begin{cases} \gamma + \gamma & 99\% \\ \gamma + e^- + e^+ & 1\% \end{cases}$$

Appendix B

Fermi-LAT log-likelihood

The likelihood L(model; data) is defined as the likelihood of any given set of parameters of the model taking certain values given that quantity data was observed. The method of maximum likelihood estimation determines values for the parameters of a certain model. The values of the parameters are optimized such that they maximize the likelihood. Although in reality there are many factors involved but in general the best model is a model with a higher likelihood maximum, where it is assumed that this model will closely describe the observed data. Thereafter, one can identify the processes behind the observed data from the model. The following is a discussion of Fermi-LAT log-likelihood (if not otherwise specified, the treatment follows from the documentation on the Fermi Science Tools website[1]).

The expression for the likelihood is usually a complex function to differentiate, thus natural logarithms are used to simplify the expression log(likelihood). The natural logarithm are chosen because it is a monotonically increasing function since x and y values increase at the same time. This ensures that the maximum value of likelihood occurs at the same point as in the original function. In the case of the Fermi-LAT data, the probability of obtaining data given an input model is equal to the likelihood of the input model parameters given the data,

$$P(\text{data}, \text{inputmodel}) = L(\text{inputmodel}, \text{data}) \tag{B.1}$$

where the input model is basically the distribution of gamma-ray sources on the sky. The input model takes account of the intensity and spectra of each source's model, and the data are the gamma-ray data measured by the Fermi-LAT telescope. Note that even though the probability of obtaining data is equal to the likelihood, the two are essentially different because they are asking two different questions. The likelihood is looking for an input model given the data whilst the probability density is looking for the data given the input model.

The data in this study are the LAT data, binned into vast bins because the counts are influenced by so many variables. This will result in each bin having few counts described by the Poisson distribution. The Poisson distribution is not normally distributed (it is asymmetric), for this reason, it fails to comply with the assumption of linear regression. This is where the maximum likelihood will come into play. By definition, it is clear that the likelihood is equal to the probability density thus in our case the likelihood is the product of the probabilities of observing counts in each given bin. Therefore binned likelihood is defined as a function of the input model, and a function of both the source input model and the observed data,

---

[1] `https://fermi.gsfc.nasa.gov/ssc/data/analysis/documentation/`

$$L = e^{-N_{pred}} \sum_i m_i^{n_i/n_i!} \tag{B.2}$$

where m$_i$ is the predicted number of counts in the ith bin, a function of the source input model, and it is affected by different input models. N_{pred} is the total counts that the source input model assumes should have been observed, and n_i is the detected counts in the ith bin. If the chosen input model correctly describes the data n_i will be equal to m_i. A smaller bin size results in a more accurate likelihood because binning destroys the information. With infinitesimally small bin sizes, the detected counts will be $n_i = 0$ or $n_i = 1$. This simplifies the binned likelihood expression into the unbinned likelihood expression,

$$L = e^{-N_{pred}} \sum_i m_i \tag{B.3}$$

where m_i is the number of predicted counts with i, now the index over the counts. The unbinned expression is more accurate because m$_i$ is calculated by the actual values for each count, unlike in the previous expression where m_i is an average over an infinite sized bin.

B.0.1 Model optimization and fitting

The input model for a certain Region of interest (ROI) consists of the source input model that describes each source spectrum of that source. The best model gives a higher probability of obtaining the data because it will describe reality better than the worst model. Each source in the ROI must be modelled with the best model that describes the reality, which will improve the results for data observed on the entire ROI. Fermi has several non-thermal models which include power law, power law with super-exponential cut-off, the log-parabola, Broken power law, and Power Law with an exponential cut-off.

The power law model has three prominent parameters including the spectral index (γ) which controls the hardness of the source, the flux value known as the prefactor normalisation (N_o), which scales the brightness of the observed source, and the energy scale (E_o). Thus, the power law distribution of photons takes the following mathematical form,

$$\frac{dN}{dE} = N_o \left[\frac{E}{E_o}\right]^{\gamma} \tag{B.4}$$

The power law with super-exponential-cut-off2 is one of the spectral models that describes gamma-ray emission from a pulsar-like system. It shares features with a power law spectral model , but it has an additional term, the super-exponential term (see equation B.5).

$$\frac{dN}{dE} = N_o \left(\frac{E}{E_o}\right)^{\gamma_1} e^{-aE^{\gamma_2}} \tag{B.5}$$

where the parameters of this spectral model have the same meaning as in the power law spectral model but this model has another index γ_2 and the exponential factor a.

Model fitting involves several steps that must be followed religiously: the first step is data selection (*gtselect* and *gmktime*), the second step is model selection, and the third step is to pre-compute files needed for fitting which will be discussed in the next few paragraphs. The final step is optimization and fitting, which includes finding the parameters that give or maximize the likelihood using the likelihood method [162]. Fermi log(likelihood) is related to the χ^2 method, where χ^2 assumes the value -2log(likelihood) in the frame where the number of counts is substantially large in each bin. Thus to maximize the likelihood, one should minimize χ^2. Now an important quantity can be introduced, i.e., the test statistics (TS), which is equivalent to the ratio of the best-fitting sky model with and without the source in question, which is expressed as,

$$TS = -2log\left(\frac{L_{max,0}}{L_{max,1}}\right) \tag{B.6}$$

where $L_{max,0}$ determines the value of the maximum likelihood of a model without an additional source known as the null hypothesis and $L_{max,1}$ determines the value of the maximum likelihood of a model with an additional source at a given location. The square-root of the test statistic defines significance, which is usually expressed in σ units.

A set of Fermi science tool algorithms are used to perform the likelihood. There are five optimization algorithms in Fermi Science tools used for maximizing the likelihood such as DRMNGB, DRMNFB, NEWMINUIT, MINUIT, and LBFGS. These optimizers determine the best parameters for the model. The algorithms iteratively calculate the log(likelihood) for different sets of trial parameters. This is achieved by estimating derivatives of the likelihood function with respect to the parameters. For each trial the algorithms choose new test parameters that maximize the likelihood function better, this process is known as optimization. The algorithms repeat this process until the maximum likelihood function value is adequately small (or when the set tolerance value is reached). Thereafter the final fit is performed on the optimized parameters.

B.0.2 log-likelihood files

In this part a description of how files are generated for both binned and unbinned log(likelihood) analyses is given, and an overview of their importance in each analysis is briefly outlined. The binned analysis is preferred for data with longer observation periods whilst unbinned is for shorter periods. Binned and unbinned analyses techniques were used in this study to search for steady gamma-ray emission from AE Aqr.

Since the Fermi-LAT telescope collects photons from the whole sky every 3 h, data selection is imperative to ensure that only good data are used for analysis. There are several parameters that can be used to ensure good data are selected. The first task is to identify and define the ROI, which is achieved by setting the coordinates of the source of interest as the central point and setting the radius in angular distance. The ROI is the region where photons are collected and its size is determined by the radial distance. Events can be selected using event type or class, i.e., FRONT+BACK event type (evtype=3) and events on the sky belonging to the event class (evclass=128). The routines *gtselect* or *filter* are used to select desired events from the event data file. These routines perform the basic regional cuts making use of energy cuts, the zenith angle (zmax) cut, the time selection cut and the above mentioned parameters. The filtered file contains selected events, and the header includes a record of the pruning history.

After defining the ROI, creating the Good Time intervals (GTIs) is the next step in order to make sure that only the good time intervals are used for analysis. GTI's are generated based on the selection made using the spacecraft data file variables with the flag (DATAQUAL>0)&&(LATCONFIG==1) which characterizes the spacecraft operation in Scientific mode. The *gtmktime* routine is applied to update the GTI extension and make cuts based on spacecraft parameters contained in the Pointing and *Livetime* History (spacecraft) Fits file. This routine takes the pointing and position history of the spacecraft file and applies it to the filtered file. A GTI is a time range when the data can be considered valid (where the telescope will be pointing in the direction of the source of interest). The routine generates a file with good time intervals (GTIs).

A map of raw data (counts map) is produced for the ROI to see the distribution of sources in the ROI. In this study it was to see whether there are any traces of activity at the source of interest's location. A counts map is summed over photon energies (photons on the same grid location are added together to produce a summed counts). A counts map is generated using the *gtbin* routine with the option CMAP. The user can choose the type of projection, e.g., AIT. For example, in this analysis, it was produced with a CAR projection with 100 × 100 pixels and 0.2 degrees/pixel (see Figure B.1). The Counts map presents a visual aspect of the gamma-ray emission from the ROI. A closer inspection of the counts map in Figure B.1 shows that there are no extremely bright sources in the ROI, the brightest source is below 800 counts. Accordingly, from counts map, one can see whether one is dealing with a faint or bright source, which leaves room to choose the appropriate analysis steps.

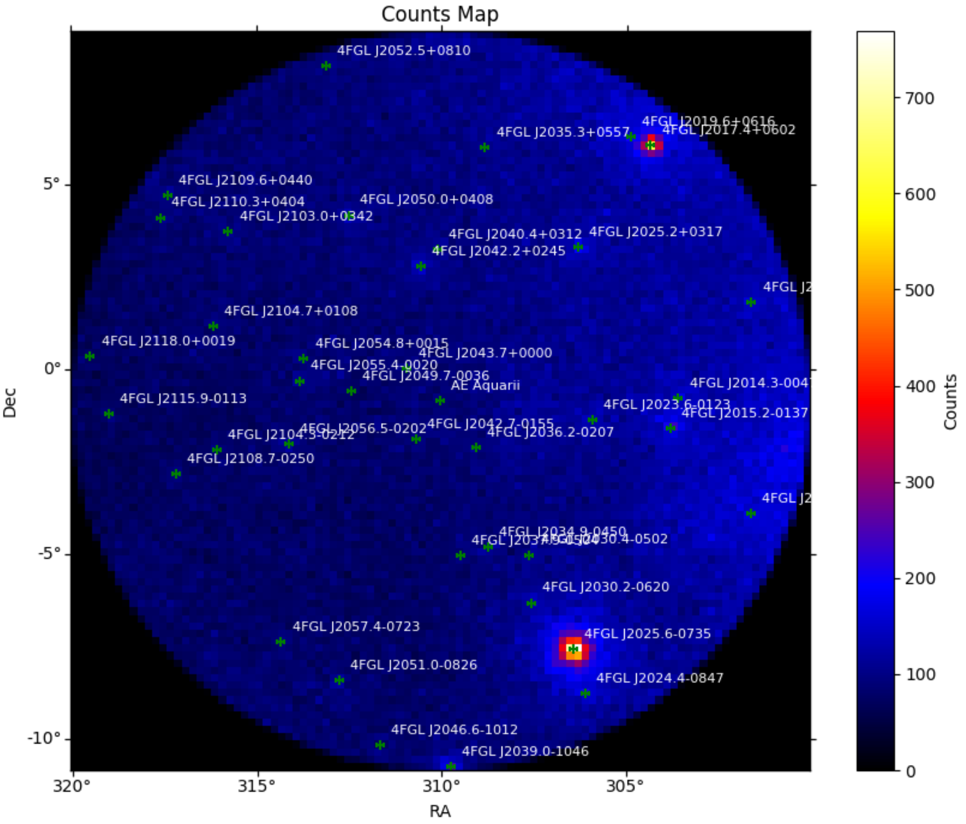

Figure B.1: The counts map is generated from raw data, it is a map of energies summed together at a certain grid to give a visual sense of the raw data

The next step is to create the counts' cube, which is basically the counts' map with an additional energy dimension. The routine *gtbin* is used to create the counts' cube with an option CCUBE. The binning used on the counts cube must be applied to determine the exposure calculation. For instance, in this analysis, 20 energy bins per decade were used for accuracy since the narrower the energy bin, the better it will accommodate more rapid variations in the effective area with decreasing energy below a few hundred MeV. The counts' cube cross-sectional area should fit inside the ROI (the optimum square area inside the circle of ROI). This routine uses the GTIs file. The energy cuts applied on the GTIs file must be specified again when generating the counts cube.

The routine *gtltcube* is used to calculate integrated *livetimes* as a function of sky position for a specified observation period and off-axis angle (inclination angle). The inclination angle characterizes the angle between the z-axis of the LAT instrument and the direction of a given source. The LAT response function depends on this angle. Thus counts detected by the instrument depend on how long it spends on that angle over the entire observation period and the *livetime*, where *livetime* is the time at which the instrument is taking the event data. The *livetime* cannot be defined as a continuous function of position on the sky and the off-axis angle. Therefore the *livetime* cube is given as a function of the off-axis angle bins and HEALPix (an acronym for Hierarchical Equal Area isolated Pixelization (`http://healpix.jpl.nasa.gov/`)) grid on the sky. The routine *gtltcube* uses the GTI's, time range, and the spacecraft pointing history file to produce *livetime* cubes that spread over the entire sky. This file is produced in the same way for both unbinned and binned analyses. In the case where there are changes in the GTI's, this file should be recomputed.

The exposure maps are used to compute the predicted number of photons within a given ROI. The likelihood exposure map is defined as the total response over the integral of the entire ROI. The PSF, which is the angular distance distribution of a photon's apparent and actual positions, plays a significant role in determining the source's total photons. The LAT PSF is a function of off-axis angle and photon energy. The PSF of sources that are outside the region specified by the counts cube can affect the counts of the sources in the ROI. Thus when creating the exposure map, the contribution from the sources ten degrees outside the ROI should be accounted for both unbinned and binned analyses. Therefore the source radius is made ten degrees larger than the ROI. The exposure maps for binned analysis are computed using the *gtexpcube2* while *gtexposure* generates unbinned exposure maps. The routine *gtexpcube2* uses the *livetime cubes* and the counts cube, although the counts cube is optional. Thus, counts cubes can be excluded and replaced by all-sky or new desired dimensions during the computation of the exposure maps. The routine makes use of the ϕ-modulation of the effective area for IRFs that establish this dependence, e.g., $\mathrm{PR3\_SOURCE\_V2}$.

Source maps are required to run the binned likelihood fit and must be precomputed before running the likelihood to reduce the computational time. Source maps are produced using the *gtsrcmaps* routine, which considers the influence of spectral models of all previously known sources in the ROI and diffuse Galactic and isotropic background. The method makes use of the *livetime* cube, counts cube, input model file, and the exposure map. The routine takes the product of each source's spectrum in the input model file and the exposure at the source's position and folds it with the effective PSF.

The unbinned maximum likelihood function is characterized in terms of the expected distribution of photons for a given source. This distribution is obtained by folding the IRFs with the input source model. On the other hand, the log(likelihood) contribution of each photon is evaluated as the integral of the instrument response function with the input source model calculated at the photon's direction, arrival time, and it's energy. The spatial component of a point source is a delta-function. Thus the computation of the spatial component of a point source log(likelihood) is generally easy, unlike a diffuse source. Diffuse sources are exceptionally computationally intensive, for example, the galactic interstellar component, which must be performed over the entire sky. It is therefore advised that the integral over the instrument response for each diffuse model component must be computed before performing the likelihood since it is possible to obtain the integral over the spatial distribution independent of the spectral part. The routine *gtdiffrsp* calculates the integral over the instrument response folded with a solid angle of a diffuse source model. The routine computes these integrations for each model component and adds the results as a new column for each diffuse source into the GTIs file. The quantities produced here are known as the diffuse responses.

B.1 Pulsed emission power spectra

In this section, some of the Rayleigh test power spectra with $> 2\ \sigma$ at either the fundamental or the first harmonic are presented.

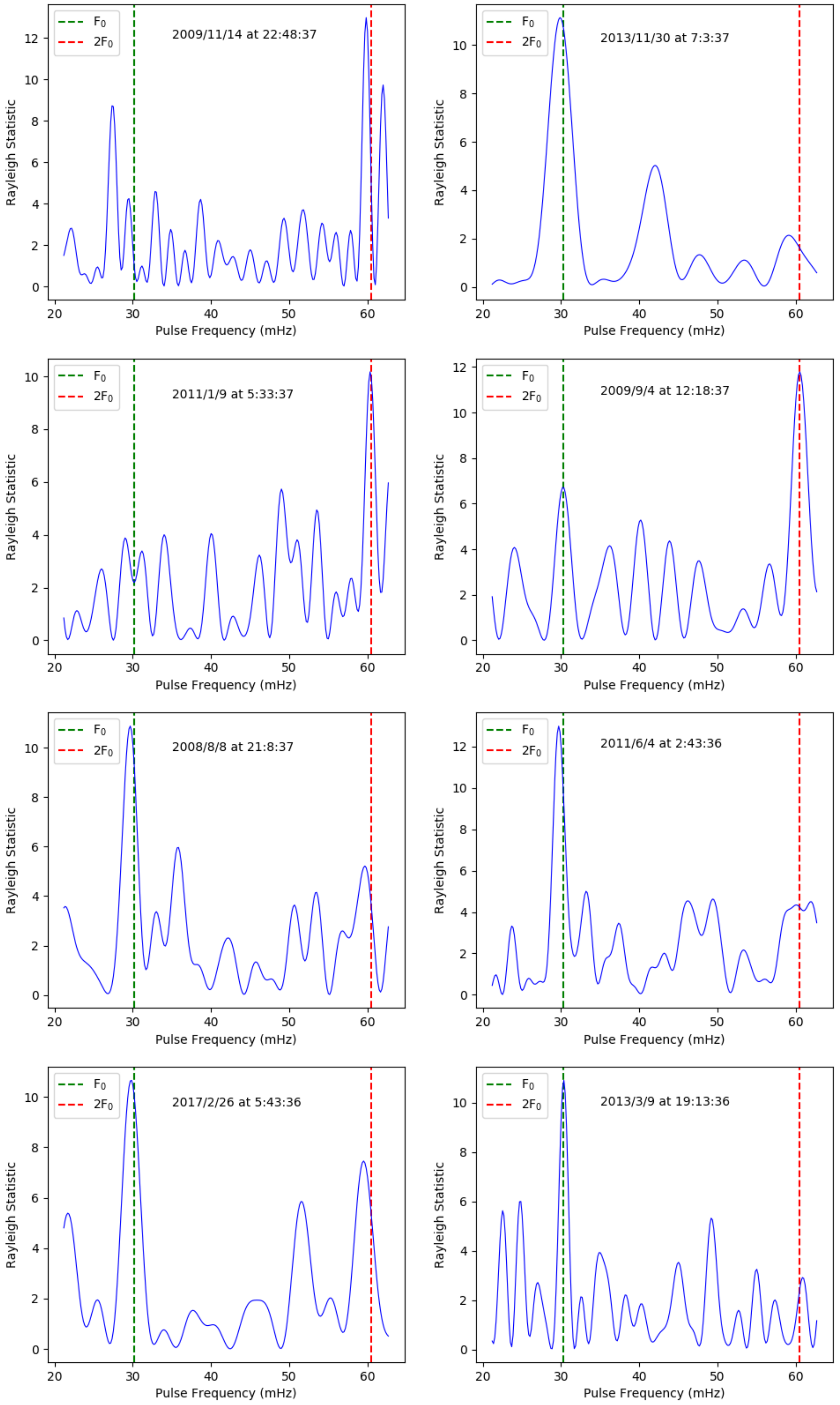

Figure B.2: The pulse profiles of AE Aqr showing the pulses at or near the fundamental frequency and the first harmonic.

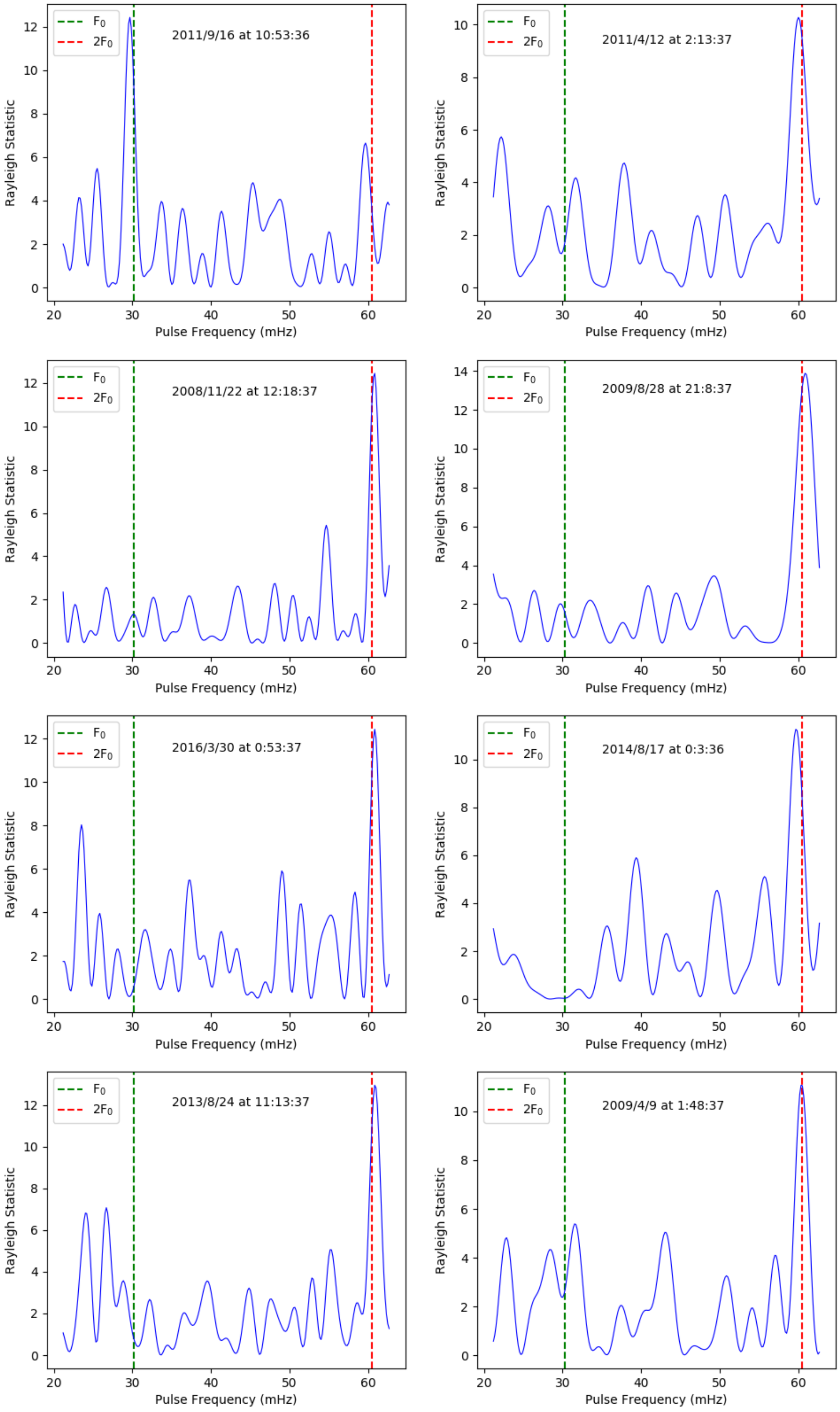

Figure B.3: The pulse profiles of AE Aqr showing the pulses at or near the fundamental frequency and the first harmonic.

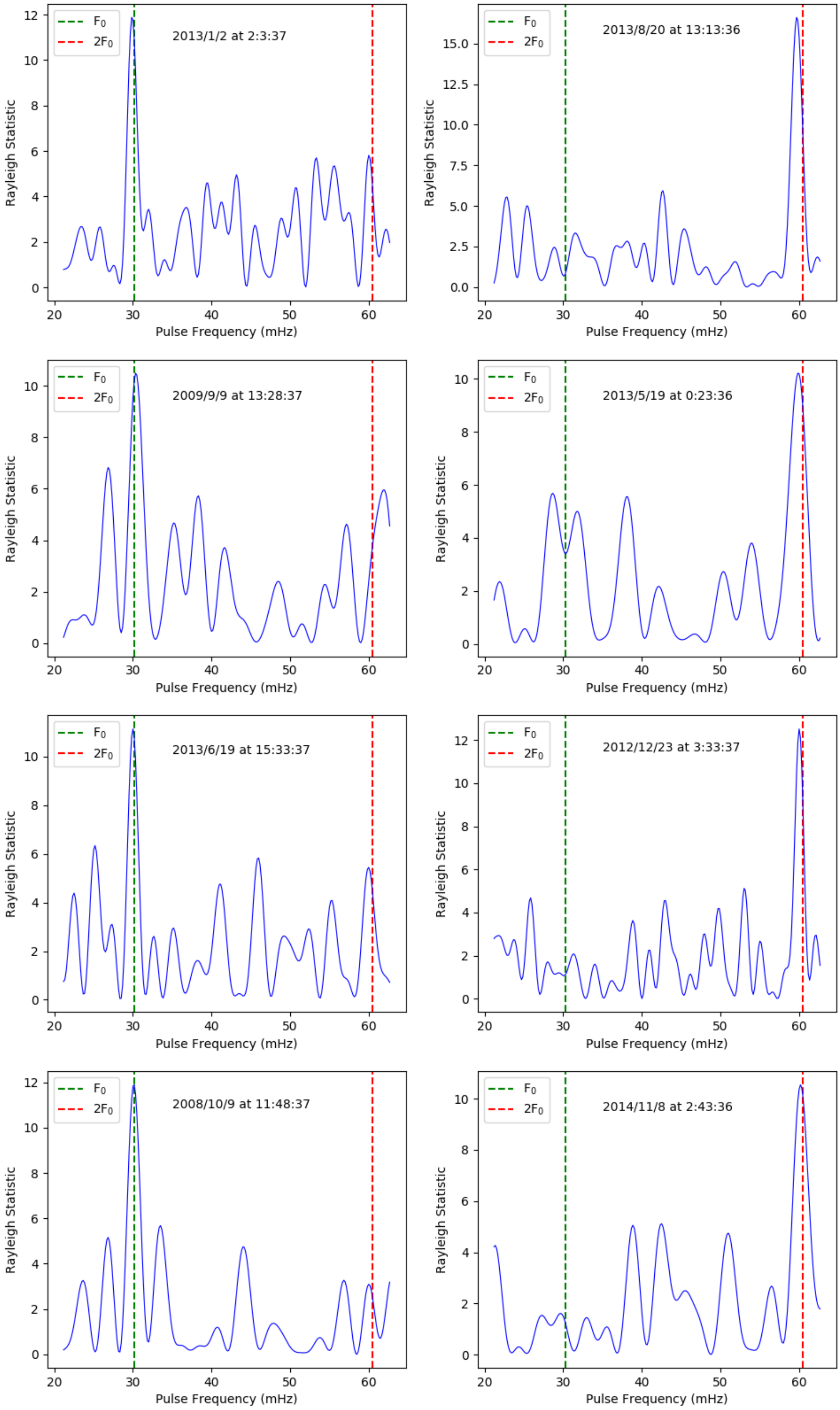

Figure B.4: The pulse profiles of AE Aqr showing the pulses at or near the fundamental frequency and the first harmonic.

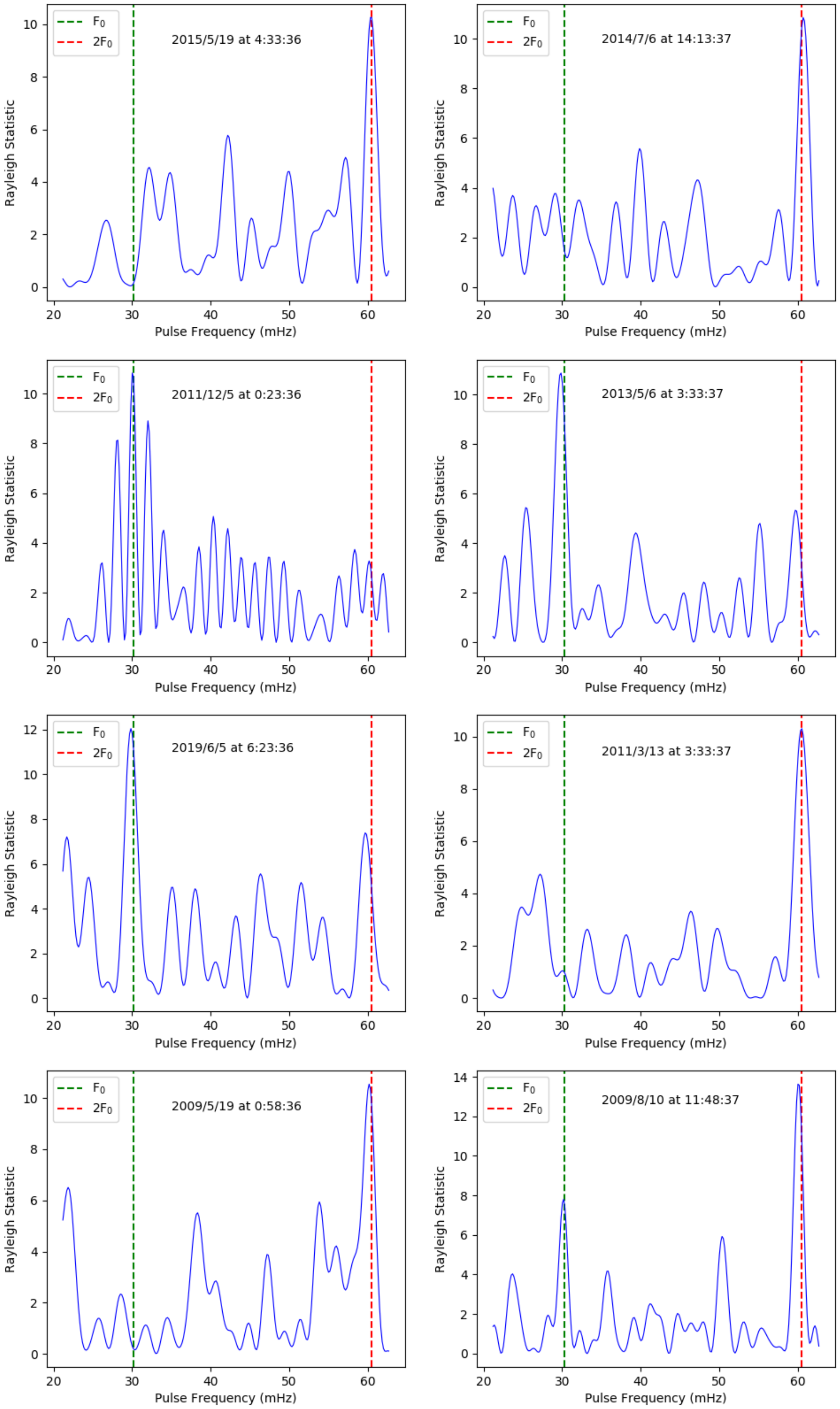

Figure B.5: The pulse profiles of AE Aqr showing the pulses at or near the fundamental frequency and the first harmonic.

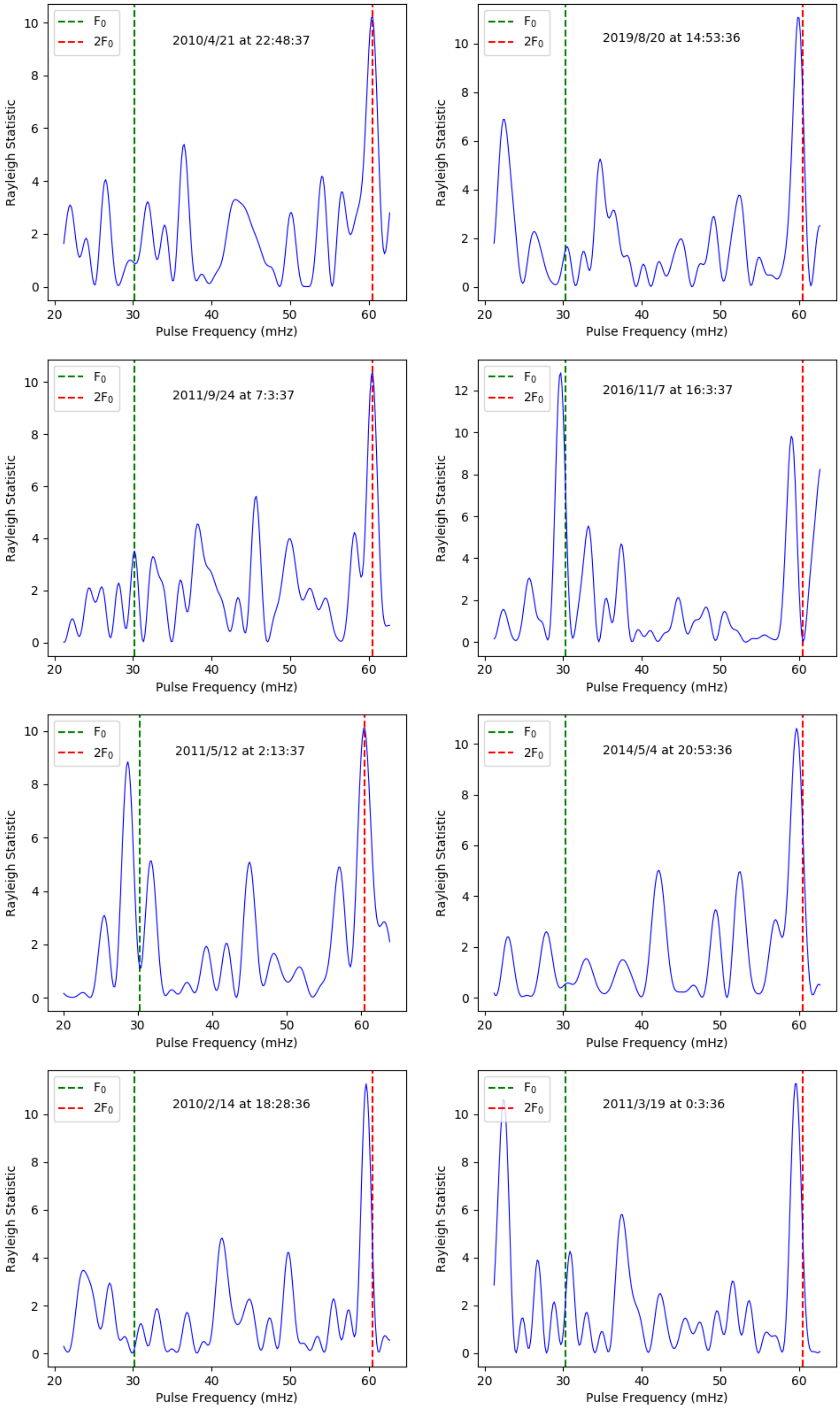

Figure B.6: The pulse profiles of AE Aqr showing the pulses at or near the fundamental frequency and the first harmonic.

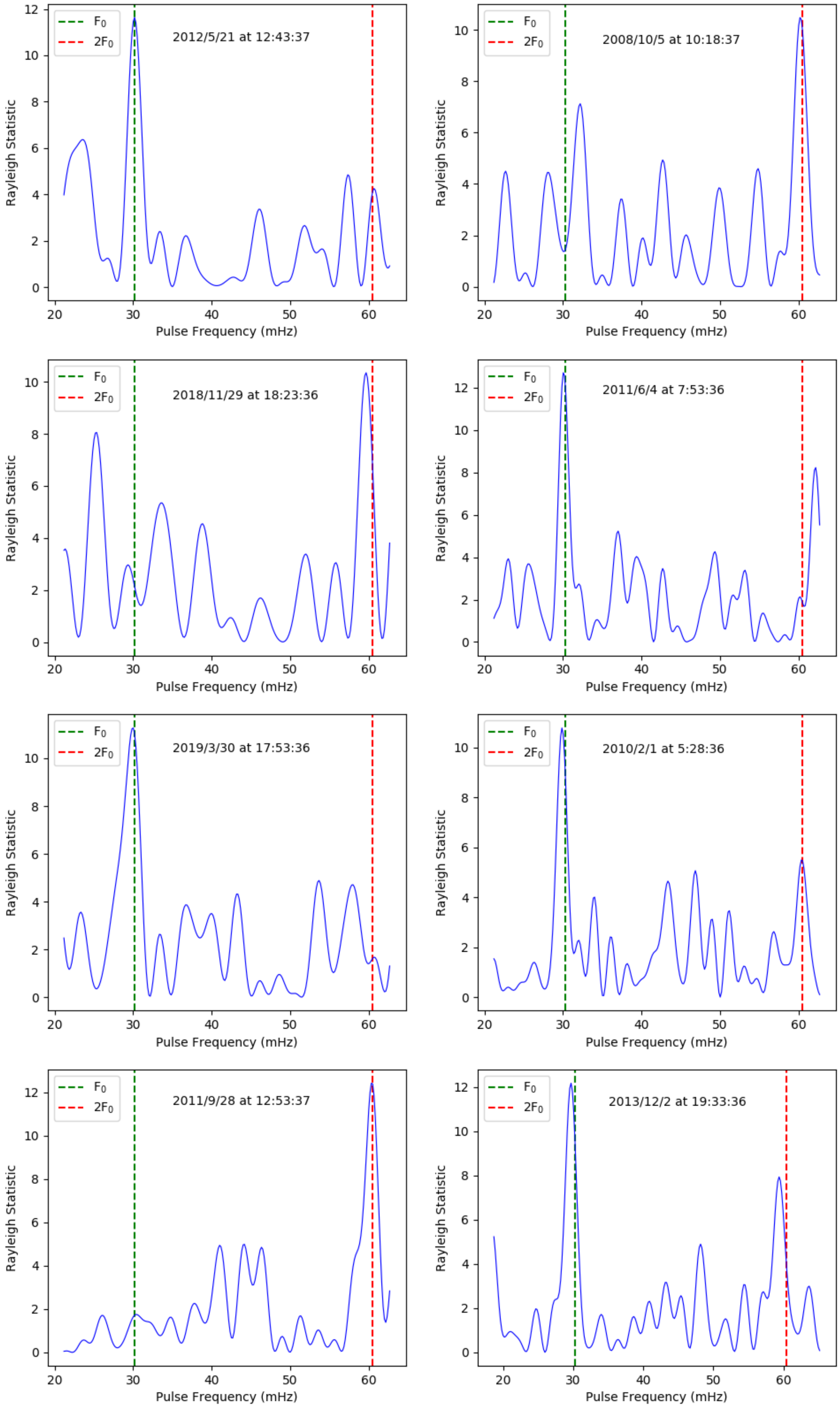

Figure B.7: The pulse profiles of AE Aqr showing the pulses at or near the fundamental frequency and the first harmonic.

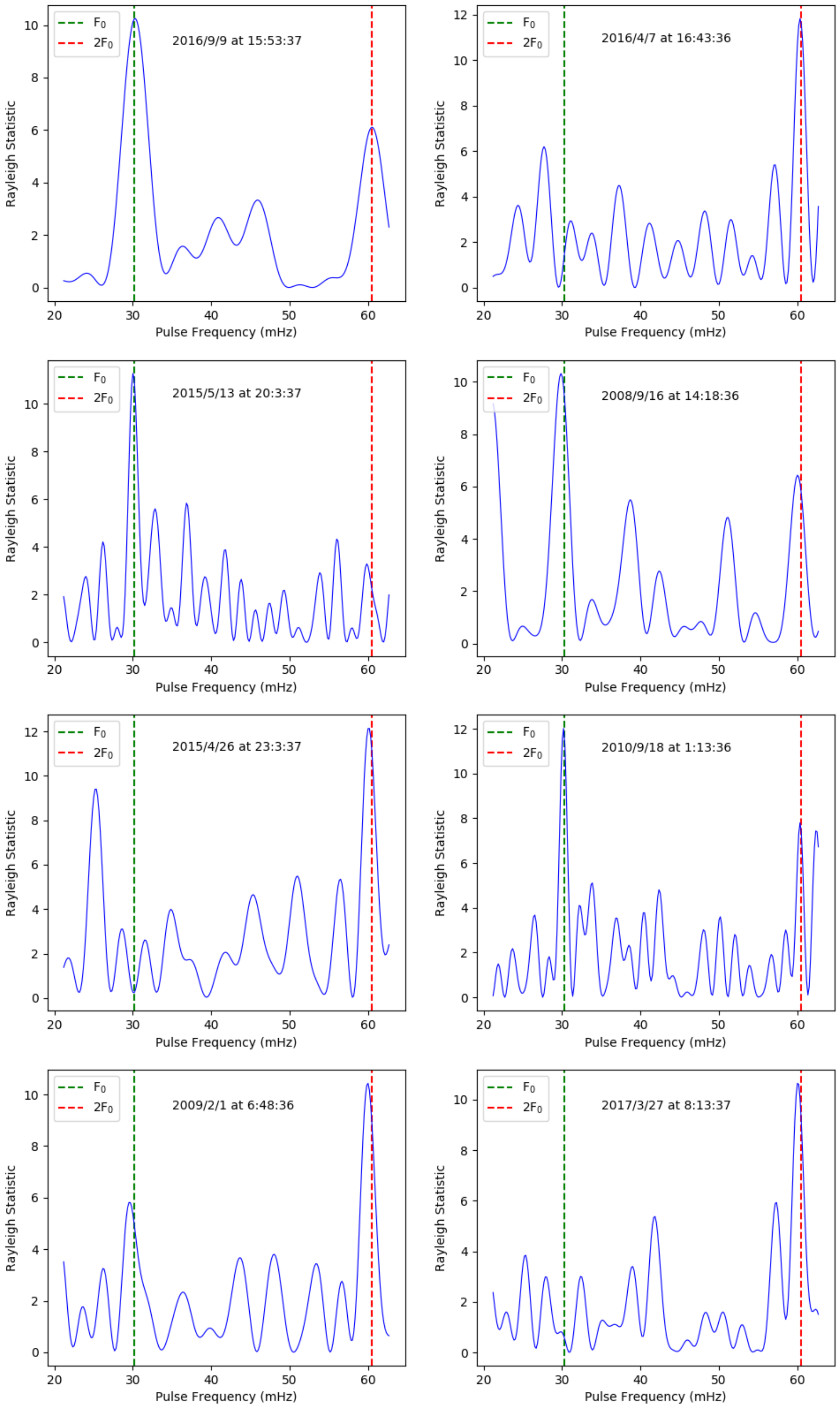

Figure B.8: The pulse profiles of AE Aqr showing the pulses at or near the fundamental frequency and the first harmonic.

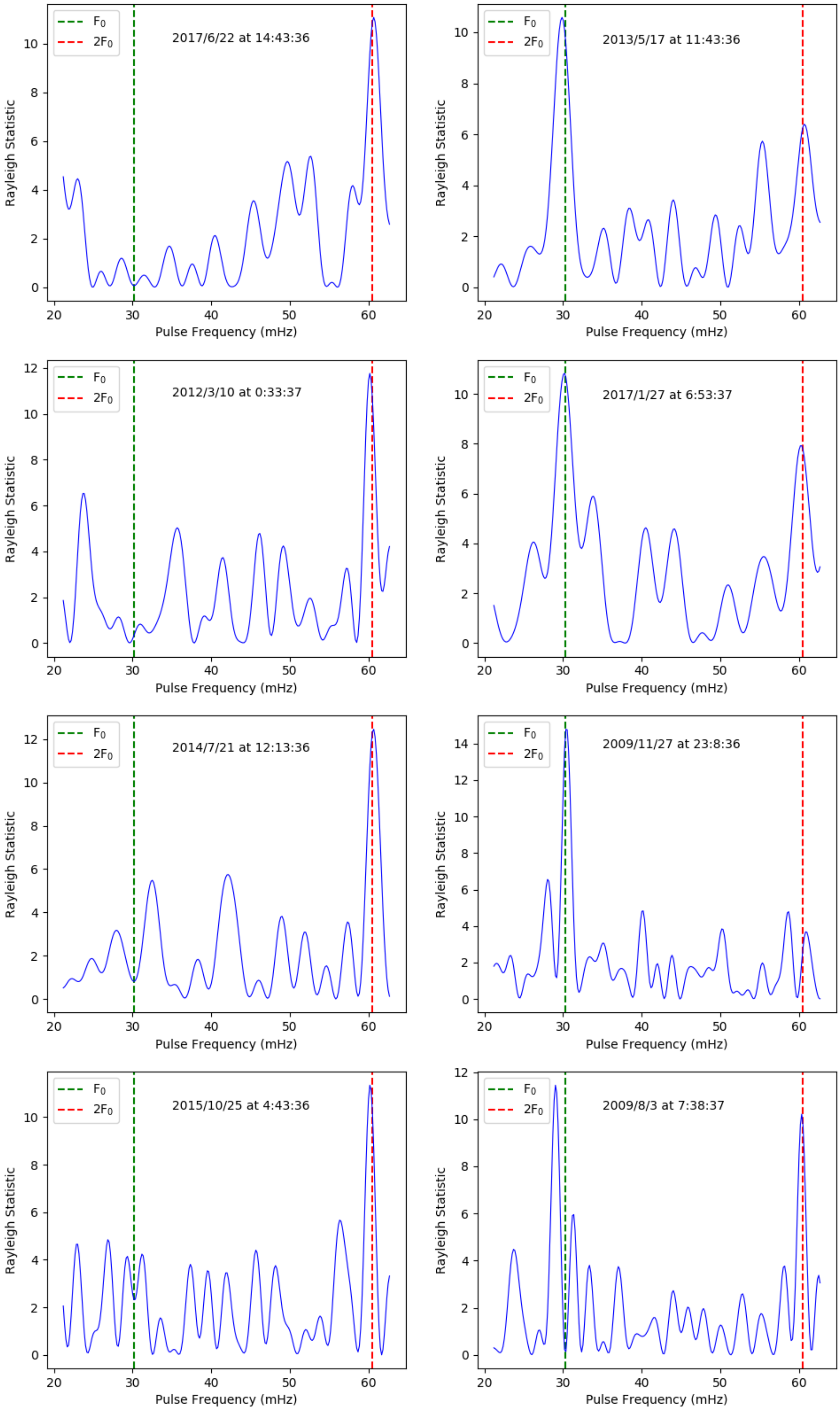

Figure B.9: The pulse profiles of AE Aqr showing the pulses at or near the fundamental frequency and the first harmonic.

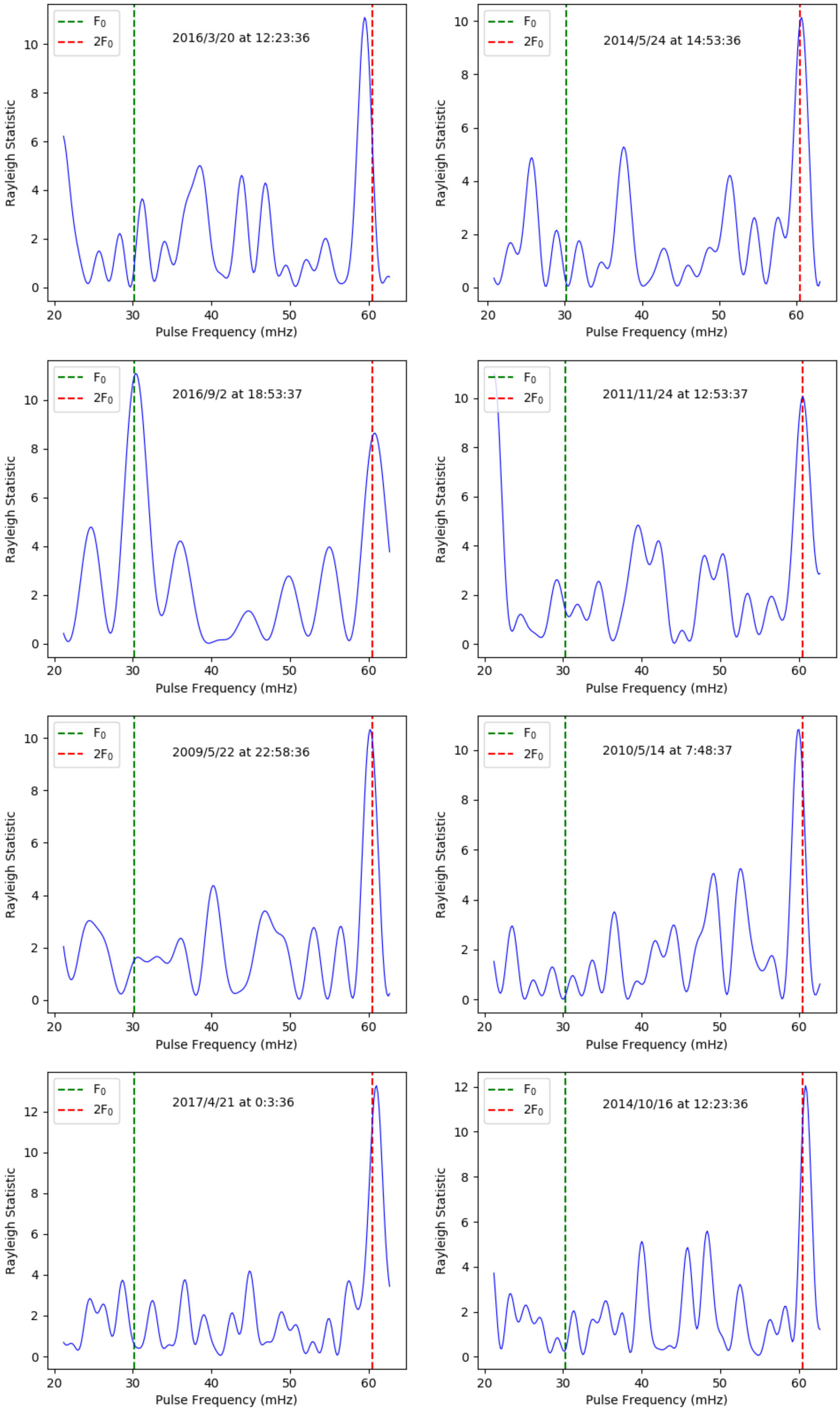

Figure B.10: The pulse profiles of AE Aqr showing the pulses at or near the fundamental frequency and the first harmonic.

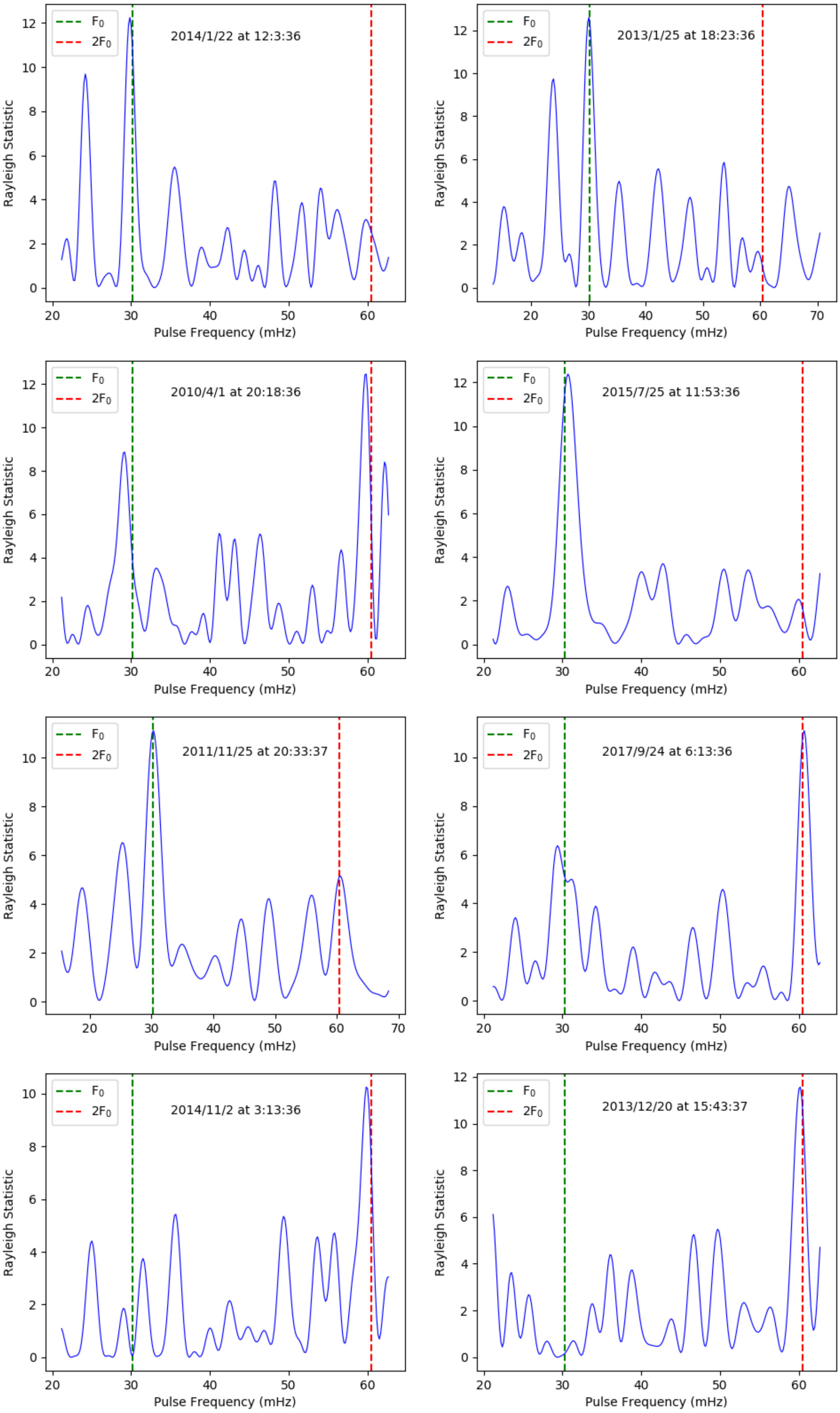

Figure B.11: The pulse profiles of AE Aqr showing the pulses at or near the fundamental frequency and the first harmonic.

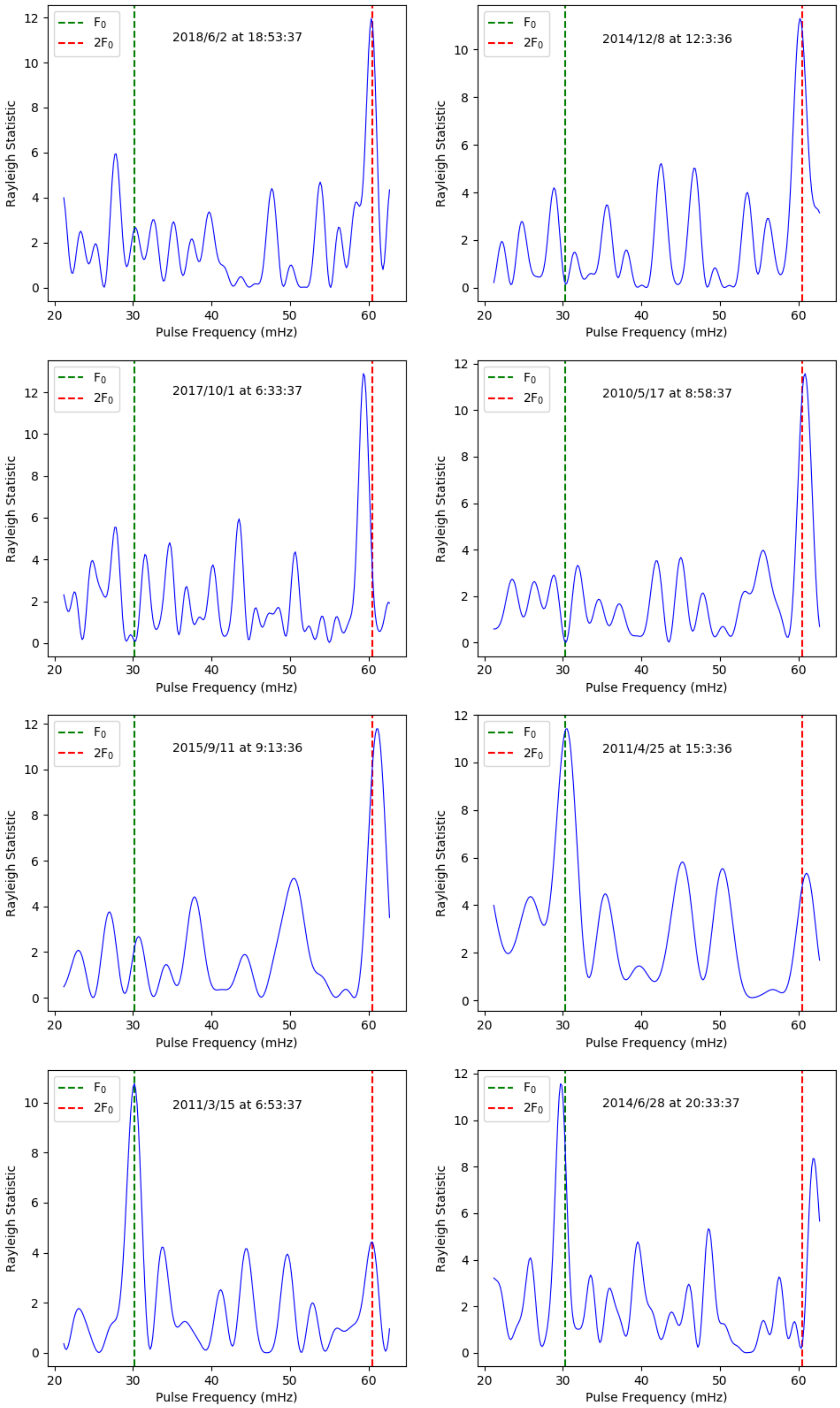

Figure B.12: The pulse profiles of AE Aqr showing the pulses at or near the fundamental frequency and the first harmonic.

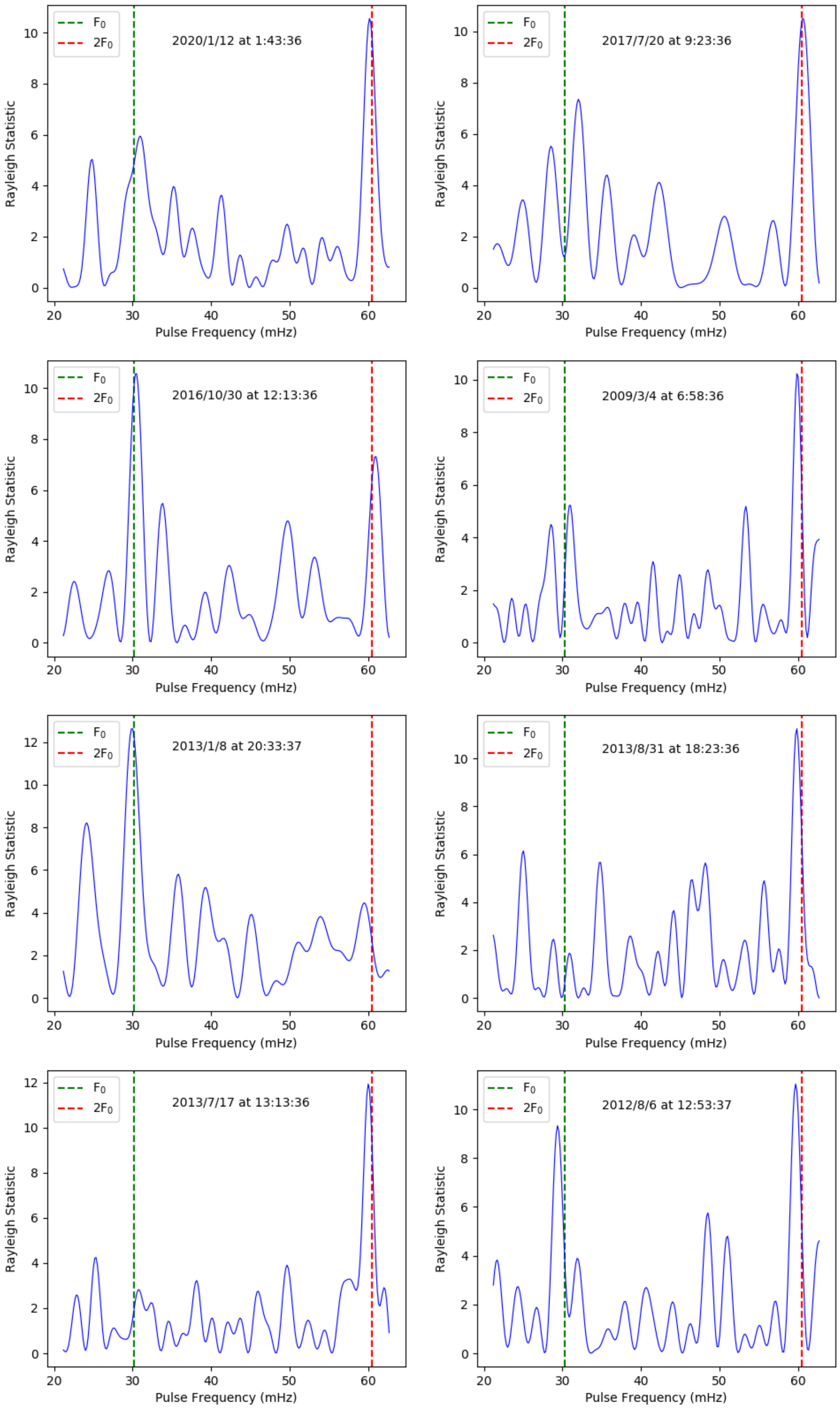

Figure B.13: The pulse profiles of AE Aqr showing the pulses at or near the fundamental frequency and the first harmonic.

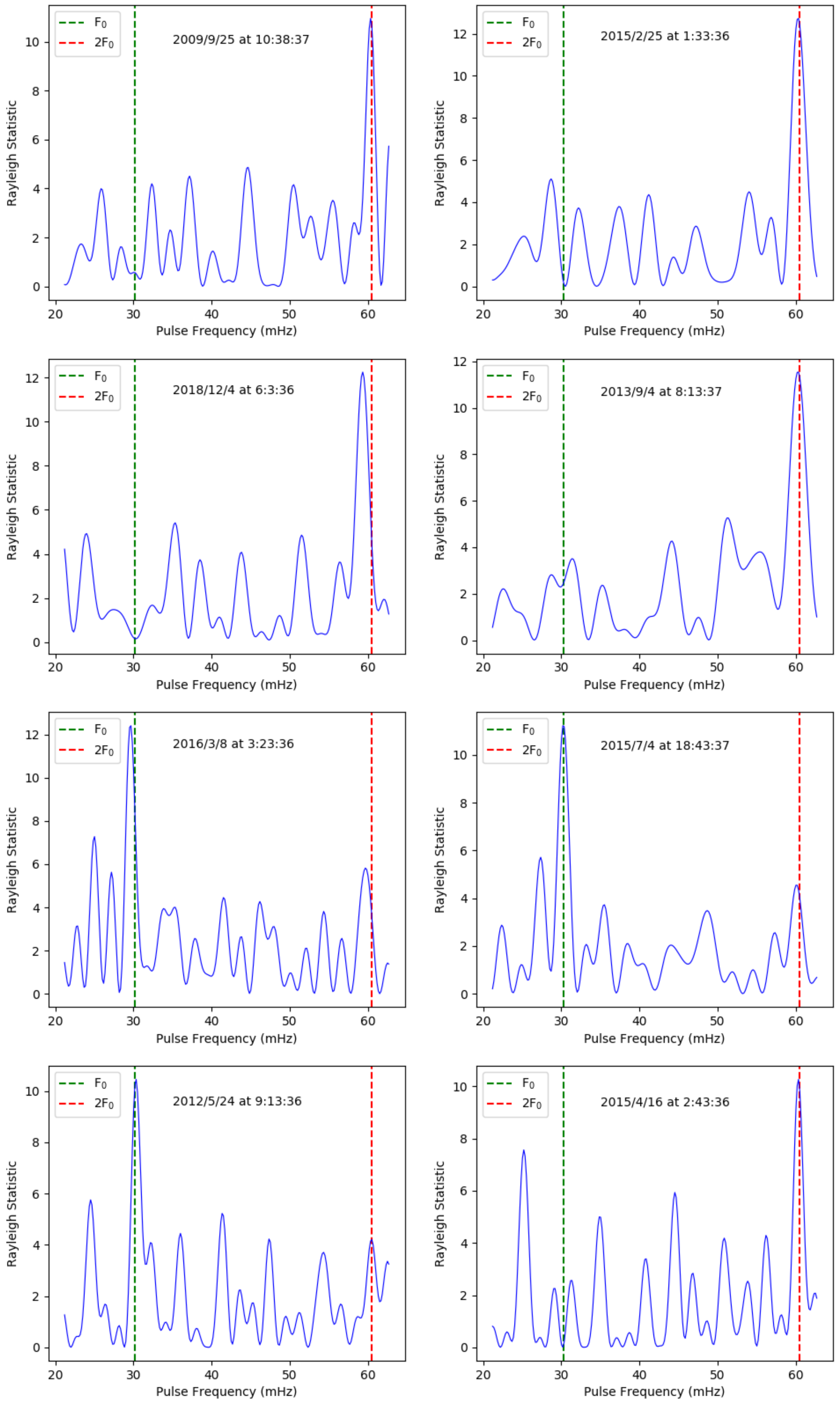

Figure B.14: The pulse profiles of AE Aqr showing the pulses at or near the fundamental frequency and the first harmonic.

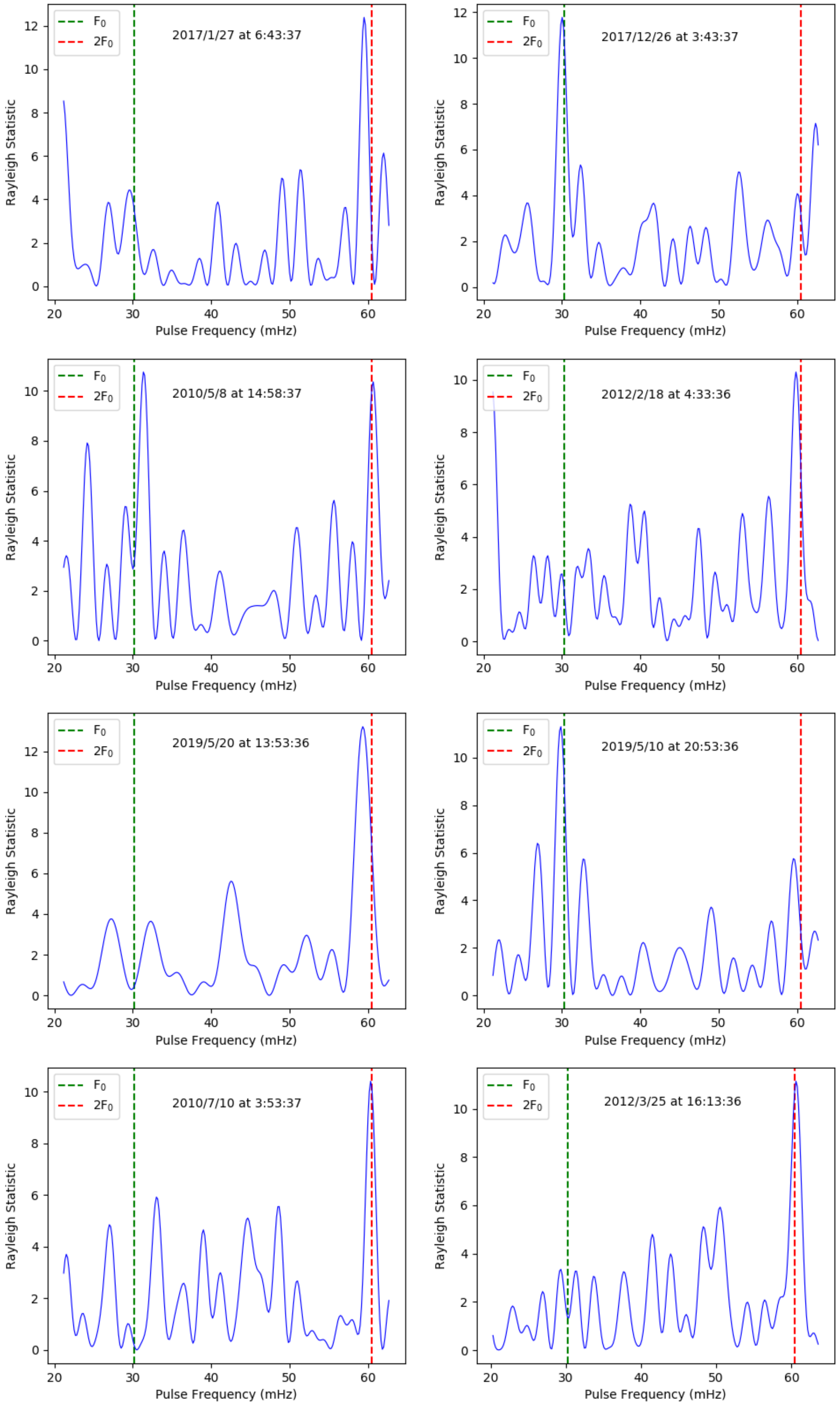

Figure B.15: The pulse profiles of AE Aqr showing the pulses at or near the fundamental frequency and the first harmonic.

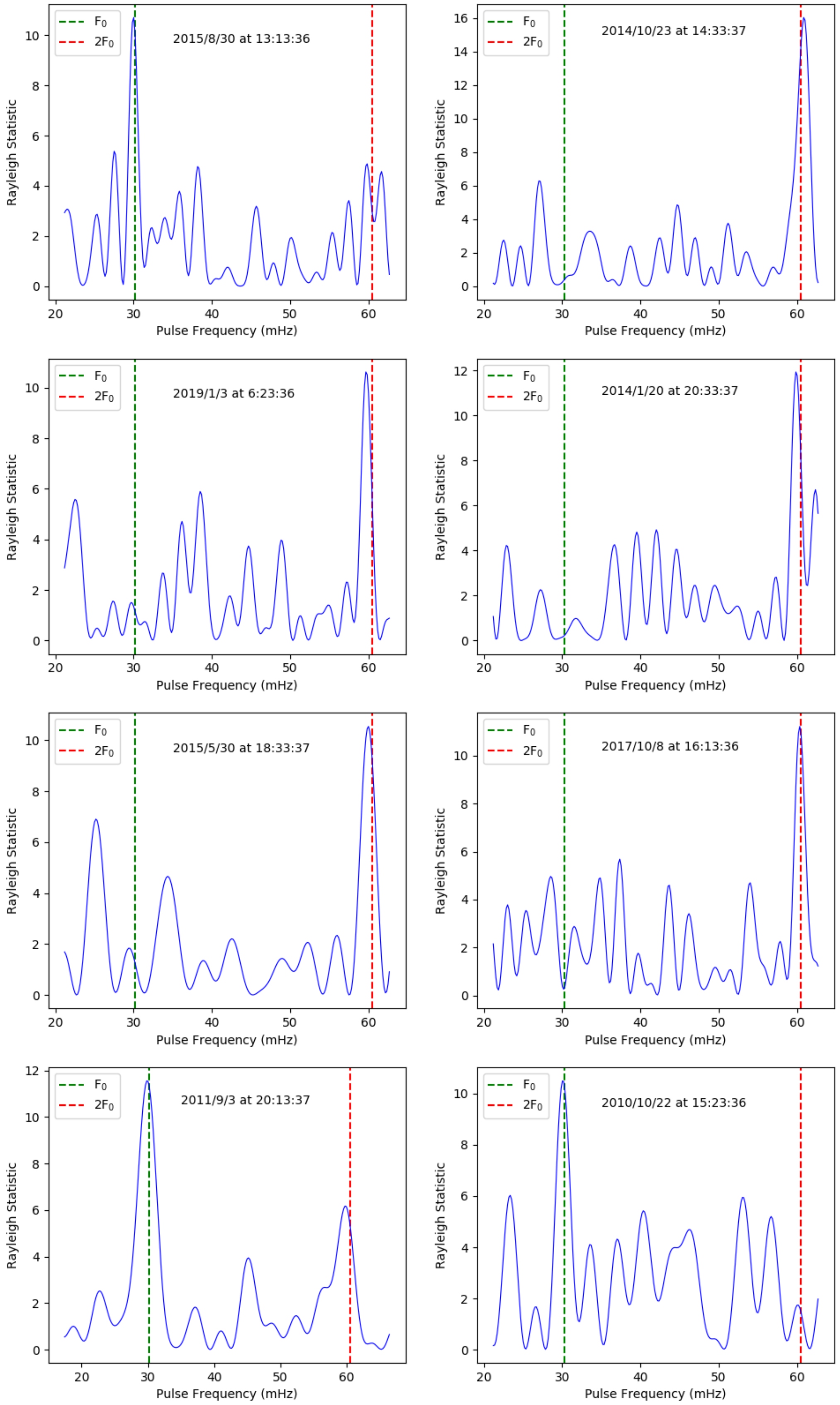

Figure B.16: The pulse profiles of AE Aqr showing the pulses at or near the fundamental frequency and the first harmonic.

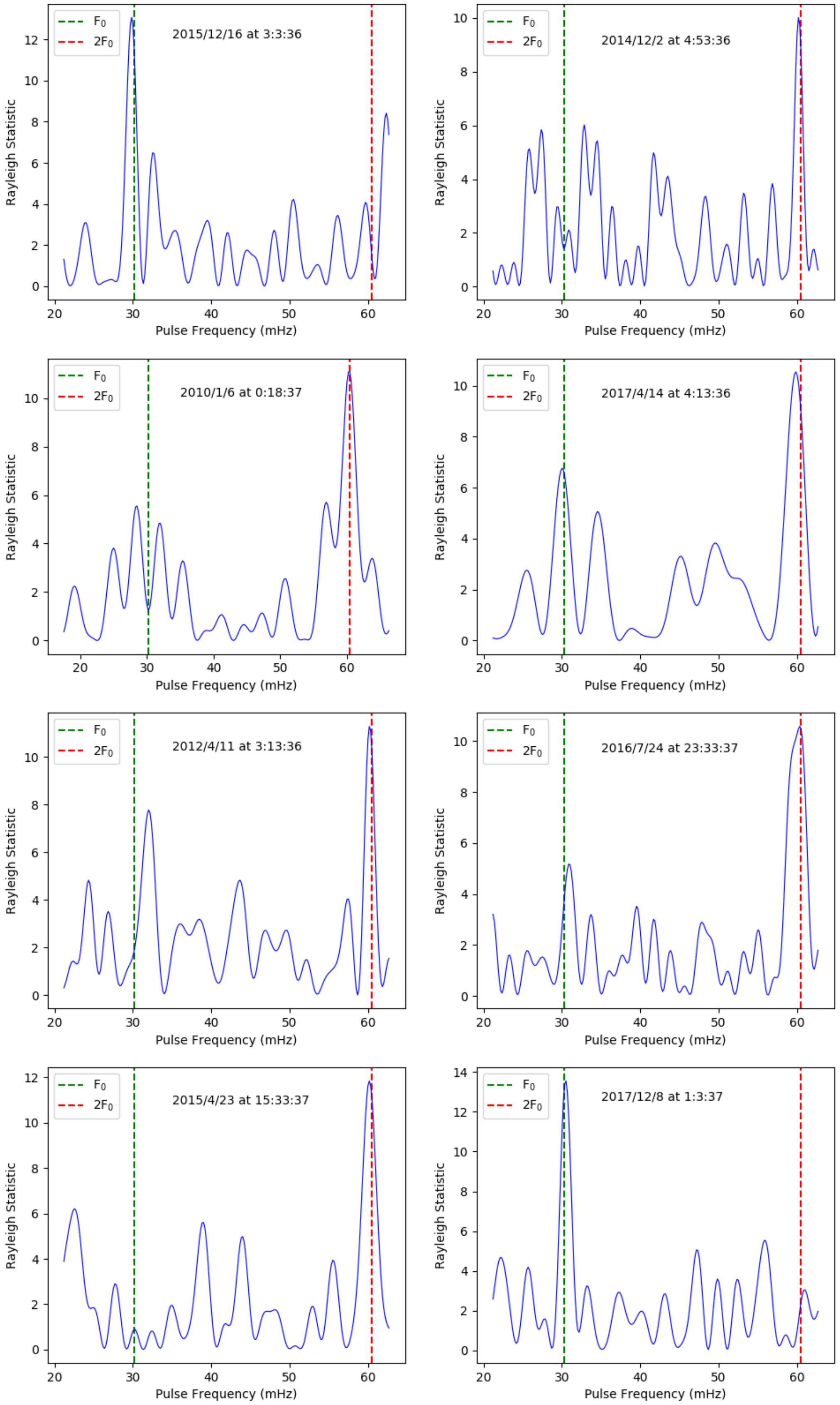

Figure B.17: The pulse profiles of AE Aqr showing the pulses at or near the fundamental frequency and the first harmonic.

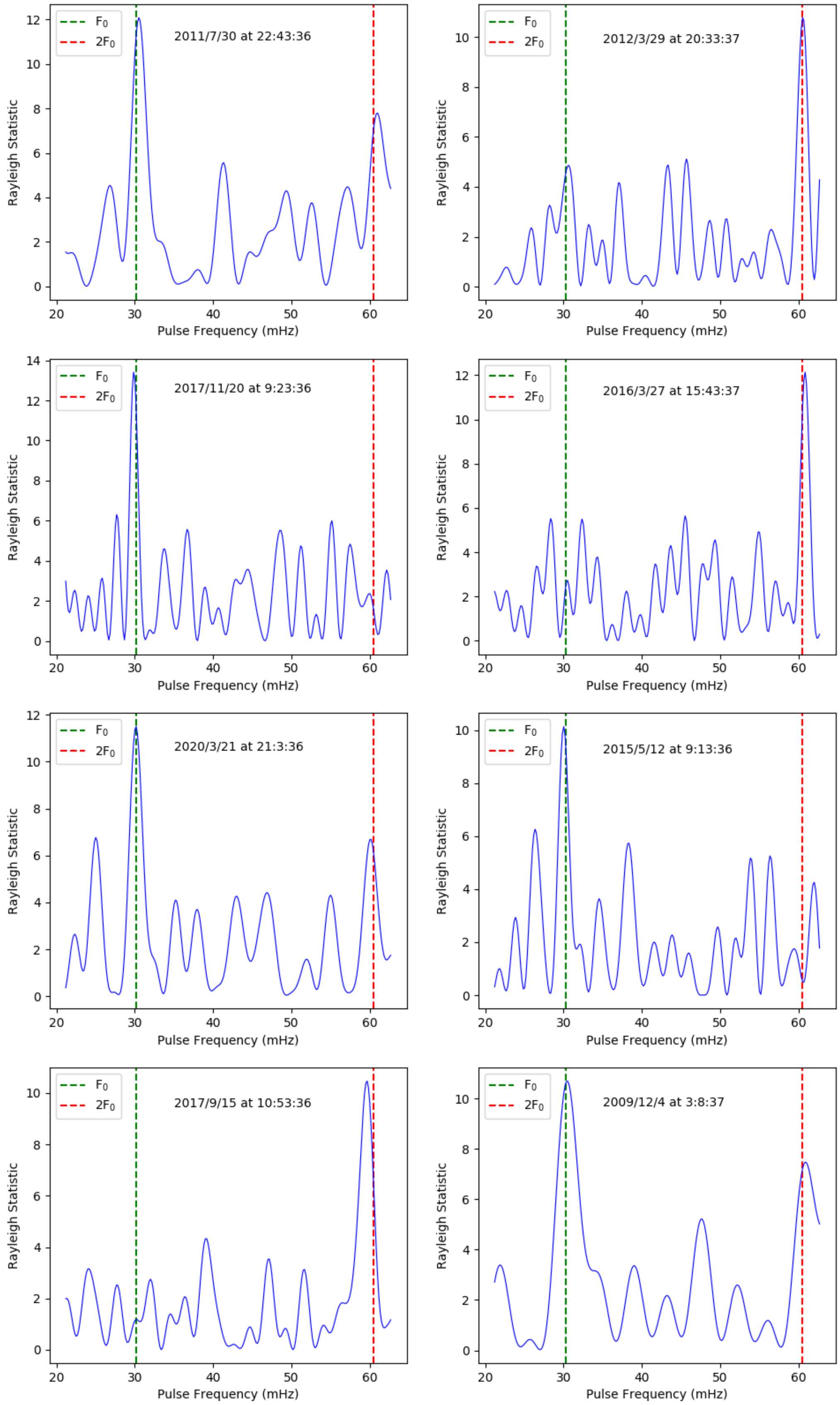

Figure B.18: The pulse profiles of AE Aqr showing the pulses at or near the fundamental frequency and the first harmonic.

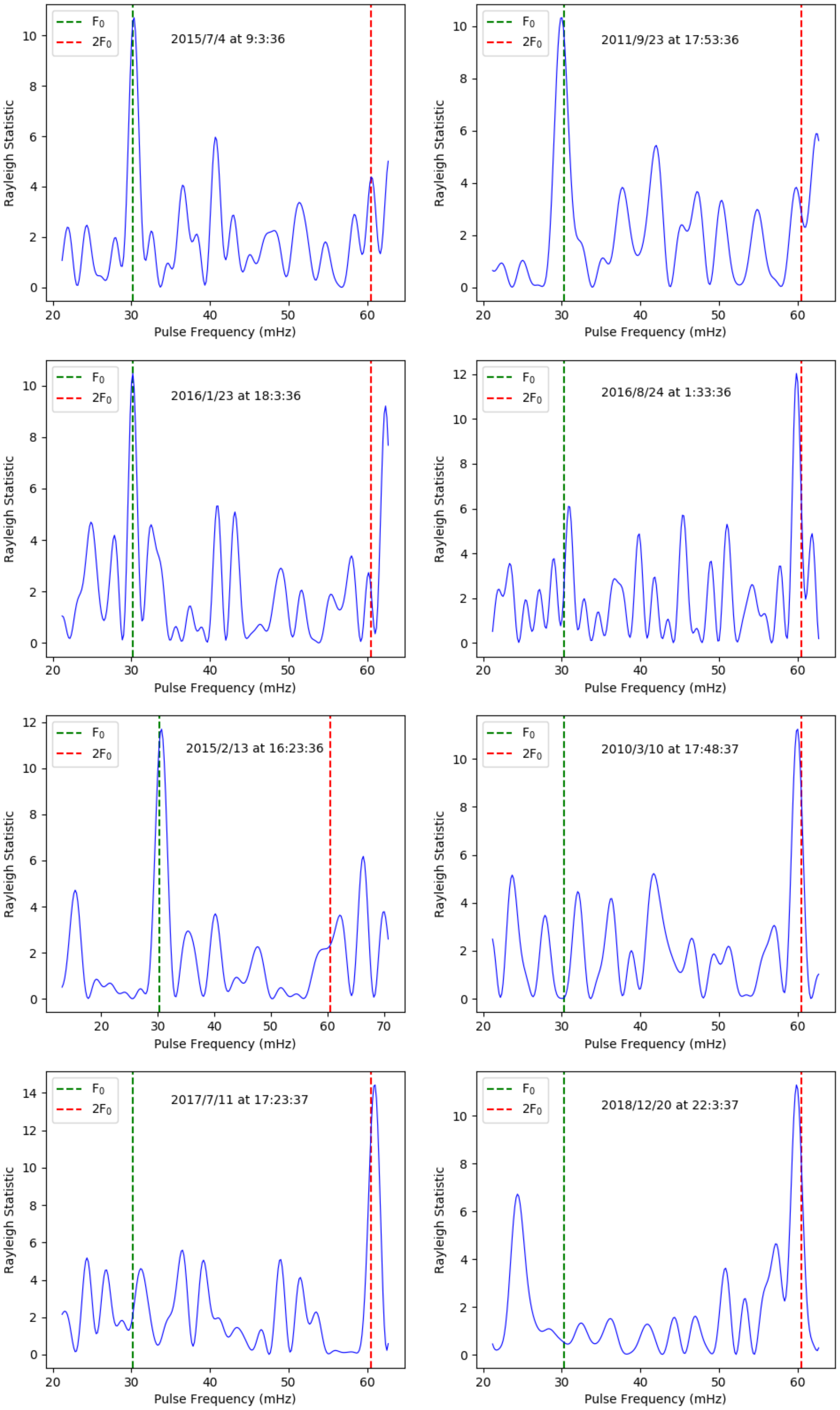

Figure B.19: The pulse profiles of AE Aqr showing the pulses at or near the fundamental frequency and the first harmonic.

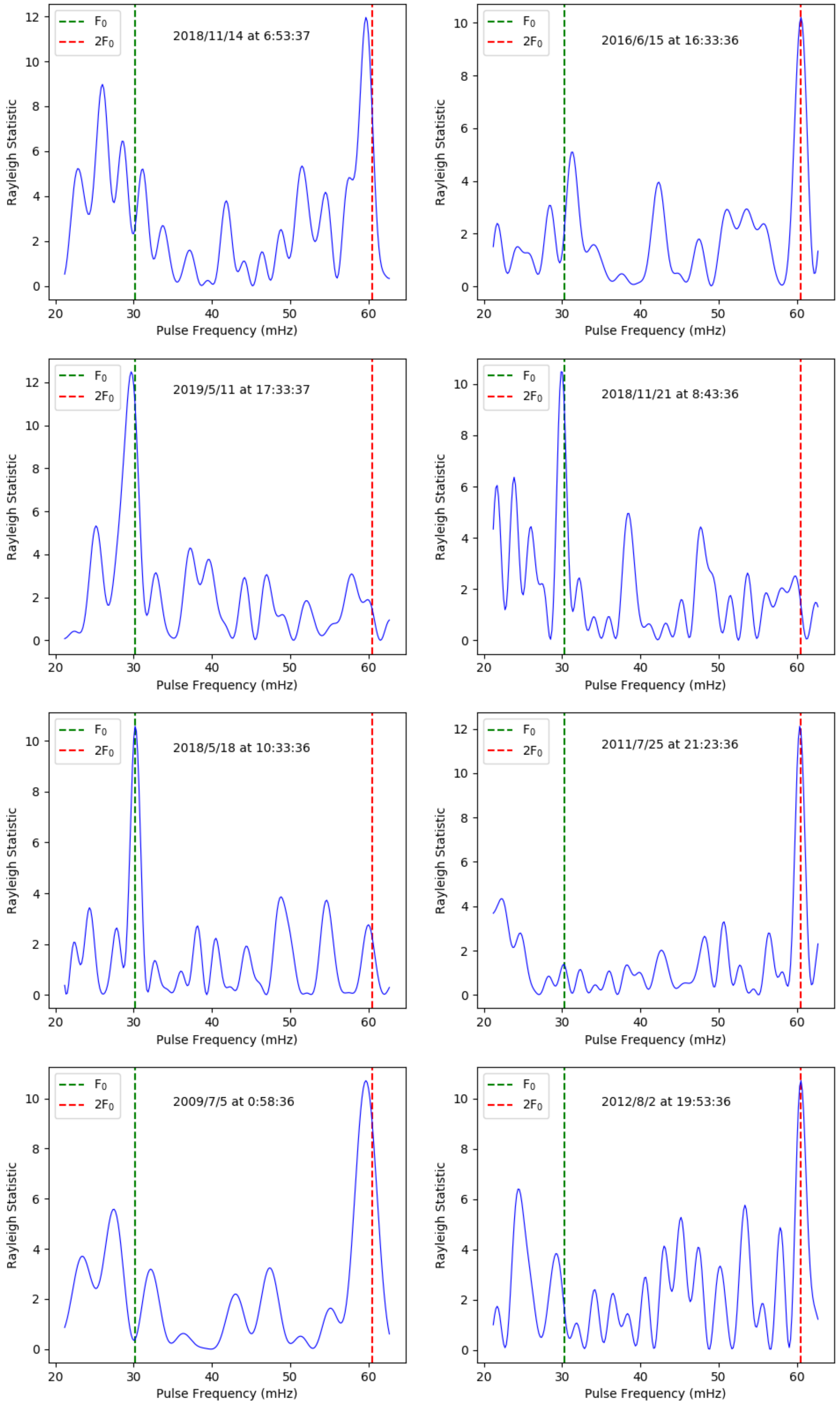

Figure B.20: The pulse profiles of AE Aqr showing the pulses at or near the fundamental frequency and the first harmonic.

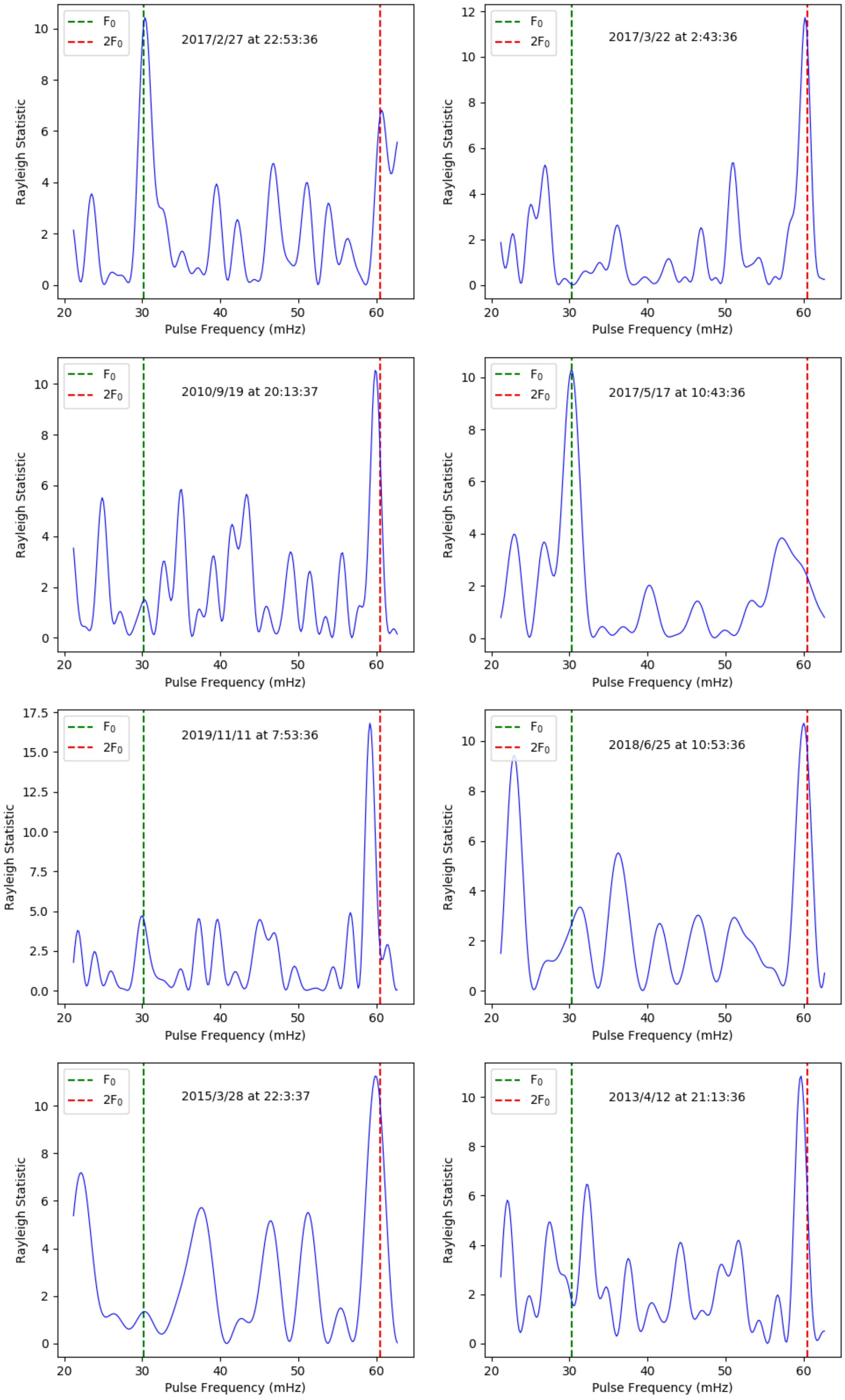

Figure B.21: The pulse profiles of AE Aqr showing the pulses at or near the fundamental frequency and the first harmonic.

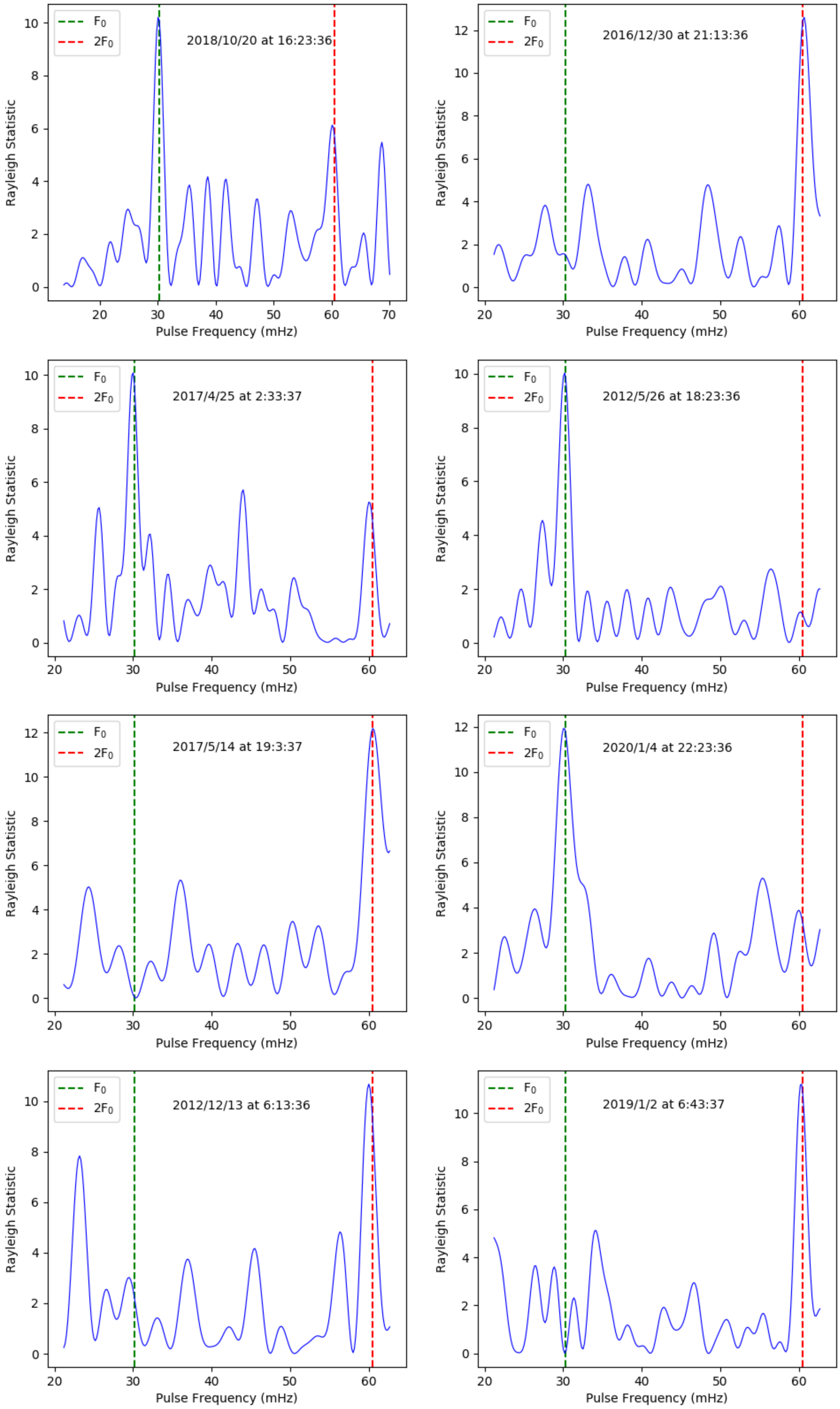

Figure B.22: The pulse profiles of AE Aqr showing the pulses at or near the fundamental frequency and the first harmonic.

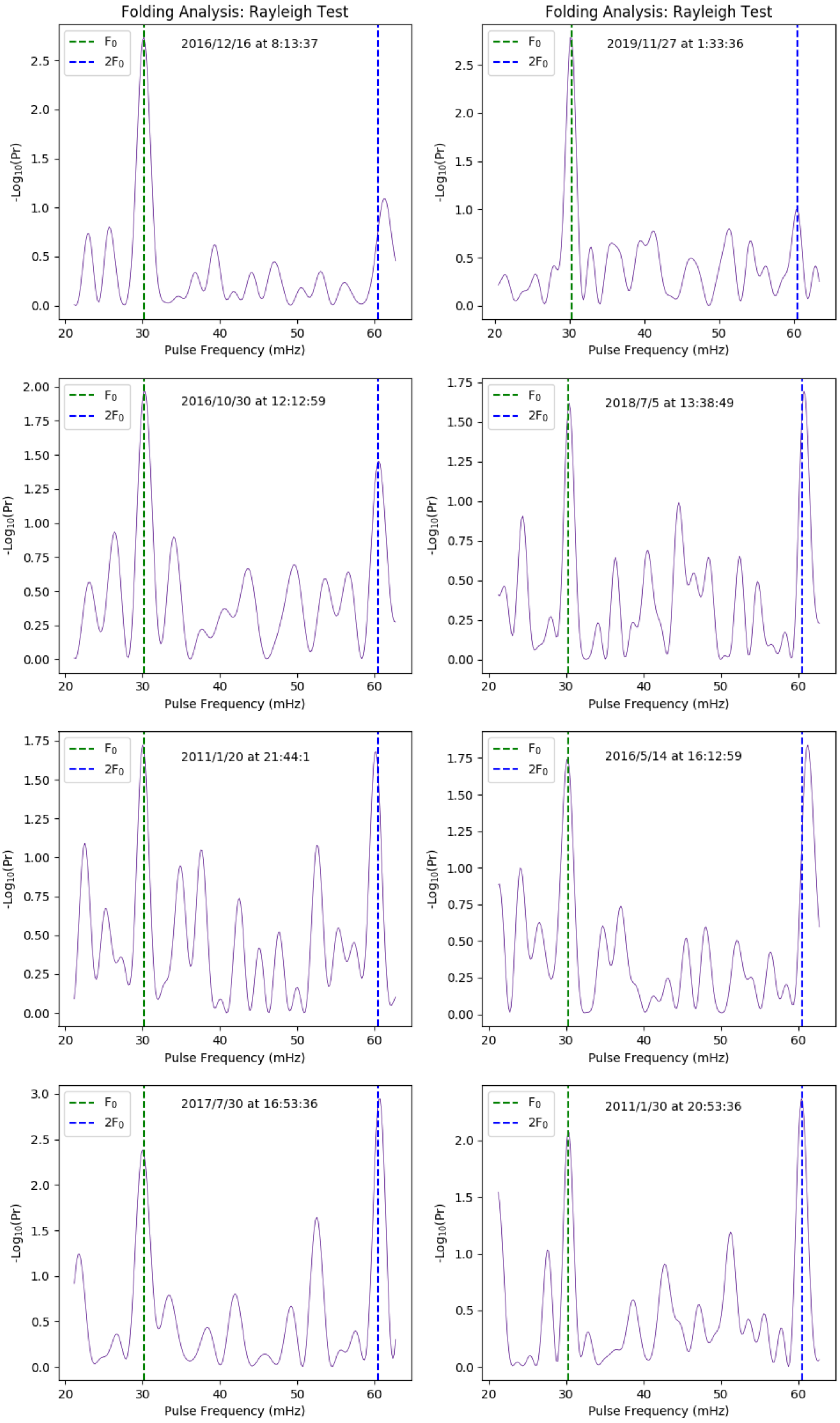

Figure B.23: The pulse profiles of AE Aqr showing the pulses at or near the fundamental frequency and the first harmonic.